# 3D nanopositioning based on tunneling current sensing and piezoactuation

Lukasz Ryba

UNIVERSITÉ GRENOBLE ALPES

# THÈSE

Pour obtenir le grade de

## DOCTEUR DE L'UNIVERSITÉ GRENOBLE ALPES

Spécialité : **AUTOMATIQUE - PRODUCTIQUE**

Arrêté ministériel : 7 août 2006

Présentée par

## « Łukasz RYBA »

Thèse dirigée par **« Alina VODA »** et
codirigée par **« Gildas BESANÇON »**

préparée au sein du **Laboratoire GIPSA-Lab (Grenoble Images Parole Signal Automatique)**
dans **l' École Doctorale EEATS (Electronique, Electrotechnique, Automatique et Traitement du Signal)**

# Nanopositionnement 3D à base de mesure à courant tunnel et piezo-actionnement

Thèse soutenue publiquement le **« 27 Novembre 2015 »**,
devant le jury composé de :

**M. Skandar BASROUR**
Professeur, Université Joseph Fourier, Président et Examinateur
**M. S.O.R. MOHEIMANI**
Professeur, Université du Texas à Dallas, Rapporteur
**M. Stéphane REGNIER**
Professeur, Université Pierre et Marie Curie, Rapporteur
**M. Micky RAKOTONDRABE**
Maître de conférences, Université de Franche-Comté, Examinateur
**Mme. Alina VODA**
Maître de conférences, Université Joseph Fourier, Directeur de thèse
**M. Gildas BESANÇON**
Professeur, Institut Polytechnique de Grenoble, Codirecteur de thèse
**M. Mohammad Al JANAIDEH**
Maître de conférences, Université de Toronto, Invitée

# Contents

# List of Figures

# List of Tables

# List of notations

## Chapter 1: State-of-the-art

| | |
|---|---|
| $E_F$ | Fermi level of metals |
| $E_{F_t}$ | Fermi level of the tip |
| $E_{F_s}$ | Fermi level of the surface |
| $\phi$ | Work function for metals |
| $V_b$ | Potential difference applied between two electrodes |
| $e$ | Electron charge |
| $m_e$ | Electron mass |
| $E$ | Electron total energy |
| $\hbar$ | Reduced Planck constant |
| $V(z)$ | Potential barrier |
| $d(t)$ | Length of the potential barrier (tunneling gap) |
| $z(t)$ | Vertical displacement of tunneling tip |
| $\psi(z)$ | Wave function of electron |
| $\psi_I(z)$ and $\psi_{III}(z)$ | Wave function of electron outside the potential barrier |
| $\psi_{II}(z)$ | Wave function of electron inside the potential barrier |
| $k_0$ | Wave number outside the potential barrier |
| $k_1$ | Wave number inside the potential barrier |
| $A_1, A_2$ and $C_1, C_2$ | Amplitude constants for the wave outside the potential barrier |
| $B_1, B_2$ | Amplitude constants for the wave inside the potential barrier |
| $\rho_{LS}(z, E)$ | Local density of states (LDOS) |
| $i_t(t)$ | Tunneling current |
| $g$ | Proportionality constant of tunneling current |
| $k$ | Constant of tunneling current |
| $u(t)$ | Input of piezoelectric actuator |
| $y(t)$ | Output of piezoelectric actuator |
| $\hat{\gamma}_{\alpha,\beta}[u(t)]$ | Relay operator of the Preisach model |
| $\alpha$ and $\beta$ | Thresholds for the relay operator in the Preisach model |
| $\mu(\alpha, \beta)$ | Density function for the realy operator in the Preisach model |
| $F_r[u](t)$ | Play operator of the Prandtl-Ishlinskii model |
| $r$ | Threshold for the play operator in the Prandtl-Ishlinskii model |
| $p(r)$ | Density function for the play operator in the Prandtl-Ishlinskii model |
| $t_0$ | Time instant at which the creep effect occurs |
| $y_0$ | Piezo output at time $t_0$ |
| $\gamma$ | Rate parameter of the nonlinear creep model |
| $k_{c_0}$ | Low frequency elastic behavior of the linear creep model |
| $k_{c_i}$ | Spring constant of a spring in the linear creep model |
| $c_{c_i}$ | Damping constant of a damper in the linear creep model |

## Chapter 2: System description and modeling

| | |
|---|---|
| $u_x(t)$ | Control signal for the X axis (voltage amplifier input) |
| $u_y(t)$ | Control signal for the Y axis (voltage amplifier input) |
| $u_z(t)$ | Control signal for the Z axis (voltage amplifier input) |
| $V_e(t)$ | Control signal for the Z axis (electrostatic actuator input) |
| $VA_x(s)$ | Model of the voltage amplifier (X axis) |
| $VA_y(s)$ | Model of the voltage amplifier (Y axis) |
| $VA_z(s)$ | Model of the voltage amplifier (Z axis) |
| $G_{vx}$ | Gain of the voltage amplifier (X axis) |
| $G_{vy}$ | Gain of the voltage amplifier (Y axis) |
| $G_{vz}$ | Gain of the voltage amplifier (Z axis) |
| $\omega_{vx}$ | Bandwidth of the voltage amplifier (X axis) |
| $\omega_{vy}$ | Bandwidth of the voltage amplifier (Y axis) |
| $\omega_{vz}$ | Bandwidth of the voltage amplifier (Z axis) |
| $v_{px}(t)$ | Piezo input voltage (X axis) |
| $v_{py}(t)$ | Piezo input voltage (Y axis) |
| $v_{pz}(t)$ | Piezo input voltage (Z axis) |
| $d_x(t)$ | Disturbance including hysteresis modeling error and creep (X axis) |
| $d_y(t)$ | Disturbance including hysteresis modeling error and creep (Y axis) |
| $d_z(t)$ | Disturbance including creep phenomenon (Z axis) |
| $\Gamma_x[v_{px}(t)]$ | Nonlinear operator representing static hysteresis model (X axis) |
| $\Gamma_y[v_{py}(t)]$ | Nonlinear operator representing static hysteresis model (Y axis) |
| $NL_x[v_{px}](t)$ | Operator representing total piezo nonlinearity (X axis) |
| $NL_y[v_{py}](t)$ | Operator representing total piezo nonlinearity (Y axis) |
| $q_{px}(t)$ | Output of quasi-static piezo nonlinearity (X axis) |
| $q_{py}(t)$ | Output of quasi-static piezo nonlinearity (Y axis) |
| $q_{pz}(t)$ | Output of quasi-static part of piezo (Z axis) |
| $D_{px}(s)$ | Direct piezo linear dynamics (X axis) |
| $D_{py}(s)$ | Direct piezo linear dynamics (Y axis) |
| $D_{pz}(s)$ | Direct piezo linear dynamics (Z axis) |
| $X_y(s)$ | Cross-coupling dynamics (from Y to X axis) |
| $Y_x(s)$ | Cross-coupling dynamics (from X to Y axis) |
| $Z_x(s)$ | Cross-coupling dynamics (from X to Z axis) |
| $Z_y(s)$ | Cross-coupling dynamics (from Y to Z axis) |
| $x_x(t)$ | Direct contribution to piezo displacement (X axis) |
| $y_y(t)$ | Direct contribution to piezo displacement (Y axis) |
| $z_z(t)$ | Direct contribution to piezo displacement (Z axis) |
| $x_y(t)$ | Cross-coupling contribution to piezo displacement (from Y to X axis) |
| $y_x(t)$ | Cross-coupling contribution to piezo displacement (from X to Y axis) |
| $z_x(t)$ | Cross-coupling contribution to piezo displacement (from X to Z axis) |
| $z_y(t)$ | Cross-coupling contribution to piezo displacement (from Y to Z axis) |

| | |
|---|---|
| $x_p(t)$ | Total piezo displacement (X axis) |
| $y_p(t)$ | Total piezo displacement (Y axis) |
| $z_p(t)$ | Total piezo displacement (Z axis) |
| $G_{px}$ | Gain of the piezoelectric actuator (X axis) |
| $G_{py}$ | Gain of the piezoelectric actuator (Y axis) |
| $G_{pz}$ | Gain of the piezoelectric actuator (Z axis) |
| $\omega_{px}$ | Bandwidth of the piezoelectric actuator (X axis) |
| $\omega_{py}$ | Bandwidth of the piezoelectric actuator (Y axis) |
| $\omega_{pz}$ | Bandwidth of the piezoelectric actuator (Z axis) |
| $\xi_{px}$ | Damping ratio of the piezoelectric actuator (X axis) |
| $\xi_{py}$ | Damping ratio of the piezoelectric actuator (Y axis) |
| $\xi_{pz}$ | Damping ratio of the piezoelectric actuator (Z axis) |
| $d_0$ | Initial tunneling gap between the tip and the surface |
| $d(t)$ | Tunneling gap between the tip and the surface |
| $i_t(t)$ | Tunneling current |
| $g$ | Proportionality constant of tunneling current |
| $k$ | Constant of tunneling current |
| $PL'_t$ | Exponential nonlinearity of the tunneling current |
| $CS_x(s)$ | Model of the capacitive sensor (X axis) |
| $CS_y(s)$ | Model of the capacitive sensor (Y axis) |
| $CS_t(s)$ | Model of the current sensor (Z axis) |
| $G_{capx}$ | Gain of the capacitive sensor (X axis) |
| $G_{capy}$ | Gain of the capacitive sensor (Y axis) |
| $G_t$ | Gain of the current sensor (Z axis) |
| $\omega_{capx}$ | Bandwidth of the capacitive sensor (X axis) |
| $\omega_{capy}$ | Bandwidth of the capacitive sensor (Y axis) |
| $\omega_t$ | Bandwidth of the current sensor (Z axis) |
| $v_x(t)$ | Output of the capacitive sensor (X axis) |
| $v_y(t)$ | Output of the capacitive sensor (Y axis) |
| $v_z(t)$ | Output of the current sensor (Z axis) |
| $n_1(t)$ | Measurement noise of the capacitive sensor (X axis) |
| $n_2(t)$ | Measurement noise of the capacitive sensor (Y axis) |
| $n_3(t)$ | Measurement noise of the current sensor (Z axis) |
| $y_1(t)$ | Final output of the capacitive sensor (X axis) |
| $y_2(t)$ | Final output of the capacitive sensor (Y axis) |
| $y_3(t)$ | Final output of the current sensor (Z axis) |
| $H$ | Hamaker constant |
| $R$ | Tip radius |
| $a_p$ | Interatomic value |
| $E^*_{eff}$ | Effective contact stiffness (between the tip and the cantilever) |
| $E_t$ | Elastic modulus of the tip |
| $E$ | Elastic modulus of the surface (cantilever) |
| $v_t$ | Poisson ratio of the tip |
| $v$ | Poisson ratio of the surface (cantilever) |
| $EA$ | Quadratic nonlinearity of the electrostatic actuator |
| $F_e(t)$ | Electrostatic force |
| $F_p(t)$ | Proximity force |
| $F_c(t)$ | Total input net force exciting the cantilever |

| | |
|---|---|
| $CNT(s)$ | Cantilever model |
| $INT_{tc}$ | Nonlinear block representing interaction force |
| $z_{c_e}(x,t)$ | Cantilver displacement (at the position $x$) due to electrostatic force |
| $z_{c_p}(x,t)$ | Cantilver displacement (at the position $x$) due to proximity force |
| $z_c(x,t)$ | Total cantilver displacement (at the position $x$) due to total force |
| $x_f$ | Position $x$ where the force $F_c(t)$ is applied at the cantilever input |
| $L$ | Length of the cantilever |
| $l_0$ | Distance between the unbended cantilever and the electrostatic plate |
| $l(t)$ | Actual distance between the cantilever and the electrostatic plate |
| $\varepsilon_0$ | Vacuum permittivity |
| $A_e$ | Common surface between the cantilever and the electrostatic plate |
| $A$ | Cross sectional area of the cantilever |
| $I$ | Area moment of inertia of the cantilever |
| $\rho$ | Density of the cantilever material |
| $\xi$ | Damping ratio for the modes (here the same for each mode) |
| $p_d(x,t)$ | Damping force (sum of the structural and electrostatic damping) |
| $m_j$ | Modal mass of $j^{th}$ mode |
| $c_j$ | Modal damping coefficient of $j^{th}$ mode |
| $k_j$ | Modal stiffness coefficient of $j^{th}$ mode |
| $\omega_j$ | Modal natural frequency of $j^{th}$ mode |
| $F_{c_j}(t)$ | Modal input force of the $j^{th}$ mode |
| $\lambda_j$ | Modal wave constant of the $j^{th}$ mode |
| $q_j(t)$ | Fundamental deformation of the $j^{th}$ mode (only time-dependent) |
| $\phi_j(x)$ | Modal shape function for the $j^{th}$ mode (only space-dependent) |
| $n_c$ | Number of modes |
| $x_{3D}(t)$ | State vector of the nonlinear 3D model |
| $u_{3D}(t)$ | Input vector of the nonlinear 3D model |
| $y_{3D}(t)$ | Output vector of the nonlinear 3D model |
| $d_{3D}(t)$ | Disturbance vector of the nonlinear 3D model |
| $n_{3D}(t)$ | Noise vector of the nonlinear 3D model |

## Chapter 3: Nonlinear hysteresis and creep

| | |
|---|---|
| $x_r(t)$ | Reference value of the capacitive voltage (X axis) |
| $y_r(t)$ | Reference value of the capacitive voltage (Y axis) |
| $u_x(t)$ | Control signal for the X axis (voltage amplifier input) |
| $u_y(t)$ | Control signal for the Y axis (voltage amplifier input) |
| $VA_x(s)$ | Model of the voltage amplifier (X axis) |
| $VA_y(s)$ | Model of the voltage amplifier (Y axis) |
| $G_{vx}$ | Gain of the voltage amplifier (X axis) |
| $G_{vy}$ | Gain of the voltage amplifier (Y axis) |
| $v_{px}(t)$ | Piezo input voltage (X axis) |
| $v_{py}(t)$ | Piezo input voltage (Y axis) |

| | |
|---|---|
| $d_x(t)$ | Disturbance including hysteresis modeling error and creep (X axis) |
| $d_y(t)$ | Disturbance including hysteresis modeling error and creep (Y axis) |
| $\hat{d}_x(t)$ | Estimate of $d_x(t)$ |
| $\hat{d}_y(t)$ | Estimate of $d_y(t)$ |
| $\Gamma_x\left[v_{px}(t)\right]$ | Nonlinear operator representing static hysteresis model (X axis) |
| $\Gamma_y\left[v_{py}(t)\right]$ | Nonlinear operator representing static hysteresis model (Y axis) |
| $NL_x[v_{px}](t)$ | Operator representing total piezo nonlinearity (X axis) |
| $NL_y[v_{py}](t)$ | Operator representing total piezo nonlinearity (Y axis) |
| $H_x[v_{px}](t)$ | Prandtl-Ishlinskii (PI) hysteresis operator (X axis) |
| $x_{p_H}(t)$ | Output of PI hysteresis operator (X axis) |
| $\boldsymbol{r}_{x_H}$ | Vector of thresholds of PI hysteresis operator (X axis) |
| $\boldsymbol{r'}_{x_H}$ | Vector of thresholds of inverse PI hysteresis operator (X axis) |
| $\boldsymbol{w}_{x_H}$ | Vector of weights of PI hysteresis operator (X axis) |
| $\boldsymbol{w'}_{x_H}$ | Vector of weights of inverse PI hysteresis operator (X axis) |
| $\boldsymbol{x}_{p_H0}$ | Vector of initial states of PI hysteresis operator (X axis) |
| $\boldsymbol{v}_{p_{x0}}$ | Vector of initial states of inverse PI hysteresis operator (X axis) |
| $\boldsymbol{H}_{r_{x_H}}[v_{px}, \boldsymbol{x}_{p_H0}](t)$ | Vector of backlashes of PI hysteresis operator (X axis) |
| $\boldsymbol{H}_{r'_{x_H}}[x_{p_H}, \boldsymbol{v}_{px0}](t)$ | Vector of backlashes of inverse PI hysteresis operator (X axis) |
| $n$ | Number of backlashes of PI hysteresis operator (X axis) |
| $S_x[x_{p_H}](t)$ | Prandtl-Ishlinskii (PI) superposition operator (X axis) |
| $x_{p_S}(t)$ | Output of PI superposition operator (X axis) |
| $\boldsymbol{r}_{x_S}$ | Vector of thresholds of PI superposition operator (X axis) |
| $\boldsymbol{r'}_{x_S}$ | Vector of thresholds of inverse PI superposition operator (X axis) |
| $\boldsymbol{w}_{x_S}$ | Vector of weights of PI superposition operator (X axis) |
| $\boldsymbol{w'}_{x_S}$ | Vector of weights of inverse PI superposition operator (X axis) |
| $\boldsymbol{S}_{r_{x_S}}[x_{p_H}](t)$ | Vector of dead-zones of PI superposition operator (X axis) |
| $\boldsymbol{S}_{r'_{x_S}}[x_{p_S}](t)$ | Vector of dead-zones of inverse PI superposition operator (X axis) |
| $m$ | Number of dead-zones of PI superposition operator (X axis) |
| $\tilde{x}_p(t)$ | Piezo displacement obtained from the measured output $y_1(t)$ (X axis) |
| $\boldsymbol{w}_x$ | Unknown MPI model weights (X axis) |
| $J_x(\boldsymbol{w}_x)$ | Loss function for the identification of model weights (X axis) |
| $F_x$ | Hessian matrix - quadratic term in the loss function (X axis) |
| $\boldsymbol{f}_{x_1}$ | Vector - linear term in the loss function (X axis) |
| $f_{x_0}$ | Scalar - absolute term in the loss function (X axis) |
| $l$ | Number of collected data |
| $\boldsymbol{U}_H, \boldsymbol{U'}_S$ | Matrices for the constrained problem |
| $\boldsymbol{u}_H, \boldsymbol{u'}_S$ | Vectors for the constrained problem |
| $q_{px}(t)$ | Output of quasi-static piezo nonlinearity (X axis) |
| $q_{py}(t)$ | Output of quasi-static piezo nonlinearity (Y axis) |
| $D_{px}(s)$ | Direct piezo linear dynamics (X axis) |
| $D_{py}(s)$ | Direct piezo linear dynamics (Y axis) |
| $x_p(t)$ | Total piezo displacement (X axis) |
| $y_p(t)$ | Total piezo displacement (Y axis) |
| $G_{px}$ | Gain of the piezoelectric actuator (X axis) |
| $G_{py}$ | Gain of the piezoelectric actuator (Y axis) |

| | |
|---|---|
| $\omega_{px}$ | Bandwidth of the piezoelectric actuator (X axis) |
| $\omega_{py}$ | Bandwidth of the piezoelectric actuator (Y axis) |
| $\xi_{px}$ | Damping ratio of the piezoelectric actuator (X axis) |
| $\xi_{py}$ | Damping ratio of the piezoelectric actuator (Y axis) |
| $CS_x(s)$ | Model of the capacitive sensor (X axis) |
| $CS_y(s)$ | Model of the capacitive sensor (Y axis) |
| $G_{capx}$ | Gain of the capacitive sensor (X axis) |
| $G_{capy}$ | Gain of the capacitive sensor (Y axis) |
| $v_x(t)$ | Output of the capacitive sensor (X axis) |
| $v_y(t)$ | Output of the capacitive sensor (Y axis) |
| $n_1(t)$ | Measurement noise of the capacitive sensor (X axis) |
| $n_2(t)$ | Measurement noise of the capacitive sensor (Y axis) |
| $y_1(t)$ | Final output of the capacitive sensor (X axis) |
| $y_2(t)$ | Final output of the capacitive sensor (Y axis) |
| $T_s$ | Sampling time |
| $f_s$ | Sampling frequency |
| $u_1(t)$ | Control input with DOB compensation (X axis) |
| $u_2(t)$ | Control input with DOB compensation (Y axis) |
| $x(t)$ | State vector (X axis) |
| $A_x, B_x, C_x$ | System matrices (X axis) |
| $B_{d_x}$ | Disturbance matrix (X axis) |
| $w_x(t)$ | Process noise (X axis) |
| $x_e(t)$ | Extended state vector (X axis) |
| $A_{e_x}, B_{e_x}, C_{e_x}$ | Matrices of the extended system (X axis) |
| $L_x$ | Kalman gain matrix (X axis) |
| $W_x$ | Process covariance (X axis) |
| $N_1$ | Noise covariance (X axis) |
| $P_x$ | Solution of Algebraic Riccati Equation (ARE) |
| $\hat{y}_1(t)$ | Estimate of $y_1(t)$ |
| $l_H$ | Major hysteresis loop width |
| $L_H$ | Range of the reference signal |
| $p$ | Order of polynomial used in adaptive approach |
| $u_k$ | Control voltage in adaptive approach |
| $\theta_k$ | Vector of unknown polynomial coefficients in adaptive approach |
| $y_{m_k}$ | Model plant output in adaptive approach |
| $y_k$ | Real plant output in adaptive approach |
| $e_k$ | Mismatch between real plant and its model in adaptive approach |
| $r_k$ | Reference signal in adaptive approach |
| $g(u_k, \theta_k)$ | Parametric model of static nonlinearity in adaptive approach |
| $h_k$ | Regression vector in adaptive approach |
| $d_k$ | Inverse of the unknown variance in adaptive approach |
| $\Theta_k$ | Vector of all uknown parameters (polynomial coefficients and variance) |
| $D_k$ | Set of the observed input/output data up to the instant $k$ |
| $f(\Theta_k \mid D^k)$ | Posterior probability density function (pdf) |
| $f_0(\Theta_{k+1})$ | Alternative for pdf, when the parameters are not changing |
| $f_1(\Theta_{k+1})$ | Alternative for pdf, when the parameters are uniquely distributed |
| $f_A(\Theta_{k+1})$ | Unknown pdf |
| $f_A^*(\Theta_{k+1})$ | Decision space of $f_A(\Theta_{k+1})$ |

| | |
|---|---|
| $\varphi_0$ | Probability that $f_A(\Theta_{k+1}) = f_0(\Theta_{k+1})$ |
| $\varphi_1$ | Probability that $f_A(\Theta_{k+1}) = f_1(\Theta_{k+1})$ |
| $\varphi$ | $\varphi \equiv \left[\varphi_0, \varphi_1\right]'$ |
| $\mathcal{D}\big(f \| f_A\big)$ | Kullback-Leibler divergence |
| $\Theta^*$ | Space of $\Theta_k$ |
| $\phi(f, \varphi)$ | Cost function in adaptive approach |
| $\varrho_0$ | Penalty coefficient for the success of alternative $f_0(\Theta_{k+1})$ |
| $\varrho_1$ | Penalty coefficient for the success of alternative $f_1(\Theta_{k+1})$ |
| $\rho$ | Positive tuning parameter in adaptive approach |
| $\lambda_{k\|k}$ | Variable forgetting factor in adaptive approach |
| $P_{k\|k}$ | Normalized covariance matrix in adaptive approach |
| $\Sigma_{k\|k}$ | Least-squares reminder in adaptive approach |
| $v_{k\|k}$ | Number of degrees of freedom in adaptive approach |
| $f(u_k, \theta_k, r_k)$ | Function of which the roots are looked for in numerical algorithm |
| $u^0$ | Starting point in the Newton's method |
| $u_L$ | Left value for the interval in the Bisection method |
| $u_R$ | Right value for the interval in the Bisection method |
| $u_B$ | Control input computed by the Newton's method |
| $u_N$ | Control input computed by the Bisection method |

## Chapter 4: Structural vibration and cross-couplings

| | |
|---|---|
| $r(t)$ | General reference signal |
| $y(t)$ | General plant output |
| $d(t)$ | General disturbance signal |
| $n(t)$ | General measurement noise signal |
| $G_p(s)$ | General perturbed plant |
| $G_{xx_p}(s)$ | Perturbed plant from the input $x_h$ to the output $y_1$ |
| $G_{yy_p}(s)$ | Perturbed plant from the input $y_h$ to the output $y_2$ |
| $G_{xy_p}(s)$ | Perturbed plant from the input $y_h$ to the output $y_1$ |
| $G_{yx_p}(s)$ | Perturbed plant from the input $x_h$ to the output $y_2$ |
| $G(s)$ | General nominal plant |
| $G_{xx}(s)$ | Nominal plant from the input $x_h$ to the output $y_1$ |
| $G_{yy}(s)$ | Nominal plant from the input $y_h$ to the output $y_2$ |
| $G_{xy}(s)$ | Nominal plant from the input $y_h$ to the output $y_1$ |
| $G_{yx}(s)$ | Nominal plant from the input $x_h$ to the output $y_2$ |
| $C(s)$ | General controller |
| $C_x(s)$ | Controller designed on the basis of $G_{xx}(s)$ |
| $C_y(s)$ | Controller designed on the basis of $G_{yy}(s)$ |
| $W_\Delta(s)$ | General uncertainty weight |
| $\Delta(s)$ | General normalized complex perturbations |
| $l_\Delta(\omega)$ | General relative magnitude of the neglected dynamics |

| | |
|---|---|
| $\sigma_{xx_p}$ | Hankel singular values of $G_{xx_p}(s)$ |
| $\sigma_{yy_p}$ | Hankel singular values of $G_{yy_p}(s)$ |
| $\sigma_{xy_p}$ | Hankel singular values of $G_{xy_p}(s)$ |
| $\sigma_{yx_p}$ | Hankel singular values of $G_{yx_p}(s)$ |
| $x_{xx}$ | State vector of $G_{xx}(s)$ |
| $x_{yy}$ | State vector of $G_{yy}(s)$ |
| $x_h$ | Control signal (X axis) |
| $y_h$ | Control signal (Y axis) |
| $y_1$ | Output signal (X axis) |
| $y_2$ | Output signal (Y axis) |
| $w_{xx}$ | Process noise of $G_{xx}(s)$ |
| $w_{yy}$ | Process noise of $G_{yy}(s)$ |
| $n_1$ | Measurement noise (X axis) |
| $n_2$ | Measurement noise (Y axis) |
| $A_{xx}, B_{xx}, C_{xx}$ | State matrices of $G_{xx}(s)$ |
| $A_{yy}, B_{yy}, C_{yy}$ | State matrices of $G_{yy}(s)$ |
| $G_{xx_a}$ | Augmented $G_{xx}(s)$ (with integral action) |
| $G_{yy_a}$ | Augmented $G_{yy}(s)$ (with integral action) |
| $x_{xx_a}$ | State vector of $G_{xx_a}(s)$ |
| $x_{yy_a}$ | State vector of $G_{yy_a}(s)$ |
| $A_{xx_a}, B_{xx_a}, C_{xx_a}$ | State matrices of $G_{xx_a}(s)$ |
| $A_{yy_a}, B_{yy_a}, C_{yy_a}$ | State matrices of $G_{yy_a}(s)$ |
| $J_x(\dot{x}_h)$ | Quadratic cost function for LQG/LTR controller (X axis) |
| $J_y(\dot{y}_h)$ | Quadratic cost function for LQG/LTR controller (Y axis) |
| $W_{xx_a}$ | Process covariance matrix of $w_{xx_a}$ |
| $W_{yy_a}$ | Process covariance matrix of $w_{yy_a}$ |
| $N_1$ | Noise covariance matrix of $n_1$ |
| $N_2$ | Noise covariance matrix of $n_2$ |
| $K_{f_{xx_a}}$ | Kalman Filter gain associated with $G_{xx_a}(s)$ |
| $K_{f_{yy_a}}$ | Kalman Filter gain associated with $G_{yy_a}(s)$ |
| $P_{xx_a}$ | Solution of Kalman Filter ARE associated with $G_{xx_a}(s)$ |
| $P_{yy_a}$ | Solution of Kalman Filter ARE associated with $G_{yy_a}(s)$ |
| $\rho_x$ | Scaling parameter for Kalman Filter associated with $G_{xx_a}(s)$ |
| $\rho_y$ | Scaling parameter for Kalman Filter associated with $G_{yy_a}(s)$ |
| $Q_{xx_a}$ | Weighting matrix for the state of $G_{xx_a}(s)$ |
| $Q_{yy_a}$ | Weighting matrix for the state of $G_{yy_a}(s)$ |
| $R_{xx_a}$ | Weighting matrix for the control of $G_{xx_a}(s)$ |
| $R_{yy_a}$ | Weighting matrix for the control of $G_{yy_a}(s)$ |
| $K_{c_{xx_a}}$ | LQR gain associated with $G_{xx_a}(s)$ |
| $K_{c_{yy_a}}$ | LQR gain associated with $G_{yy_a}(s)$ |
| $S_{xx_a}$ | Solution of LQR ARE associated with $G_{xx_a}(s)$ |
| $S_{yy_a}$ | Solution of LQR ARE associated with $G_{yy_a}(s)$ |
| $q_x$ | Recovery gain for LQG/LTR associated with $G_{xx_a}(s)$ |
| $q_y$ | Recovery gain for LQG/LTR associated with $G_{yy_a}(s)$ |
| $K_{x_{LQG/LTR}}(s)$ | LQG/LTR controller (without integral action) for the X axis |
| $K_{y_{LQG/LTR}}(s)$ | LQG/LTR controller (without integral action) for the Y axis |
| $LTF_{P_{1_x}}(s)$ | Loop Transfer Function (LTF) at point $P_{1_x}$ |
| $LTF_{P_{1_y}}(s)$ | Loop Transfer Function (LTF) at point $P_{1_y}$ |

| | |
|---|---|
| $LTF_{P_{2_x}}(s)$ | Loop Transfer Function (LTF) at point $P_{2_x}$ |
| $LTF_{P_{2_y}}(s)$ | Loop Transfer Function (LTF) at point $P_{2_y}$ |
| $P(s)$ | General augmented plant (with weighting functions) |
| $F_l(P(s), C(s))$ | Lower linear fractional transformation |
| $\gamma^*$ | Optimal cost in $\mathcal{H}_\infty$ design |
| $\gamma$ | Sub-optimal cost in $\mathcal{H}_\infty$ design |
| $\Delta\phi$ | Phase margin |
| $\Delta G$ | Gain margin |
| $\Delta M$ | Module margin |
| $S(s)$ | General output sensitivity function |
| $R(s)$ | General input sensitivity function |
| $T(s)$ | General complementary sensitivity function |
| $W_S(s)$ | General weighting function for $S(s)$ |
| $W_R(s)$ | General weighting function for $R(s)$ |
| $W_T(s)$ | General weighting function for $T(s)$ |
| $W_\Delta(s)$ | General weighting function for system uncertainty |
| $\omega_\Delta$ | Bandwidth of $W_\Delta(s)$ |
| $A_\Delta$ | Lower bound of $W_\Delta(s)$ |
| $M_\Delta$ | Upper bound of $W_\Delta(s)$ |
| $n_\Delta$ | Order of $W_\Delta(s)$ |
| $W_e(s)$ | General weighting function for tracking |
| $\omega_e$ | Bandwidth of $W_e(s)$ |
| $A_e$ | Lower bound of $W_e(s)$ |
| $M_e$ | Upper bound of $W_e(s)$ |
| $n_e$ | Order of $W_e(s)$ |
| $W_u(s)$ | General weighting function for control |
| $\omega_u$ | Bandwidth of $W_u(s)$ |
| $A_u$ | Lower bound of $W_u(s)$ |
| $M_u$ | Upper bound of $W_u(s)$ |
| $n_u$ | Order of $W_u(s)$ |
| $\gamma_x$ | Sub-optimal cost in $\mathcal{H}_\infty$ design (X axis) |
| $\gamma_y$ | Sub-optimal cost in $\mathcal{H}_\infty$ design (Y axis) |
| $S_x(s)$ | Output sensitivity function (X axis) |
| $S_y(s)$ | Output sensitivity function (Y axis) |
| $R_x(s)$ | Input sensitivity function (X axis) |
| $R_y(s)$ | Input sensitivity function (Y axis) |
| $T_x(s)$ | Complementary sensitivity function (X axis) |
| $T_y(s)$ | Complementary sensitivity function (Y axis) |
| $W_{S_x}(s)$ | Weighting function for $S_x(s)$ |
| $W_{S_y}(s)$ | Weighting function for $S_y(s)$ |
| $W_{R_x}(s)$ | Weighting function for $R_x(s)$ |
| $W_{R_y}(s)$ | Weighting function for $R_y(s)$ |
| $W_{T_x}(s)$ | Weighting function for $T_x(s)$ |
| $W_{T_y}(s)$ | Weighting function for $T_y(s)$ |
| $W_{x_\Delta}(s)$ | Weighting function for system uncertainty (X axis) |
| $W_{y_\Delta}(s)$ | Weighting function for system uncertainty (Y axis) |

| | |
|---|---|
| $\omega_{x_\Delta}$ | Bandwidth of $W_{x_\Delta}(s)$ |
| $\omega_{y_\Delta}$ | Bandwidth of $W_{y_\Delta}(s)$ |
| $A_{x_\Delta}$ | Lower bound of $W_{x_\Delta}(s)$ |
| $A_{y_\Delta}$ | Lower bound of $W_{y_\Delta}(s)$ |
| $M_{x_\Delta}$ | Upper bound of $W_{x_\Delta}(s)$ |
| $M_{y_\Delta}$ | Upper bound of $W_{y_\Delta}(s)$ |
| $n_{x_\Delta}$ | Order of $W_{x_\Delta}(s)$ |
| $n_{y_\Delta}$ | Order of $W_{y_\Delta}(s)$ |
| $W_{e_x}(s)$ | Weighting function for tracking (X axis) |
| $W_{e_y}(s)$ | Weighting function for tracking (Y axis) |
| $\omega_{e_x}$ | Bandwidth of $W_{e_x}(s)$ |
| $\omega_{e_y}$ | Bandwidth of $W_{e_y}(s)$ |
| $A_{e_x}$ | Lower bound of $W_{e_x}(s)$ |
| $A_{e_y}$ | Lower bound of $W_{e_y}(s)$ |
| $M_{e_x}$ | Upper bound of $W_{e_x}(s)$ |
| $M_{e_y}$ | Upper bound of $W_{e_y}(s)$ |
| $n_{e_x}$ | Order of $W_{e_x}(s)$ |
| $n_{e_y}$ | Order of $W_{e_y}(s)$ |
| $W_{u_x}(s)$ | Weighting function for control (X axis) |
| $W_{u_y}(s)$ | Weighting function for control (Y axis) |
| $\omega_{u_x}$ | Bandwidth of $W_{u_x}(s)$ |
| $\omega_{u_y}$ | Bandwidth of $W_{u_y}(s)$ |
| $A_{u_x}$ | Lower bound of $W_{u_x}(s)$ |
| $A_{u_y}$ | Lower bound of $W_{u_y}(s)$ |
| $M_{u_x}$ | Upper bound of $W_{u_x}(s)$ |
| $M_{u_y}$ | Upper bound of $W_{u_y}(s)$ |
| $n_{u_x}$ | Order of $W_{u_x}(s)$ |
| $n_{u_y}$ | Order of $W_{u_y}(s)$ |
| $\boldsymbol{S}(s)$ | Output sensitivity function for MIMO system |
| $\boldsymbol{R}(s)$ | Input sensitivity function for MIMO system |
| $\boldsymbol{T}(s)$ | Complementary sensitivity function for MIMO system |
| $\boldsymbol{W}_S(s)$ | Weighting function for $\boldsymbol{S}_S(s)$ |
| $\boldsymbol{W}_R(s)$ | Weighting function for $\boldsymbol{R}_R(s)$ |
| $\boldsymbol{W}_T(s)$ | Weighting function for $\boldsymbol{T}_T(s)$ |
| $\underline{\sigma}(X(j\omega))$ | Minimum singular value of matrix $X$ |
| $\overline{\sigma}(X(j\omega))$ | Maximum singular value of matrix $X$ |

## Chapter 5: Tunneling current

| | |
|---|---|
| $u_z(t)$ | Control signal for the Z axis (voltage amplifier input) |
| $VA_z(s)$ | Model of the voltage amplifier (Z axis) |
| $G_{vz}$ | Gain of the voltage amplifier (Z axis) |
| $\omega_{vz}$ | Bandwidth of the voltage amplifier (Z axis) |
| $v_{pz}(t)$ | Piezo input voltage (Z axis) |
| $d_z(t)$ | Disturbance including creep (Z axis) |
| $D_{pz}(s)$ | Direct piezo linear dynamics (Z axis) |
| $z_z(t)$ | Direct contribution to piezo displacement (Z axis) |
| $z_x(t)$ | Cross-coupling contribution to piezo displacement (from X to Z axis) |
| $z_y(t)$ | Cross-coupling contribution to piezo displacement (from Y to Z axis) |
| $z_p(t)$ | Total piezo displacement (Z axis) |
| $z_s(t)$ | Surface variations |
| $Piezo_z(s)$ | Model of the piezoelectric actuator (Z axis) |
| $G_{pz}$ | Gain of the piezoelectric actuator (Z axis) |
| $\omega_{pz}$ | Bandwidth of the piezoelectric actuator (Z axis) |
| $\xi_{pz}$ | Damping ratio of the piezoelectric actuator (Z axis) |
| $d_0$ | Initial tunneling gap between the tip and the surface |
| $d(t)$ | Tunneling gap between the tip and the surface |
| $d_{eq}$ | Equilibrium gap between the tip and the surface |
| $\Delta d(t)$ | Gap deviation from its equilibrium $d_{eq}$ |
| $i_t(t)$ | Tunneling current |
| $i_{eq}$ | Equilibrium tunneling current |
| $\Delta i_t(t)$ | Tunneling current deviation from its equilibrium $i_{eq}$ |
| $V_b$ | Bias Voltage |
| $g$ | Proportionality constant of tunneling current |
| $k$ | Constant of tunneling current |
| $PL'_t$ | Exponential nonlinearity of the tunneling current |
| $e$ | Electron charge |
| $m_e$ | Electron mass |
| $\phi$ | Work function for metals |
| $CS_t(s)$ | Model of the current sensor |
| $G_t$ | Gain of the current sensor |
| $\omega_t$ | Bandwidth of the current sensor |
| $v_z(t)$ | Output of the current sensor |
| $n_3(t)$ | Measurement noise of the current sensor |
| $y_3(t)$ | Final output of the current sensor |
| $z_r(t)$ | Reference value of the tunneling voltage |
| $G_z(s)$ | Continuous-time plant model (Z axis) |
| $H(z^{-1})$ | Discrete-time plant model (Z axis) |
| $f_s$ | Sampling frequency |
| $d_l$ | System pure delay expressed in number of sampling periods |

| | |
|---|---|
| $B(z^{-1})$ | Polynomial representing numerator of $H(z^{-1})$ |
| $A(z^{-1})$ | Polynomial representing denominator of $H(z^{-1})$ |
| $R(z^{-1})$ | Polynomial representing numerator of the digital controller |
| $S(z^{-1})$ | Polynomial representing denominator of the digital controller |
| $P_D(z^{-1})$ | Polynomial representing desired closed-loop poles |
| $P_F(z^{-1})$ | Polynomial representing auxiliary closed-loop poles |
| $P(z^{-1})$ | Polynomial representing closed-loop poles |
| $H_R(z^{-1})$ | Polynomial representing fixed part of $R(z^{-1})$ |
| $H_S(z^{-1})$ | Polynomial representing fixed part of $S(z^{-1})$ |
| $R'(z^{-1})$ | Polynomial representing free part of $R(z^{-1})$ |
| $S'(z^{-1})$ | Polynomial representing free part of $S(z^{-1})$ |
| $n_A$ | Degree of polynomial $A(z^{-1})$ |
| $n_B$ | Degree of polynomial $B(z^{-1})$ |
| $n_R$ | Degree of polynomial $R(z^{-1})$ |
| $n_S$ | Degree of polynomial $S(z^{-1})$ |
| $n_{H_R}$ | Degree of polynomial $H_R(z^{-1})$ |
| $n_{H_S}$ | Degree of polynomial $H_S(z^{-1})$ |
| $\omega_0$ | Desired closed-loop bandwidth |
| $\xi$ | Desired closed-loop damping |
| $H_{CL}(z^{-1})$ | Closed-loop transfer function |
| $S_{yp}(z^{-1})$ | Output sensitivity function |
| $S_{yr}(z^{-1})$ | Complementary sensitivity function |
| $S_{up}(z^{-1})$ | Input sensitivity function |

## Chapter 6: 3D results for nanopositioning and STM applications

| | |
|---|---|
| $x_r(t)$ | Reference value of the capacitive voltage (X axis) |
| $y_r(t)$ | Reference value of the capacitive voltage (Y axis) |
| $z_r(t)$ | Reference value of the tunneling voltage |
| $x_{r_0}$ | Starting point (initial value) for $x_r(t)$ |
| $y_{r_0}$ | Starting point (initial value) for $y_r(t)$ |
| $A_r$ | Amplitude of the triangle reference signal $x_r(t)$ |
| $f_r$ | Frequency of the triangle reference signal $x_r(t)$ |
| $\alpha_r$ | Slope of the ramp reference signal $y_r(t)$ |
| $r_s(t)$ | Instantaneous spiral radius |
| $\theta_s(t)$ | Instantaneous spiral angle |
| $\omega_s(t)$ | Spiral angular velocity |
| $P_s$ | Spiral pitch |
| $R_s$ | Non-instantaneous spiral radius |
| $N_s$ | Number of crossing points of the spiral signal |
| $u_x(t)$ | Control signal for the X axis (voltage amplifier input) |
| $u_y(t)$ | Control signal for the Y axis (voltage amplifier input) |
| $u_z(t)$ | Control signal for the Z axis (voltage amplifier input) |

| | |
|---|---|
| $VA_x(s)$ | Model of the voltage amplifier (X axis) |
| $VA_y(s)$ | Model of the voltage amplifier (Y axis) |
| $VA_z(s)$ | Model of the voltage amplifier (Z axis) |
| $G_{vx}$ | Gain of the voltage amplifier (X axis) |
| $G_{vy}$ | Gain of the voltage amplifier (Y axis) |
| $G_{vz}$ | Gain of the voltage amplifier (Z axis) |
| $\omega_{vx}$ | Bandwidth of the voltage amplifier (X axis) |
| $\omega_{vy}$ | Bandwidth of the voltage amplifier (Y axis) |
| $\omega_{vz}$ | Bandwidth of the voltage amplifier (Z axis) |
| $v_{px}(t)$ | Piezo input voltage (X axis) |
| $v_{py}(t)$ | Piezo input voltage (Y axis) |
| $v_{pz}(t)$ | Piezo input voltage (Z axis) |
| $H_x[v_{px}](t)$ | Nonlinear operator representing static hysteresis PI model (X axis) |
| $H_y[v_{py}](t)$ | Nonlinear operator representing static hysteresis PI model (Y axis) |
| $q_{px}(t)$ | Output of static piezo nonlinearity (X axis) |
| $q_{py}(t)$ | Output of static piezo nonlinearity (Y axis) |
| $q_{pz}(t)$ | Output of static part of piezo (Z axis) |
| $G_{creepx}(s)$ | Creep linear dynamics (X axis) |
| $G_{creepy}(s)$ | Creep linear dynamics (Y axis) |
| $D_{px}(s)$ | Direct piezo linear dynamics (X axis) |
| $D_{py}(s)$ | Direct piezo linear dynamics (Y axis) |
| $D_{pz}(s)$ | Direct piezo linear dynamics (Z axis) |
| $G_{px}$ | Gain of the piezoelectric actuator (X axis) |
| $G_{py}$ | Gain of the piezoelectric actuator (Y axis) |
| $G_{pz}$ | Gain of the piezoelectric actuator (Z axis) |
| $\omega_{px}$ | Bandwidth of the piezoelectric actuator (X axis) |
| $\omega_{py}$ | Bandwidth of the piezoelectric actuator (Y axis) |
| $\omega_{pz}$ | Bandwidth of the piezoelectric actuator (Z axis) |
| $\xi_{px}$ | Damping ratio of the piezoelectric actuator (X axis) |
| $\xi_{py}$ | Damping ratio of the piezoelectric actuator (Y axis) |
| $\xi_{pz}$ | Damping ratio of the piezoelectric actuator (Z axis) |
| $Z_x(s)$ | Cross-coupling dynamics (from X to Z axis) |
| $Z_y(s)$ | Cross-coupling dynamics (from Y to Z axis) |
| $\hat{Z}_x(s)$ | Estimate of $Z_x(s)$ |
| $\hat{Z}_y(s)$ | Estimate of $Z_y(s)$ |
| $G_{zx}$ | Gain of the cross-coupling dynamics (from X to Z axis) |
| $G_{zy}$ | Gain of the cross-coupling dynamics (from Y to Z axis) |
| $\hat{G}_{zx}$ | Estimate of $G_{zx}$ |
| $\hat{G}_{zy}$ | Estimate of $G_{zy}$ |
| $\omega_{zx}$ | Bandwidth of the cross-coupling dynamics (from X to Z axis) |
| $\omega_{zy}$ | Bandwidth of the cross-coupling dynamics (from Y to Z axis) |
| $\hat{\omega}_{zx}$ | Estimate of $\omega_{zx}$ |
| $\hat{\omega}_{zy}$ | Estimate of $\omega_{zy}$ |

| | |
|---|---|
| $x_x(t)$ | Direct contribution to piezo displacement (X axis) |
| $y_y(t)$ | Direct contribution to piezo displacement (Y axis) |
| $z_z(t)$ | Direct contribution to piezo displacement (Z axis) |
| $z_x(t)$ | Cross-coupling contribution to piezo displacement (from X to Z axis) |
| $z_y(t)$ | Cross-coupling contribution to piezo displacement (from Y to Z axis) |
| $\hat{z}_z(t)$ | Estimate of $z_z(t)$ |
| $\hat{z}_x(t)$ | Estimate of $z_x(t)$ |
| $\hat{z}_y(t)$ | Estimate of $z_y(t)$ |
| $x_p(t)$ | Total piezo displacement (X axis) |
| $y_p(t)$ | Total piezo displacement (Y axis) |
| $\hat{x}_p(t)$ | Estimate of $x_p(t)$ |
| $\hat{y}_p(t)$ | Estimate of $y_p(t)$ |
| $z_p(t)$ | Total piezo displacement (Z axis) |
| $z_s(t)$ | Surface variations |
| $u_s(t)$ | Proper (non-compensating) part of control input $u_z(t)$ |
| $u_c(t)$ | Compensating part of control input $u_z(t)$ |
| $u_{cx}(t)$ | Compensating control for cross-coupling (from X to Z axis) |
| $u_{cy}(t)$ | Compensating control for cross-coupling (from Y to Z axis) |
| $\hat{G}_{zz}(s)$ | Estimate of piezo transfer function |
| $d_0$ | Initial tunneling gap between the tip and the surface |
| $d(t)$ | Tunneling gap between the tip and the surface |
| $\hat{d}(t)$ | Estimate of $d(t)$ |
| $d_{eq}$ | Equilibrium gap between the tip and the surface |
| $\Delta d(t)$ | Gap deviation from its equilibrium $d_{eq}$ |
| $i_t(t)$ | Tunneling current |
| $i_{eq}$ | Equilibrium tunneling current |
| $\Delta i_t(t)$ | Tunneling current deviation from its equilibrium $i_{eq}$ |
| $V_b$ | Bias Voltage |
| $g$ | Proportionality constant of tunneling current |
| $k$ | Constant of tunneling current |
| $PL'_t$ | Exponential nonlinearity of the tunneling current |
| $CS_x(s)$ | Model of the capacitive sensor (X axis) |
| $CS_y(s)$ | Model of the capacitive sensor (Y axis) |
| $CS_t(s)$ | Model of the current sensor (Z axis) |
| $G_{capx}$ | Gain of the capacitive sensor (X axis) |
| $G_{capy}$ | Gain of the capacitive sensor (Y axis) |
| $G_t$ | Gain of the current sensor (Z axis) |
| $\omega_{capx}$ | Bandwidth of the capacitive sensor (X axis) |
| $\omega_{capy}$ | Bandwidth of the capacitive sensor (Y axis) |
| $\omega_t$ | Bandwidth of the current sensor (Z axis) |
| $v_x(t)$ | Output of the capacitive sensor (X axis) |
| $v_y(t)$ | Output of the capacitive sensor (Y axis) |
| $v_z(t)$ | Output of the current sensor (Z axis) |
| $n_1(t)$ | Measurement noise of the capacitive sensor (X axis) |
| $n_2(t)$ | Measurement noise of the capacitive sensor (Y axis) |
| $n_3(t)$ | Measurement noise of the current sensor (Z axis) |

| | |
|---|---|
| $y_1(t)$ | Final output of the capacitive sensor (X axis) |
| $y_2(t)$ | Final output of the capacitive sensor (Y axis) |
| $y_3(t)$ | Final output of the current sensor (Z axis) |
| $x(t)$ | State vector of the 3D model for surface reconstruction |
| $u(t)$ | Input vector of the 3D model for surface reconstruction |
| $y(t)$ | Output vector of the 3D model for surface reconstruction |
| $x_{eq}$ | Equilibrium state vector |
| $u_{eq}$ | Equilibrium input vector |
| $y_{eq}$ | Equilibrium output vector |
| $\Delta x(t)$ | Deviation of the state vector from its equilibrium |
| $\Delta u(t)$ | Deviation of the input vector from its equilibrium |
| $\Delta y(t)$ | Deviation of the output vector from its equilibrium |
| $\Delta\hat{x}(t)$ | Estimate of $\Delta x(t)$ |
| $e(t)$ | Tracking error vector |
| $r(t)$ | Reference vector |
| $\Delta x_e(t)$ | Extended state vector deviations (with surface variations) |
| $\Delta\hat{x}_e(t)$ | Estimate of $\Delta x_e(t)$ |
| $A, B, C$ | System matrices |
| $A_e, B_e, C_e$ | Matrices of the extended system (for estimation) |
| $B_d$ | Disturbance matrix |
| $n(t)$ | Measurement noise vector |
| $w(t)$ | Process noise vector |
| $N$ | Measurement noise covariance matrix |
| $W$ | Process noise covariance matrix |
| $L$ | Kalman gain matrix |
| $P$ | Solution of the Kalman Filter ARE |
| $x_i(t)$ | Integrated tracking error |
| $x_c(t)$ | Extended state vector deviations (with an integral action) |
| $A_c, B_c$ | Matrices of the extended system (for control) |
| $Q$ | LQR weighting matrix for the state |
| $R$ | LQR weighting matrix for the control |
| $K$ | LQR gain matrix |
| $S$ | Solution of the LQR ARE |

## Chapter 7: Cantilever nanopositioning with electrostatic actuation

| | |
|---|---|
| $F_e(t)$ | Electrostatic force |
| $\hat{F}_e(t)$ | Estimate of $F_e(t)$ |
| $F_p(t)$ | Proximity force |
| $\hat{F}_p(t)$ | Estimate of $F_p(t)$ |
| $F_c(t)$ | Total input net force exciting the cantilever |
| $\hat{F}_c(t)$ | Estimate of $F_c(t)$ |

| | |
|---|---|
| $z_{c_e}(x,t)$ | Cantilver displacement (at the position $x$) due to electrostatic force |
| $\hat{z}_{c_e}(x,t)$ | Estimate of $z_{c_e}(x,t)$ |
| $z_{c_p}(x,t)$ | Cantilver displacement (at the position $x$) due to proximity force |
| $\hat{z}_{c_p}(x,t)$ | Estimate of $z_{c_p}(x,t)$ |
| $z_c(x,t)$ | Total cantilver displacement (at the position $x$) due to total force |
| $\hat{z}_c(x,t)$ | Estimate of $z_c(x,t)$ |
| $z_{c_{e_r}}$ | Reference for cantilever displacement due to electrostatic force |
| $z_{c_r}$ | Reference for total cantilever displacement |
| $A$ | Cross sectional area of the cantilever |
| $I$ | Area moment of inertia of the cantilever |
| $\rho$ | Density of the cantilever material |
| $\xi$ | Damping ratio for the modes (here the same for each mode) |
| $p_d(x,t)$ | Damping force (sum of the structural and electrostatic damping) |
| $Q$ | Quality factor |
| $L$ | Length of the cantilever |
| $m_j$ | Modal mass of $j^{th}$ mode |
| $c_j$ | Modal damping coefficient of $j^{th}$ mode |
| $k_j$ | Modal stiffness coefficient of $j^{th}$ mode |
| $\omega_j$ | Modal natural frequency of $j^{th}$ mode |
| $\lambda_j$ | Modal wave constant of the $j^{th}$ mode |
| $q_j(t)$ | Fundamental deformation of the $j^{th}$ mode (only time-dependent) |
| $\phi_j(x)$ | Modal shape function for the $j^{th}$ mode (only space-dependent) |
| $CNT(s)$ | Cantilever model |
| $CNT_{3m}(s)$ | Cantilever model (with 3 modes) |
| $CNT_{1m}(s)$ | Cantilever model (with 1 mode) |
| $INT_{tc}$ | Nonlinear block representing interaction force |
| $k_f = CNT_{DC}^{-1}$ | Cantilever force constant |
| $x_f$ | Position $x$ where the force $F_c(t)$ is applied at the cantilever input |
| $l_0$ | Distance between the unbended cantilever and the electrostatic plate |
| $l(t)$ | Actual distance between the cantilever and the electrostatic plate |
| $\varepsilon_0$ | Vacuum permittivity |
| $A_e$ | Common surface between the cantilever and the electrostatic plate |
| $u_z(t)$ | Control signal for the Z axis (voltage amplifier input) |
| $V_e(t)$ | Control signal for the Z axis (electrostatic actuator input) |
| $u_e(t)$ | Control signal for the Z axis (after exact linearization) |
| $b$ | Proportionality constant of electrostatic actuator |
| $VA_z(s)$ | Model of the voltage amplifier (Z axis) |
| $G_{vz}$ | Gain of the voltage amplifier (Z axis) |
| $v_{pz}(t)$ | Piezo input voltage (Z axis) |
| $d_z(t)$ | Disturbance including creep phenomenon (Z axis) |
| $q_{pz}(t)$ | Output of static part of piezo (Z axis) |
| $D_{pz}(s)$ | Direct piezo linear dynamics (Z axis) |
| $G_{pz}$ | Gain of the piezoelectric actuator (Z axis) |
| $\omega_{pz}$ | Bandwidth of the piezoelectric actuator (Z axis) |
| $\xi_{pz}$ | Damping ratio of the piezoelectric actuator (Z axis) |
| $z_p(t)$ | Total piezo displacement (Z axis) |
| $z_t(t)$ | Tip displacement (Z axis) |
| $\hat{z}_t(t)$ | Estimate of $z_t(t)$ |

| | |
|---|---|
| $d_0$ | Initial tunneling gap between the tip and the surface |
| $d(t)$ | Tunneling gap between the tip and the surface |
| $\hat{d}(t)$ | Estimate of $d(t)$ |
| $i_t(t)$ | Tunneling current |
| $i_{eq}$ | Equilibrium tunneling current |
| $g$ | Proportionality constant of tunneling current |
| $k$ | Constant of tunneling current |
| $V_b$ | Bias Voltage |
| $CS_t(s)$ | Model of the current sensor (Z axis) |
| $G_t$ | Gain of the current sensor (Z axis) |
| $v_z(t)$ | Output of the current sensor (Z axis) |
| $n_3(t)$ | Measurement noise of the current sensor (Z axis) |
| $y_3(t)$ | Final output of the current sensor (Z axis) |
| $EA$ | Electrostatic actuator |
| $FE$ | Proximity force estimator |
| $G_{u_e->y_{3_p}}(s)$ | Perturbed linear model for $\mathcal{H}_\infty$ cantilever control |
| $G_{u_e->y_3}(s)$ | Nominal linear model for $\mathcal{H}_\infty$ cantilever control |
| $\Delta(s)$ | Normalized complex perturbation |
| $W_\Delta(s)$ | Model uncertainty weight |
| $l_\Delta(\omega)$ | Relative magnitude of the neglected dynamics |
| $W_{S_z}(s)$ | Weight for the output sensitivity function |
| $W_{T_z}(s)$ | Weight for the complementary sensitivity function |
| $W_{R_z}(s)$ | Weight for the input sensitivity function |
| $H$ | Hamaker constant |
| $R$ | Tip radius |
| $a_p$ | Interatomic value |
| $E^*_{eff}$ | Effective contact stiffness (between the tip and the cantilever) |
| $E_t$ | Elastic modulus of the tip |
| $E$ | Elastic modulus of the surface (cantilever) |
| $v_t$ | Poisson ratio of the tip |
| $v$ | Poisson ratio of the surface (cantilever) |

# Introduction

## General context

The recent years show rapidly growing popularity of nanotechnology and related sciences which can be explained by the continuous need for object miniaturization. One of the most extensively studied branch by the researchers is the Scanning Probe Microscopy (SPM), which was originated in the early 80s by the invention of the Scanning Tunneling Microscope (STM), for which its creators Gerd Binnig and Heinrich Rohrer from IBM laboratory, received the Nobel Prize. This device has the capability of scanning the surface (conductive or semi-conductive) with the aim of obtaining its morphological (or electrical) properties with an atomic resolution. Together with its successor - Atomic Force Microscope (AFM) (which can be used with non-conductive materials as well), it has changed many areas like physics, biology and material sciences, where not only the atomic-resolution measurement but also manipulation at such small scale is possible. One of the key requirements of these devices is *nanopositioning*, which is the positioning of a small object with high accuracy and over high bandwidth. These features are the main aspects that have attracted the researchers working around this area. However, the measurement noise, disturbances and nonlinearities strongly affect the positioning at such a small scale. Those problems, which are usually treated by physicists or electronics specialists are solved here using system theory (modeling, identification, observation and control).

## Thesis objectives and contribution

The main **objective** of this thesis is to elaborate high performance control strategies for a three-dimensional (X,Y,Z) model of nanopositioning system and their real-time validation on an experimental tunneling current-based platform, started in GIPSA-lab a few years ago [Blanvillain, 2010], [Ahmad, 2011]. The main challenge is to take into account different nonlinear dynamics, disturbances and noises appearing in such 3D system, composed mainly of a piezoelectrically actuated tunneling tip (like in STM) and a microcantilever (like in AFM) and to control the whole system with nanoscale accuracy and high bandwidth.

The **contribution** of this thesis is twofold. First, the development of a new three-dimensional model of the nanopositioning device is done, based on the tunneling current phenomenon, with piezoelectrically actuated tunneling tip and electrostatically actuated cantilever, taking into account the adverse effects of different nature. They are associated mainly with piezoelectric actuators (like nonlinear hysteresis, creep, structural vibration, or cross-couplings between the axes) but also with the tunneling current phenomenon (exponential nonlinearity) and with the electrostatic actuator (quadratic nonlinearity). Such a 3D model, to the authors' knowledge, does not appear in the literature. The second contribution is the development of different control approaches for such 3D model. To that end, the horizontal motion in X and Y directions is first studied. The nonlinear hysteresis and creep exhibited by piezoelectric

actuators are compensated using different methods (operator-based Prandtl-Ishlinskii model, its modified version, disturbance observer and combination of the two, as well as an adaptive approach). The effects of piezo vibration and cross-couplings between X and Y axes are reduced using robust control methods (SISO LQG/LTR, SISO $\mathcal{H}_\infty$ and MIMO $\mathcal{H}_\infty$). Next, the horizontal motion is combined with the vertical motion of the Z axis, based on the tunneling current phenomenon, controlled by the piezoelectrically actuated tip and the electrostatically actuated cantilever (by means of pole-placement with sensitivity functions shaping and $\mathcal{H}_\infty$ design). The results for three applications are presented. First, 3D nanopositioning on the fixed part of the cantilever is validated experimentally. In the second application, tested in simulation, the model of STM-like device is used with the aim of surface reconstruction (using three SISO PID controllers with decoupling method and MIMO LQI control). Finally, the aim of the last application is the nanopositioning of the multi-mode cantilever model on its mobile part by means of electrostatic actuation with piezoelectrically actuated tunneling tip and with proximity force (appearing between the tip and the cantilever) compensation. All applications are based on the tunneling current phenomenon.

## Thesis organization

**Chapter 1**: In this chapter a state-of-the-art is presented. Among the nanoscale applications, the focus is mainly on Scanning Tunneling Microscopy. The key components used in such nanoscale applications, like piezoelectric actuators or tunneling current sensor (in case of STM) are described in detail, together with the associated challenge of their control, especially connected with tunneling nonlinearity and with the adverse phenomena of piezoelectric actuators like hysteresis, creep, vibration and cross-couplings between axes. At the end, an overview of the nanopositioning control in three dimensions is tackled.

**Chapter 2**: This chapter is focused on the description of the lab-made experimental nanopositioning platform based on tunneling current phenomenon, used in this thesis. The full nonlinear system model in three dimensions is developed. It includes the horizontal model (motion along X and Y axes) with focus on the piezoelectric actuators, driven by voltage amplifiers and read by capacitive sensors, and the vertical model (motion along the Z axis) of piezoelectrically actuated tunneling tip with a high-gain tunneling current sensor and electrostatically actuated cantilever.

**Chapter 3**: In this chapter the problem of modeling and compensation of nonlinear hysteresis and creep present in piezoelectric actuators (in X and Y directions) is considered. Experimental data are used for hysteresis model identification and results for real-time hysteresis compensation are presented. To that end, several modeling/compensation methods are used, starting from the classical and modified inverse-based Prandtl-Ishlinskii (PI/MPI) model, disturbance observer (DOB) and the hybrid method, which combines both of them (MPI/DOB). Finally, a polynomial-based model of hysteresis with adaptively changing coefficients is used together with Newton-based inversion algorithm. All the results are obtained experimentally using the nanopositioning platform of GIPSA-lab.

**Chapter 4**: Here the 2D horizontal system (X and Y axes) already compensated for hysteresis is considered, with the purpose of structural vibration and cross-coupling reduction. The two-input two-output (TITO) high-order linear model is identified and its order is reduced using balanced truncation method. Such a model together with specified uncertainty, serves as a nominal model for the controller design. Three kinds of robust controllers are designed and experimentally tested on the nanopositioning platform: single variable LQG/LTR, single variable $\mathcal{H}_\infty$ and multivariable $\mathcal{H}_\infty$.

**Chapter 5**: This chapter is devoted to the vertical system of piezoelectrically actuated metallic tip. The tip is approached to the fixed metallic surface of the cantilever and the tunneling current phenomenon is observed. Its exponential dependence on the tip/surface gap is confirmed by fitting the model curve to the experimental data. The model with tunneling nonlinearity is then linearized around an equilibrium point and a pole placement controller with sensitivity functions shaping is designed on the basis of this linearized model. Finally, experimental results for tunneling current stabilization and tracking are shown.

**Chapter 6**: In this chapter the horizontal motion in X and Y directions is coupled with the vertical motion in Z direction (not including the cantilever motion). Two kinds of applications are considered here: the nanopositioning in three dimensions, validated experimentally, and STM-like application, tested in simulation. In the nanopositioning application the tunneling tip tracks the reference trajectory along X, Y and Z axes (in the Z axis, the tunneling current tracks the prespecified reference called "virtual surface"). Here, three kinds of hysteresis compensation methods (open-loop MPI, closed-loop DOB and a hybrid MPI/DOB) are tested in horizontal directions in the presence of tunneling current in the vertical direction. In the STM-like application, the tunneling tip is moved along horizontal X and Y axes, tracking the prespecified trajectory, while the tunneling current in vertical Z direction is stabilized at a constant level. To that end, two control approaches are tested with the aim of surface reconstruction: SISO PID decentralized control with decoupling compensators and MIMO Linear Quadratic Integral (LQI) centralized control. In the first (more classical) case, the surface is retrieved from the control signal of the vertical piezo, and in the second one, a Kalman observer is used for its reconstruction.

**Chapter 7**: In this chapter, modeling, analysis and simulation of a multi-mode cantilever model are done. Properties of mode vanishing near the singular points of the associated modal shape function are used for actuator and sensor location in order to damp the modes. This allows to reduce the order of the system, as well as to increase its bandwidth. The application of three-mode cantilever model nanopositioning based on the tunneling current phenomenon is presented. The control of tunneling gap through electrostatically actuated cantilever is done using $H_\infty$ design and the cantilever positioning over a distance greater than 1 nm is done through piezoelectrically actuated tunneling tip using PID control. A proximity force estimator is designed for estimation and subsequent compensation of the interaction force between the tip and the cantilever.

**Chapter 8**: This chapter concludes the manuscript and gives some perspectives and possible extensions.

## Publications

This work gave rise to the following publications:

**Journal paper**:

- Ryba Ł., Voda A., Besançon G., "Experimental comparison of disturbance observer and inverse-based hysteresis compensation in 3D nanopositioning piezoactuation", *Sensors and Actuators A: Physical* 236, pp. 190-205, Elsevier, 2015.

**International conference proceedings**:

- Ryba Ł., Voda A., Besançon G., "A real-time inverse-based hysteresis compensation with adaptation", accepted to: *54th IEEE Conference on Decision and Control (CDC 2015)*, Osaka, Japan, 15-18 December 2015.
- Oubellil R., Ryba Ł., Voda A., Rakotondrabe M., "Experimental model inverse-based hysteresis compensation on a piezoelectric actuator", *19th International Conference on System Theory, Control and Computing (ICSTCC 2015)*, Cheile Gradistei - Fundata Resort, Romania, 14-16 October 2015.
- Ryba Ł., Voda A., Besançon G., "3DOF nanopositioning control of an experimental tunneling current-based platform", *2014 IEEE Conference on Control Applications (CCA), (part of 2014 IEEE Multi-Conference on Systems and Control (MSC2014))*, Antibes, France, 8-10 October 2014, pp. 1976-1981.
- Ryba Ł., Voda A., Besançon G., "An LQG/LTR approach towards piezoactuator vibration reduction with observer-based hysteresis compensation", *19th IFAC World Congress (IFAC 2014)*, Cape Town, South Africa, 24-29 August 2014, pp. 5623-5628.
- Ryba Ł., Voda A., Besançon G., "Modelling and control of 3D STM-like scanning device with application to surface reconstruction", *18th IEEE International Conference on Methods and Models in Automation and Robotics (MMAR 2013)*, Miedzyzdroje, Poland, 26-29 August 2013, pp. 479-484.

Chapter 1

# State-of-the-art

Contents



## 1.1 Introduction

In this first chapter, a short state-of-the-art is given as a starting point to the work on nanopositioning, considered in this thesis. First, some micro-/nanoscale applications are briefly reviewed. Then, an overview of main phenomena (such as tunneling current) and tools (such as piezoelectric actuators), that will be useful for us, as well as related control issues are given. Finally, 3D operation, which plays a fundamental role in the present work, is discussed.

## 1.2 Micro-/Nanoscale applications

The Scanning Tunneling Microscope (STM), since its invention in the beginning of the 1980s by Gerd Binnig and Heinrich Rohrer [Binnig and Rohrer, 1986], has experienced extensive research and gained wide acceptance in nanotechnology, mainly due to its capability of measuring topographical/electrical properties of the surfaces with an atomic resolution. The scheme of an STM-like scanning device is shown in Fig. 1.1. When the conductive tip is approached to the metallic surface at a distance lower than $1 \cdot 10^{-9}$ m and if it is electrically biased w.r.t. the surface (bias voltage applied in-between), electrons can leave one material and pass to another one. Such flow of electrons is called then tunneling current and its intensity depends on the tip/surface gap. Now, by keeping the tunneling current (and as a result this gap)

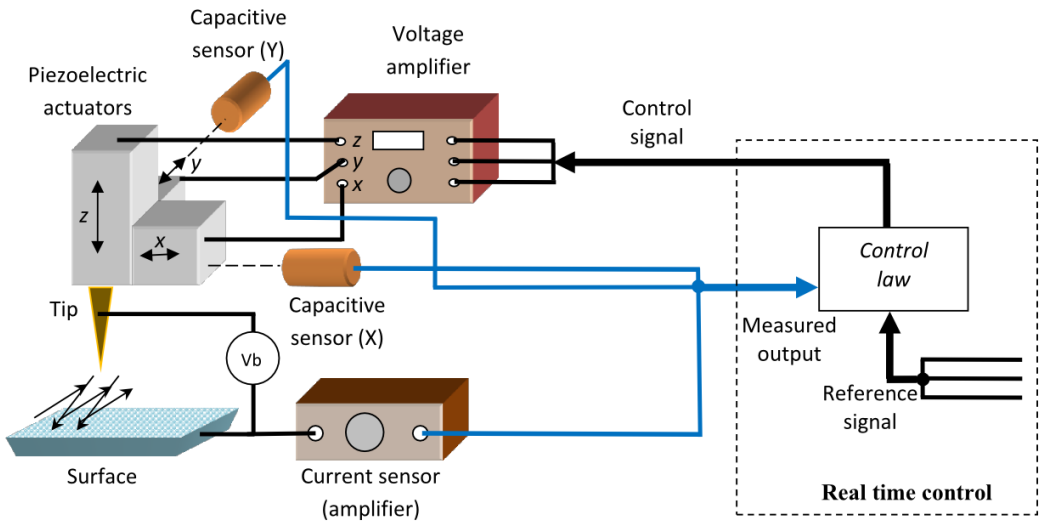


Figure 1.1: 3D Scanning tunneling control system.

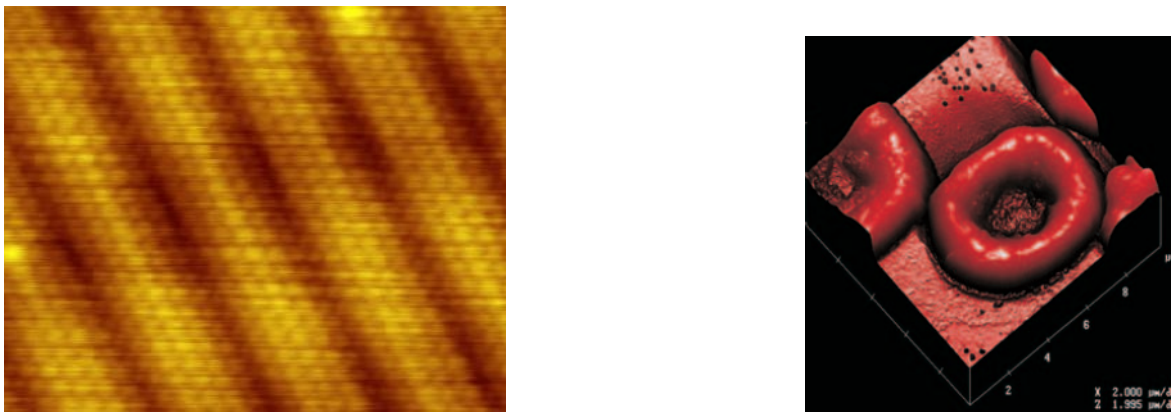

(a) (b)

Figure 1.2: STM/AFM applications examples [Abramovitch et al., 2007]: (a) STM image of a gold surface. (b) 3D AFM image of blood cells.

constant using proper control, and by simultaneously moving the tip along the surface horizontally using piezoelectric actuators, the tip is forced to follow the topographical variations (or more precisely the contour of constant density of states) of the surface. The amount of this variations (topographical/electrical) can be retrieved via control signal of the vertical piezo [Abramovitch et al., 2007].

The Atomic Force Microscope (AFM) [Binnig et al., 1986], which unlike STM uses position sensor instead of tunneling current sensor, became even more popular, since it applies also to non-conductive surfaces, thus more focus has been devoted to it in the literature. It has fundamentally changed research in such areas as biology [Zou et al., 2004], chemistry [Jandt et al., 2000], physics [Tsukada et al., 2000], materials science [Yamanaka et al., 1999] and micro-/nanorobotics [Xie et al., 2012].

Other applications where the nanopositioning plays very important role include Hard Disk Drives (HDDs) [Hu et al., 1999], where the read/write head is positioned over data tracks or nanolithography [Gentili et al., 1993]. Fig. 1.2 provides a couple of STM/AFM illustrative applications.

## 1.3 Tools, challenges and associated control issues

### 1.3.1 Tunneling current phenomenon

In metals the electrons fill the energy levels up the the particular top energy known as the Fermi level $E_F$ as shown in Fig. 1.3a. If two conductive materials (here the tip and the surface) are brought close enough to each other, there is a small vacuum gap between them which is a potential barrier. The electrons of one metal can leave it, overcome an energy barrier and travel to the other metal only if an additional amount of energy, so-called work function $\phi$, is delivered to them. Both, the tip and the surface without any external supply have the same electrical potential and therefore their Fermi levels are aligned. Biasing the surface w.r.t. the tip with the potential $V_b$, as shown in Fig. 1.3b, decreases the Fermi level of the latter by the energy $eV_b$. Such a difference between the Fermi levels of the surface $E_{F_s} = E_F$ and of the tip $E_{F_t} = E_F - eV_b$ results in filled energy states in the former and empty energy states in the latter. The filled/empty states force the electrons to jump from one material to the other one and such a flow of electrons is called tunneling current. The direction of tunneling depends on the polarity of the constant bias voltage $V_b$ (*i.e.* if the negative electrode of the supply is connected to the tip, its Fermi level will increase w.r.t. the one of the surface and the tunneling direction will be reversed).

In classical mechanics, if a particle of total energy $E$ accounters a potential barrier of energy $V > E$ it cannot pass through it and will be reflected. In case of quantum mechanics, the wave–particle duality concept states that every elementary particle (in this case the electron) can be treated not only as a particle but also as a wave and even if its total energy is smaller than the potential energy of the barrier there is still a non-zero probability that it may pass this forbidden region and reappear on the other side as shown in Fig. 1.4. Mathematically, the electron state can be described by referring to the following time-independent Schrödinger equation in one dimension ($z$ in this case), that describes the stationary states (indeed in atoms the potential on the orbits does not change with time):

$$-\frac{\hbar^2}{2m}\frac{d^2}{dz^2}\psi(z) + V(z)\psi(z) = E\psi(z) \tag{1.1}$$

where $\psi(z)$ is the wave function describing the wave-like behavior of the electron, $E$ is its total energy, which equals to the sum of the potential energy $V(z)$ and the kinetic energy (described by the first term in equation (1.1)) and $\hbar = 1.05 \cdot 10^{-34}\mathrm{J} \cdot \mathrm{s}$ is a reduced Planck constant. Assuming the square potential barrier of length $d$, described as follows:

$$V(z) = \begin{cases} V_0, & 0 < z < d \\ 0, & \text{otherwise} \end{cases} \tag{1.2}$$

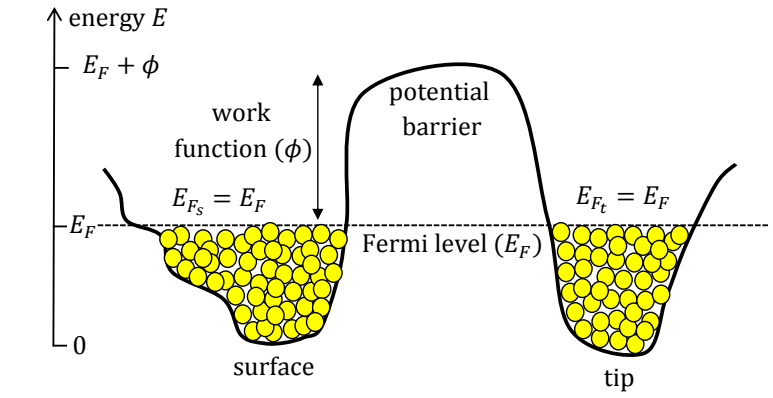


(a)

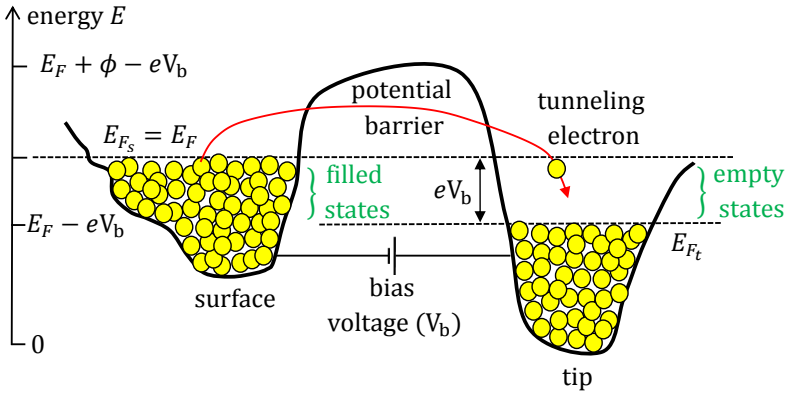


(b)

Figure 1.3: Tunneling effect: (a) Unbiased tip/surface. (b) Surface biased w.r.t. the tip.

the space $z$ is divided into three regions as shown in Fig. 1.4: region I ($z < 0$), region III ($z > d$), both outside the barrier, with zero potential energy and region II ($0 < z < d$) inside the barrier with constant potential energy $V_0$. For each region one searches the solution of (1.1).
Outside the barrier (in regions I and III) $E - V(z) > 0$. From (1.2), $V(z) = 0$ and the total energy of electron is equal to its kinetic energy. Equation (1.1) takes the following form:

$$\frac{\hbar^2}{2m_e}\frac{d^2}{dz^2}\psi(z) + E\psi(z) = 0 \tag{1.3}$$

This linear ordinary differential equation can be expressed using Laplace operator as follows:

$$\left(\frac{\hbar^2}{2m_e}s^2 + E\right)\psi(s) = 0 \tag{1.4}$$

which has the following solutions:

$$s_{1,2} = \pm i\frac{\sqrt{2m_eE}}{\hbar} \tag{1.5}$$

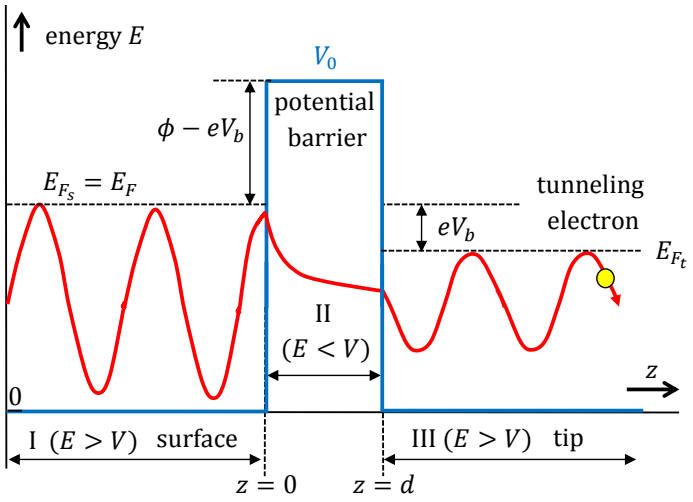


Figure 1.4: Electron behaviour in three energy regions during tunneling effect.

Hence, the final solution for the wave function in regions I and III is a linear combination of solutions (1.5) as follows:

$$\psi_I(z) = A_1 e^{s_1 z} + A_2 e^{s_2 z} = A_1 e^{ik_0 z} + A_2 e^{-ik_0 z} \tag{1.6}$$

$$\psi_{III}(z) = C_1 e^{s_1 z} + C_2 e^{s_2 z} = C_1 e^{ik_0 z} + C_2 e^{-ik_0 z} \tag{1.7}$$

where $k_0 = \frac{\sqrt{2m_e E}}{\hbar}$ is a wave number outside the barrier. One can notice that the solutions (1.6) and (1.7) represent oscillating waves.
Inside the barrier (region II) $E - V(z) < 0$. From (1.2), $V(z) = V_0$ and equation (1.1) takes the following form:

$$\frac{\hbar^2}{2m_e}\frac{d^2}{dz^2}\psi(z) + (E - V_0)\,\psi(z) = 0 \tag{1.8}$$

or in Laplace domain:

$$\left(\frac{\hbar^2}{2m_e}s^2 + E - V_0\right)\psi(s) = 0 \tag{1.9}$$

The following solutions are obtained:

$$s_{1,2} = \pm i\frac{\sqrt{2m_e\,(E - V_0)}}{\hbar} = \mp\frac{\sqrt{2m_e\,(V_0 - E)}}{\hbar} \tag{1.10}$$

This gives the following solution for the wave function inside the barrier:

$$\psi_{II}(z) = B_1 e^{s_1 z} + B_2 e^{s_2 z} = B_1 e^{-k_1 z} + B_2 e^{k_1 z} \tag{1.11}$$

where $k_1 = \frac{\sqrt{2m_e(V_0 - E)}}{\hbar}$ is a wave number inside the barrier. One can notice that the solution (1.11) represents a combination of an exponentially increasing and exponentially decaying terms with decaying rate $k_1$. Only the decaying term is taken into account for further considerations, since it corresponds to the tunneling through the barrier.

Knowing the wave function $\psi(z)$ allows one to calculate the probability density for the electron to be found at the specific location $z$. This probability is proportional to the wave

function squared $|\psi(z)|^2$. We are interested in the case when the tunneling occurs, *i.e.* we want to assess the probability that the electron at position $z = 0$ can cross the barrier and be found at position $z = d$. Taking only the decaying part of equation (1.11), $\psi_{II}(z) = B_1 e^{-k_1 z}$ (where $B_1 = \psi_{II}(0)$), this probability can be expressed as follows:

$$P \propto |\psi_{II}(d)|^2 = |\psi_{II}(0)|^2 e^{-2k_1 d} \tag{1.12}$$

In an unbiased case, like in Fig. 1.3a, $V_0 - E = \phi$ and in case of tunneling effect when two metals are biased w.r.t. each other, like in Fig. 1.3b, $V_0 - E = \phi - eV_b$ and when the bias voltage $V_b$ is chosen to be small enough (such that $eV_b << \phi$), the wave number $k_1 \approx \frac{\sqrt{2m_e\phi}}{\hbar}$ (when the materials for the tip and the sample surface differ electrically, the work function is assumed to be an average of the work functions corresponding to each material).
The tunneling current can be related to the density of empty states of the tip or filled states of the surface (see Fig. 1.3b). The higher the number of these states, the higher value of the tunneling current. Assuming that after biasing $E_{F_s} = E_F$ is the Fermi level of the sample surface, the states filled by electrons in the surface lie on the energy levels between $E_F - eV_b$ and $E_F$, hence the electrons will flow to the empty states of the tip between the same energy levels $E_{F_t} = E_F - eV_b$ and $E_F$. The formed tunneling current is proportional to the sum of the probabilities (1.12) taken over this energy range as follows:

$$i_t \propto \sum_{E_F - eV_b}^{E_F} |\psi_{II}(0)|^2 e^{-2\frac{\sqrt{2m_e\phi}}{\hbar}d} \tag{1.13}$$

Defining the local density of states (LDOS) near some energy region $E$ in an interval $\epsilon$ and at the position $z$ as:

$$\rho_{LS}(z, E) = \frac{1}{\epsilon} \sum_{E-\epsilon}^{E} |\psi(z)|^2 \tag{1.14}$$

and assuming the continuity of the wave function (*i.e.* $\psi(0) = \psi_I(0) = \psi_{II}(0)$ and $\psi(d) = \psi_{II}(d) = \psi_{III}(d)$) the tunneling current (1.13) can be rewritten in terms of LDOS (filled) in an interval $\epsilon = eV_b$ near the Fermi level of the sample surface $E_F$ at the surface location $z = 0$ as follows:

$$i_t \propto eV_b \frac{1}{eV_b} \sum_{E_F - eV_b}^{E_F} |\psi_{II}(0)|^2 e^{-2\frac{\sqrt{2m_e\phi}}{\hbar}d} = eV_b \rho_{LS}(0, E_F) e^{-2\frac{\sqrt{2m_e\phi}}{\hbar}d} \tag{1.15}$$

or in terms of LDOS (empty) in the same interval $\epsilon = eV_b$ and again near the Fermi level of the sample surface $E_F$ but at the tip location $z = d$:

$$i_t \propto eV_b \rho_{LS}(d, E_F) \tag{1.16}$$

Defining a constant $g = e\rho_{LS}(0, E_F)$ and $k = -2\frac{\sqrt{2m_e}}{\hbar}\sqrt{\phi}$, which depends on the metal electrical properties, the tunneling current equation is given by:

$$i_t = gV_b e^{-kd} \tag{1.17}$$

One can see that $i_t$ depends not only on the distance $d$, but also on the bias voltage $V_b$ and the electrical properties of the used surfaces ($\phi$). Since the principle of STM device is based

on the tunneling current phenomenon, in order to have a reliable images of LDOS (which may approximate the surface topography) one has to keep the bias voltage $V_b$ constant and the scanned surface must be composed of only one material in order to obtain constant effective work function $\phi$.

### 1.3.2 Piezoelectric actuators - modeling and control

Due to their high resolution, high stiffness and fast response piezoelectric actuators are widely used in micro-/nanoscale applications such as in STM [Binnig and Rohrer, 1986] or AFM [Abramovitch et al., 2007] and other nanopositioning applications [Devasia et al., 2007], [Sebastian and Salapaka, 2005]. However, they exhibit some adverse phenomena of nonlinear hysteresis, creep, structural vibration and cross-couplings between the axes shown in Fig. 1.5. Overcoming these difficulties can substantially improve positioning precision, range of operation and increase the bandwidth.

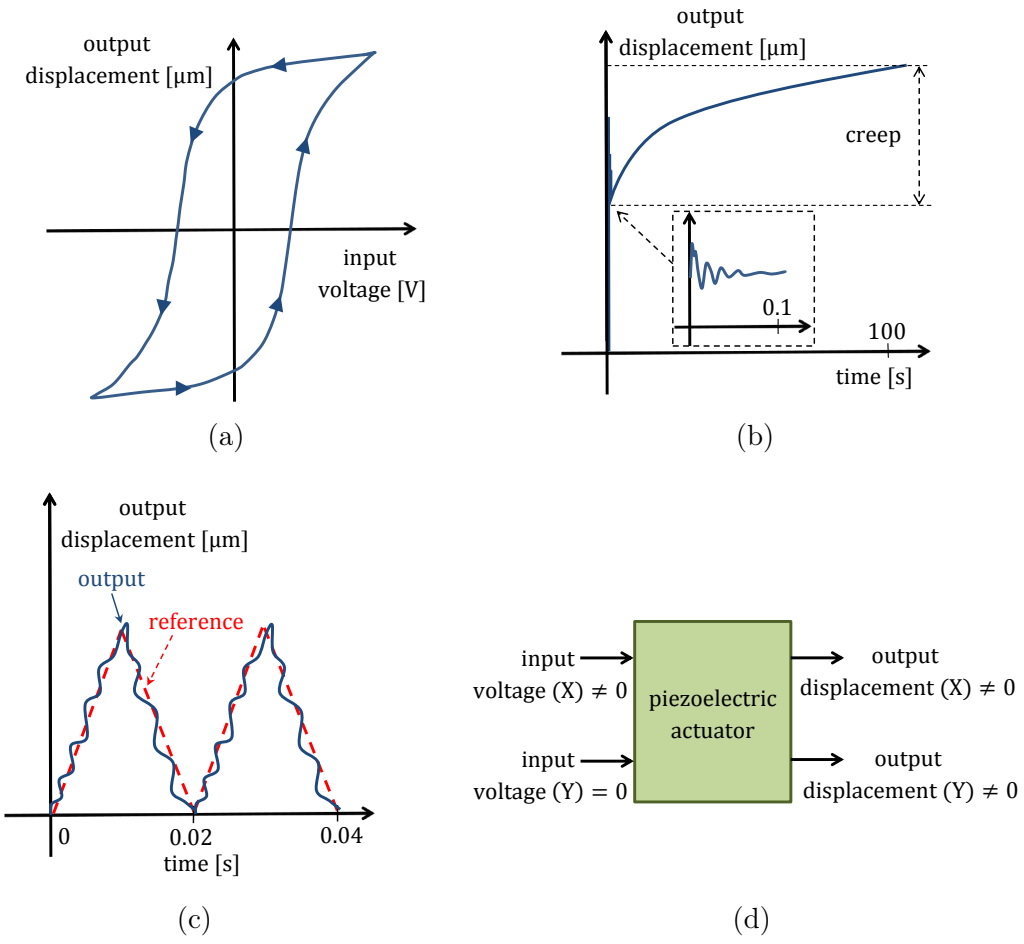


Figure 1.5: Adverse phenomena of piezoelectric actuators: (a) Hysteresis. (b) Creep. (b) Structural vibration. (d) Cross-coupling (from X to Y axis).

**Hysteresis.**
Hysteresis is a nonlinear phenomenon between the applied input voltage and the output displacement of piezoelectric actuator as shown in Fig. 1.5a [Bertotti and Mayergoyz, 2006]. The displacement depends not only on the current input voltage but also on its past history (memory effect). Hysteresis is amplitude-dependent and is more visible in response to high input voltages (in long-range positioning like during imaging large samples over large displacements). Moreover, recent studies have shown that this effect is frequency-dependent, as well [Janaideh et al., 2009b]. Uncompensated, it can significantly limit the accuracy (in case of positioning the error can reach 15% of the piezo travel range or even go beyond 35% for high frequencies [Gu et al., 2014b]), lead to high image distortions (in case of scanning applications) or even be the reason of instability in a controlled system [Shan and Leang, 2012].

Many hysteresis models have been studied in the literature and generally they can be divided into two categories: physics-based models and phenomenological models. As the name suggests, the models from the first category are developed based on the physical rules. The most common models in this group are the Jiles-Atherton model [Jiles and Atherton, 1986] (applied to the ferromagnetic hysteresis) and domain wall model [Smith and Ounaie, 2000] derived from the first one. The main drawback of these models is their complexity and often limited applicability, since the model derived from the physical rules for one kind of materials may not be valid for the other kind of materials governed by other physical rules. Therefore, they are mostly replaced by the phenomenological models, which do not require the physical insight into the modeling but use mathematical equations to describe hysteresis. Phenomenological models based on differential equations such as Duhem model [Lin and Lin, 2012] Bouc-Wen model [Rakotondrabe, 2011] or Dahl model [Xu and Li, 2010] can be very easily added to the dynamical state-space models describing the whole piezoactuated system, though the general solution is quite difficult to obtain. The most popular phenomenological models for hysteresis based on integral equations are so-called operator-based models, where the hysteresis output is obtained as an integral of weighted elementary operators. The models in this group include Preisach model, Krasnosel'skii-Pokrovskii (KP) model and Prandtl-Ishlinskii (PI) model and the difference between them lies in the elementary operators they use. The Preisach model uses a relay operator $\hat{\gamma}_{\alpha,\beta}[u(t)]$ and its output is a weighted integral of many of these operators expressed as:

$$y(t) = P[u](t) = \int\int_{\alpha\geq\beta} \mu(\alpha,\beta)\hat{\gamma}_{\alpha,\beta}[u(t)]d\alpha d\beta \tag{1.18}$$

with

$$\hat{\gamma}_{\alpha,\beta}[u(t)] = \begin{cases} 0, \quad u(t) \leq \beta \\ 1, \quad u(t) \geq \alpha \\ \hat{\gamma}_{\alpha,\beta}[u_0], \forall\tau \in [t_0,t], u(\tau) \in (\beta,\alpha) \\ 0, \text{ if } u(\tau) \in (\beta,\alpha), \ \exists t_1 \in [t_0,t), \text{s.t.} \\ \quad u(t_1) = \alpha \text{ and } \forall\tau \in (t_1,t] \ u(\tau) \in (\beta,\alpha) \\ 1, \text{ if } u(\tau) \in (\beta,\alpha), \ \exists t_1 \in [t_0,t), \text{s.t.} \\ \quad u(t_1) = \beta \text{ and } \forall\tau \in (t_1,t] \ u(\tau) \in (\beta,\alpha) \end{cases} \tag{1.19}$$

where $\alpha$ and $\beta$ are the thresholds such that $\alpha \geq \beta$ and $\mu(\alpha, \beta)$ is called the density function. The Preisach model is the oldest one among the operator-based models and is widely recognized owing to its general structure, but due to double integrals appearing in (1.18) the identification procedure becomes quite complicated. Moreover, this model due to discontinuous nature of the relay operator is not analytically invertible and thus the numerical approximations are usually used for implementation of the inverse compensators. On the other hand, Prandtl-Ishlinskii model uses so-called play operator $F_r[u](t)$ and its output is again a weighted integral of these operators expressed as:

$$y(t) = \Pi[u](t) = p_0 u(t) + \int_0^R p(r) F_r[u](t) dr \tag{1.20}$$

with

$$\begin{aligned} &y(0) = F_r[u](0) = f_r(u(0), 0) \\ &y(t) = F_r[u](t) = f_r(u(t), y(t_i)) \\ &\text{for } t_i < t \leq t_{i+1}, \quad 0 \leq i \leq N-1 \\ &f_r(u, y) = \max(u - r, \min(u + r, y)) \end{aligned} \tag{1.21}$$

where $r$ is the model threshold, $p(r)$ is a density function and $p_0 > 0$ and $R$ is the upper integration limit. The Prandtl-Ishlinskii model can be considered as a subclass of the Preisach model, since it was derived from the latter. The advantage of the PI model w.r.t. the Preisach model is that it is simpler and it is analytically invertible, hence it can be used in real-time applications without any numerical approximations. The drawback of this model is that due to its symmetry, it cannot describe the asymmetric hysteresis loops. Therefore, several Modified/Generalized Prandtl-Ishlinskii (MPI/GPI) models for asymmetric and saturated behavior have been reported in literature like dead-zone operators cascaded with the play operators [Kuhnen, 2003], the model with asymmetric backlash as an elementary operator [Dong and Tan, 2009] or the play operators based upon hyperbolic-tangent envelope functions [Janaideh et al., 2009a]. All of these models assume that the hysteresis effect does not depend on the rate of input signals, though as it was mentioned before, in reality it is rate-dependent. Therefore, several works have emerged which include the Preisach model with rate-dependent density function [Mayergoyz, 1988] and Prandtl-Ishlinskii model where the rate-dependence is included in both the threshold and the density function [Janaideh et al., 2008]. In [Ang et al., 2007], the model used in [Kuhnen, 2003] has been extended to the rate-dependent Modified Prandtl–Ishlinskii model, where the slope of the hysteresis was modeled (based only on the experimental data) as a linear function of the rate of the control input. Other hysteresis models include polynomial-based models [Sun et al., 2004], [Bashash and Jalili, 2008], ellipse-based models [Gu and Zhu, 2010], [Gu and Zhu, 2011] and intelligent modeling such as using neural networks [Chuntao and Yonghong, 2004], [Dong et al., 2008] or fuzzy systems [Li et al., 2013b]. In [Cruz-Hernandez and Hayward, 2001] the hysteresis is modeled as a phase lag between input and output.

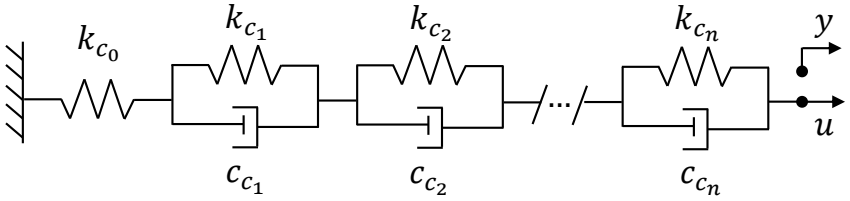


Figure 1.6: Viscoelastic creep model [Croft et al., 2001].

**Creep.**
Another adverse phenomenon present in piezoelectric actuators, which also leads to the loss of precision, is a creep phenomenon (*i.e.* the piezo can drift when positioned over extended periods of time [Abramovitch et al., 2007] and slow-speed operations) shown in Fig. 1.5b. Two most popular models reported in the literature are the nonlinear logarithmic model [Jung and Gweon, 2000] and the linear viscoelastic model [Croft et al., 2001]. The first model assumes that the creep response has a logarithmic shape over time and can be represented by the following equation:

$$y(t) = y_0 \left[1 + \gamma \log_{10}\left(\frac{t}{t_0}\right)\right] \tag{1.22}$$

where $y(t)$ is the response of piezoelectric actuator to a fixed input voltage and the parameters $t_0$, $y_0$ and $\gamma$ are practically identified from the experimental data, $t_0$ refers to the time at which the creep effect is obvious (after applying the input voltage and after oscillations vanishing in the output response, from Fig. 1.5b $t_0 \approx 0.1$ s), $y_0$ is the displacement at time $t_0$ and $\gamma$ determines the rate of the logarithmic response. The linear model of creep, as proposed in [Croft et al., 2001] consists of a series connection of springs and dampers as shown in Fig. 1.6 and can be described in Laplace domain as follows:

$$G_{creep}(s) = \frac{y(s)}{u(s)} = \frac{1}{k_{c_0}} + \sum_{i=1}^{n} \frac{1}{c_{c_i} s + k_{c_i}} \tag{1.23}$$

where $u(s)$ and $y(s)$ are the measured response and input voltage of piezoelectric actuator in Laplace domain, respectively, $k_{c_0}$ models low frequency elastic behavior (but not creep itself) of the piezo, $k_{c_i}$ is the spring constant of each spring, $c_{c_i}$ is the damping constant of each damper and $n$ is the number of spring-damper elements. The advantage of this model over its logarithmic counterpart is that, unlike the latter, its output does not become unbounded for sufficiently small ($t \to 0$) or large ($t \to \infty$) time [Devasia et al., 2007], [Gu et al., 2014b]. Moreover, both $y_0$ and $\gamma$ depend on $t_0$ and the identification of parameter $\gamma$ of model (1.22) is difficult to determine (even for a fixed time $t_0$). Since the creep occurs at low frequencies, it is usually not taken into account during fast operations.

**Structural vibration.**
In STM/AFM applications high resolution of the scanned images is often required, however, the scanning procedure can take sometimes several minutes or even fractions of an hour [Abramovitch et al., 2007]. This time can be shortened when the scanning frequency is increased. However, fast scanning input signals with high frequency components (especially

triangular waveforms, which include odd harmonics) may excite lightly-damped resonance peaks of the positioning device. This resonant nature of piezoelectric actuators causes another adverse phenomenon called structural vibration (see Fig. 1.5c or the inset of Fig. 1.5b), which leads to high positioning errors or even instability and is the main phenomenon limiting high-speed operation of the nanopositioning devices. Therefore without proper control the scanning speed is often limited from 1% up to 10% of piezo's first resonant frequency [Moheimani, 2008]. The vibration modeling mainly consists of finding a linear model, after hysteresis phenomenon (or without taking it into account). The structure of the considered dynamical system is usually quite uncertain or not known a priori, hence only the input and output data sets are taken into account for the identification procedure, which can use such techniques/tools as MATLAB System Identification Toolbox [Li et al., 2013a], sub-space state space technique [Yong et al., 2010b] or using dynamic signal analyzer [Croft and Devasia, 1999]. These methods very often lead to high order models and therefore proper model reduction is looked either for the obtained model only (before the controller design), for the controller model only (after controller design), or in both cases.

**Cross-couplings.**
Another adverse phenomenon exhibited by piezoelectric actuators is the cross-coupling between different axes, observed as a nonzero displacement in the axis other than the excited one, as shown in Fig. 1.5d. This effect increases with both the increased frequency and amplitude of the input signals. In STM/AFM applications in the case when the raster scan is used, one horizontal axis serves as the fast one (typically excited with a triangle input) and the other one as the slow one (excited with a ramp input). In this case the coupling-based positioning errors from the faster axis to the probing vertical one is more significant than from the slower one [Tien et al., 2004]. The coupling effect is one of the major limitations for high speed imaging in STM/AFM devices and can lead not only to large topography distortions but can even damage the cantilever/tip probe and/or the sample [Shi et al., 2009]. Moreover, the cross-couplings between the horizontal X and Y axes are present as well [Yong et al., 2010b].

**Control of piezoelectric actuators.**
A large number of works has been devoted to overcoming the above-mentioned phenomena in order to improve positioning accuracy, increase range of operation and bandwidth. Generally they can be classified into open-loop feedforward and closed-loop feedback methods, or combination of the two as shown in Fig. 1.7. In the feedforward control, models of the addressed phenomena (such as hysteresis, creep or vibration) are used in order to compensate for them, by cascading their corresponding inverses one after another in the feedforward path of the system [Croft et al., 2001] while in the feedback control the nonlinear hysteresis or creep are assumed as disturbances over a linear system. Inverse-based methods, though computationally intensive, are common solutions in cases where sensors are not available. On the other hand, closed-loop techniques are accurate and need not model inversion, but the drawback is that they require (sometimes expensive) sensors for feedback control. The combination of both, feedforward and feedback control, usually gives better results than feedforward or feedback alone, since it allows to take advantage of both approaches - the feedforward control ensures good tracking, while the feedback control robustness w.r.t. modeling errors of the inverse

models, parameter variations as well as disturbances of different nature [Butterworth et al., 2008].

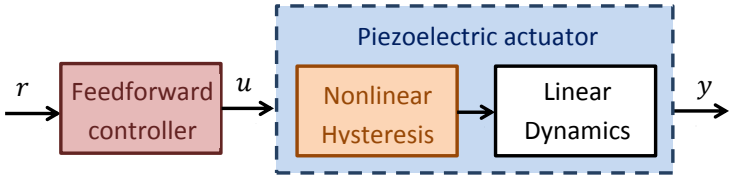


(a)

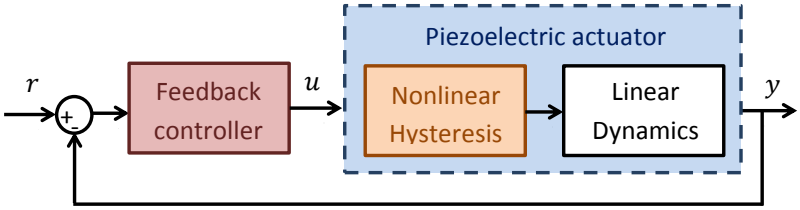


(b)

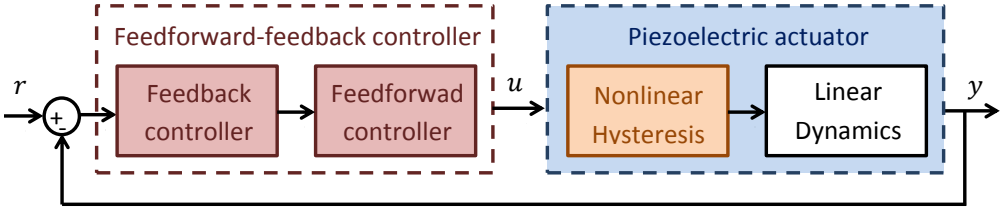


(c)

Figure 1.7: Control architectures used to control piezoelectric actuator: (a) Feedforward control. (b) Feedback control. (d) Feedforward with feedback control.

There exists a vast amount of works on feedforward compensation of hysteresis phenomenon and they are mainly based on the inverse model such as the operator-based Preisach model [Hughes and Wen, 1997], [Tan and Bennani, 2008] the Prandtl-Ishlinskii (PI) model [Kuhnen and Janocha, 2001], [Rakotondrabe et al., 2010] or its modifications/generalizations for asymmetric hysteresis loops [Ang et al., 2007], [Janaideh et al., 2009a], [Gu et al., 2014a]. Adaptive inverses of Preisach and PI models can be found in [Tan and Baras, 2005] and [Kuhnen and Janocha, 1999], respectively. For the differential-based models like Duhem or Bouc-Wen model the inversion is either impossible or extremely difficult to obtain [Gu et al., 2014b] and to overcome this problem, the feedforward compensator can be obtained like in [Rakotondrabe, 2011], where so-called multiplicative-inverse structure is used, which does not require constructing the model inverse explicitly. Moreover, since inverse PI model is also PI-type, one can model the hysteresis inverse directly, from the experimental input/output data, by inverting the input/output axes (*i.e.* by taking the input data as the output and vice-versa) and fitting the PI model to such data. The hysteresis can be considered as a nonlinear bounded disturbance and eliminated in the feedback loop as well using PID con-

trol [Leang and Devasia, 2007], robust H$\infty$ [Chuang et al., 2011] approach or disturbance observer (DOB) [Yi et al., 2009], [Ryba et al., 2014b]. In [El-Shaer et al., 2013] a Generalized Prandtl-Ishlinskii (GPI)-based robust performance enhancement using DOB was studied and illustrated in simulation. As reported in [Amin-Shahidi and Trumper, 2013] the hysteresis can be almost completely avoided using charge amplifiers, which are an interesting alternative for a voltage-based control. However, due to high complexity and cost of the circuit designs of charge amplifiers, voltage-based control is mainly used.

The creep phenomenon can be compensated by the feedforward control using either inverse model of (1.22) [Jung et al., 2001] or (1.23) [Croft et al., 2001] or it can be integrated with PI model and canceled together with hysteresis by its inverse model [Krejci and Kuhnen, 2001]. It can be also assumed as a disturbance and eliminated by the feedback control, mainly PID control [Leang and Devasia, 2007], or via disturbance observer together with hysteresis [Ryba et al., 2014b]. In [Sun and Pang, 2006] post-correction of the AFM image has been done to compensate for the effect of creep and hysteresis.

The open-loop feedforward control using the inverse model of vibration can be found for example in [Croft et al., 2001]. As pointed in [Clayton et al., 2009], the exact vibration inverse [Silverman, 1969] is possible when the dynamical model is minimum-phase (*i.e.* no zeros on the open right half of the complex plane). In case of non-minimum systems a the standard inverse would result in an unbounded feedforward input causing an internal instability in the controlled system. One can inverse only the minimum-phase part and adjust for the overall system gain or use for example more accurate Fourier-transform approach [Leang and Devasia, 2007] which leads to the optimal inversion w.r.t. cost function based on the trade-off between the tracking accuracy and the control effort, similar to LQR designs. When the desired reference trajectory is known a priori Repetitive Control (RC) [Necipoglu et al., 2011] can be used. In [Wu and Zou, 2007] an iterative control approach (IIC) was used for compensating both, hysteresis and vibration of the piezo scanner during high-speed, large-range positioning. The feedforwad approaches for vibration compensation which do not require model inversion, include input-shaping methods as in [Schitter et al., 2008a] (where the scanning speed has been increased by three orders of magnitude compared to conventional AFM) or notch filters as reported in [Leang and Devasia, 2007], where both hysteresis and creep were eliminated via high-gain feedback and the resonant peak of dynamic response was modified by the notch filter, improving the stability margin of the system. The advantage of these methods is that they do not require to model full system dynamics, but only need the values of the resonant frequencies and their corresponding damping ratios. A simple proportional-integral-derivative (PID) controller often fails in dealing with highly resonant positioners especially at high frequencies. When charge control is used to reduce hysteresis phenomenon, an active damping proved to be an effective way to cope with vibration effects such as Integral Resonant Controller (IRC) [Bhikkaji and Moheimani, 2008] or Positive Position Feedback controller (PPF) [Mahmood and Moheimani, 2009b]. The combination of inversion-based feedforward control with active damping feedback control and charge actuation as in [Aphale et al., 2008] proved to increase the tracking bandwidth in the presence of parameter variations such as resonance frequencies. In [Habib et al., 2012], an LQG control is used as another damping technique for lateral positioning of the AFM. However, pure LQG controller is not guaranteed to be

robust, unlike LQR [Safonov and Athans, 1977]. Unfortunately, not all the states can be available and the LQR controller has to work with a state observer. To recover nice properties of LQR design (at least 60° phase margin and 6dB gain margin), an LQG/LTR (Loop Transfer Recovery) procedure was proposed by [Kwakernaak, 1972] and furtherly developed by [Doyle and Stein, 1979], [Doyle and Stein, 1981]. This technique has been successfully applied to suppress the vibration in piezo smart composite wing [Munteanu and Ursu, 2008], at micro-/nanoscale for dual-stage actuators in HDDs [Hu et al., 1999], in vertical direction in AFM [Yeh et al., 2008] as well as to reduce the vibration of lightly-damped resonant system equipped with piezoelectric actuator [Ryba et al., 2014b]. In the recent years, a rapid growth of modern robust control designs has been recorded in nanopositioning due to uncertainties of different nature (different operating conditions, hysteresis, unmodeled dynamics etc.). In [Sebastian and Salapaka, 2005] two kinds of robust controllers were tested experimentally: the Glover–McFarlane loop-shaping and mixed-sensitivity $\mathcal{H}_\infty$ controllers. In the first one, the design task of meeting the performance specifications and robustness are separated into two steps, which appears to be particularly attractive when the controller already exists and one wants to robustify it. Moreover, the uncertainty does not need to be explicitly characterized in this design. The second approach offers more degrees of freedom and achieves simultaneously performance and robustness and is used when the uncertainty model is available. In [Halim and Moheimani, 2001] spatial resonant $\mathcal{H}_2$ controller applied to piezoelectric laminate beam has been designed. Both bandwidth and scanning range can be increased significantly by using a dual actuated system as reported in [Schitter et al., 2008b] or [Kuiper et al., 2010] for AFM. The idea is to combine a long-range, low-bandwidth actuator with a short-range, high-bandwidth actuator. The bandwidth can be also increased by using proper reference scanning inputs like triangular waveform with cutted sharp top [Schitter et al., 2008a] or other scanning trajectories including archimedean spiral [Mahmood and Moheimani, 2009a], cycloid [Yong et al., 2010a] or Lissajous [Tuma et al., 2012] curves.

Finally, to deal with cross-coupling phenomena several works have been reported in the literature. In [Tien et al., 2004] and [Shi et al., 2009], the Inversion-based Iterative Control (IIC) method is proposed to cancel the cross-coupling phenomena from the horizontal X and Y axes to the vertical Z axis in AFM application. The control of cross-couplings between horizontal X and Y axes of nanopositioning stages have been studied in [Mahmood and Moheimani, 2009c], where both vibration and cross-couplings have been tackled via Positive Position Feedback (PPF) control. In [Das et al., 2012], the experimental implementation of the multi-variable resonant controller is used to reduce both vibration and cross-couplings between the axes of the piezoelectric tube scanner of AFM. In [Yong et al., 2010b] a parallel flexure-based nanopositioner based on the compliant mechanism is developed to minimize the cross-coupling effects with $\mathcal{H}_\infty$ control to furtherly eliminate these adverse phenomena for fast raster scanning.

### 1.3.3 Sensors and measurement noises

As mentioned previously, the closed-loop techniques provide an accurate performance, since they assure robustness w.r.t. model uncertainties, disturbances of different nature and system parameter variations. This would not be possible without a feedback from the measured system

outputs. Both, the speed and positioning accuracy crucially depend on the sensing mechanism used in the system [Devasia et al., 2007]. A variety of sensors are used in nanopositioning and differ from their sensing techniques, including inductive [Brinkerhoff and Devasia, 2000], capacitive [Horowitz et al., 2004], piezoresistive [Pedrak et al., 2003] and optical [Schneir et al., 1994] ones. The optical sensors such as laser interferometer [Alexander et al., 1989] are often quite expensive, but they provide high accuracy. On the other hand, cheaper alternatives, such as strain gauge sensor (which measures the strain of the object, based on change of its resistance), do exist. Their resolution is much lower than the one of the optical sensor and they can even bring non-minimum phase behavior into the controlled system, resulting in a serious bandwidth limitation [Schitter et al., 2002].

The most popular sensor used to measure displacements in the horizontal scanning axes of STM/AFM is the capacitive sensor. It is based on a simple technique of non-contact measurement, based on the change in capacitance between the fixed and movable electrode (which depends on the distance between the two of them) converted by an electronic circuitry to voltage units [Devasia et al., 2007]. In the vertical direction of STM, the quantum effect of tunneling current described in section 1.3.1 appears when the distance between the two conductive materials is less than 1 nm, which is very difficult to maintain. Due to very small value of tunnel current (order of nano-amperes), a high-gain sensor is required ($10^9$ [V/A]) to capture and amplify it in order to be properly controlled. Among the noises of different nature [Blanvillain, 2010], the measurement noise introduced by this lab-made high-gain sensor is the main reason of low signal-to noise ratio at such sub-angstrom scale. The tunneling phenomenon allows to measure the displacements of electrodes with a very high precision (several angstroms), but limits the measurement range to 1nm, and [Blanvillain, 2010], [Blanvillain et al., 2009] [Blanvillain et al., 2014] proposed a new approach of using the tunnel current to precisely control the motion of a cantilever beyond the range of 1 nm by means of electrostatic actuation of the latter. So called pull-in effect has been observed *i.e.* when the tunneling tip is approached to the freely vibrating part of the cantilever sufficiently close, the proximity Casimir and van der Waals forces attract the latter towards the tip. An electrostatic actuation with proper control was used to generate the electrostatic effect which counteract these forces [Blanvillain, 2010], [Blanvillain et al., 2008].

## 1.4 3D operation

The aim of this work is to control the experimental tunneling current-based nanopositioning platform in three dimensions. In [Merry et al., 2008], [Habib et al., 2012] or [Das et al., 2012] 3D approaches for AFMs are described, but to the author's knowledge, there is a lack of publications devoted to 3D control of STMs. While the horizontal control of STM and AFM is similar, the principle of work in vertical axis is completely different. The most considered cases are 1D or 2D control. In previous works it was in particular considered the problem of 1D robust digital control in vertical Z direction in experiments by pole placement with sensitivity functions shaping [Ahmad et al., 2012b], and $H\infty$ design (see [Ahmad et al., 2010], [Ahmad et al., 2012a]), as well as in horizontal X direction [Ryba et al., 2014b] using observer-based

hysteresis compensation with vibration reduction by LQG/LTR technique. In [Ahmad et al., 2012a] also 2D extension is proposed taking into account cross-coupling phenomenon but only in simulation. Most popular approaches use a SISO strategy (three controllers, one for each axis). Its performance can yet be deteriorated in case of large model uncertainties, sensor noises and other external disturbances. In this manuscript a comparison of 3D SISO PID and MIMO LQI control of STM in simulation is presented with the purpose of surface reconstruction [Ryba et al., 2013]. The nanopositioning in three dimensions is tested in experiments, with this difference that tunneling current is not kept on a constant level but tracks a prespecified reference signal, playing the role of "virtual surface". The above mentioned phenomena of hysteresis, creep, vibration, cross-coupling between the axes and tunneling nonlinearity are tackled.

## 1.5 Conclusions

In this chapter the Scanning Probe Microscopy such as STM and AFM has been briefly presented together with other nanopositioning applications. The importance, challenges and difficulties arising from the control of such devices at such small scale have been discussed. The tools (such as piezoelectric or electrostatic actuators and capacitive or current sensors) that are used to control the physical laws considered in this manuscript have been presented with the associated modeling and existing control approaches to account for the adverse phenomena of piezoelectric actuators (such as nonlinear hysteresis, creep, vibration and cross-coupling between the axes) in both horizontal and vertical directions, the exponential tunneling nonlinearity, as well as the measurement noise of the high-gain current sensor. Finally, a brief look at the control of nanopositioning devices in 3 dimensions has been given. The considered experimental setup, which is presented in the next chapter, is a micro-/nanopositioning device, which shares some components with both STM (tunneling current phenomenon) and AFM (cantilever). However, its principle of work is much more similar to the STM, and therefore it will be sometimes called as STM-like device.

Chapter 2

# System description and modeling

**Contents**



## 2.1 Introduction

In this chapter, the experimental setup used throughout the work is briefly described and novel 3D nonlinear model is introduced including horizontal X and Y axes, followed by vertical Z axis. The source of its nonlinear behavior is due to: nonlinear hysteresis of piezoelectric actuators, exponential dependence of tunneling current on the distance between two electrodes, quadratic nonlinearity of the electrostatic actuator and nonlinear interaction force between the tip and the surface.

## 2.2 Experimental setup

The researches in this thesis are carried out on tunneling current-based platform of GIPSA-lab shown in Fig. 2.1. Three piezoelectric actuators are driven by control signals from 16-bit D/A converter of the control card, amplified by a high voltage amplifier E-240-100 of gain 15 [V/V] and bandwidth 4 kHz. A platinum/iridium (Pt-Ir) tunneling tip is moved along metallic surface in X and Y directions by piezoelectric actuator Tritor T-402-00 of gain 235 [nm/V] and bandwidth 630 Hz while much smaller and stiffer piezoelectric actuator of gain 1.2 [nm/V] and bandwidth 120 kHz moves the tip in Z direction as shown in Fig. 2.2. Two capacitive sensors CS005 with capaNCDT 6500C device (gain 200 [V/mm] and bandwidth 8.5 kHz) are used to measure the displacements along X and Y axes. In the Z direction, the distance between tip and surface ($< 1$ nm) is determined by the value of tunneling current (nA), measured via high gain ($10^9$ [V/nA]) sensor. These three analog outputs are converted

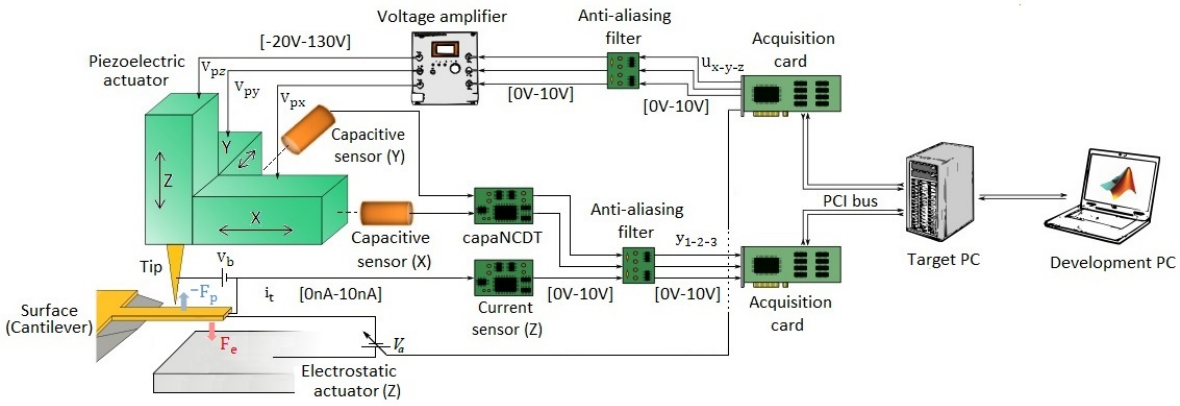


Figure 2.1: Schema of the experimental setup.

into digital values by 16-bit A/D converter of the measurement card and used subsequently by the real-time application working in Target PC with the sampling rate $f_s$ of 20 kHz. The control algorithms and compensators are developed in Matlab & Simulink$^{TM}$ software on a development PC, and downloaded via Ethernet interface into a Target PC. Two acquisition cards (one for control and one for measurement signals) connected with Target PC through PCI bus are used together with two anti-aliasing Butterworth filters with cutoff frequency of 20 kHz.

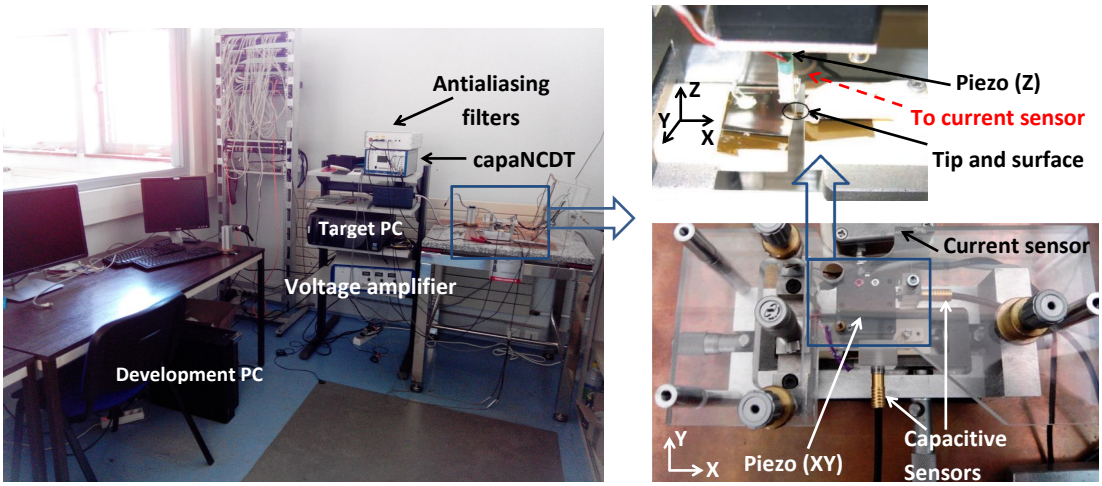


(a) (b)

Figure 2.2: Experimental setup of 3D nanopositioning platform: (a) General view. (b) The heart of the platform.

## 2.3 3D System modeling

In this subsection a full 3D nonlinear model of the considered system, shown in Fig. 2.3 as $Plant_{xyz}$, is developed. In this scheme, the nonlinear parts are distinguished as dashed orange blocks. More details about modeling, control or compensation of each specific subsystem are given in the subsequent chapters.

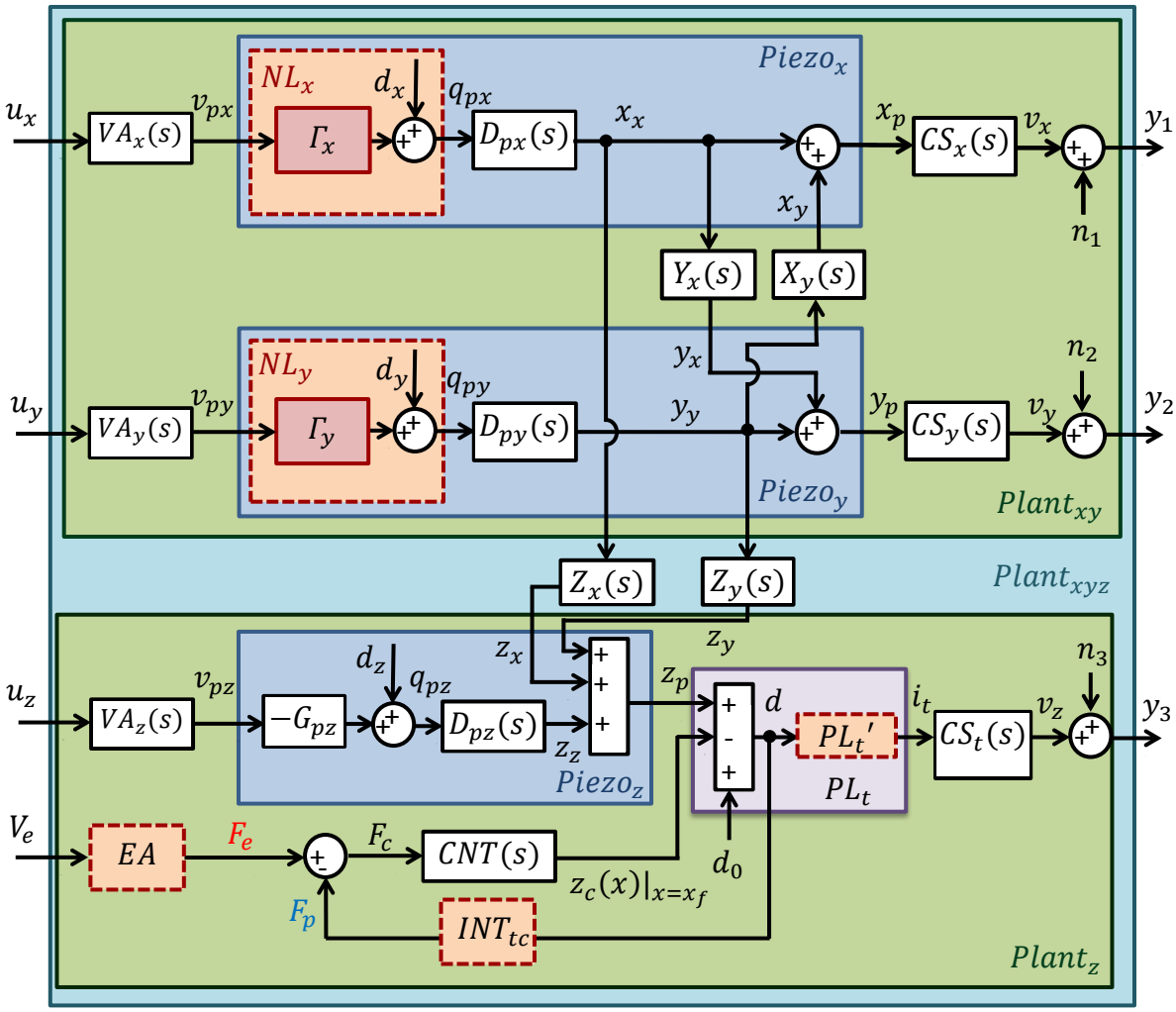


Figure 2.3: Schema of the full 3D nonlinar model.

### 2.3.1 Horizontal X and Y axes

A 2D scanning system of X and Y horizontal axes is shown in Fig. 2.3 as subsystem $Plant_{xy}$. The horizontal piezoelectric actuators in X and Y axes are used to move the tunneling tip along the surface. As pointed in the previous chapter they are widely used in nanopositioning applications due to their high resolution, high stiffness and fast response. However, they

exhibit nonlinear hysteresis, creep, vibration and cross-coupling between the axes. Now, taking into account all the above-mentioned adverse phenomena, the piezoelectric actuator for the X (resp. Y axis) can be modeled as follows (see also Fig. 2.3):

$$Piezo_x : \begin{cases} q_{px}(t) = NL_x[v_{px}](t) = \Gamma_x\left[v_{px}(t)\right] + d_x(t) \\ D_{px}(s) : \begin{cases} \dot{x}_{px}(t) = A_{px}x_{px}(t) + B_{px}q_{px}(t) \\ x_x(t) = C_{px}x_{px}(t) + D_{px}q_{px}(t) \end{cases} \\ X_y(s) : \begin{cases} \dot{x}_{xy}(t) = A_{xy}x_{xy}(t) + B_{xy}y_y(t) \\ x_y(t) = C_{xy}x_{xy}(t) + D_{xy}y_y(t) \end{cases} \\ x_p(t) = x_x(t) + x_y(t) \end{cases} \tag{2.1}$$

$$Piezo_y : \begin{cases} q_{py}(t) = NL_y[v_{py}](t) = \Gamma_y\left[v_{py}(t)\right] + d_y(t) \\ D_{py}(s) : \begin{cases} \dot{x}_{py}(t) = A_{py}x_{py}(t) + B_{py}q_{py}(t) \\ x_x(t) = C_{py}x_{py}(t) + D_{py}q_{py}(t) \end{cases} \\ Y_x(s) : \begin{cases} \dot{x}_{yx}(t) = A_{yx}x_{yx}(t) + B_{yx}x_x(t) \\ y_x(t) = C_{yx}x_{yx}(t) + D_{yx}x_x(t) \end{cases} \\ y_p(t) = y_y(t) + y_x(t) \end{cases} \tag{2.2}$$

or in Laplace domain:

$$Piezo_x : \begin{cases} q_{px}(s) = NL_x[v_{px}](s) = \Gamma_x[v_{px}](s) + d_x(s) \\ x_x(s) = D_{px}(s)q_{px}(s) \\ x_y(s) = X_y(s)y_y(s) \\ x_p(s) = x_x(s) + x_y(s) \end{cases} \tag{2.3}$$

$$Piezo_y : \begin{cases} q_{py}(s) = NL_y[v_{py}](s) = \Gamma_y[v_{py}](s) + d_y(s) \\ y_y(s) = D_{py}(s)q_{py}(s) \\ y_x(s) = Y_x(s)x_x(s) \\ y_p(s) = y_y(s) + y_x(s) \end{cases} \tag{2.4}$$

where $NL_x[v_{px}](t)$ (resp. $NL_y[v_{py}](t)$) is a nonlinear part which consists of the model of static nonlinear hysteresis $\Gamma_x[v_{px}](t)$ (resp. $\Gamma_y[v_{py}](t)$) (more details on how to modelize hysteresis are given in chapter 3) and a slowly varying disturbance $d_x(t)$ (resp. $d_y(t)$), which gathers the effect of creep, unmodeled hysteresis and other low-frequency disturbances. This static (or low frequency) part of piezo is followed by the direct dynamics $D_{px}(s)$ (resp. $D_{py}(s)$) and cross-coupling $X_y(s)$ (resp. $Y_x(s)$), where $x_x(t)$ (resp. $y_y(t)$) is a direct contribution to the piezo displacement $x_p(t)$ (resp. $y_p(t)$) and $x_y(t)$ (resp. $y_x(t)$) is a contribution due to cross-coupling phenomenon. The intermediate variables $q_{px}(t)$ (resp. $q_{py}(t)$) link the nonlinear and linear parts of piezoelectric actuators. The piezo gain $G_{px}$ (resp. $G_{py}$) is hidden in the hysteresis models $\Gamma_x[v_{px}](t)$ (resp. $\Gamma_y[v_{py}](t)$), thus the direct dynamical parts have unit static gain (*i.e.* $D_{px}(0) \approx 1$ and $D_{py}(0) \approx 1$). For the quasi-static behavior (*e.g.* for the design of the disturbance observer for hysteresis and creep compensation, described in chapter 3), a simple second order model $D_{px}(s) = \omega_{px}^2/(s^2 + 2\xi_{px}\omega_{px}s + \omega_{px}^2)$ is used (where $\xi_{px}$ is the damping ratio and $\omega_{px}$ the undamped natural frequency of piezo). However, for the operation at high frequencies a full high-order black box dynamical model is needed and identified as shown in chapter 4.

The voltage amplifier which feeds piezoelectric actuator in X (resp. Y) axis can be described by a first order system as follows:

$$\begin{aligned} \dot{x}_{1,vx}(t) &= -\omega_{vx} x_{1,vx}(t) + u_x(t) \\ v_{px}(t) &= G_{vx}\omega_{vx} x_{1,vx}(t) \end{aligned} \tag{2.5}$$

$$\begin{aligned} \dot{x}_{1,vy}(t) &= -\omega_{vy} x_{1,vy}(t) + u_y(t) \\ v_{py}(t) &= G_{vy}\omega_{vy} x_{1,vy}(t) \end{aligned} \tag{2.6}$$

or in Laplace domain:

$$VA_x(s) = \frac{v_{px}(s)}{u_x(s)} = \frac{G_{vx}\omega_{vx}}{s+\omega_{vx}} \tag{2.7}$$

$$VA_y(s) = \frac{v_{py}(s)}{u_y(s)} = \frac{G_{vy}\omega_{vy}}{s+\omega_{vy}} \tag{2.8}$$

where $u_x(s)$ (resp. $u_y(s)$) and $v_{px}(s)$ (resp. $v_{py}(s)$) are the Laplace transforms of the amplifier input and output, and $G_{vx}$, $\omega_{vx}$ (resp. $G_{vy}$, $\omega_{vy}$) are its gain and bandwidth, respectively.

Finally, the piezo displacements $x_p(t)$, $y_p(t)$ are converted into the voltage units by two capacitive sensors which can be modeled as follows:

$$\begin{aligned} \dot{x}_{1,capx}(t) &= -\omega_{capx} x_{1,capx}(t) + x_p(t) \\ v_x(t) &= G_{capx}\omega_{capx} x_{1,capx}(t) \end{aligned} \tag{2.9}$$

$$\begin{aligned} \dot{x}_{1,capy}(t) &= -\omega_{capy} x_{1,capy}(t) + y_p(t) \\ v_y(t) &= G_{capy}\omega_{capy} x_{1,capy}(t) \end{aligned} \tag{2.10}$$

or in Laplace domain:

$$CS_x(s) = \frac{v_x(s)}{x_p(s)} = \frac{G_{capx}\omega_{capx}}{s+\omega_{capx}} \tag{2.11}$$

$$CS_y(s) = \frac{v_y(s)}{y_p(s)} = \frac{G_{capy}\omega_{capy}}{s+\omega_{capy}} \tag{2.12}$$

where $v_x(s)$ (resp. $v_y(s)$) is the Laplace transform of the capacitive sensor output $v_x(t)$ (resp. $v_y(t)$), and $G_{capx}$, $\omega_{capx}$ (resp. $G_{capy}$, $\omega_{capy}$) are its gain and bandwidth, respectively. The final readout from the sensors is noised in practice as follows:

$$y_1(t) = v_x(t) + n_1(t) \tag{2.13}$$

$$y_2(t) = v_y(t) + n_2(t) \tag{2.14}$$

where $n_1(t)$ and $n_2(t)$ are the noises of the measured outputs $y_1(t)$ and $y_2(t)$, respectively.

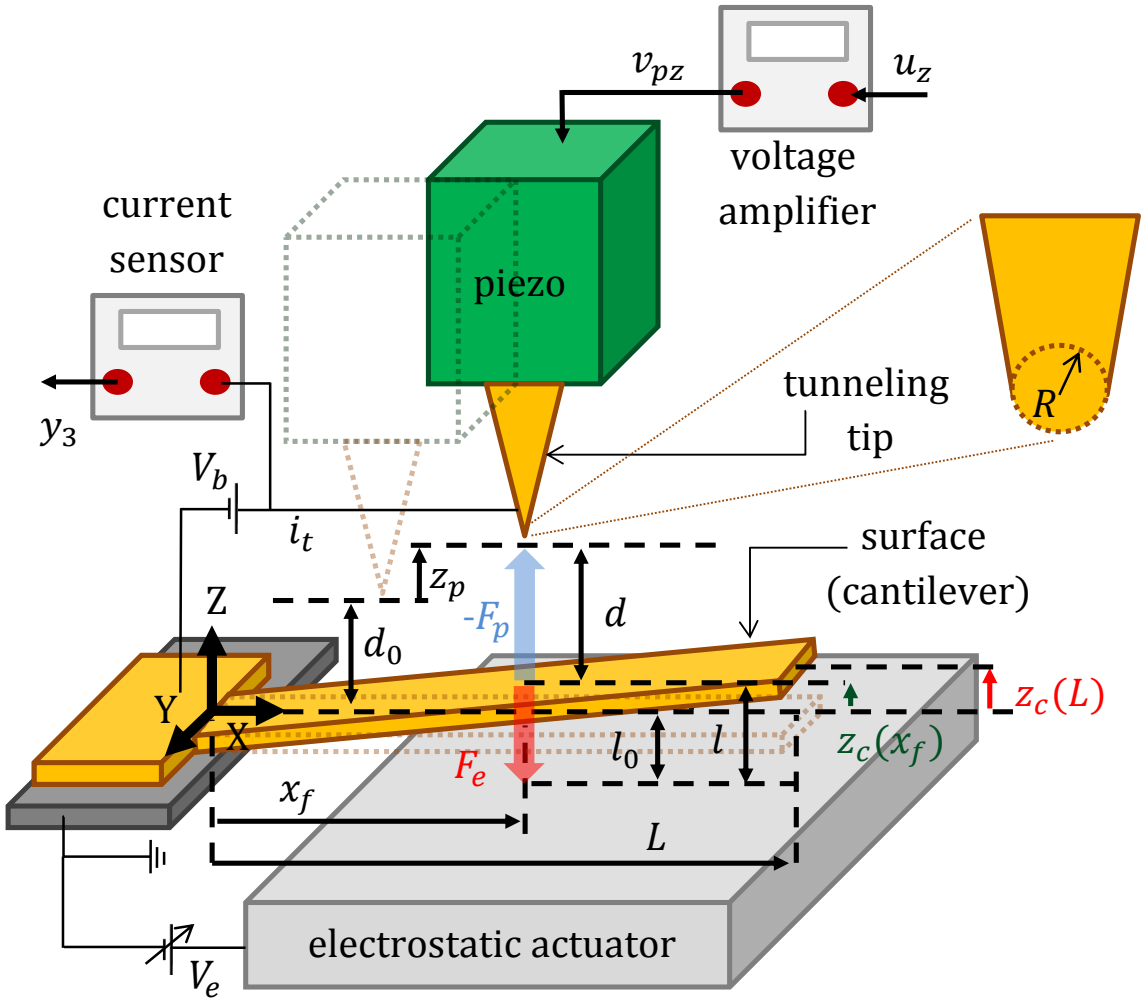


Figure 2.4: Schema of the experimental setup in vertical (Z) direction.

### 2.3.2 Vertical Z axis

The scheme of the vertical system, referred in Fig. 2.3 as $Plant_z$, is shown in Fig. 2.4. The heart of the vertical system model is the tunneling phenomenon between the metallic tip and the metallic surface. As mentioned in the previous chapter, practically, this phenomenon is possible if the distance $d(t)$ between the sharp tip and the clean surface is smaller than 1 nm, therefore the aim is to maintain the tunneling gap $d(t)$ within this distance. The model of the tunneling current used in this manuscript (shown in Fig. 2.3 as a nonlinear block $PL'_t$) is expressed as follows:

$$PL'_t: \quad i_t(t) = \begin{cases} gV_b e^{-kd(t)}, & 0 < d(t) \leq 1\,\text{nm} \\ 0, & d(t) > 1\,\text{nm} \end{cases} \tag{2.15}$$

This distance can be expressed as (see also Fig. 2.3 and Fig. 2.4):

$$d(t) = d_0 + z_p(t) - z_c(x_f, t)) \tag{2.16}$$

where $d_0$ is a tip/surface initial distance, $z_p(t)$ is the actual tip position, $z_c(x_f, t)$ represents the cantilever displacement (see Fig. 2.3) at position $x_f$ (in chapter 6 in STM-like application, surface variations $z_s(t)$ are used instead of cantilever displacement). Due to the exponential term in (2.15), even small variations of the tip/surface distance $d(t)$ greatly influence the tunneling current (decreasing the gap by 1Å (0.1 nm) causes an increase of this current by an order of magnitude and vice versa), which makes the control quite difficult and challenging (an open-loop operation is not possible in this case). On the other hand, taking into account the fact that a typical atomic diameter is of around 0.3 nm, such strong dependency on the distance makes the value of the tunneling current dominated by the contribution between the last atoms of the surface and the tip which in turn results in an atomic resolution of the obtained images.

The piezoelectric actuator in the Z direction is used to approach/withdraw the tip vertically to/from the scanned surface. Since the displacements in this direction are very small (order of nanometers), the hysteresis phenomenon is negligible and the static part of piezo is simply its gain $G_{pz}$. However, the creep is still present and it will be considered as a disturbance $d_z(t)$. The model of the piezoactuator can be defined as follows:

$$Piezo_z : \begin{cases} q_{pz}(t) = -G_{pz} v_{pz}(t) + d_z(t) \\ D_{pz}(s) : \begin{cases} \dot{x}_{1,pz}(t) = x_{2,pz}(t) \\ \dot{x}_{2,pz}(t) = -\omega_{pz}^2 x_{1,pz}(t) - 2\xi_{pz}\omega_{pz} x_{2,pz}(t) + \omega_{pz}^2 q_{pz}(t) \\ z_z(t) = x_{1,pz}(t) \end{cases} \\ Z_x(s) : \begin{cases} \dot{x}_{zx}(t) = A_{zx} x_{zx}(t) + B_{zx} x_x(t) \\ z_x(t) = C_{zx} x_{zx}(t) + D_{zx} x_x(t) \end{cases} \\ Z_y(s) : \begin{cases} \dot{x}_{zy}(t) = A_{zy} x_{zy}(t) + B_{zy} y_y(t) \\ z_y(t) = C_{zy} x_{zy}(t) + D_{zy} y_y(t) \end{cases} \\ z_p(t) = z_z(t) + z_x(t) + z_y(t) \end{cases} \tag{2.17}$$

or in Laplace domain:

$$Piezo_z : \begin{cases} q_{pz}(s) = -G_{pz} v_{pz}(s) + d_z(s) \\ z_z(s) = q_{pz}(s) D_{pz}(s) \\ D_{pz}(s) = \frac{\omega_{pz}^2}{s^2 + 2\xi_{pz}\omega_{pz} s + \omega_{pz}^2} \\ z_x(s) = Z_x(s) x_x(s) \\ z_y(s) = Z_y(s) y_y(s) \\ z_p(s) = z_z(s) + z_x(s) + z_y(s) \end{cases} \tag{2.18}$$

where $z_z(s)$ is a direct contribution to the piezo displacement $z_p(s)$ and $z_x(s)$, $z_y(s)$ are the contributions due to cross-couplings from X and Y axes, respectively. $D_{pz}(s)$ is a vibrational part of piezo, and $\xi_{pz}$, $\omega_{pz}$ are piezo damping and bandwidth, respectively. The piezo moves downwards (in the negative direction), when the input voltage $v_{pz}$ is increased, hence the minus appears near the piezo gain $G_{pz}$ in the first equation of (2.18).

Similarly to the horizontal axes, the voltage amplifier in the vertical axes, which feeds the vertical piezo can be modeled as the following first order system:

$$\begin{aligned} \dot{x}_{1,vz}(t) &= -\omega_{vz} x_{1,vz}(t) + u_z(t) \\ v_{pz}(t) &= G_{vz}\omega_{vz} x_{1,vz}(t) \end{aligned} \tag{2.19}$$

or in Laplace domain:

$$VA_z(s) = \frac{v_{pz}(s)}{u_z(s)} = \frac{G_{vz}\omega_{vz}}{s + \omega_{vz}} \tag{2.20}$$

where $u_z(s)$ and $v_{pz}(s)$ are the Laplace transforms of the amplifier input and output, and $G_{vz}$, $\omega_{vz}$ are its gain and bandwidth, respectively.

Since the value of the tunneling current is very small (order of magnitude of nA), a high-gain current sensor is used to capture and amplify it. This sensor can be modeled as follows:

$$\begin{aligned} \dot{x}_{1,t}(t) &= x_{2,t}(t) \\ \dot{x}_{2,t}(t) &= -\omega_t^2 x_{1,t}(t) - 2\xi_t\omega_t x_{2,t}(t) + \omega_t^2 G_t i_t(t) \\ v_z(t) &= x_{1,t}(t) \end{aligned} \tag{2.21}$$

or in Laplace domain:

$$CS_t(s) = \frac{v_z(s)}{i_t(s)} = \frac{G_t\omega_t^2}{s^2 + 2\xi_t\omega_t + \omega_t^2} \tag{2.22}$$

where $i_t(s)$ and $v_z(s)$ are the Laplace transforms of the tunneling current $i_t(t)$ and current sensor output $v_z(t)$, respectively and $G_t$, $\xi_t$, $\omega_t$ are its gain, damping and bandwidth, respectively. The sub-nanometer scale causes high sensitivity of the tunneling current to the external disturbances and noises. The signal to noise ratio in this direction is much smaller than in the horizontal ones. The final measured output is expressed as follows:

$$y_3(t) = v_z(t) + n_3(t) \tag{2.23}$$

where $n_3(t)$ is the noise of the measured output $y_3(t)$.

**Proximity and counteracting forces.**
Due to small distance between the materials the inter-atomic proximity forces appear and depending on this distance they can be either attractive or repulsive. This interaction is a nonlinear function of the distance $d$ between the tip and the surface and is shown in Fig. 2.3 as an internal physical feedback from this distance through the nonlinear function $INT_{tc}$ to the cantilever input as follows García and San Paulo, 2000, Stark et al., 2004:

$$F_p(t) = INT_{tc}(d(t)) = \begin{cases} -HR/6d(t)^2, & d(t) \geq a_p \\ -HR/6a_p^2 + \frac{4}{3}E^*_{eff}\sqrt{R}(a_p - d(t))^{3/2}, & d(t) < a_p \end{cases} \tag{2.24}$$

where $R$ is the tip radius, $H$ the Hamaker constant. The value of $a_p$ separates the attractive ($d(t) \geq a_p$) and repulsive ($d(t) < a_p$) zones. In the attractive zone van der Waals forces attract the tip versus the surface (it is assumed that the tip apex is spherical and the surface is plate). When the distance tip/surface is decreased to the interatomic value $a_p$, the adhesion

force appears in addiction to the pure van der Waals force according to the Dejarguin-Muller-Toporov (DMT) theory Derjaguin et al., 1975, which models the repulsive zone. This adhesive force successively decreases the effect of the van der Waals force and when the two forces are equal, the atoms of the two materials are in mechanical contact and start to repeal each other. The effective contact stiffness appearing in the adhesive force is given by $E^*_{eff} = [(1-v_t^2)/E_t + (1-v^2)/E]^{-1}$, where $v_t$ and $v_c$ are the Poisson ratios and $E_t$ and $E$ the elastic moduli of the tip and the cantilever, respectively. During normal STM operation the tip is not in contact with the surface, hence the range of tip/surface distances coincides with the range of attractive force only ($d(t) \geq a_p$). Due to the attractiveness of the proximity force during normal STM operation, the minus appears in (2.24). However this force bends the cantilever upwards (see Fig. 2.4) in the positive direction of the Z axis, hence it is taken with minus sign in the scheme from Fig. 2.3.

In order to avoid a stuck between the tip and the cantilever, the proximity force should be counteracted by another external force. To that end, a metalic plate is added and biased w.r.t the base of the cantilever with the potential $V_e(t)$. This electrostatic actuator $EA$ (see Fig. 2.3 and Fig. 2.4) bends the cantilever in opposite direction to the proximity force direction (with minus sign) and together with the cantilever creates a capacitor with the capacitance expressed as follows:

$$C(l(t)) = \frac{\varepsilon_0 A_e}{l(t)} \tag{2.25}$$

where $A_e$ is the cantilever surface under the electrostatic plate and $l(t)$ is the distance between the two. The total energy of this capacitor is equal to the work needed to transport all the charge from one plate to another and is given by:

$$W = \frac{1}{2} C(l(t)) V_e(t)^2 \tag{2.26}$$

Due to the potential difference between these two conductive materials an electrostatic force appears which can be expressed as follows:

$$F_e(t) = \frac{dW}{dl} = \frac{1}{2}\frac{d}{dl} C(l(t)) V_e(t)^2 = -\frac{1}{2}\frac{\varepsilon_0 A_e}{l(t)^2} V_e(t)^2 \tag{2.27}$$

where $l(t) = l_0 + z_c(x_f, t)$ and $l_0$ is the distance between the unbended cantilever (at zero position) and the electrostatic actuator as shown in Fig. 2.4, $z_c(x_f, t)$ is the total cantilever displacement at the tip position $x_f$, defined as the superposition of the displacements caused by the proximity and the counteracted electrostatic forces as follows:

$$z_c(x_f, t) = z_{c_p}(x_f, t) + z_{c_e}(x_f, t) \tag{2.28}$$

where $z_{c_p}(x_f, t) > 0$, since it has the direction of $-F_p > 0$ and $z_{c_e}(x_f, t) < 0$, since it has the direction of $F_e < 0$. The total force that is acting on the cantilever is expressed as follows:

$$F_c(t) = -F_p(t) + F_e(t) \tag{2.29}$$

**Cantilever model.**
In this thesis a multi-mode cantilever of length $L$ with forced vibration and damping is adopted like in Salapaka et al., 1997 to model the subsystem $CNT(s)$ shown in Fig. 2.3. The cantilever motion is govern by the following partial differential equation:

$$EI\frac{\partial^4 z_c(x,t)}{\partial x^4} + p_d(x,t) + \rho A\frac{\partial^2 z_c(x,t)}{\partial t^2} = -F_p(t) \tag{2.30}$$

The behavior of this model depends on both the position $x$ and time $t$. For convenience of notation, $v' = \frac{dv}{dx}$ will stand for the spatial derivative (here w.r.t. the $x$ variable) and $\dot{v} = \frac{dv}{dt}$ time derivative of variable $v$. The interaction force is applied at the position $x_f$ from the base of the cantilever (in this manuscript this force is the proximity force in the positive direction $-F_p(t)$ (2.24)). The value of the damping force $p_d(x,t)$ can be expressed as follows:

$$p_d(x,t) = \xi\frac{\partial z_c(x,t)}{\partial t} - F_e(t) \tag{2.31}$$

and is the sum of the natural structural cantilever damping force and the damping force that is introduced to the system (here $-F_e(t)$ (2.27)). Using (2.31) in (2.30) one obtains the following equation:

$$EI\frac{\partial^4 z_c(x,t)}{\partial x^4} + \xi\frac{\partial z_c(x,t)}{\partial t} + \rho A\frac{\partial^2 z_c(x,t)}{\partial t^2} = \underbrace{F_c(t)}_{-F_p(t)+F_e(t)} \tag{2.32}$$

The cantilever displacement can be expressed as a weighed sum of the time-dependent fundamental mode deformations $q_j(t)$ (corresponding to the $j^{th}$ mode), with spatially-dependent weighting functions referred as the modal shape functions $\phi_j(x)$, as follows:

$$z_c(x,t) = \sum_{j=1}^{\infty} \phi_j(x) q_j(t) \tag{2.33}$$

where the modal shape function $\phi_j(x)$ is given by:

$$\begin{aligned} \phi_j(x) \quad &= (\sin\,\lambda_j L + \sinh\,\lambda_j L)(\cos\,\lambda_j x - \cosh\,\lambda_j x) \\ &+(\cos\,\lambda_j L + \cosh\,\lambda_j L)(\sinh\,\lambda_j x - \sin\,\lambda_j x) \end{aligned} \tag{2.34}$$

with $\lambda_j L$ being $j^{th}$ mode wavelength which satisfies the following equation:

$$\cos\,\lambda_j L\,\cosh\,\lambda_j L + 1 = 0 \tag{2.35}$$

The modal shape function (2.34) satisfies the following formulas:

$$\int_0^L \phi_j(x)^2 dx = L(\sin\,\lambda_j L + \sinh\,\lambda_j L)^2 \tag{2.36}$$

$$\int_0^L (\phi_j''(x))^2 dx = \lambda_j^4 L(\sin\,\lambda_j L + \sinh\,\lambda_j L)^2 \tag{2.37}$$

The fundamental deformation $q_j(t)$ of $j^{th}$ mode is the solution of the following $2^{nd}$ order differential equation:

$$m_j\ddot{q}_j(t) + c_j\dot{q}_j(t) + k_j q_j(t) = F_{c_j}(t) \tag{2.38}$$

where $m_j$, $k_j$, $c_j$ and $F_{c_j}(t)$ are respectively the mass, spring constant, damping coefficient and force corresponding to $j^{th}$ mode. Using (2.36) and (2.37) they can be expressed as follows:

$$m_j = \rho A \int_0^L \phi_j(x)^2 dx = \rho AL(\sin\,\lambda_j L + \sinh\,\lambda_j L)^2 \tag{2.39}$$

$$k_j = EI \int_0^L (\phi_j''(x))^2 dx = EI\lambda_j^4 L(\sin\,\lambda_j L + \sinh\,\lambda_j L)^2 \tag{2.40}$$

$$c_j = \xi L \int_0^L \phi_j(x)^2 dx = \xi L(\sin\,\lambda_j L + \sinh\,\lambda_j L)^2 \tag{2.41}$$

$$F_{c_j}(t) = \phi_j(x_f) F_c(t) \tag{2.42}$$

In state-space with standard state variables $x_{2j-1,c}(t) = q_j(t)$, $x_{2j,c}(t) = \dot{q}_j(t)$ and using (2.42) in (2.38), the $j^{th}$ mode can be expressed as follows:

$$\begin{bmatrix} \dot{x}_{2j-1,c}(t) \\ \dot{x}_{2j,c}(t) \end{bmatrix} = \begin{bmatrix} 0 & 1 \\ -\frac{k_j}{m_j} & -\frac{c_j}{m_j} \end{bmatrix} \begin{bmatrix} x_{2j-1,c}(t) \\ x_{2j,c}(t) \end{bmatrix} + \begin{bmatrix} 0 \\ \frac{\phi_j(x_f)}{m_j} \end{bmatrix} F_c(t) \tag{2.43}$$

Taking first $n_c$ modes ($j = 1..n_c$), the state space representation for the cantilever takes the following form:

$$\begin{bmatrix} \dot{x}_{1,c}(t) \\ \dot{x}_{2,c}(t) \\ \vdots \\ \dot{x}_{2n_c-1,c}(t) \\ \dot{x}_{2n_c,c}(t) \end{bmatrix} = \underbrace{\begin{bmatrix} 0 & 1 & \cdots & 0 & 0 \\ -\frac{k_1}{m_1} & -\frac{c_1}{m_1} & \cdots & 0 & 0 \\ \vdots & \vdots & \ddots & \vdots & \vdots \\ 0 & 0 & \cdots & 0 & 1 \\ 0 & 0 & \cdots & -\frac{k_{n_c}}{m_{n_c}} & -\frac{c_{n_c}}{m_{n_c}} \end{bmatrix}}_{A_c} \begin{bmatrix} x_{1,c}(t) \\ x_{2,c}(t) \\ \vdots \\ x_{2n_c-1,c}(t) \\ x_{2n_c,c}(t) \end{bmatrix} + \underbrace{\begin{bmatrix} 0 \\ \frac{\phi_1(x_f)}{m_1} \\ \vdots \\ 0 \\ \frac{\phi_{n_c}(x_f)}{m_{n_c}} \end{bmatrix}}_{B_c} F_c(t) \tag{2.44}$$

$$y_c(t) = \underbrace{\begin{bmatrix} 1 & 0 & \cdots & 1 & 0 \end{bmatrix}}_{C_c} \begin{bmatrix} x_{1,c}(t) \\ x_{2,c}(t) \\ \vdots \\ x_{2n_c-1,c}(t) \\ x_{2n_c,c}(t) \end{bmatrix} + \underbrace{0}_{D_c} \cdot F_c \tag{2.45}$$

with $2n_c$-dimensional state vector:

$$x_c(t) = \begin{bmatrix} x_{1,c}(t) \\ x_{2,c}(t) \\ \vdots \\ x_{2n_c-1,c}(t) \\ x_{2n_c,c}(t) \end{bmatrix} = \begin{bmatrix} q_1(t) \\ \dot{q}_1(t) \\ \vdots \\ q_{n_c}(t) \\ \dot{q}_{n_c}(t) \end{bmatrix} \tag{2.46}$$

or in compact way:

$$\begin{aligned} \dot{x}_c &= A_c x_c + B_c F_c \\ y_c &= C_c x_c + D_c F_c \end{aligned} \tag{2.47}$$

Finally, inserting $q_j(t) = x_{2j-1,c}(t)$ into (2.33), the displacement of the cantilever with $n_c$ modes can be expressed in state coordinates as follows:

$$z_c(x,t) = \sum_{j=1}^{n_c} \phi_j(x) x_{2j-1,c}(t) \tag{2.48}$$

Especially, when $x = x_f$, one considers the cantilever displacement at the tip position (see Fig. 2.4) and (2.48) takes the following form:

$$z_c(x,t)|_{x=x_f} = z_c(x_f,t) = \sum_{j=1}^{n_c} \phi_j(x_f) x_{2j-1,c}(t) \tag{2.49}$$

Cantilever displacement can be expressed also in Laplace domain (assuming first $n_c$ modes, zero initial conditions for $q_j(0) = \dot{q}_j(0) = 0$, taking the Laplace transform of (2.38) and using it in (2.33)) as follows:

$$z_c(x,s) = \sum_{j=1}^{n_c} \phi_j(x) \frac{1}{s^2 + \frac{c_j}{m_j}s + \frac{k_j}{m_j}} \frac{1}{m_j} F_{c_j}(s) = \sum_{j=1}^{n_c} \phi_j(x) \frac{\phi_j(x_f)}{s^2 + \frac{c_j}{m_j}s + \frac{k_j}{m_j}} \frac{1}{m_j} F_c(s) \tag{2.50}$$

One can say that the modal shape function $\phi_j(x)$ allows to distribute in space the modal contributions. It is a convenient way, since only this shaping function depends on position and the other part (modal) depends only on time.
Finally, taking into account all the equations from this chapter, one can write the following full nonlinear 3D state-space model which corresponds to the schema in Fig. 2.3:

$$\underbrace{\begin{bmatrix} \dot{x}_{1,vx}(t) \\ \dot{x}_{px}(t) \\ \dot{x}_{xy}(t) \\ \dot{x}_{1,capx}(t) \\ \dot{x}_{1,vy}(t) \\ \dot{x}_{py}(t) \\ \dot{x}_{yx}(t) \\ \dot{x}_{1,capy}(t) \\ \dot{x}_{1,vz}(t) \\ \dot{x}_{1,pz}(t) \\ \dot{x}_{2,pz}(t) \\ \dot{x}_{zx}(t) \\ \dot{x}_{zy}(t) \\ \dot{x}_{c}(t) \\ \dot{x}_{1,t}(t) \\ \dot{x}_{2,t}(t) \end{bmatrix}}_{\dot{x}_{3D}(t)} = \underbrace{\begin{bmatrix} -\omega_{vx} x_{1,vx}(t) + u_x(t) \\ A_{px} x_{px}(t) + B_{px} q_{px}(t) \\ A_{xy} x_{xy}(t) + B_{xy} y_y(t) \\ -\omega_{capx} x_{1,capx}(t) + \underbrace{x_x(t) + x_y(t)}_{x_p(t)} \\ -\omega_{vy} x_{1,vy}(t) + u_y(t) \\ A_{py} x_{py}(t) + B_{py} q_{py}(t) \\ A_{yx} x_{yx}(t) + B_{yx} x_x(t) \\ -\omega_{capy} x_{1,capy}(t) + \underbrace{y_y(t) + y_x(t)}_{y_p(t)} \\ -\omega_{vz} x_{1,vz}(t) + u_z(t) \\ x_{2,pz}(t) \\ -\omega_{pz}^2 x_{1,pz}(t) - 2\xi_{pz}\omega_{pz} x_{2,pz}(t) + \omega_{pz}^2 q_{pz}(t) \\ A_{zx} x_{zx}(t) + B_{zx} x_x(t) \\ A_{zy} x_{zy}(t) + B_{zy} y_y(t) \\ A_c x_c(t) + B_c F_c(t) \\ x_{2,t}(t) \\ -\omega_t^2 x_{1,t}(t) - 2\xi_t \omega_t x_{2,t}(t) + \omega_t^2 G_t \underbrace{g V_b e^{-kd(t)}}_{i_t(t)} \end{bmatrix}}_{f(x_{3D}(t), u_{3D}(t), d_{3D}(t))} \tag{2.51}$$

$$\underbrace{\begin{bmatrix} y_1(t) \\ y_2(t) \\ y_3(t) \end{bmatrix}}_{y_{3D}(t)} = \underbrace{\begin{bmatrix} G_{capx}\omega_{capx}x_{1,capx}(t) + n_1(t) \\ G_{capy}\omega_{capy}x_{1,capy}(t) + n_2(t) \\ x_{1,t} + n_3(t) \end{bmatrix}}_{h(x_{3D}(t),n_{3D}(t))} \tag{2.52}$$

$$u_{3D}(t) = \begin{bmatrix} u_1(t) \\ u_2(t) \\ u_3(t) \\ V_e(t) \end{bmatrix}, \quad d_{3D}(t) = \begin{bmatrix} d_x(t) \\ d_y(t) \\ d_z(t) \end{bmatrix}, \quad n_{3D}(t) = \begin{bmatrix} n_1(t) \\ n_2(t) \\ n_3(t) \end{bmatrix} \tag{2.53}$$

where:

$$q_{px}(t) = \Gamma_x \underbrace{[G_{vx}\omega_{vx}x_{1,vx}(t)]}_{v_{px}(t)} + d_x(t) \tag{2.54}$$

$$q_{py}(t) = \Gamma_y \underbrace{[G_{vy}\omega_{vy}x_{1,vy}(t)]}_{v_{py}(t)} + d_y(t) \tag{2.55}$$

$$q_{pz}(t) = -G_{pz} \underbrace{G_{vz}\omega_{vz}x_{1,vz}(t)}_{v_{pz}(t)} + d_z(t) \tag{2.56}$$

$$x_x(t) = C_{px}x_{px}(t) + D_{px}q_{px}(t) \tag{2.57}$$

$$y_y(t) = C_{py}x_{py}(t) + D_{py}q_{py}(t) \tag{2.58}$$

$$x_y(t) = C_{xy}x_{xy}(t) + D_{xy}y_y(t) \tag{2.59}$$

$$y_x(t) = C_{yx}x_{yx}(t) + D_{yx}x_x(t) \tag{2.60}$$

$$z_x(t) = C_{zx}x_{zx}(t) + D_{zx}x_x(t) \tag{2.61}$$

$$z_y(t) = C_{zy}x_{zy}(t) + D_{zy}y_y(t) \tag{2.62}$$

$$d(t) = d_0 + \underbrace{\underbrace{x_{1,pz}(t)}_{z_z(t)} + z_x(t) + z_y(t)}_{z_p(t)} - \underbrace{\sum_{j=1}^{n_c} \phi_j(x_f)x_{2j-1,c}(t)}_{z_c(x_f,t)} \tag{2.63}$$

$$F_c(t) = \underbrace{\frac{HR}{6d(t)^2}}_{-F_p(t)} + \underbrace{\frac{-\varepsilon_0 A_e V_e^2(t)}{2(l_0 + z_c(x_f,t))^2}}_{F_e(t)} \tag{2.64}$$

## 2.4 Conclusion

In this chapter, the full nonlinear 3D model has been developed for the considered tunneling current-based platform. First, the horizontal motion in X and Y axes has been considered. The

model of piezoelectric actuators (driven by voltage amplifier and read by capacitive sensor) including nonlinear hysteresis, creep, structural vibration and cross-coupling is given. Next, the model in vertical Z direction includes the exponential behavior of the tunneling nonlinearity between the tip (driven by the piezoelectric actuator) and the cantilever (driven by the electrostatic actuator). The current sensor catches and amplifies the small value of tunneling current. The next chapters give more insight to the modeling of the single components of the full nonlinear model as well as to appropriate control and compensation.

Chapter 3

# Static hysteresis and creep

Contents



## 3.1 Introduction

In this section the nonlinear effect of hysteresis is studied. The measured data from the capacitive sensors of the experimental nanopositioning platform in X and Y directions are used together with the corresponding control signals in these directions to identify the model of static nonlinearity. To that end, the Prandtl-Ishlinskii model in its classical (referred simply as PI) and modified (referred as MPI) version is first fitted to the measured data, inverted and cascaded with the corresponding axis of the real plant in the feedforward path. The presentation of this open-loop technique is followed by that of observer-based hysteresis compensation as proposed in [Yi et al., 2009]. In this method the hysteresis modeling is given up and this nonlinear effect is assumed as an unknown slowly varying disturbance over piezo displacement and reconstructed via disturbance observer (DOB). This technique is considered as a closed-loop method, since it uses the feedback from the measured displacement. However, differently from [Yi et al., 2009], the disturbance is considered as a new entry of a state vector

and reconstructed via state observer together with the system state (see also [Ryba et al., 2014b] and [Ryba et al., 2014a]), hence the direct inversion of system dynamics is avoided. Next, the open-loop MPI is combined with closed-loop DOB (*i.e.* the observed disturbance is now the mismatch between the real hysteresis response and its MPI model), which is shown to improve the accuracy of modeling and compensation (see [Ryba et al., 2015b]). Finally, one parametric polynomial model with adaptively changing coefficients is used to modelize hysteresis and the proper compensation input is determined in real-time using Newton-based algorithm, which does not require model inversion (see [Ryba et al., 2015a]).

## 3.2 Prandtl-Ishlinskii approach

In this section the PI approach is used to model and compensate hysteresis effect. In static case, for identification purpose of a static hysteresis, the piezo dynamics $D_{px}(s)$ can be neglected (*i.e.* $q_{px}(t) = x_p(t)$ in Fig. 3.1). The backlash operator of the Prandtl-Ishlinskii (PI)

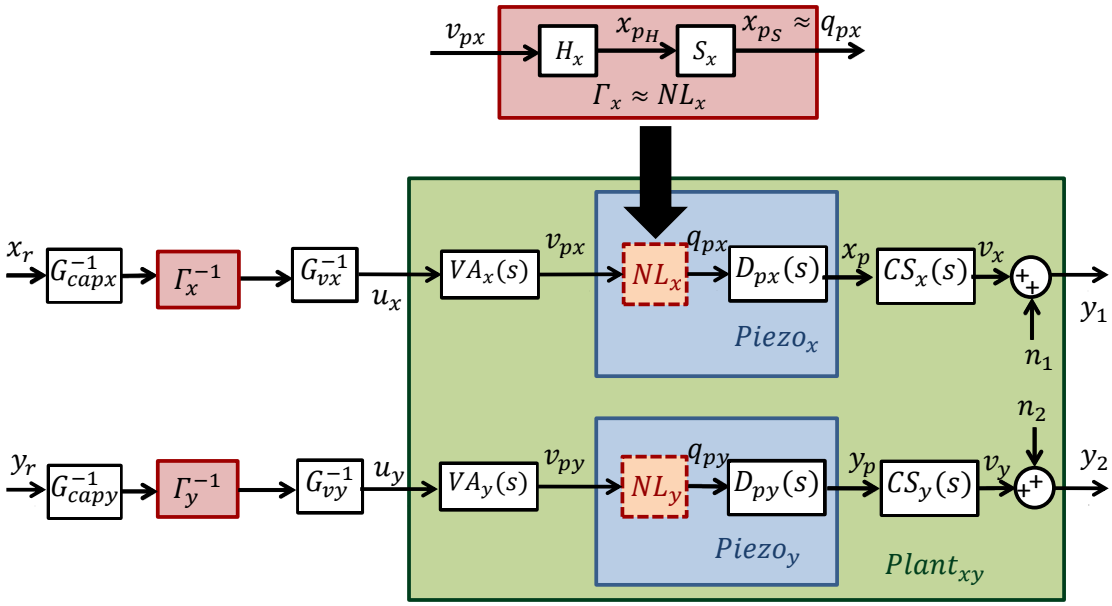


Figure 3.1: 2D Schema (inverse-based approach).

model is an elementary nonlinear transformation between the input $v_{px}(t)$ and the output $x_{p_H}(t)$ as follows:

$$\begin{aligned} x_{p_H}(t) &= H_{x_{r_H}}[v_{px}, x_{p_H 0}](t) \\ &= \max\{v_{px}(t) - r_{x_H}, \\ &\quad \min\{v_{px}(t) + r_{x_H}, x_{p_H}(t - T_s)\}\}, \end{aligned} \tag{3.1}$$

where $r_{x_H}$ is an input threshold for $v_{px}$ and $T_s$ is the sampling time. The elementary backlash operator (3.1) multiplied by a weight value $w_{x_H}$ forms so called weighted backlash operator

(see Fig. 3.2a). The linear weighted superposition of $n+1$ backlash operators with different threshold values finally defines the PI hysteresis operator $H_x$ as follows (see Fig. 3.2b):

$$x_{p_H}(t) = H_x[v_{px}](t) = \boldsymbol{w}_{x_H}{}^T \boldsymbol{H}_{\boldsymbol{r}_{x_H}}[v_{px}, \boldsymbol{x}_{p_H 0}](t), \tag{3.2}$$

where $\boldsymbol{w}_{x_H}$ is the vector of weights, $\boldsymbol{r}_{x_H}$ is the vector of thresholds such that $0 = r_{x_{H_0}} < r_{x_{H_1}} < ... < r_{x_{H_n}} < +\infty$, $\boldsymbol{x}_{p_H 0}$ is the vector of initial states of the backlash operators and $\boldsymbol{H}_{\boldsymbol{r}_{x_H}}[v_{px}, \boldsymbol{x}_{p_H 0}](t)$ is the vector of backlash operators. In its classical form the PI model is symmetric, it consists of hysteresis operator $H_x$ only and the superposition operator $S_x$ in Fig. 3.1 is omitted (*i.e.* $S_x[x_{p_H}](t) = x_{p_H}(t)$). Therefore the PI model $\Gamma_x[v_{px}](t) = H_x[v_{px}](t)$ approximates static nonlinearity $NL_x$ and $x_{p_H}(t) \approx q_{p_x}$ (see Fig. 3.1). The procedure for hysteresis compensator $\Gamma_x$ design consists of three consecutive steps: model initialization, model identification and model inversion.

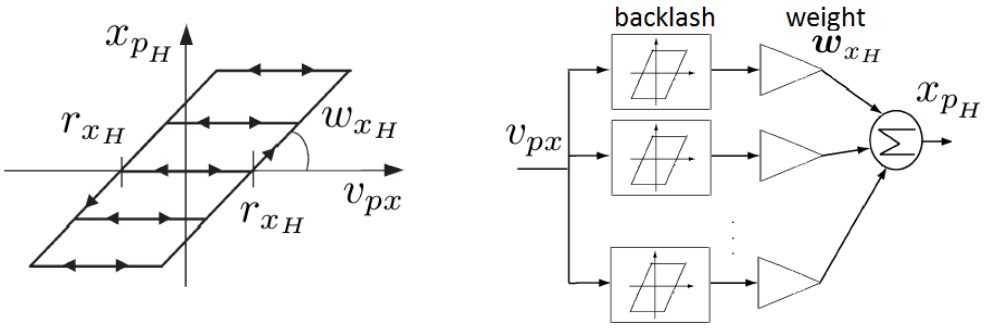


(a) (b)

Figure 3.2: Hysteretic nonlinearity: (a) Weighted backlash operator. (b) Hysteresis operator as a superposition of $n+1$ backlash operators [Ang et al., 2007], [Rakotondrabe et al., 2010].

### 3.2.1 Model initialisation, identification and inversion

In model initialization step, the range of input voltage $\max\{v_{px}\}$ is divided into $n+1$ (often equal) intervals defining the threshold values $\boldsymbol{r}_{x_H}$ as follows:

$$r_{x_{H_i}} = \frac{i}{n+1}\max\{v_{px}\}, \quad i = 0..n. \tag{3.3}$$

and the backlash operators are initialized to zero (deenergized state):

$$x_{p_H 0_i} = 0, \quad i = 0..n. \tag{3.4}$$

Fig. 3.3 shows the identification procedure of the PI approach, which is the second step of the compensator design. One searches for the optimal weights $\boldsymbol{w}^*_{x_H}$ that minimize (in the least squares sense) the following model error:

$$\begin{aligned} E_x[v_{px}, \tilde{x}_p](t) &= H_x[v_{px}](t) - \tilde{x}_p(t) \\ &= \boldsymbol{w}^T_{x_H} \boldsymbol{H}_{r_{x_H}}[v_{px}, \boldsymbol{x}_{p_H 0}](t) - \tilde{x}_p(t) \end{aligned} \tag{3.5}$$

with an output displacement $\tilde{x}_p(t) = \frac{y_1(t)}{G_{capx}}$ measured at each time instant $t$. The quadratic loss function to be minimized is given by:

$$\begin{aligned} J_x(\boldsymbol{w}_{x_H}) &= \frac{1}{2}\sum_{i=1}^{l}(E_x[v_{px}, \tilde{x}_p](t_i))^2 \\ &= \frac{1}{2}\boldsymbol{w}_{x_H}^T \boldsymbol{F}_x \boldsymbol{w}_{x_H} + \boldsymbol{w}_{x_H}^T \boldsymbol{f}_{x_1} + f_{x_0} \end{aligned} \tag{3.6}$$

where $t_i = i \cdot T_s$ and $l$ is a size of the collected experimental data set. The quadratic term represented by the Hessian matrix $\boldsymbol{F}_x$, the linear term represented by the vector $\boldsymbol{f}_{x_1}$ and the scalar $f_{x_0}$ in (3.6) are defined as follows:

$$\boldsymbol{F}_x = \sum_{i=1}^{l} \boldsymbol{H}_{r_{x_H}}[v_{px}, \boldsymbol{x}_{p_H 0}](t_i) \boldsymbol{H}_{r_{x_H}}^T[v_{px}, \boldsymbol{x}_{p_H 0}](t_i) \tag{3.7}$$

$$\boldsymbol{f}_{x_1} = \sum_{i=1}^{l} \tilde{x}_p(t_i) \boldsymbol{H}_{r_{x_H}}[v_{px}, \boldsymbol{x}_{p_H 0}](t_i) \tag{3.8}$$

$$f_{x_0} = \sum_{i=1}^{l} \frac{1}{2}\tilde{x}_p^2(t_i) \tag{3.9}$$

To ensure the existence of the model inverse, the slope of the PI model has to be monotonous function of the input voltage and since this slope is defined as the sum of the weights of the activated backlashes, these weights $\boldsymbol{w}_{x_H}$ have to be constrained by the following convex polyhedron:

$$P_x = \left\{ \boldsymbol{w}_{x_H} : \boldsymbol{U}_H \boldsymbol{w}_{x_H} - \boldsymbol{u}_H \geq \boldsymbol{0} \right\} \tag{3.10}$$

where $\boldsymbol{U}_H \in \Re^{n+1 \times n+1}$, $\boldsymbol{u}_H \in \Re^{n+1}$ are defined as:

$$\boldsymbol{U}_H = \begin{pmatrix} 1 & 0 & \cdots & 0 \\ 1 & 1 & \cdots & 0 \\ \vdots & \vdots & \ddots & \vdots \\ 1 & 1 & \cdots & 1 \end{pmatrix}, \boldsymbol{u}_H = \begin{pmatrix} \epsilon \\ \epsilon \\ \vdots \\ \epsilon \end{pmatrix} \tag{3.11}$$

and $\epsilon > 0$ is a possibly infinitely small value. This condition ensures strong monotonicity of the hysteresis curve. Note, that the absolute term (3.9) does not depend on $\boldsymbol{w}_{x_H}$, and as a result it can be neglected during the optimization procedure. In this case the quadratic optimization problem constrained by (3.10) and (3.11) boils down to:

$$QP_x : \min_{\boldsymbol{w}_{x_H} \in P_x} \{J_x(\boldsymbol{w}_{x_H})\} = \min_{\boldsymbol{w}_{x_H} \in P_x} \left\{ \frac{1}{2}\boldsymbol{w}_{x_H}^T \boldsymbol{F}_x \boldsymbol{w}_{x_H} + \boldsymbol{w}_{x_H}^T \boldsymbol{f}_{x_1} \right\} \tag{3.12}$$

The third step is the inversion of the hysteresis model identified in the previous step. The inverse model is also PI type as follows:

$$v_{px}(t) = \Gamma_x^{-1}[x_{p_H}](t) = H_x^{-1}[x_{p_H}](t) = \boldsymbol{w'}_{x_H}^T \boldsymbol{H}_{r'_{x_H}}[x_{p_H}, \boldsymbol{v}_{px0}](t) \tag{3.13}$$

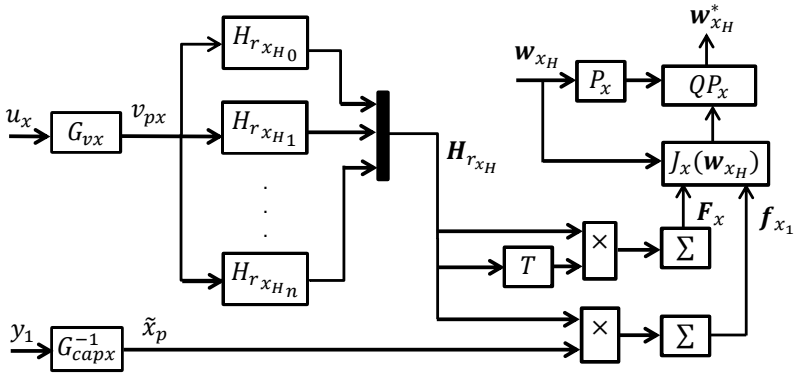


Figure 3.3: Identification procedure for X direction (PI approach).

with the transformed vector of thresholds:

$$\underbrace{r'_{x_{H_i}} = \sum_{j=0}^{i} w_{x_{H_j}}(r_{x_{H_i}} - r_{x_{H_j}}), \quad i = 0..n,}_{\boldsymbol{r}'_{x_H} = \boldsymbol{\Xi}_H(\boldsymbol{r}_{x_H}, \boldsymbol{w}_{x_H})} \tag{3.14}$$

vector of weights:

$$\begin{aligned} w'_{x_{H0}} &= \frac{1}{w_{x_{H0}}}, \quad i = 1..n \\ \underbrace{w'_{x_{H_i}} &= -\frac{w_{x_{H_i}}}{\left(w_{x_{H0}} + \sum_{j=1}^{i} w_{x_{H_j}}\right)\left(w_{x_{H0}} + \sum_{j=1}^{i-1} w_{x_{H_j}}\right)},}_{\boldsymbol{w}'_{x_H} = \boldsymbol{\Phi}_H(\boldsymbol{w}_{x_H})} \end{aligned} \tag{3.15}$$

and vector of initial states of the inverted backlash operators:

$$\underbrace{v_{px0_i} = \sum_{j=0}^{i} w_{x_{H_j}} x_{pH0_i} + \sum_{j=i+1}^{n} w_{x_{H_j}} x_{pH0_j}, \quad i = 0..n\,.}_{\boldsymbol{v}_{px0} = \boldsymbol{\Theta}_H(\boldsymbol{x}_{pH0}, \boldsymbol{w}_{x_H})} \tag{3.16}$$

Symbol $'$ refers to the parameters of the inverted model (for instance $\boldsymbol{w}'_{x_H}$ is a vector of weights of the inverted model of hysteresis operator).

### 3.2.2 Hysteresis compensation

In this subsection hysteresis compensation in real time is performed on the two horizontal piezoactuated axes of the nanopositioning platform. To that end, the PI model is fitted to the experimental data, inverted and cascaded with the plant in the feedforward path. A triangular voltage input signal of positive variable amplitude and frequency 0.1 Hz is chosen

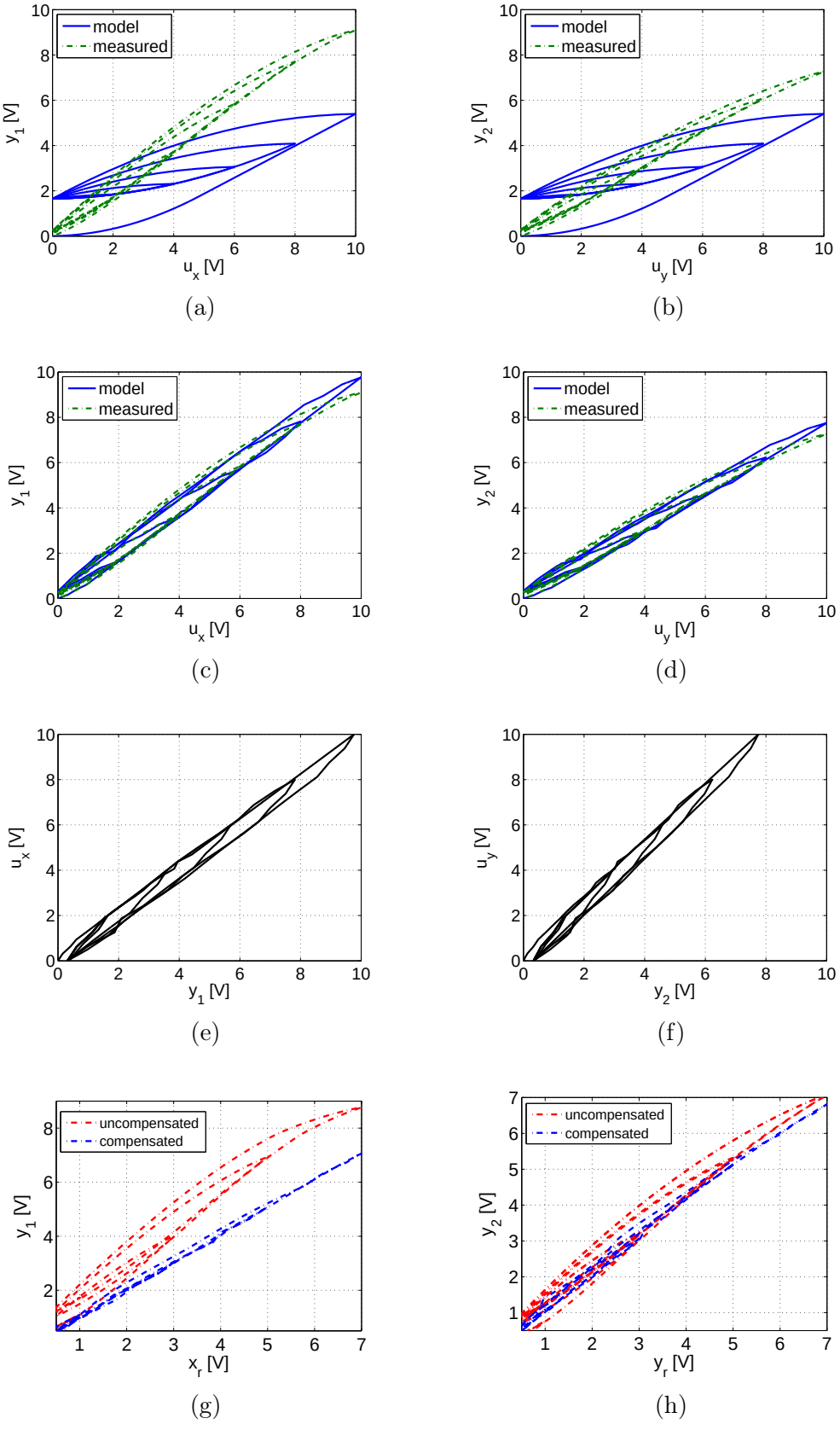


Figure 3.4: PI approach for hysteresis compensation (in X (left) and Y (right) direction) with 16 backlashes: (a), (b) Before identification. (c), (d) After identification. (e), (f) Inverted model. (g), (h) Compensation.

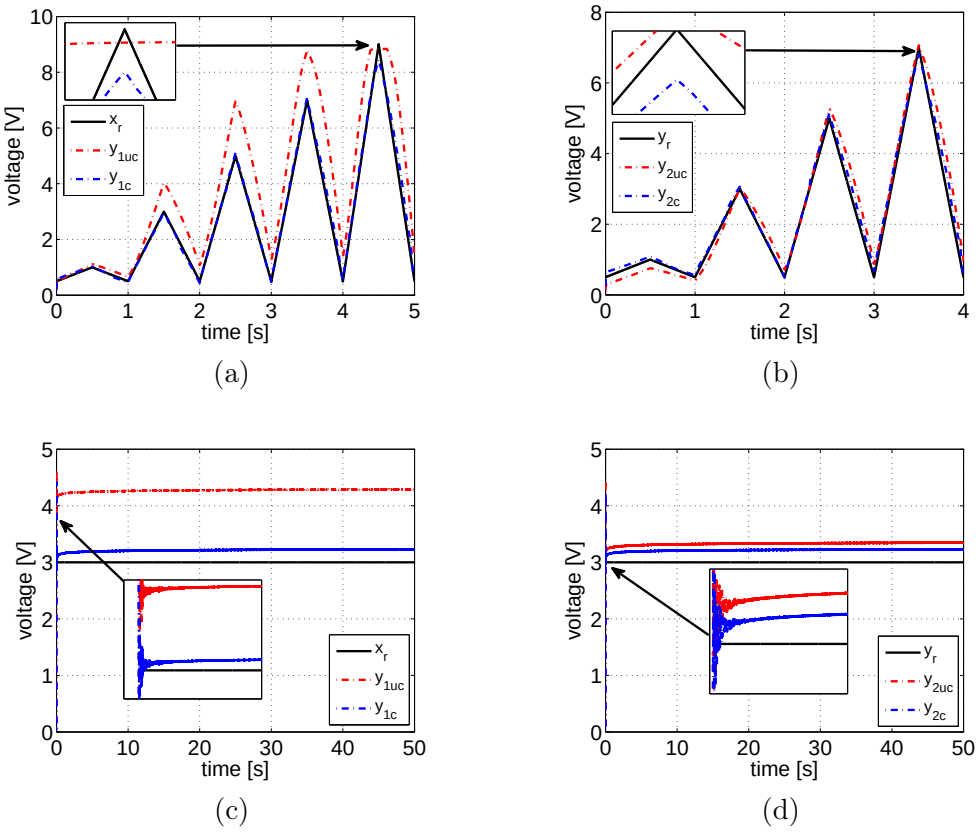


Figure 3.5: Reference tracking using PI approach for X (left) and Y (right) directions (subscripts 'uc' and 'c' refer to the uncompensated and compensated case, respectively): (a), (b) Triangle of variable amplitude. (c), (d) Step response.

as an identification signal. This frequency has to be low enough in order not to excite piezo dynamics, and sufficiently high in order to avoid the creep phenomenon. Fitting the model curve into the measured data is done using the Quadratic Programming algorithm of Matlab Optimization Toolbox$^{TM}$. The identification procedure at each iteration modifies the model weights until the proper tolerance is achieved. The fitting accuracy increases with the number of backlashes and in the considered case 16 backlashes have been chosen. Fig. 3.4a (resp. Fig. 3.4b) shows the hysteresis of a measured response of the piezoactuator and the hysteresis model with the initial weights, while Fig. 3.4c (resp. Fig. 3.4d) shows the results after the identification procedure for X (resp. Y) directions. The corresponding inverted PI model shown in Fig. 3.4e (resp. Fig. 3.4f) is cascaded with the plant system as shown in Fig. 3.1. The effect of hysteresis was successfully cancelled in both directions (see Fig. 3.4g and Fig. 3.4h, respectively). Since the classical PI model is symmetric and the measured hysteresis curve is evidently asymmetric (especially for higher voltages), the model does not catches the hysteresis to the end (despite high accuracy of 16 backlashes). The fitting accuracy can be substantially improved using the modified version of the PI approach called MPI, which is presented in the next section. However, even with PI model the tracking performance is quite good as shown

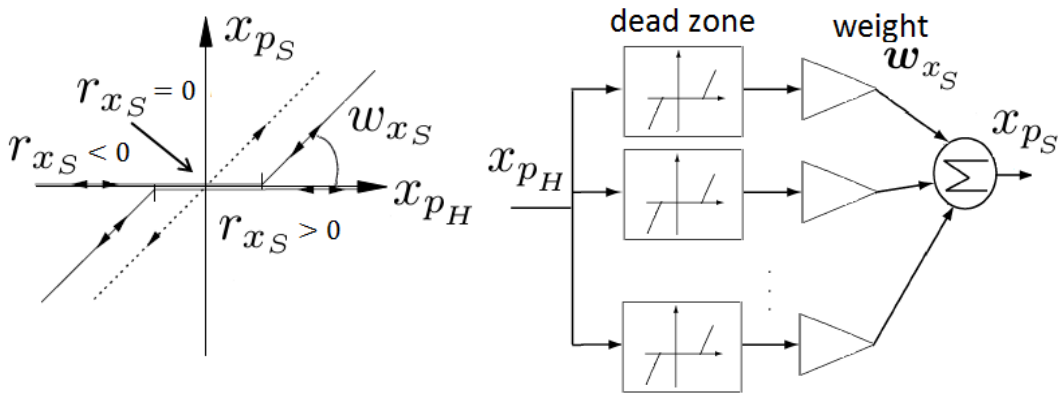


(a) (b)

Figure 3.6: Weighted dead-zone operator (a) and superposition operator consisting of $m+1$ one-sided dead-zone operators (b) [Ang et al., 2007].

in Fig. 3.5a (resp. Fig. 3.5b). The creep phenomenon is however still present as shown in Fig. 3.5c and Fig. 3.5d and to compensated its effect, additional modeling should be done, or it can be eliminated by feedback control.

## 3.3 Modified Prandtl-Ishlinskii approach

Since the PI model in its classical form cannot catch asymmetric hysteresis loops (due to the property of symmetry of the elementary play operator it uses), the Modified Prandtl-Ishlinskii (MPI) model has been elaborated in order to solve this problem. The idea behind this method lies in introduction of an asymmetric elementary one-sided dead-zone operator (in addition to the backlash operator) defined as follows:

$$x_{p_s}(t) = S_{r_{x_S}}[x_{p_H}](t) = \begin{cases} \max\{x_{p_H}(t) - r_{x_S}, 0\}, & r_{x_S} > 0 \\ x_{p_H}(t), & r_{x_S} = 0 \end{cases} \tag{3.17}$$

where $r_{x_S}$ is a threshold for $x_{p_H}$. Next, an elementary one-sided dead-zone operator (3.17) is multiplied by a weight value $w_{x_S}$ as shown in Fig. 3.6a forming a weighted one-sided dead-zone operator. The PI superposition operator $S_x$ is given by the linear weighted superposition of many one-sided dead-zone operators with different threshold values (see Fig. 3.6b) as follows:

$$x_{p_s}(t) = S_x[x_{p_H}](t) = \boldsymbol{w}_{x_S}{}^T \boldsymbol{S}_{\boldsymbol{r}_{x_S}}[x_{p_H}](t), \tag{3.18}$$

where $\boldsymbol{r}_{x_S}$ is the vector of thresholds such that $0 = r_{x_{S0}} < r_{x_{S1}} < \ldots < r_{x_{Sm}} < +\infty$, $\boldsymbol{w}_{x_S}$ is the vector of weights and $\boldsymbol{S}_{\boldsymbol{r}_{x_S}}[x_{p_H}](t)$ is the vector of dead-zone operators. Finally, the concatenation of PI hysteresis operator $H_x$ defined by (3.2) and PI superposition operator $S_x$ defined by (3.18) defines MPI operator $\Gamma_x$, which is an approximation of the static nonlinearity

$NL_x$ (see Fig. 3.1) as follows:

$$\begin{aligned} x_{p_s}(t) &= \Gamma_x[v_{px}](t) = S_x[H_x[v_{px}]](t) \\ &= \boldsymbol{w}_{x_S}{}^T \boldsymbol{S}_{r_{x_S}}[\boldsymbol{w}_{x_H}{}^T \boldsymbol{H}_{r_{x_H}}[v_{px}, \boldsymbol{x}_{p_H 0}]](t) \end{aligned} \tag{3.19}$$

The procedure for compensator design for MPI method is similar to the PI approach and it consists of 3 consecutive steps described in the following subsections.

### 3.3.1 Model initialisation, identification and inversion

In the initialization step, the threshold values $\boldsymbol{r}_{x_H}$ and $\boldsymbol{r}'_{x_S}$ are equally distributed over the range of input $v_{px}$ and output $x_{p_s}$, respectively, as follows:

$$r_{x_{H_i}} = \frac{i}{n+1}\max\{v_{px}\}, \quad i = 0..n, \tag{3.20}$$

$$r'_{x_{S_i}} = \frac{i}{m+1}\max\{x_{p_s}\}, \quad i = 0..m, \tag{3.21}$$

and it is assumed that the backlash operators are in their deenergized state as follows:

$$x_{p_H 0_i} = 0, \quad i = 0..n. \tag{3.22}$$

In the identification step, the optimal weights $\boldsymbol{w}_x^{*T} = \begin{bmatrix} \boldsymbol{w}_{x_H}^{*T} & \boldsymbol{w}_{x_S}^{\prime *T} \end{bmatrix}$ are looked for in the sense of least-square minimization of the following error model (see Fig. 3.7):

$$\begin{aligned} E_x[v_{px}, \tilde{x}_p](t) &= H_x[v_{px}](t) - S_x^{-1}[\tilde{x}_p](t) \\ &= \boldsymbol{w}_{x_H}^T \boldsymbol{H}_{r_{x_H}}[v_{px}, \boldsymbol{x}_{p_H 0}](t) - \boldsymbol{w'}_{x_S}^T \boldsymbol{S}_{r'_{x_S}}[\tilde{x}_p](t) \\ &= \underbrace{\begin{pmatrix} \boldsymbol{w}_{x_H}^T & \boldsymbol{w'}_{x_S}^T \end{pmatrix}}_{\boldsymbol{w}_{\boldsymbol{x}}{}^T} \underbrace{\begin{pmatrix} \boldsymbol{H}_{r_{x_H}}[v_{px}, \boldsymbol{x}_{p_H 0}](t) \\ -\boldsymbol{S}_{r'_{x_S}}[\tilde{x}_p](t) \end{pmatrix}}_{\boldsymbol{\Psi}_x[v_{px}, \boldsymbol{x}_{p_H 0}, \tilde{x}_p](t)} \end{aligned} \tag{3.23}$$

The loss function $J_x(\boldsymbol{w}_{\boldsymbol{x}})$ to be minimized is given by:

$$J_x(\boldsymbol{w}_{\boldsymbol{x}}) = \frac{1}{2}\sum_{i=1}^{l}(E_x[v_{px}, \tilde{x}_p](t_i))^2 = \frac{1}{2}\boldsymbol{w}_{\boldsymbol{x}}{}^T \boldsymbol{F}_{\boldsymbol{x}} \boldsymbol{w}_{\boldsymbol{x}} \tag{3.24}$$

with the Hessian matrix $\boldsymbol{F}_x$ defined as follows:

$$\boldsymbol{F}_{\boldsymbol{x}} = \sum_{i=1}^{l} \boldsymbol{\Psi}_x[v_{px}, \boldsymbol{x}_{p_H 0}, \tilde{x}_p](t_i) \boldsymbol{\Psi}_x^T[v_{px}, \boldsymbol{x}_{p_H 0}, \tilde{x}_p](t_i) \tag{3.25}$$

Again the monotonicity of the hysteresis loading curve is required for the existence of the model inverse. This can be assured if the weights $\boldsymbol{w}_{x_H}$ and $\boldsymbol{w}'_{x_S}$ are constrained by the following convex polyhedron:

$$P_x = \left\{ \boldsymbol{w}_{x_H}, \boldsymbol{w}'_{x_S} : \begin{pmatrix} \boldsymbol{U}_H & \boldsymbol{0} \\ \boldsymbol{0} & \boldsymbol{U}'_S \end{pmatrix} \begin{pmatrix} \boldsymbol{w}_{x_H} \\ \boldsymbol{w}'_{x_S} \end{pmatrix} - \begin{pmatrix} \boldsymbol{u}_H \\ \boldsymbol{u}'_S \end{pmatrix} \geq \begin{pmatrix} \boldsymbol{0} \\ \boldsymbol{0} \end{pmatrix} \right\} \tag{3.26}$$

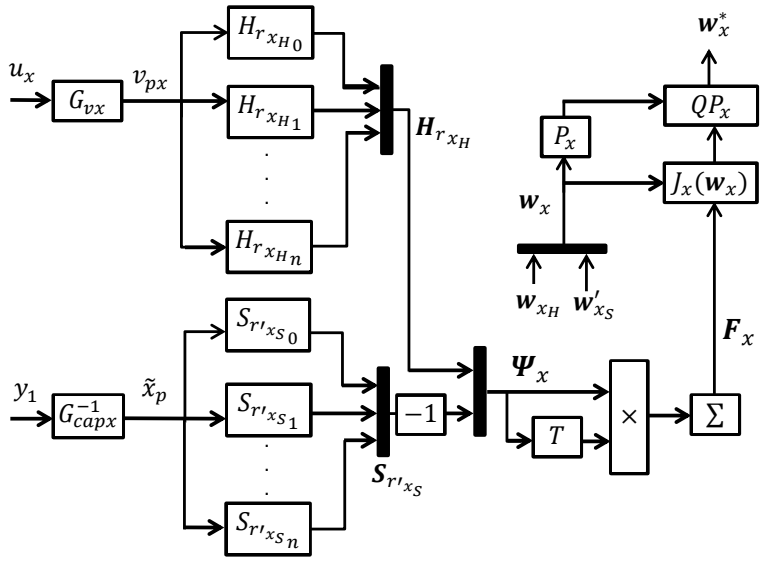


Figure 3.7: Identification procedure for X direction (MPI approach).

where $\boldsymbol{U}_H$ and $\boldsymbol{u}_H$ are defined like in (3.11) and $\boldsymbol{U}'_S \in \Re^{m+1\times m+1}$, $\boldsymbol{u}'_S \in \Re^{m+1}$ are given by:

$$\boldsymbol{U}'_S = \begin{pmatrix} 1 & 0 & \cdots & 0 \\ 1 & 1 & \cdots & 0 \\ \vdots & \vdots & \ddots & \vdots \\ 1 & 1 & \cdots & 1 \end{pmatrix}, \boldsymbol{u}'_S = \begin{pmatrix} \epsilon \\ \epsilon \\ \vdots \\ \epsilon \end{pmatrix}. \tag{3.27}$$

The constrained quadratic optimization problem for finding unknown weights $\boldsymbol{w}_x$ can be formulated as below:

$$QP_x : \min_{\boldsymbol{w}_x \in P_x} \{J_x(\boldsymbol{w}_x)\} = \min_{\boldsymbol{w}_x \in P_x} \left\{ \frac{1}{2} \boldsymbol{w_x}^T \boldsymbol{F_x} \boldsymbol{w_x} \right\} \tag{3.28}$$

Using identified weights $\boldsymbol{w}'_{x_S}$ and thresholds $\boldsymbol{r}'_{x_S}$ defined by (3.21), the vector of thresholds $\boldsymbol{r}_{x_S}$ and vector of weights $\boldsymbol{w}_{x_S}$ of the one-sided dead-zone operators can be computed as follows:

$$\underbrace{r_{x_{S_i}} = \sum_{j=0}^{i} w'_{x_{S_j}} (r'_{x_{S_i}} - r'_{x_{S_j}}), \quad i = 0..m,}_{\boldsymbol{r}_{x_S} = \boldsymbol{\Xi}_S(\boldsymbol{r}'_{x_S}, \boldsymbol{w}'_{x_S})} \tag{3.29}$$

$$\underbrace{\begin{aligned} w_{x_{S0}} &= \frac{1}{w'_{x_{S0}}}, \quad i = 1..m \\ w_{x_{Si}} &= -\frac{w'_{x_{Si}}}{\left(w'_{x_{S0}} + \sum_{j=1}^{i} w'_{x_{Sj}}\right)\left(w'_{x_{S0}} + \sum_{j=1}^{i-1} w'_{x_{Sj}}\right)}, \end{aligned}}_{\boldsymbol{w}_{x_S} = \boldsymbol{\Phi}_S(\boldsymbol{w}'_{x_S})} \tag{3.30}$$

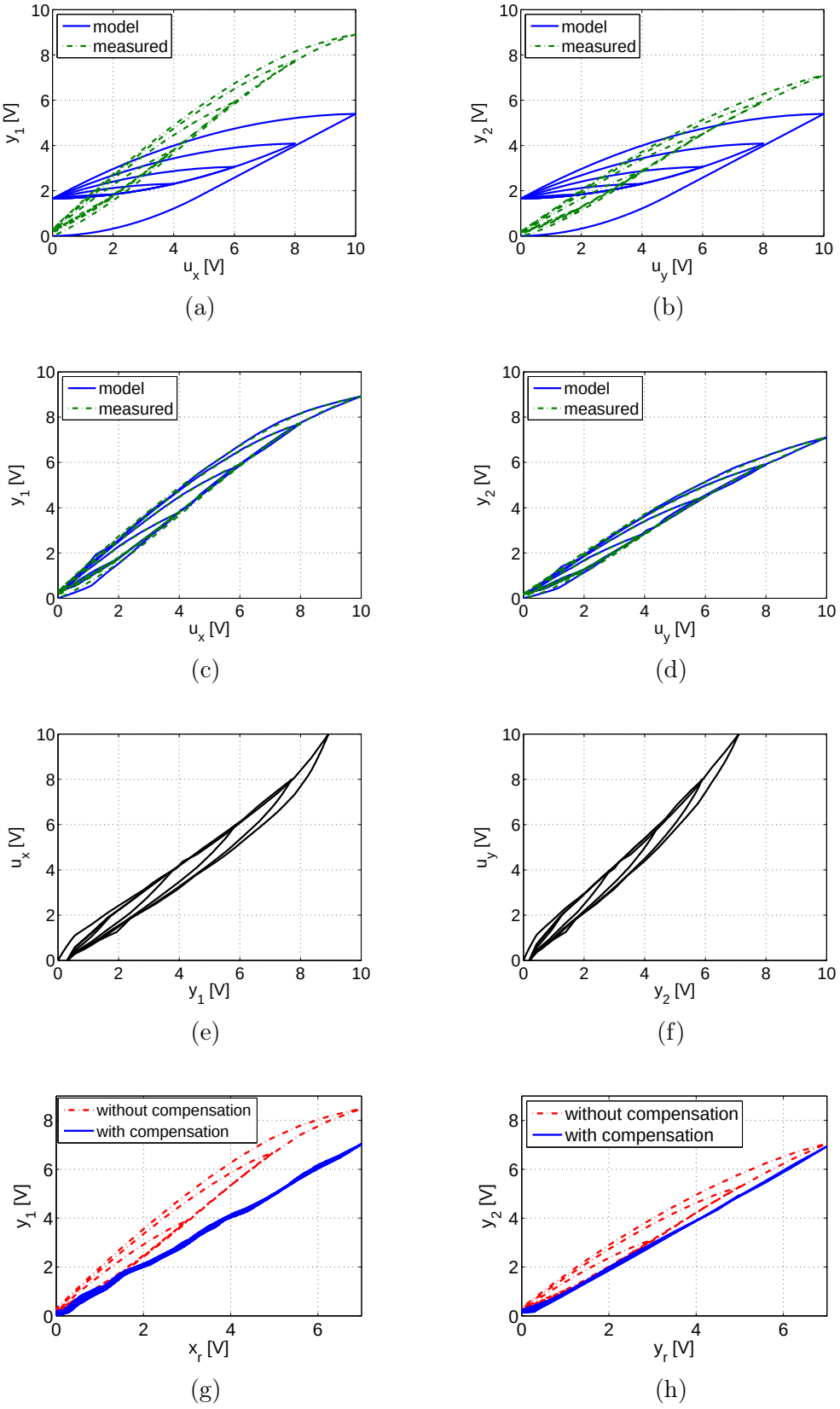


Figure 3.8: MPI approach for hysteresis compensation (in X (left) and Y (right) direction) with 16 backlashes and 16 dead-zones: (a), (b) Before identification. (c), (d) After identification. (e), (f) Inverted model. (g), (h) Compensation.

The inverse of the MPI model is finally given by:

$$\begin{aligned} v_{px}(t) &= \Gamma_x^{-1}[x_{p_s}](t) = H_x^{-1}[S_x^{-1}[x_{p_s}]](t) \\ &= {\boldsymbol{w}'_{x_H}}^T \boldsymbol{H}_{r'_{x_H}}[{\boldsymbol{w}'_{x_S}}^T \boldsymbol{S}_{r'_{x_S}}[x_{p_s}], \boldsymbol{v}_{px0}](t) \end{aligned} \tag{3.31}$$

with the transformed vector of thresholds $\boldsymbol{r}'_{x_H}$, vector of weights $\boldsymbol{w}'_{x_H}$ and vector of initial states $\boldsymbol{v}_{px0}$ of the inverted backlash operators as defined in (3.14)-(3.16). The inverse model $S_x^{-1}$ of superposition operator $S_x$ has been already determined by $\boldsymbol{r}'_{x_S}$ and $\boldsymbol{w}'_{x_S}$ during initialization and identification steps, respectively. The number of backlashes and dead-zone operators has been set to 16. The other identification conditions are the same as in case of PI model.

### 3.3.2 Hysteresis compensation

The feedforward hysteresis compensator is obtained by cascading the inverse MPI model $\Gamma_x^{-1}$ with the real plant as shown in Fig. 3.1. The compensation results for each axis are given in Fig. 3.8 and the tracking performance in Fig. 3.9. Comparing these results with the ones corresponding to the PI model, one can clearly see that MPI model outperforms its classical PI version, as unlike the latter it can capture the asymmetric hysteresis curves. However the creep phenomenon is still present as shown in Fig. 3.9c and Fig. 3.9d. Its effect will be compensated in the next subsections.

## 3.4 Observer-based approach

Apart from the hysteresis phenomenon, piezoelectric actuators can drift when positioned over extended periods of time during slow-speed operation. This adverse effect is called the creep phenomenon. A low-order state-space disturbance observer is designed for hysteresis and creep reconstruction and subsequent compensation in both horizontal axes as shown in Fig. 3.10. Both hysteresis and creep are treated as a slowly varying disturbance $d_x$ over the linear affine representation of hysteresis (see Fig. 3.11a). This disturbance is assumed to be bounded as shown in [Ryba et al., 2015b] and the first equation of (2.3) is expressed as:

$$NL_x[v_{px}] = G_{px} v_{px} + d_x \tag{3.32}$$

Since the bandwidths of voltage amplifier (4 kHz) and capacitive sensor (8.5 kHz) are relatively high w.r.t. the bandwidth of the piezoelectric actuator (630 Hz), they can be treated as constant gains ($G_{vx}$ and $G_{capx}$, respectively). Similarly, the bandwidth of anti-aliasing filters is around 20 kHz and as a result it can be neglected as well. The following second order model of the X axis is used to estimate the slowly varying disturbance $d_x$:

$$\begin{aligned} \ddot{x}_p + 2\xi_{px}\omega_{px}\dot{x}_p + \omega_{px}^2 x_p = \omega_{px}^2 \underbrace{(G_{px} v_{px} + d_x)}_{NL_x[v_{px}]} = \\ \omega_{px}^2 \underbrace{(G_{px} G_{vx} u_x + d_x)}_{NL_x[u_x]} = \omega_{px}^2 \underbrace{(u_1 + d_x)}_{NL_x[u_1]} \end{aligned} \tag{3.33}$$

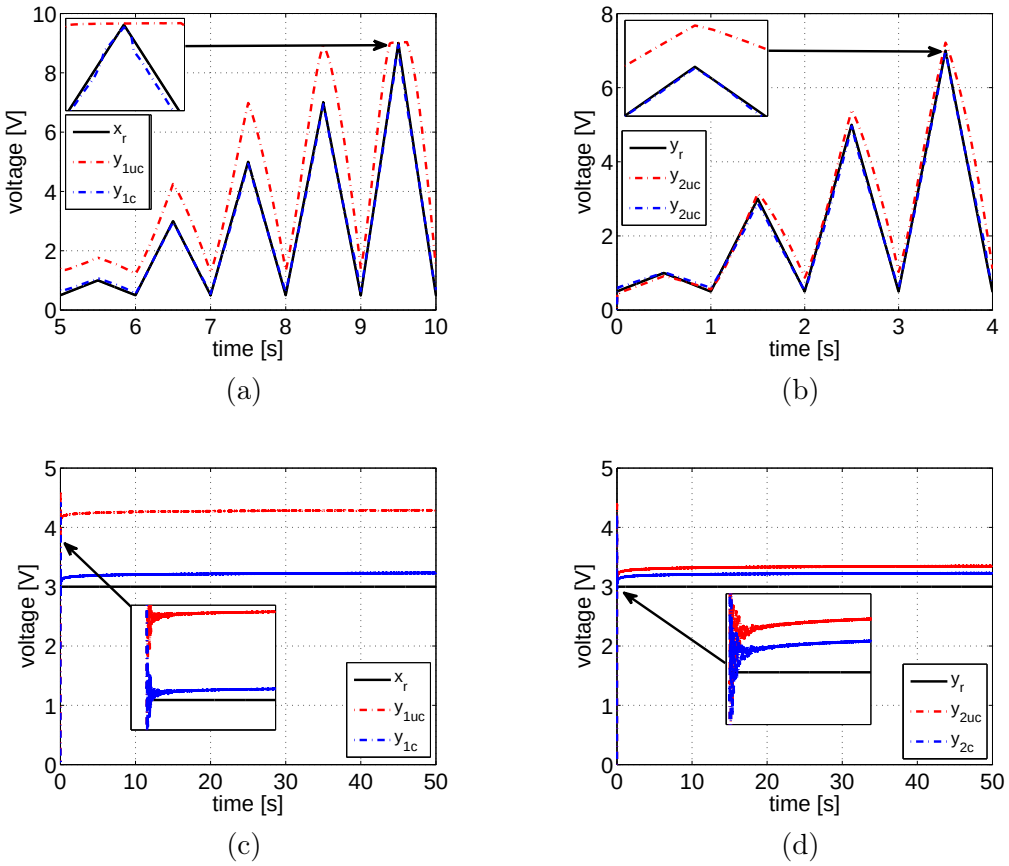


Figure 3.9: Reference tracking using MPI approach for X (left) and Y (right) directions: (a), (b) Triangle of variable amplitude. (c), (d) Step response.

It includes the gain $G_{vx}$ of the voltage amplifier $VA_x(s)$, the piezo dynamics $D_{px}(s)$ and the gain $G_{capx}$ of the capacitive sensor $CS_x(s)$ and can be rewritten in state-space (with state variables: $x_1 = x_p$, $x_2 = \dot{x}_p$) as follows:

$$\begin{aligned}\begin{pmatrix} \dot{x}_1 \\ \dot{x}_2 \end{pmatrix} &= \underbrace{\begin{pmatrix} 0 & 1 \\ -\omega_{px}^2 & -2\xi_{px}\omega_{px} \end{pmatrix}}_{A_x} \begin{pmatrix} x_1 \\ x_2 \end{pmatrix} \\ &+ \underbrace{\begin{pmatrix} 0 \\ \omega_{px}^2 \end{pmatrix}}_{B_x} u_1 + \underbrace{\begin{pmatrix} 0 \\ \omega_{px}^2 \end{pmatrix}}_{B_{d_x}} d_x + w_x \\ y_1 &= \underbrace{\begin{pmatrix} G_{capx} & 0 \end{pmatrix}}_{C_x} \begin{pmatrix} x_1 \\ x_2 \end{pmatrix} + n_1 \end{aligned} \tag{3.34}$$

where $u_x$ is the voltage amplifier input, $y_1$ is the capacitive sensor output, $w_x$ and $n_1$ are the process and measurement noises, respectively. The observer dynamics is chosen to be much faster then the disturbance variations and therefore those variations can be "seen" by the

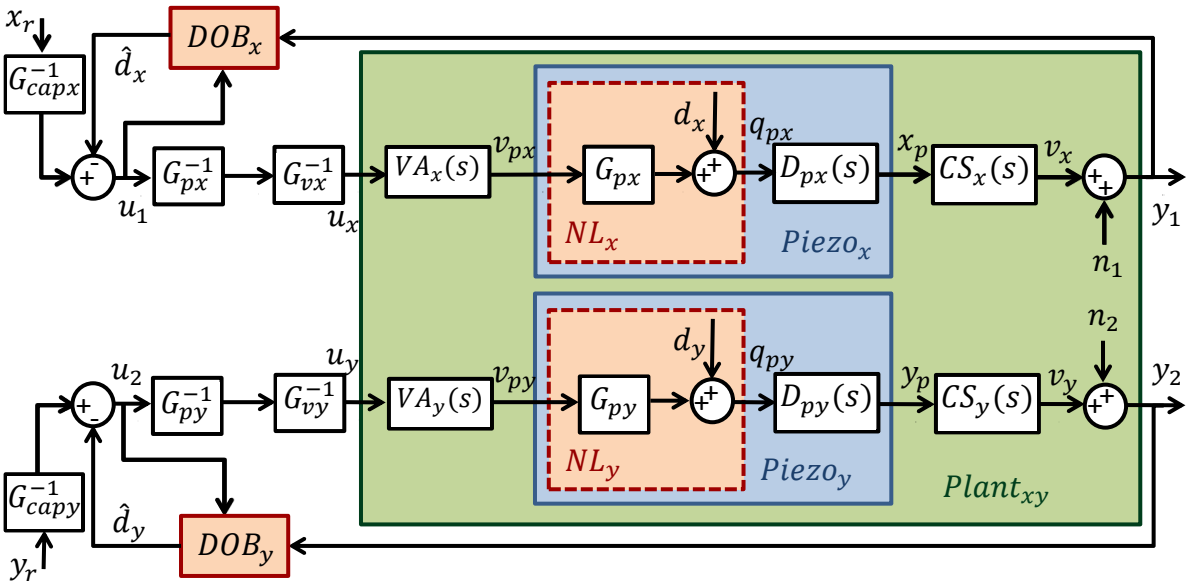


Figure 3.10: 2D schema (observer-based approach).

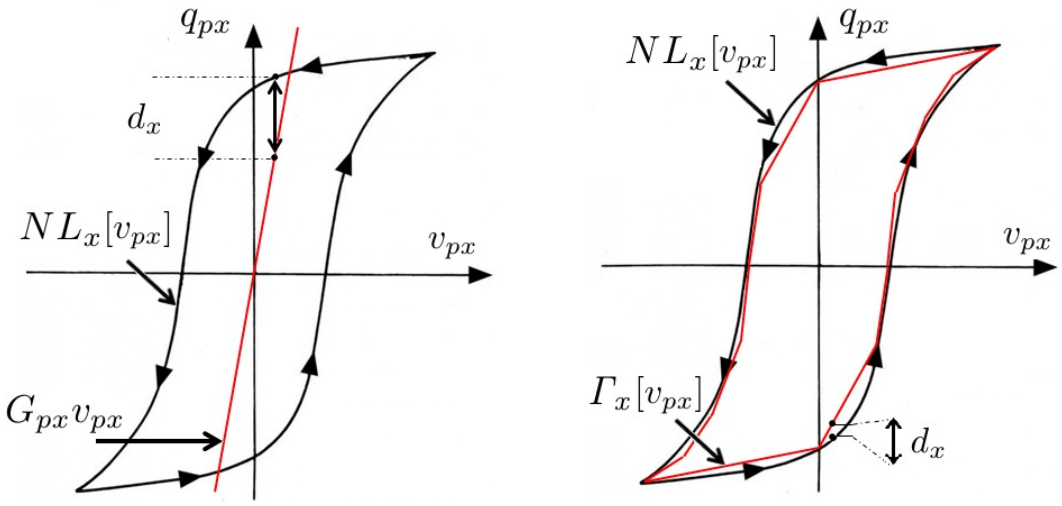


(a) (b)

Figure 3.11: Hysteresis approximation: (a) Affine approximation. (b) MPI approximation.

observer as constant ($\dot{d}_x \approx 0$) between two consecutive time instants. Next, the state-space model (3.34) is augmented with the disturbance dynamics (*i.e.* with the extended state vector $x_e = [x^T \; d_x]^T$) as follows:

$$\begin{aligned} \dot{x}_e &= A_{e_x} x_e + B_{e_x} u_1 + w_{e_x} \\ y_1 &= C_{e_x} x_e + n_1 \end{aligned} \tag{3.35}$$

$$A_{e_x} = \begin{pmatrix} A_x & B_{d_x} \\ 0 & 0 \end{pmatrix}, B_{e_x} = \begin{pmatrix} B_x \\ 0 \end{pmatrix}, C_{e_x} = \begin{pmatrix} C_x^T \\ 0 \end{pmatrix}^T \tag{3.36}$$

The steady-state Kalman observer of this system is defined as:

$$\dot{\hat{x}}_e = A_{e_x}\hat{x}_e + B_{e_x}u_1 + L_x(y_1 - C_{e_x}\hat{x}_e) \tag{3.37}$$

where $L_x = P_x C_{e_x}^T N_1^{-1}$ is the observer gain matrix and $P_x$ is the solution of the following associated Algebraic Riccati Equation (ARE):

$$A_{e_x}P_x + P_x A_{e_x}^T - L_x N_1 L_x^T + W_x = 0 \tag{3.38}$$

with the process $W_x$ and measurement $N_1$ covariance matrices.

Now, using the estimated disturbance $\hat{d}_x$ in (3.32) gives the following input/output dependency:

$$\hat{y}_1 = \hat{N}L_{xv}[u_x] = G_{capx}\hat{N}L_x[u_x] = G_{capx}(G_{px}G_{vx}u_x + \hat{d}_x) \tag{3.39}$$

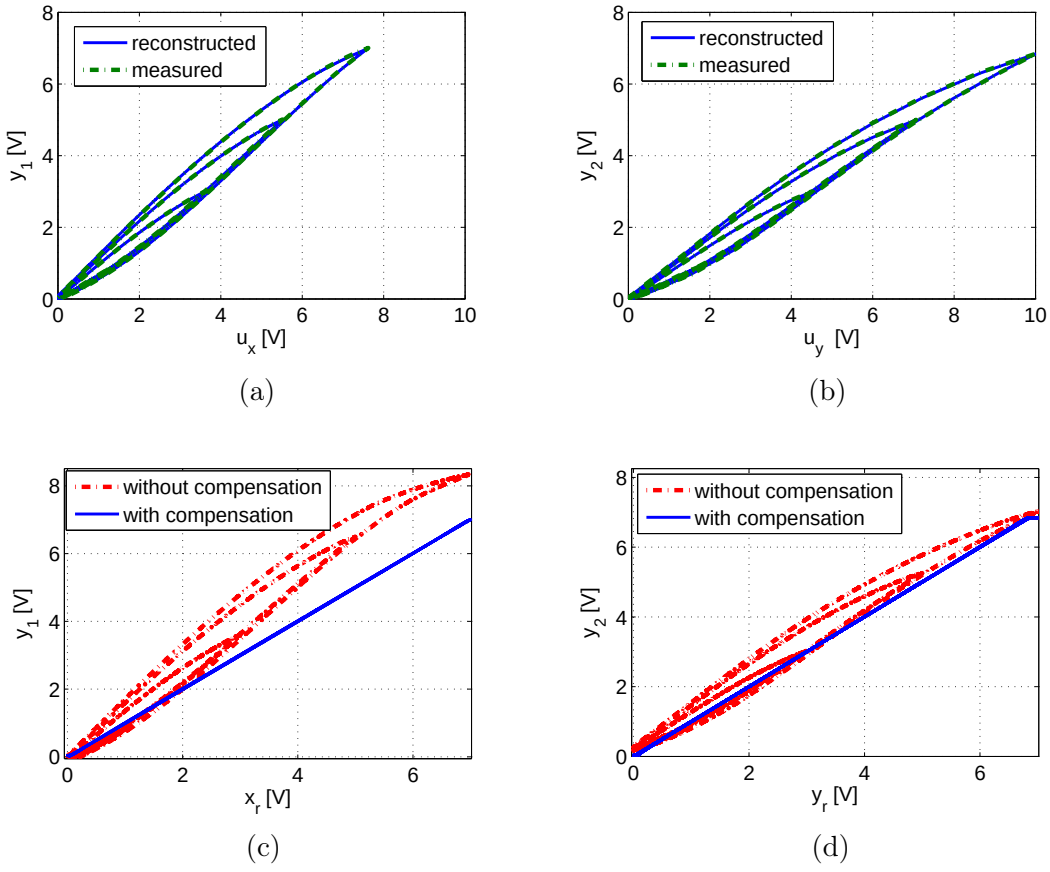


Figure 3.12: Observer-based approach for hysteresis compensation (in X (left) and Y (right) direction) (a), (b) Hysteresis reconstruction. (c), (d) Compensation.

Fig. 3.12a (resp. Fig. 3.12b) shows a good consistency of the measured and reconstructed hysteresis between the input $u_x$ (resp. $u_y$) and output $y_1$ (resp. $y_2$). To compensate for

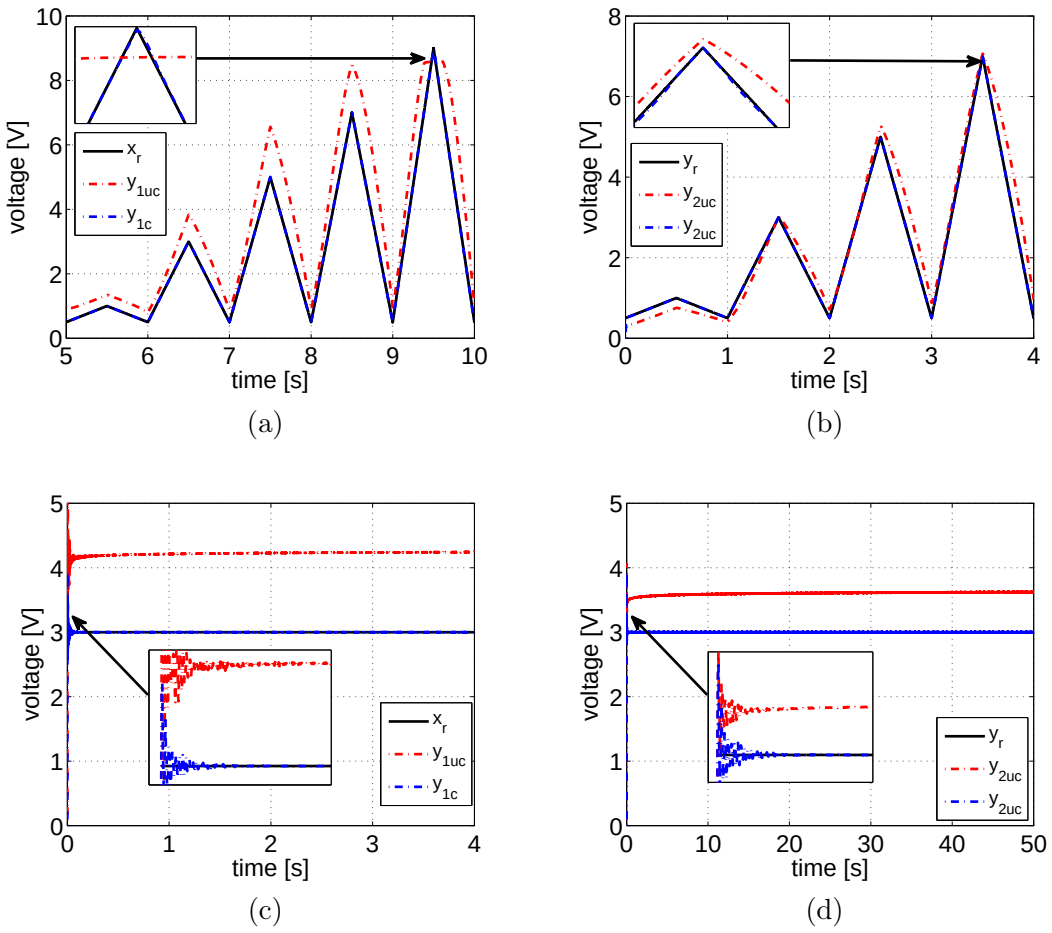


Figure 3.13: Reference tracking using observer-based approach for X (left) and Y (right) directions: (a), (b) Triangle of variable amplitude. (c), (d) Step response.

the output disturbance $d_x$ (resp. $d_y$), its estimate $\hat{d}_x$ (resp. $\hat{d}_y$) is then substracted from the input $G_{capx}^{-1}x_r$ (resp. $G_{capy}^{-1}y_r$) forming new input $u_1$ (resp. $u_2$) as shown in Fig. 3.10. In Fig. 3.12c (resp. Fig. 3.12d) the reference voltage $x_r$ (resp. $y_r$) (see Fig. 3.10) being a triangle of variable amplitude and frequency 1 Hz was applied and the corresponding output voltage $y_1$ (resp. $y_2$) was measured without (in red) and with (in blue) DOB. The hysteresis was successfully compensated as shown in Fig. 3.12c (resp. Fig. 3.12d). The corresponding tracking triangular reference is shown in Fig. 3.13a (resp. Fig. 3.13b). Unlike MPI, DOB approach cancels also the creep phenomenon as shown in Fig. 3.13c (resp. Fig. 3.13d).

## 3.5 Observer-based approach with MPI model

In this section a disturbance observer (DOB) is combined with MPI approach as shown in Fig. 3.14 and the affine hysteresis approximation (3.32) is replaced by MPI model as follows

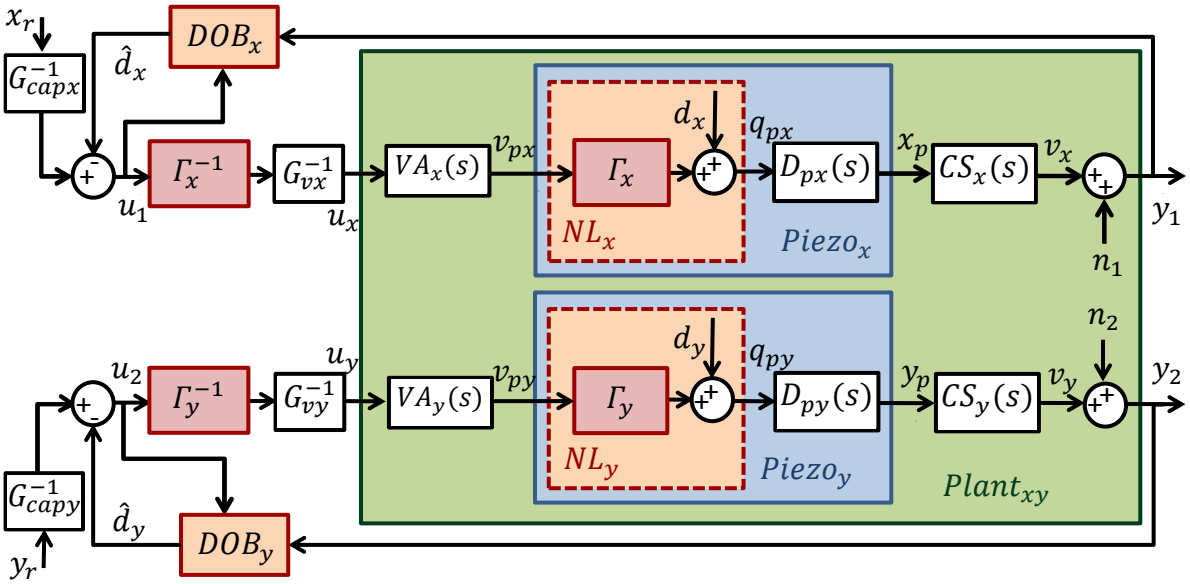


Figure 3.14: 2D schema (observer-based approach with MPI model).

(see Fig. 3.11(b)):

$$NL_x[v_{px}] = \Gamma_x[v_{px}] + d_x \tag{3.40}$$

The disturbance $d_x$ is combining now the mismatch between the real hysteresis and the MPI model. This mismatch includes the creep and other external disturbances as well and is considered as smaller in magnitude (almost everywhere) than in case of the affine hysteresis approximation. Fig. 3.15 shows comparison of MPI, DOB and hybrid MPI/DOB in terms of hysteresis compensation in the X axis and for different input frequencies. One can see the effect of excited dynamics with increasing frequency. Table 3.1 shows the corresponding percentage compensation errors. They are evaluated by taking the ratio of the major hysteresis loop width and the full range of the reference (i.e. $H_{\%} = \frac{l_H}{L_H} \times 100\%$) as shown in Fig. 3.15a.

Table 3.1: Amount of hysteresis $H_{\%}$ using different compensation methods and different frequencies - experimental result (uncompensated system has $H_{\%} = 11.37\%$ of hysteresis)

| | MPI | DOB | MPI+DOB |
|---|---|---|---|
| 1Hz | 1.10% | 0.53% | 0.26% |
| 20Hz | 3.12% | 2.12% | 0.98% |
| 50Hz | 5.01% | 6.25% | 4.03% |

The corresponding tracking performance is shown in Fig. 3.16. For low frequencies DOB outperforms MPI approach, however for higher frequencies the performance of low-order DOB worsens and it can be improved by combining it with MPI approach. The creep phenomenon is compensated only when DOB is used as shown in Fig. 3.17.

The disturbance model is assumed as constant (i.e. $\dot{d}_x = 0$), which is not true. However,

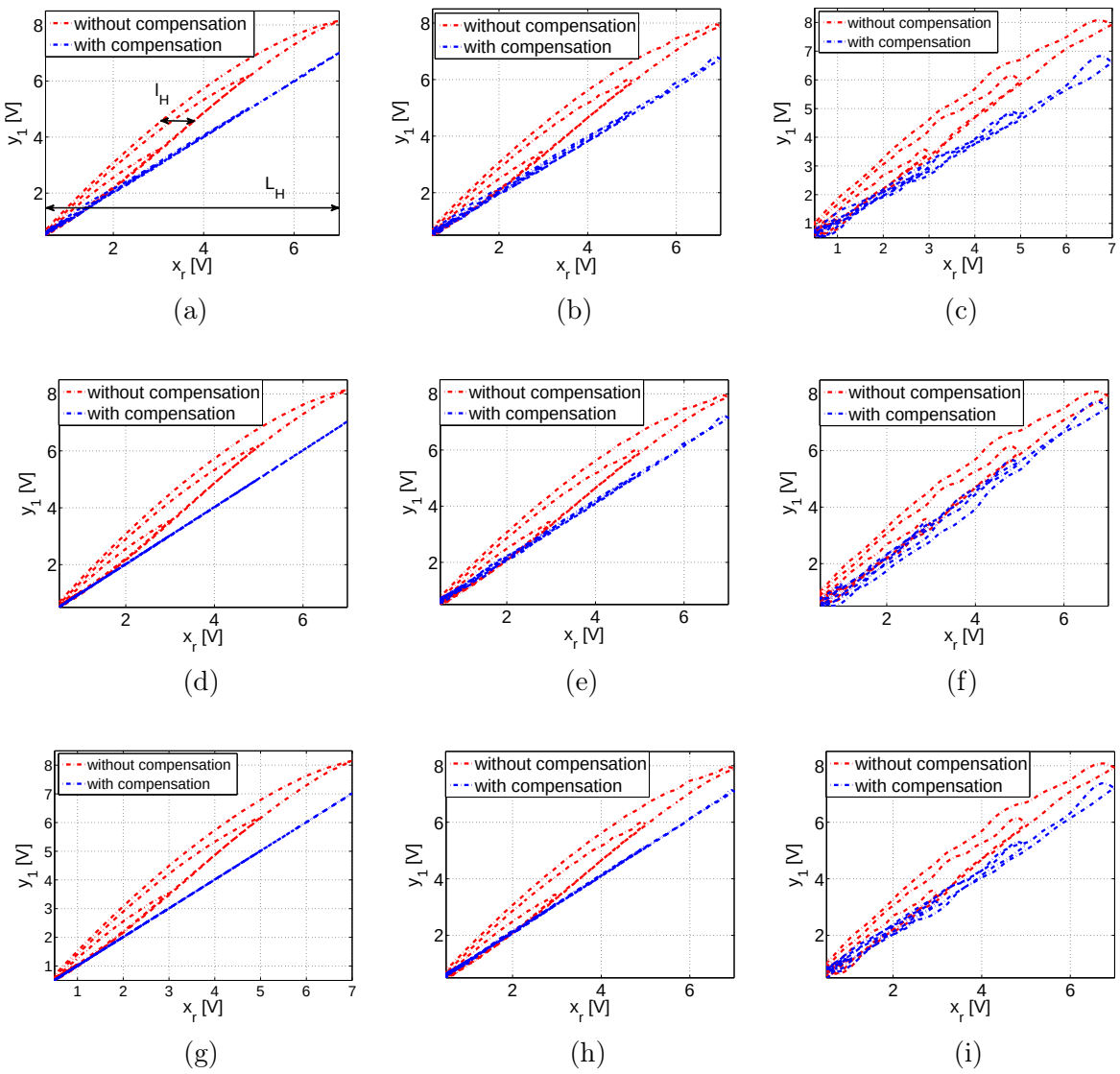


Figure 3.15: Hysteresis compensation in the X direction and for 1 Hz (left), 20 Hz (middle) and 50 Hz (right) for: (a)-(c) MPI approach, (d)-(f) DOB approach, (g)-(i) MPI+DOB approach.

this assumption is less restrictive in the case of DOB based on MPI model (3.40) than in the case of DOB with the affine model (3.32), which can be seen in Fig. 3.18, where the rate of change $\dot{d}_x$ is smaller in magnitude in case of MPI-based approach. This can be understood as follows: adding MPI model linearizes the system to some extent and as a result one may expect the improved performance w.r.t. the DOB alone or MPI alone.

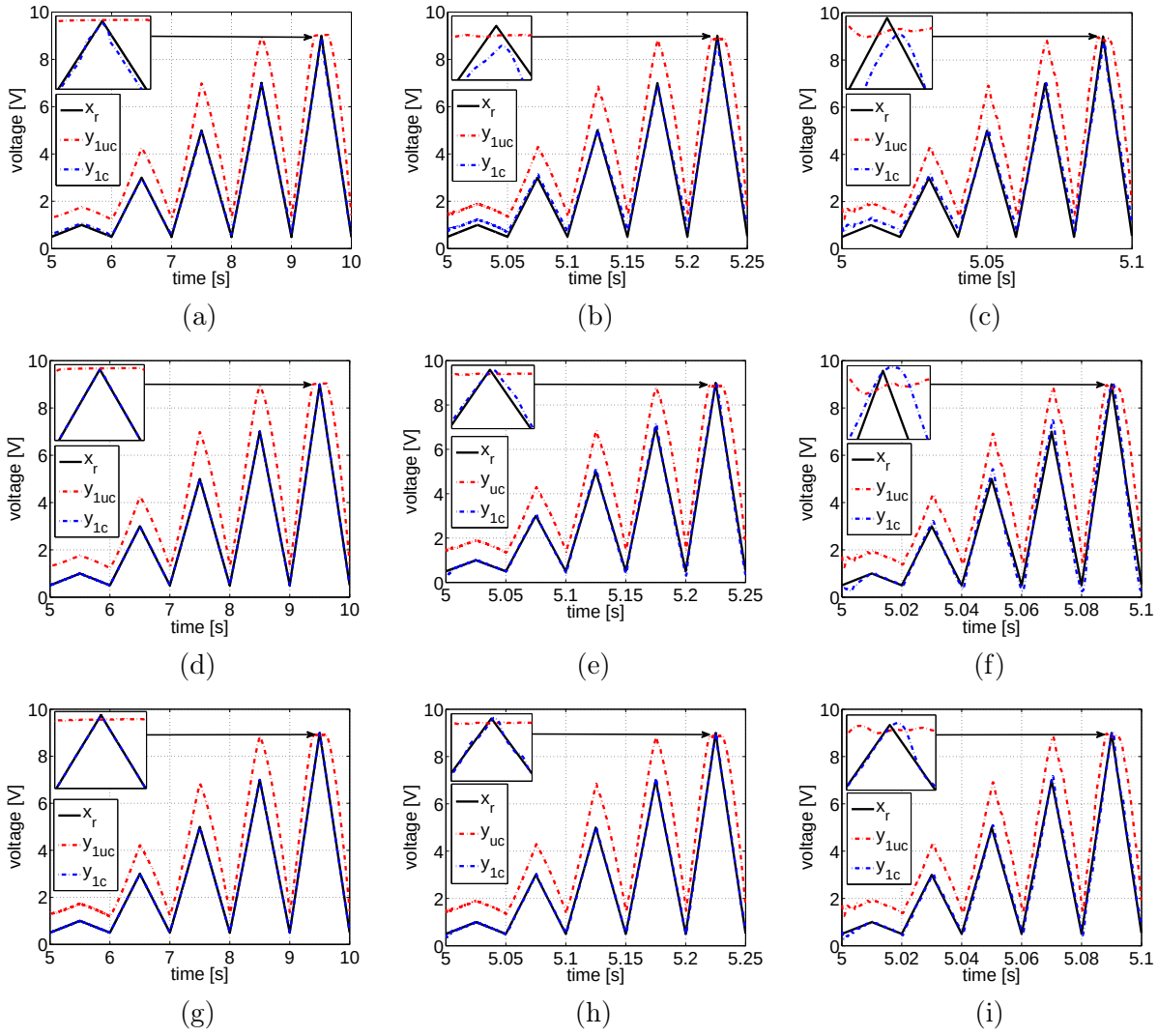


Figure 3.16: Triangular reference tracking for 1 Hz (left), 20 Hz (middle) and 50 Hz (right) for: (a)-(c) MPI approach, (d)-(f) DOB approach, (g)-(i) MPI+DOB approach.

## 3.6 Numerical inverse-based hysteresis compensation with adaptation

In this section a $p^{th}$ order polynomial with adaptively changing coefficients is chosen to model static hysteresis [Ryba et al., 2015a]. For brevity, only the equations of motion for the X axis (including gains $G_{vx}$, $G_{capx}$, nonlinear hysteresis $H_x[v_{px}(t)]$ and assuming $D_{px}(s) = 1$ for low-frequency behavior) are given and therefore subscript $x$ is omitted. This simple parametric

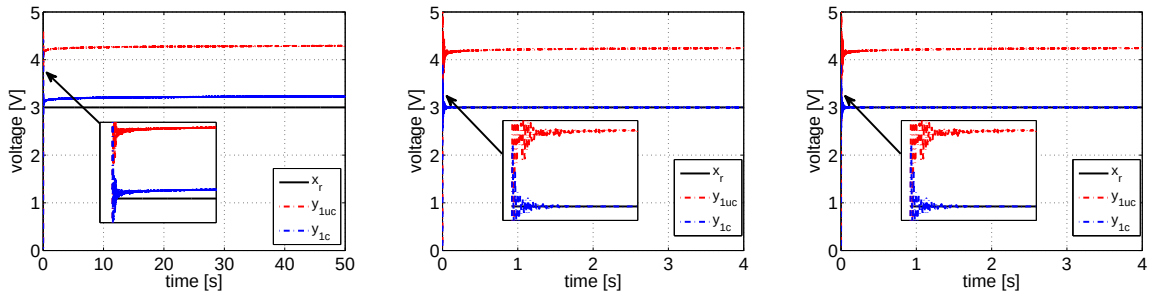


Figure 3.17: Step tracking for: (a) MPI approach, (b) DOB approach, (c) MPI+DOB approach.

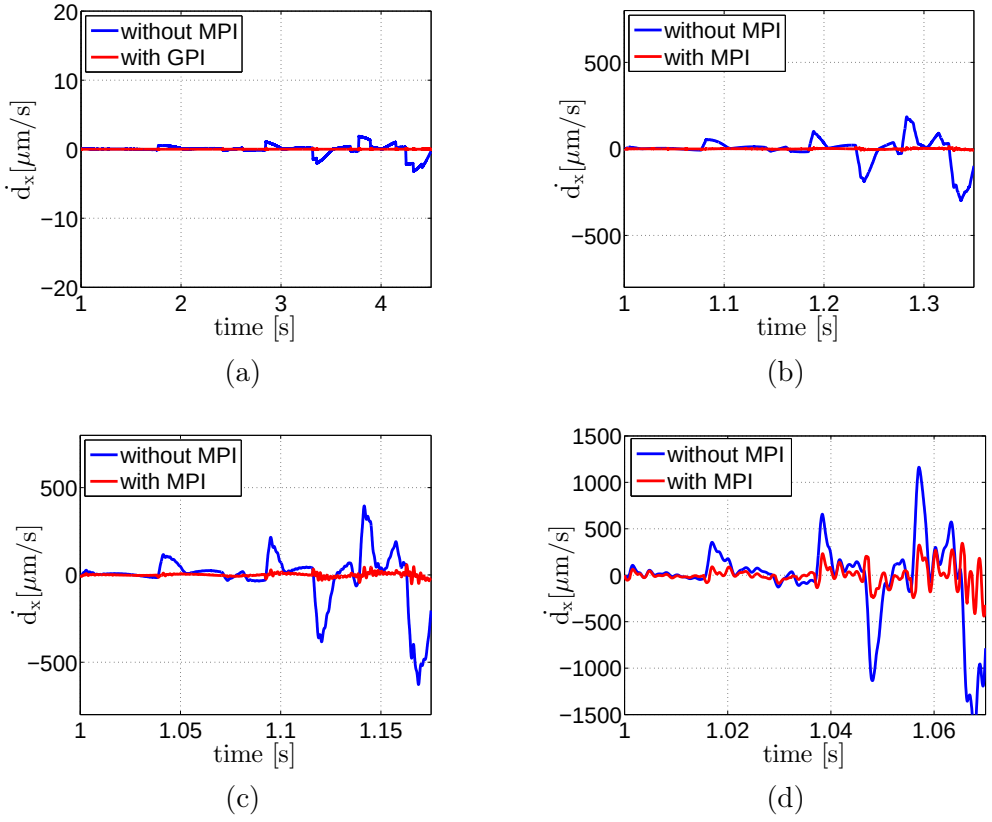


Figure 3.18: Disturbance rate of change ($\dot{d_x}$) for different frequencies: (a) 1 Hz, (b) 10 Hz, (c) 20 Hz, (d) 50 Hz.

model is described as follows:

$$y_{m_k} = g(u_k, \theta_k) = \sum_{i=0}^{p} \theta_{i_k} u_k^i, \tag{3.41}$$

$$y_k = y_{m_k} + e_k, \tag{3.42}$$

where $\theta_k$ is a time-varying vector of model parameters (to be adapted) and $e_k$ is the mismatch (including measurement noise) between the real plant output $y_k$ and the model output $y_{m_k}$.

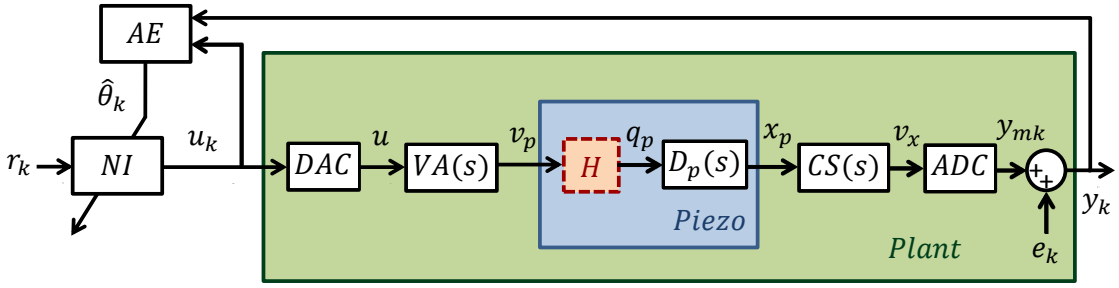


Figure 3.19: The considered model of X axis with adaptive estimator ($AE$) and numerical inversion block ($NI$) for hysteresis compensation.

### 3.6.1 Adaptive forgetting as a statistical decision problem

This subsection is devoted to the adaptive parameter estimator $AE$ shown in Fig. 3.19. Using (3.41)-(3.42), the case when the output $y_k$ depends on the observations in the following way is considered:

$$\begin{aligned} \theta_{k+1} &= \theta_k, \\ y_k &= h_k'\theta_k + e_k, \quad e_k \sim \mathcal{N}\left(0, 1/d_k\right)\big|_{d_{k+1}=d_k}. \end{aligned} \tag{3.43}$$

where $\theta_k \in \mathbb{R}^p$ is a randomly variable vector of unknown parameters, $h_k \in \mathbb{R}^p$ is the known regression vector, $'$ stands for the transposition operator. The error $e_k$ is assumed to be normally distributed, discrete with unknown variance $1/d_k$ (to be estimated as well). It is assumed that there is no drift in the evolution of $1/d_k$. The following posterior probability density function (pdf) is used to describe the uncertainty of the set of parameters $\Theta_k = \{\theta_k, d_k\}$ having the observed data $D^k = \{u_\gamma, y_\gamma\}_{\gamma=1}^k$:

$$\begin{aligned} &f\left(\Theta_k \middle| D^k\right) \propto \left(2\pi/d_k\right)^{-(v_{k|k}+p-2)/2} \\ &\times \exp\left[-(\theta_k - \hat{\theta}_{k|k})' P_{k|k}^{-1} (\theta_k - \hat{\theta}_{k|k}) d_k/2\right] \\ &\times \exp\left[-\Sigma_{k|k} d_k/2\right] \end{aligned} \tag{3.44}$$

In $k|k-1$, $k$ indicates the current time, and $k-1$ the time of the last recognized output and symbol $\propto$ denotes the proportionality. The data learning step (with accordance with Kalman

Filter equations) is given as follows:

$$K_k \equiv P_{k|k-1}h_k/\big(1+h_k'P_{k|k-1}h_k\big), \tag{3.45}$$
$$\epsilon_{k|k-1} \equiv y_k - h_k'\theta_{k|k-1}, \tag{3.46}$$
$$\hat{\theta}_{k|k} = \hat{\theta}_{k|k-1} + K_k\epsilon_{k|k-1}, \tag{3.47}$$
$$P_{k|k} = (I - K_k h_k')P_{k|k-1}, \tag{3.48}$$
$$\Sigma_{k|k} = \Sigma_{k|k-1} + \epsilon_{k|k-1}^2/\big(1+h_k'P_{k|k-1}h_k\big), \tag{3.49}$$
$$v_{k|k} = v_{k|k-1} + 1. \tag{3.50}$$

where $\equiv$ stands for the equality by definition. In [Karny, 2006] a detailed discussion about the particular statistics and their prior settings is given.

In (3.43) it is assumed that the set of parameters $\Theta_k$ does not change, which is an unrealistic assumption. Here, one wants to determine the predictive pdf $f\big(\Theta_{k+1}\big|D^k\big)$ and compensate for this unrealistic assumption. Suppose that no explicit time evolution model is available and only the following pair of alternatives gives the prior information about model parameters:

$$f_0(\Theta_{k+1}) \equiv f(\Theta_k|D^k), \tag{3.51}$$
$$f_1(\Theta_{k+1}) \propto (2\pi/d_{k+1})^{-(p+2)/2}, \tag{3.52}$$

where $f_0(\Theta_{k+1})$ refers to the case when the parameters are not changing within time interval $(k, k+1)$ and $f_1(\Theta_{k+1})$ to the case when all the parameters are uniquely distributed between $(k, k+1)$.

One defines an unknown pdf $f_A\big(\Theta_{k+1}\big)$ restricted to the decision space $f_A^*\big(\Theta_{k+1}\big) \equiv \{f_0\big(\Theta_{k+1}\big), f_1\big(\Theta_{k+1}\big)\}$ equal to $f_0\big(\Theta_{k+1}\big)$ with a probability $\varphi_0 > 0$ and to $f_1\big(\Theta_{k+1}\big)$ with a probability $\varphi_1 > 0$ subject to the constraint $\varphi_0 + \varphi_1 = 1$. For the forthcoming manipulation $\varphi \equiv \big[\varphi_0, \varphi_1\big]'$. The distance between the reality $f\big(\Theta_{k+1}\big)$ and $f_A\big(\Theta_{k+1}\big)$ is assessed using so called Kullback-Leibler divergence [Karny, 2006] defined as follows:

$$\mathcal{D}\big(f\big(\Theta_{k+1}\big)\|f_A\big(\Theta_{k+1}\big)\big) \equiv \int_{\Theta^*} f\big(\Theta_{k+1}\big)\ln\left(\frac{f\big(\Theta_{k+1}\big)}{f_A\big(\Theta_{k+1}\big)}\right)d\Theta. \tag{3.53}$$

where for an arbitrary $k$, $\Theta^*$ is the space of $\Theta_k$. The following cost function is defined:

$$\begin{aligned}\phi\big(f\big(\Theta_{k+1}\big),\varphi\big) \equiv\ & \varphi_0\big[\mathcal{D}\big(f\big(\Theta_{k+1}\big)\|f_0\big(\Theta_{k+1}\big)\big)\\ -(1+\rho)\varrho_0\big] + \varphi_1\big[&\mathcal{D}\big(f\big(\Theta_{k+1}\big)\|f_1\big(\Theta_{k+1}\big)\big) - \varrho_1\big]\end{aligned} \tag{3.54}$$

with the penalties coefficients $\varrho_0$ and $\varrho_1$ for the success of the corresponding alternatives (3.51) and (3.52), respectively:

$$\varrho_0 \equiv \mathcal{D}\big(f\big(\Theta_k|D^k\big)\|f\big(\Theta_k|D^{k-1}\big)\big), \tag{3.55}$$
$$\varrho_1 \equiv \mathcal{D}\big(f\big(\Theta_k|D^k\big)\|f_1\big(\Theta_k\big)\big). \tag{3.56}$$

The only tuning parameter in the considered adaptive method is the scalar $\rho \geq 0$. The higher value of this parameter, the more trust in the alternative $f_1(\Theta_{k+1})$. The decision max-min problem is then defined as follows:

$$\max_{\varphi} \min_{f(\Theta_{k+1})} \phi\big(f(\Theta_{k+1}), \varphi\big). \tag{3.57}$$

Substituting $\varphi_0 = \lambda_{k+1|k}$ ($\varphi_1 = 1 - \lambda_{k+1|k}$) allows to write the result of the decision problem (3.57) as follows:

$$\begin{aligned} P_{k+1|k} &= P_{k|k}/\lambda_{k+1|k}, \quad & \Sigma_{k+1|k} &= \lambda_{k+1|k}\Sigma_{k|k}, \\ \hat{\theta}_{k+1|k} &= \hat{\theta}_{k|k}, & v_{k+1|k} &= \lambda_{k+1|k} v_{k|k}, \end{aligned} \tag{3.58}$$

where the variable forgetting factor $\lambda_{k+1|k}$ is defined by:

$$\begin{aligned} \lambda_{k+1|k}^{-1} =& 1 + \frac{\rho+1}{p+1}\Bigg\{ \ln\left(1 + h_k' P_{k|k-1} h_k\right) \\ &+ v_{k|k-1} \ln\left(\frac{\Sigma_{k|k}}{\Sigma_{k|k-1}}\right) \\ &+ \frac{h_k' P_{k|k-1} h_k - v_{k|k}\big(1 - \Sigma_{k|k-1}\Sigma_{k|k}^{-1}\big)}{1 + h_k' P_{k|k-1} h_k} \\ &+ \big(v_{k|k-1} - 1\big) \ln\left(\frac{v_{k|k-1}}{v_{k|k}}\right) + \frac{v_{k|k-1}}{v_{k|k}} \Bigg\}. \end{aligned} \tag{3.59}$$

Equations (3.58) and (3.59) close the time updating step of the sufficient statistics w.r.t. (3.57).

### 3.6.2 Numerical indirect model inverse

In this subsection having a parametric model of static nonlinearity defined by (3.41) one searches an input $u_k$ such that the output of the model $y_{m_k}$ follows the reference $r_k$. To that end, the numerical root-finding algorithm is used to solve for the proper $u_k$ in the following equation:

$$f(u_k, \theta_k, r_k) = y_{m_k} - r_k = g(u_k, \theta_k) - r_k = 0. \tag{3.60}$$

Note that in this way one does not need to find an explicit inverse model $g^{-1}(r_k, \theta_{k_i})$ (not necessarily linear in parameters $\theta_{k_i}$). The Newton's iteration algorithm is used for solving (3.60). It is well known that this algorithm does not guarantee the convergence, unlike for example the bisection method. On the other hand, it has better (quadratic) convergence than the latter (linear). Therefore a combination of both approaches is used here. The numerical algorithm needs the starting point $u^0$, which in the considered case is restricted to the allowable control voltage interval from 0 to 10 V. Since the Newton's method solves the problem locally, (3.60) may have several solutions even in this interval. Therefore, a natural choice for the starting point value is the one that is sufficiently close to the expected solution (for example the control voltage in the previous time instant $u^0 = u_{k-1}$).

First, the algorithm tries to find an interval $[u_L\ u_R]$ around the starting point $u^0$ where the solution of (3.60) is located, as follows:

$$u_L = u_R = u^0, \tag{3.61}$$
$$\left\{ \begin{array}{l} u_L := u_L - a \\ u_R := u_R + b \end{array} \right\} \text{ until } f(u_L, \theta_k, r_k) f(u_R, \theta_k, r_k) < 0.$$

where $a > 0,\ b > 0$ are possibly small values. Next, the combined Newton/bisection numerical algorithm is used (starting from $u^0$) with an iteration described by the following equations:

$$u_N^{i+1} = u^i - \frac{f(u^i, \theta_k, r_k)}{f'_{u^i}(u^i, \theta_k, r_k)}, \tag{3.62}$$
$$u_B^{i+1} = \frac{(u_L + u_R)}{2}, \tag{3.63}$$
$$u^{i+1} = \left\{ \begin{array}{ll} u_N^{i+1} & \text{if } u_N^{i+1} \in [u_L\ u_R] \\ u_B^{i+1} & \text{if } u_N^{i+1} \notin [u_L\ u_R] \end{array} \right. , \tag{3.64}$$
$$u_L = u_B^{i+1} \text{ if } f(u_R, \theta_k, r_k) f(u_B^{i+1}, \theta_k, r_k) < 0, \tag{3.65}$$
$$u_R = u_B^{i+1} \text{ if } f(u_L, \theta_k, r_k) f(u_B^{i+1}, \theta_k, r_k) < 0.$$

where $u_N^{i+1}$ and $u_B^{i+1}$ stand for control input computed by Newton iteration and bisection step, respectively. The Newton iteration (3.62) is done everytime when possible and the bisection (3.63) only if the Newton's iteration gives solution out of the interval (3.64)-(3.65) where the solution exists. Therefore, the convergence (which is quadratic) is always assured. The found voltage (after reaching the maximum number of iterations or the required accuracy) is applied to the piezoelectric actuator as $u_k$. Fig. 3.20a shows tracking triangular trajectory of variable amplitude in simulation using Newton approach alone while Fig. 3.20b shows the result of combined Newton with bisection method. One can clearly see that the latter approach, unlike Newton's method alone, is robust against solutions that can be found outside the local neighbourhood of the previous control voltage (which can be seen as sudden jumps in Fig. 3.20a).

### 3.6.3 Hysteresis compensation

In this section experimental results for horizontal (X) axis of a GIPSA-lab system, are presented. These results are obtained for $3^{rd}$ order time-varying polynomial (*i.e.* $p = 3$ in (3.41)).

The following sinusoidal reference of variable amplitude is applied to the considered system in the X direction:

$$x_r(t) = 5 + 2\sin(2\pi t) + 2\sin(2\pi 1.2t + \pi) \tag{3.66}$$

Fig. 3.21a and Fig. 3.21b show the measured and the reconstructed hysteresis curves via adaptation algorithm for parameter values $\rho = 0.4$ and 0.8, respectively. The actual parameters of the polynomial model (3.41) estimated by the adaptive estimator $AE$ are passed in real-time

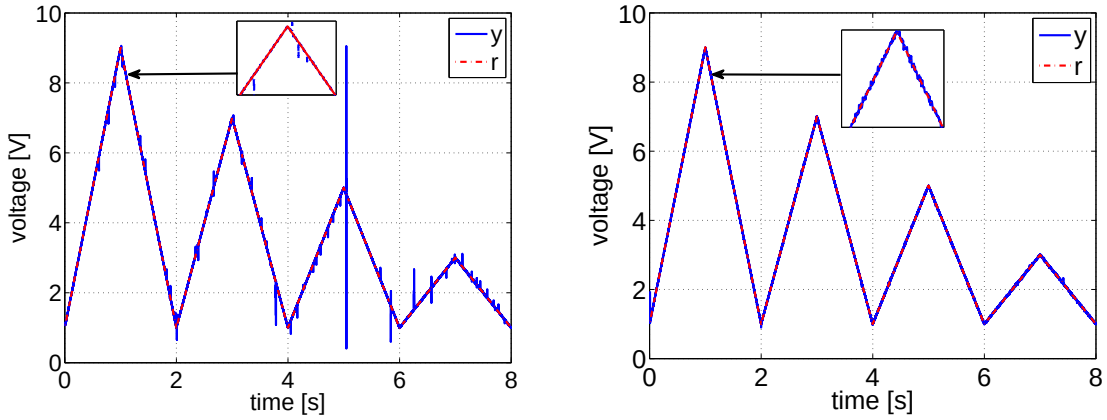


Figure 3.20: Triangular reference tracking with adaptation using numerical algorithm $NI$: (a) only Newton method, (b) Newton combined with bisection.

to the numerical inversion algorithm $NI$ (see Fig. 3.19), which searches for the proper compensation input. The corresponding adapted inverse model, shown in Fig. 3.21c and Fig. 3.21d is applied in cascade with the real plant. The compensation results are shown in Fig. 3.21e and Fig. 3.21f, respectively. Note that parameter $\rho$ highly influences the parameter estimation (and as a result the fitting accuracy). Better fit is obtained for $\rho = 0.8$

Fig. 3.22a-Fig. 3.22f show the corresponding tracking results. Fig. 3.22a shows tracking without any compensation. In the intervals 20-25 s, 25-30 s and 30-35 s the adaptive compensator is switched between different values of parameter $\rho$ ($\rho = 0.8, 0.4$ and $0.0$, respectively). The tracking error increases when $\rho$ decreases as shown in Fig. 3.22e. Fig. 3.22f shows time evolution of the variable forgetting factor $\lambda$ during this experiment. The estimator $AE$ forgets mostly the data at the time instant when the input voltage changes direction (i.e. the polynomial parameters rapidly change their values from ascending to descending curve). The forgetting level depends on the input amplitude as well. The higher value of parameter $\rho$, the faster adaptivity to changing conditions. Finally, Fig. 3.23a, Fig. 3.23c and Fig. 3.23e show tracking performance for triangular reference of variable amplitude without any compensation, with well-known MPI approach and with the proposed adaptive compensator (with $\rho = 0.5$), respectively. The corresponding tracking errors are given in Fig. 3.23b, Fig. 3.23d and Fig. 3.23f, respectively. The results clearly show that the proposed compensator adapts to both changing amplitude as well as to the direction of the input, thus one avoids additional modeling for different amplitudes and ascending or descending hysteresis curves. Since the parameters are updated on-line it outperforms non adaptive approaches based on off-line identification such as MPI approach.

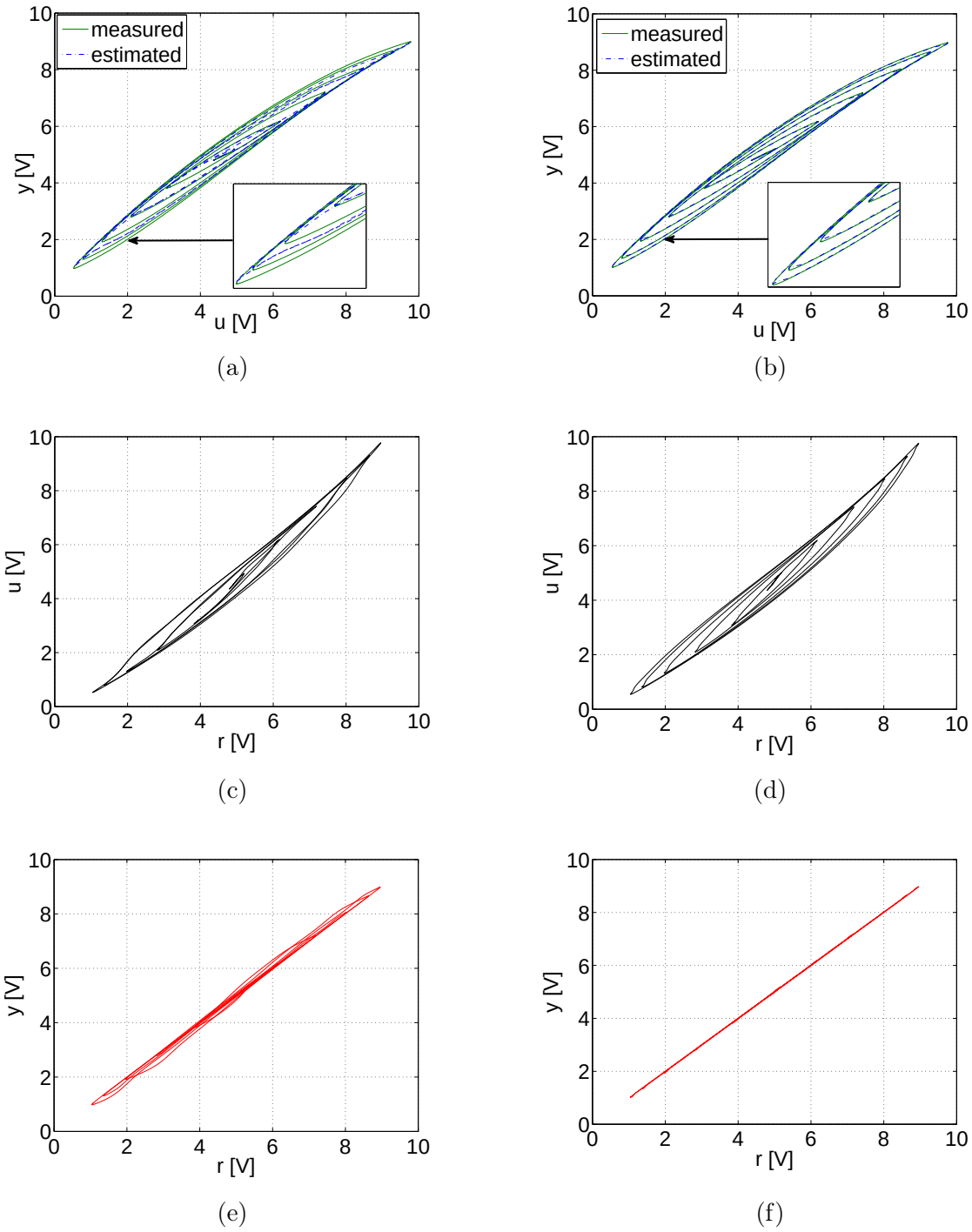


Figure 3.21: Experimental results of hysteresis compensation for sinusoidal reference of variable amplitude $x_r(t) = 5 + 2\sin(2\pi t) + 2\sin(2\pi 1.2t + \pi)$ for $\rho = 0.4$ (left) and $\rho = 0.8$ (right): (a), (b) Measured and estimated hysteresis. (c), (d) Inverted model. (e), (f) Compensation.

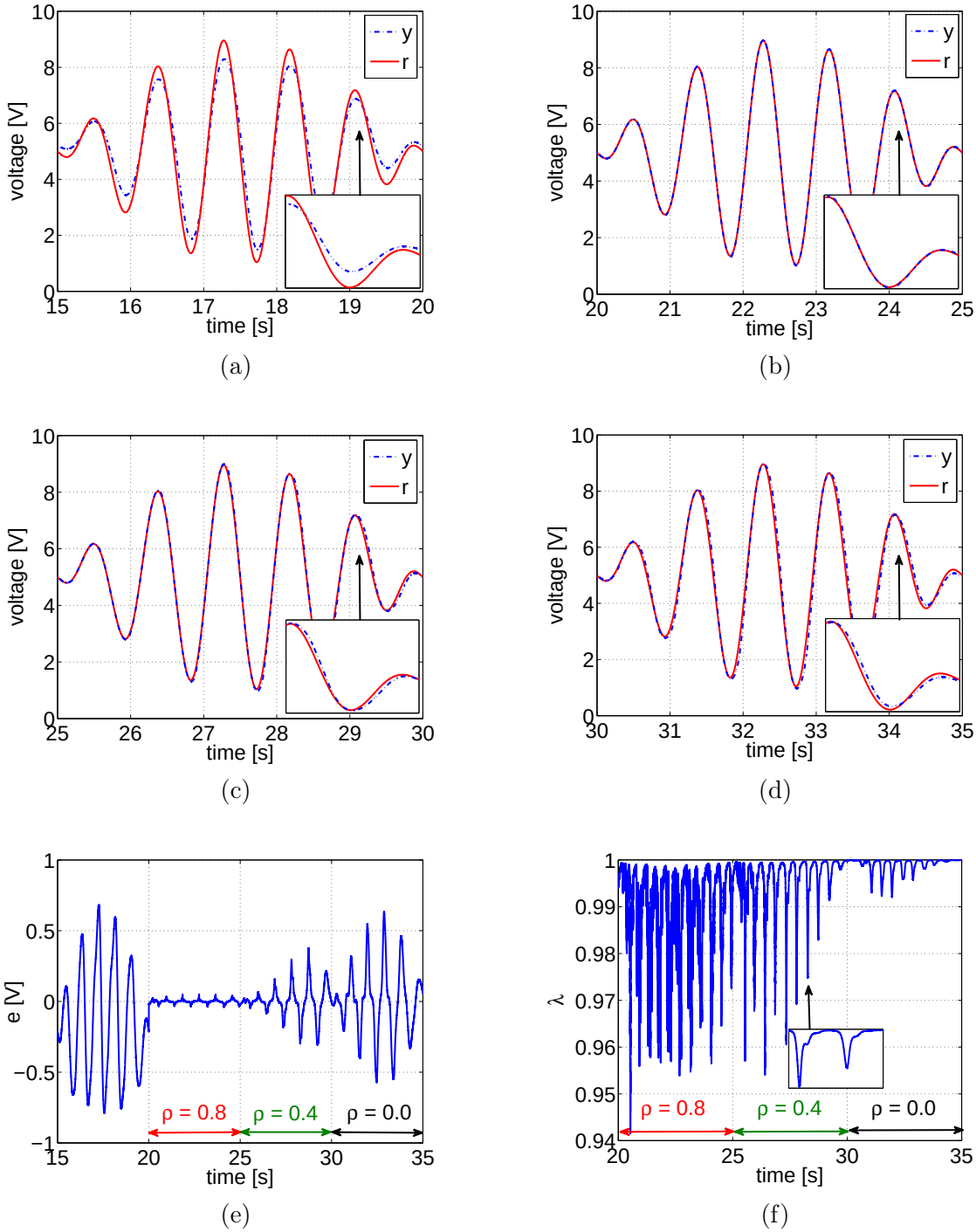


Figure 3.22: Experimental results for tracking sinusoidal reference of variable amplitude: (a) Without compensation. (b), (c), (d) With compensation for $\rho = 0.8, 0.4, 0.0$, respectively. (e) Corresponding tracking errors. (f) Corresponding variable forgetting factor.

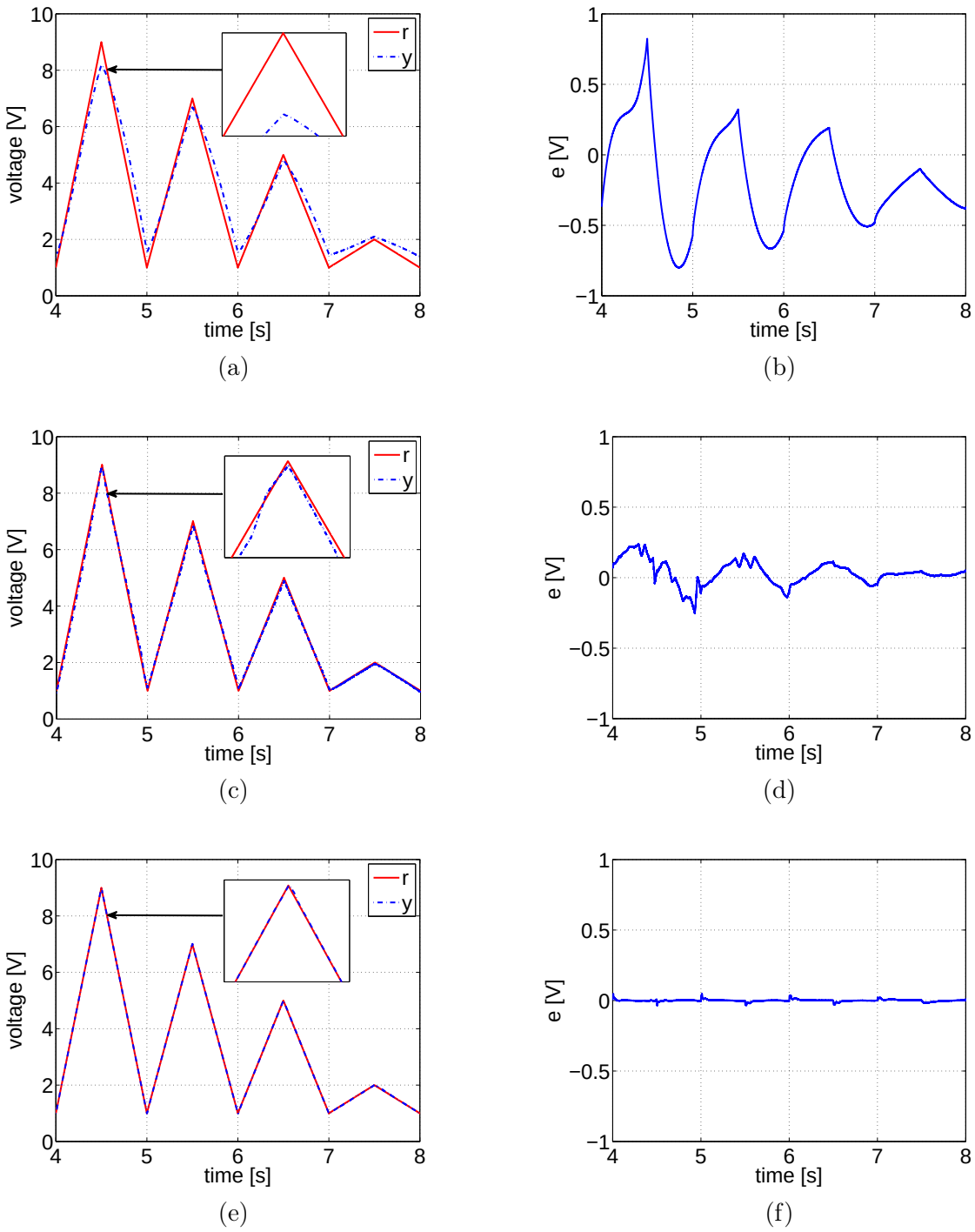


Figure 3.23: Experimental results for tracking triangular reference of variable amplitude: (a), (c), (e) Without any compensation, with MPI and with the proposed adaptive compensator, respectively. (b), (d), (f) Corresponding tracking errors.

## 3.7 Conclusion

In this chapter the nonlinear hysteresis and creep phenomena have been investigated. To that end, several methods for their subsequent modeling, identification and compensation have been tested on the horizontal axes of the the experimental platform. The Prandtl-Ishlinskii (PI) model due to its symmetric nature cannot capture asymmetric hysteresis curves, however it still gives much better results than without any compensation. The Modified Prandtl-Ishlinskii (MPI) model extends the PI approach for the asymmetric curves and therefore substantially increases the accuracy. Unlike MPI, the observer-based approach (DOB) successfully compensates the creep phenomenon in addiction to hysteresis. Further improvement (especially for higher frequencies) can be achieved by combining the DOB with MPI. A nice alternative is an adaptive approach, which uses in the considered case a simple polynomial model with adaptively changing coefficients. The numerical inversion algorithm works in real-time and one avoids the explicit model inversion.

Chapter 4

# Structural vibration and cross-couplings

**Contents**



## 4.1 Introduction

This chapter is devoted to the structural vibration and cross-coupling reduction of horizontal piezoelectric actuators used to move the tunneling tip in X-Y plane along the scanned surface. Such a horizontal 2D system is already compensated for hysteresis as treated in the previous chapter. In [Habib et al., 2012], LQG control was used to tackle for the vibration effects while positioning the lateral axes of the AFM. As mentioned in chapter 1, pure LQG controller is not guaranteed to be robust w.r.t. the model uncertainties. It is commonly known that full state feedback LQR controller has at least 60° phase margin and 6dB gain margin and as a result the closed-loop system with this controller is always stable (see [Safonov and Athans, 1977]). However, from the practical point of view not all the states can be available for state feedback design, either because there is a lack of sensors in the system or some states are impossible to measure. In this case a state observer is added to the system to estimate its states on the basis of the measured outputs and the LQR controller is now based not on the states but on their estimates (output feedback controller). The performance of this observer, which is based on the nominal model of the system, depends on how much uncertainty is in the system and since the real system differs from the nominal one, the robust stability

margins of LQR cannot be more assured. In [Doyle and Stein, 1979], it has been shown that these margins can be arbitrarily small even for minimum phase, stable systems. One may try to "speed-up" observer dynamics by playing with its process and measurement covariance matrices but this may be not sufficient. To overcome this limitation the LQG/LTR (Loop Transfer Recovery) procedure was proposed by [Kwakernaak, 1972] and furtherly developed by [Doyle and Stein, 1981]. The idea behind this method lies in LQR loop recovery w.r.t. the uncertainty on the intput or output of the minimum-phase plant by relaxing the optimality either of the quadratic feedback controller or the Kalman filter, respectively. This method has been applied for example in [Munteanu and Ursu, 2008] for vibration control of smart composite wing of the aircraft or in [Hu et al., 1999] to assure high track density for dual-stage actuators in HDDs as well as to piezoelectric tuning fork in Z direction of the AFM [Yeh et al., 2008]. However, due to small displacements (less than 100 nm), the hysteresis effect has been completely omitted in this work, which was the main motivation for the present work to experimentally validate the efficiency of this method for vibration reduction in the presence of nonlinear hysteresis in long-range positioning. Inspired by [Sebastian and Salapaka, 2005], other robust $\mathcal{H}_\infty$ controllers based on the mixed-sensitivity design have been designed and tested as well.

First, the full 2D linear model (together with cross-couplings) is identified and subsequently reduced in section 4.2. The model uncertainty is given here as well. Next, in sections 4.3 and 4.4, the experimental studies on robust control of the Multi-Input Multi-Output (MIMO) 2D plant are presented using Single-Input Single-Output (SISO) LQG/LTR and SISO/MIMO $\mathcal{H}_\infty$ strategies, respectively, together with some comparison.

## 4.2 Linear nominal and perturbed model

### 4.2.1 Model identification

The linear model of the system already compensated for hysteresis with unit static gain, used as a vibration model, is identified here. The input identification signal is a chirp voltage of amplitude 0.5 V around 4 V with frequencies linearly growing with time from 0.1 Hz to Shannon frequency $0.5f_s$, where $f_s$ is the sampling rate of 20 kHz. Firstly, this input is applied on the X axis of the system as $x_h$, while the Y axis remains on a constant level (i.e. $y_h = 4V$). The corresponding response, measured via two capacitive sensors for the X and Y axes is shown in Fig. 4.1a and Fig. 4.1c, respectively. The same identification signal is applied subsequently on the Y axis of the system as $y_h$, while the X axis remains on a constant level (i.e. $x_h = 4V$) and again the two measurements are recorded (see Fig. 4.1b and Fig. 4.1d).

$40^{\text{th}}$-order models were fitted to the measured responses in order to obtain very good accordance with the real data as shown in Fig. 4.2. The diagonal sub-figures correspond to the direct dynamic behavior (i.e. from the input to the corresponding output), while the off-diagonal sub-figures show the cross-coupling between the two axes in the frequency domain. These four high-order single-input single-output (SISO) models together create a full-order

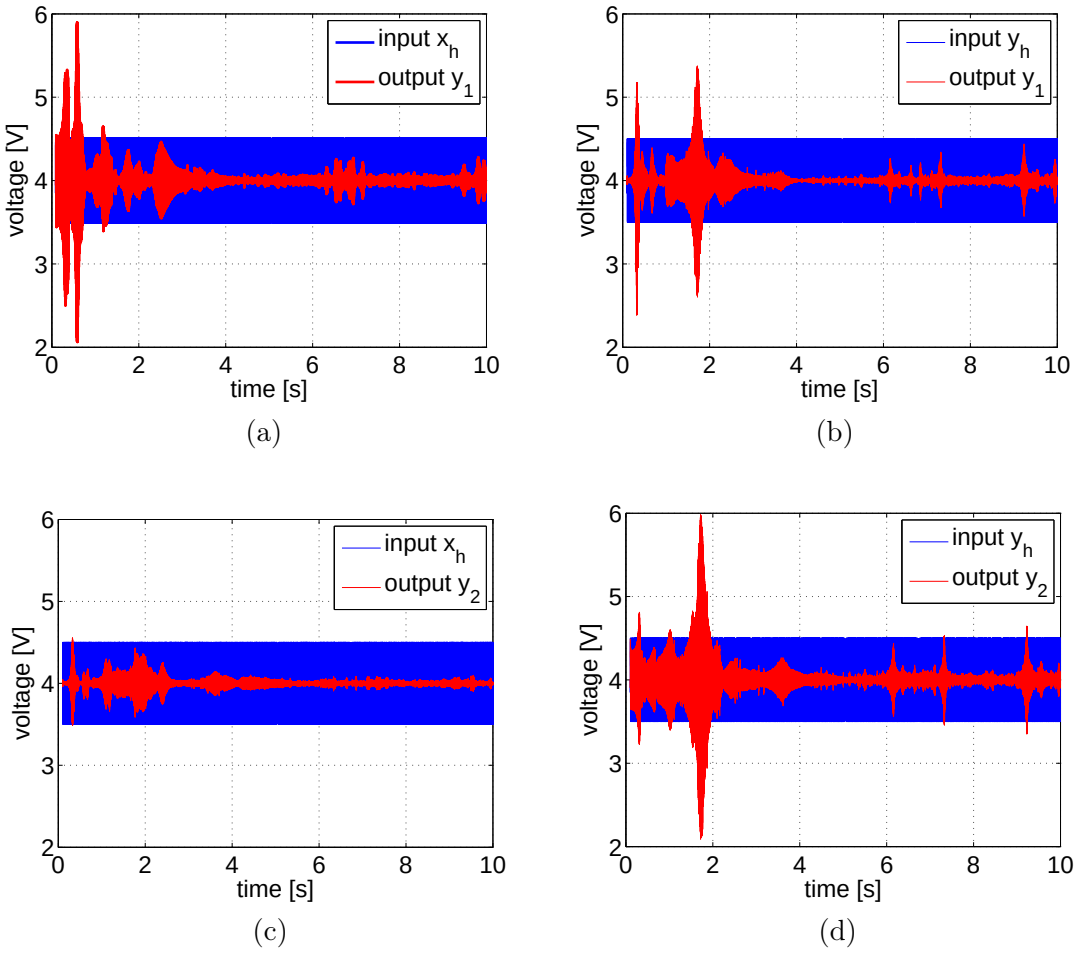


Figure 4.1: Experimental input/output data used for identification: (a) from X to X (b) from Y to X (c) from X to Y (d) from Y to Y.

two-input two-output (TITO) model as follows:

$$G_p(s) = \begin{pmatrix} G_{xx_p}(s) & G_{xy_p}(s) \\ G_{yx_p}(s) & G_{yy_p}(s) \end{pmatrix} \tag{4.1}$$

This model will reflect the behavior of the real system as much as possible and will only serve as a perturbed model for robustness considerations and not for the controller design. The step response of the full-order TITO model (4.1) is shown in Fig. 4.3. Again, the non-zero response on the off-diagonal sub-figures shows that the cross-coupling effect is evident. The amount of coupling in the low frequencies is almost zero (see Fig. 4.2), since the observers designed in the previous chapter, mainly for hysteresis compensation, cancel any other low frequency disturbances, including creep and low frequency cross-couplings. However, with increasing frequencies the coupling-based positioning errors become quite significant.

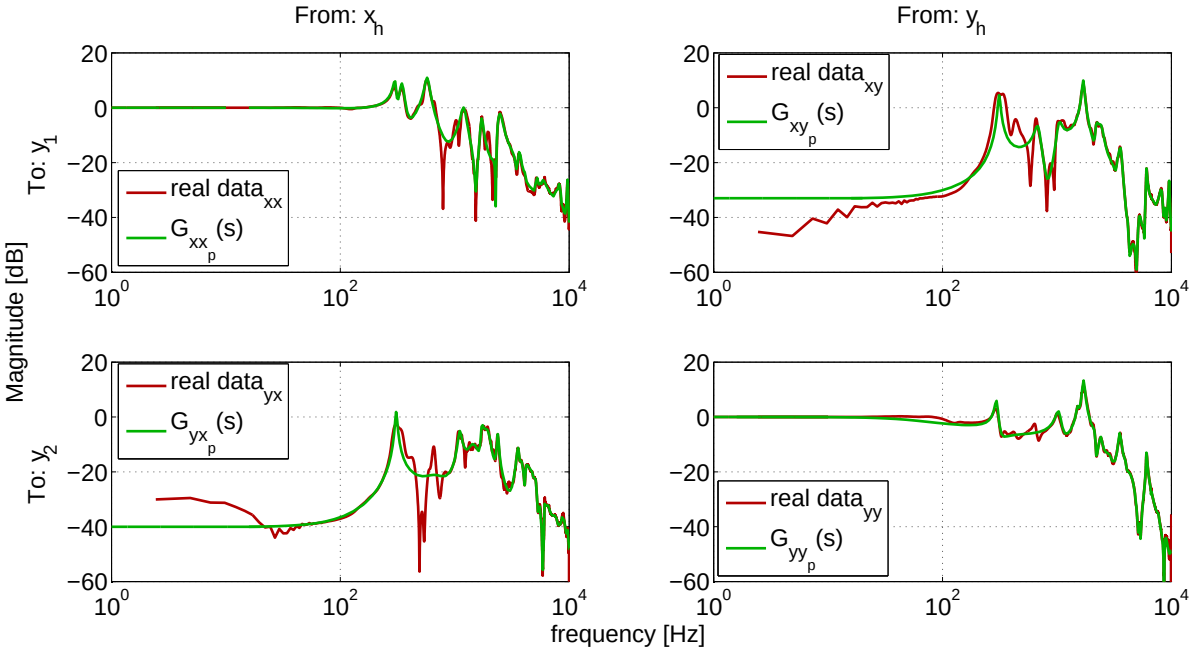


Figure 4.2: Frequency response of the real system and full-order TITO model.

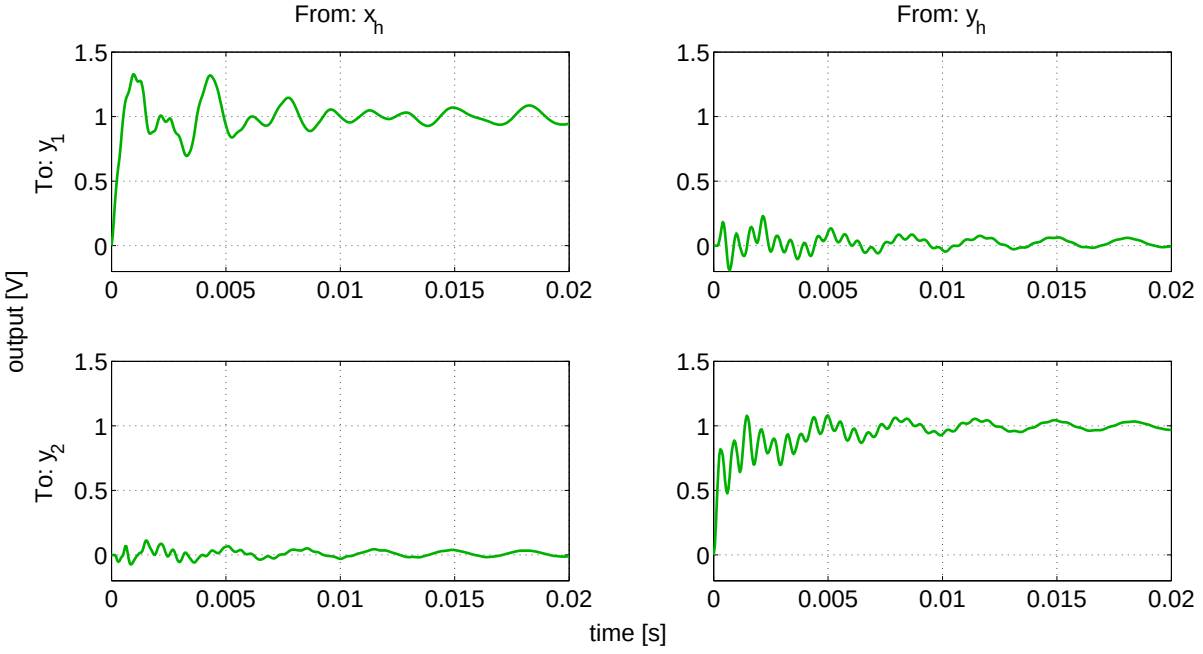


Figure 4.3: Step response of the full-order TITO model.

### 4.2.2 Model reduction and model uncertainty

The full-order TITO model presented previously is an idealistic case and cannot be used for the controller design due to its complexity. Therefore, a proper model reduction is looked for

in this subsection. This reduced-order TITO model is described as follows:

$$G(s) = \begin{pmatrix} G_{xx}(s) & G_{xy}(s) \\ G_{yx}(s) & G_{yy}(s) \end{pmatrix} \tag{4.2}$$

To that end, the balanced truncation method is used. First the full order model is converted to its balanced form and next the states which are weakly controllable/observable (with small corresponding singular values) are neglected. Here the reduction has been performed for all of the components of $G_p(s)$ separately, for having more degree of freedom. Fig. 4.4 shows Hankel singular values of each of the component of the full-order model. The states with singular values less than the prespecified thresholds (pointed by the black lines) are then neglected resulting in reduced models of components with the number of states pointed by the red line. The values of thresholds for the singular values for each of the component were chosen to be 0.35, 0.18, 0.2 and 0.17, respectively, which results in three $10^{\text{th}}$-order and one $11^{\text{th}}$-order models. The magnitude plot in the frequency domain and step responses of both full- and

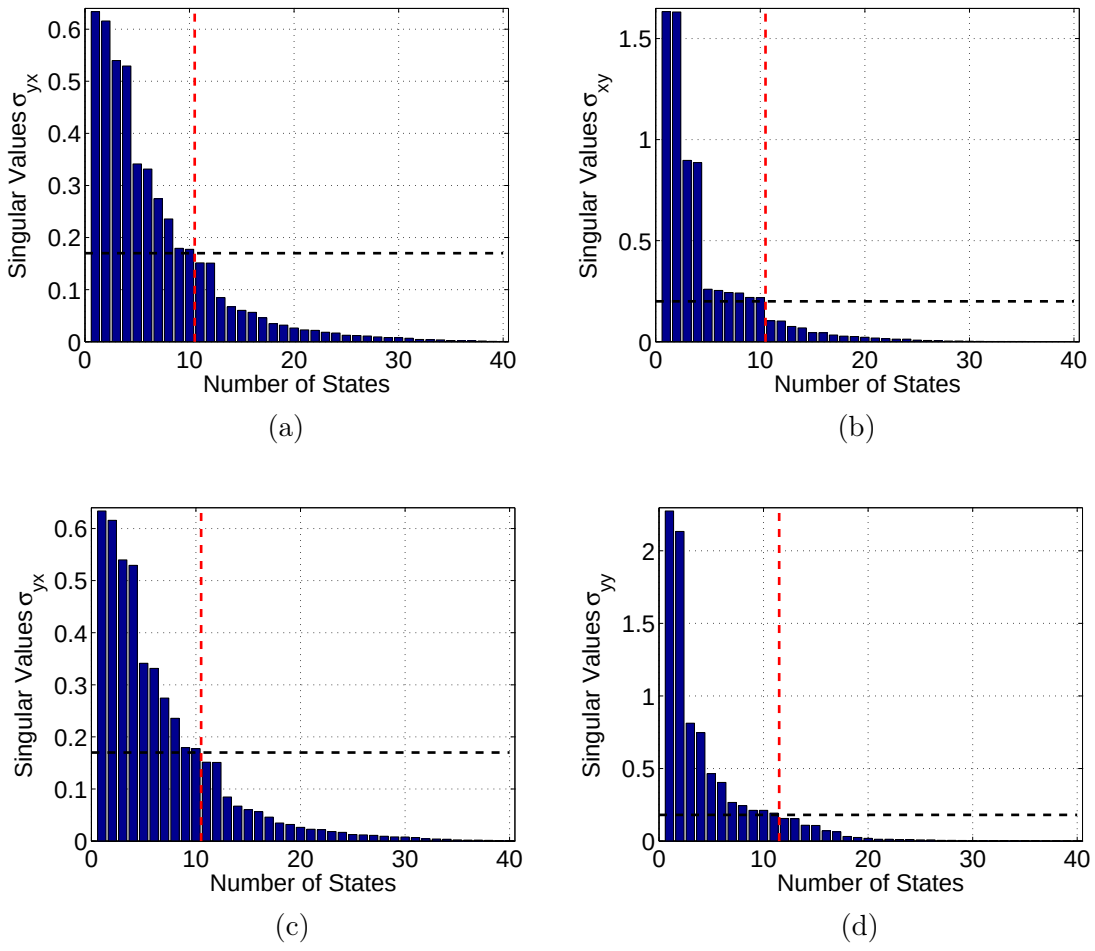


Figure 4.4: Hankel singular values of the components of the full-order TITO model (red lines point at the number of states of the reduced model): (a) $\sigma_{xx_p}$ (b) $\sigma_{xy_p}$ (c) $\sigma_{yx_p}$ (d) $\sigma_{yy_p}$.

reduced-order TITO models are shown in Fig. 4.5 and Fig. 4.6, respectively. One can see a very good accordance of both models despite order reduction.

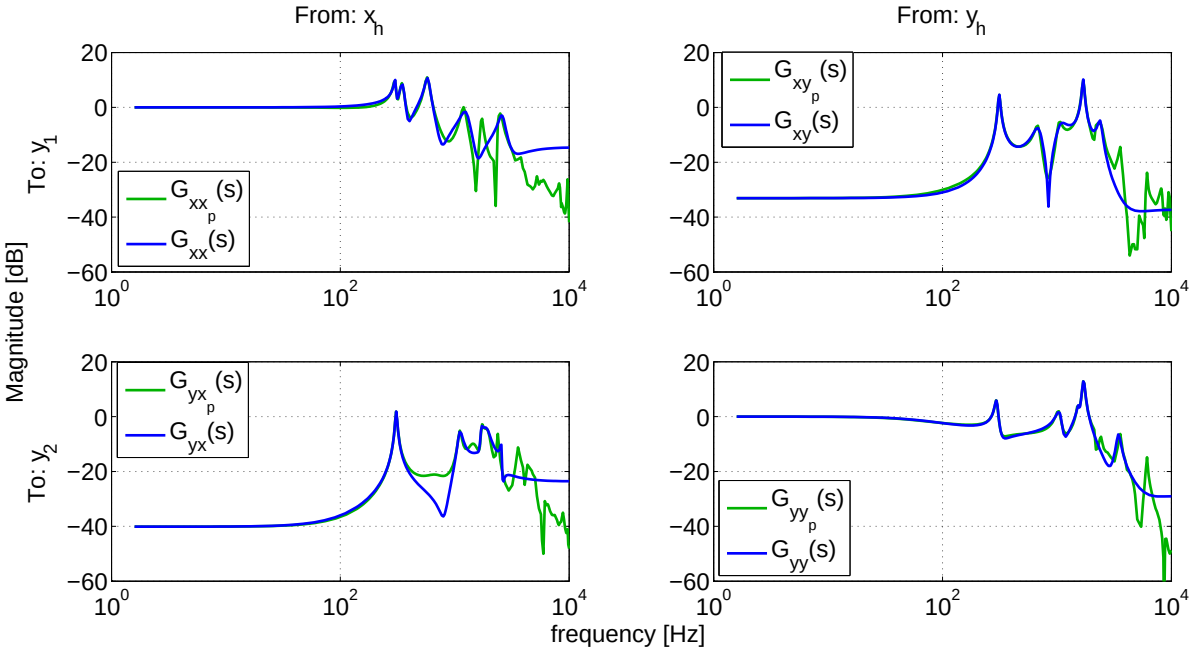


Figure 4.5: Frequency response of the full- and reduced-order TITO model.

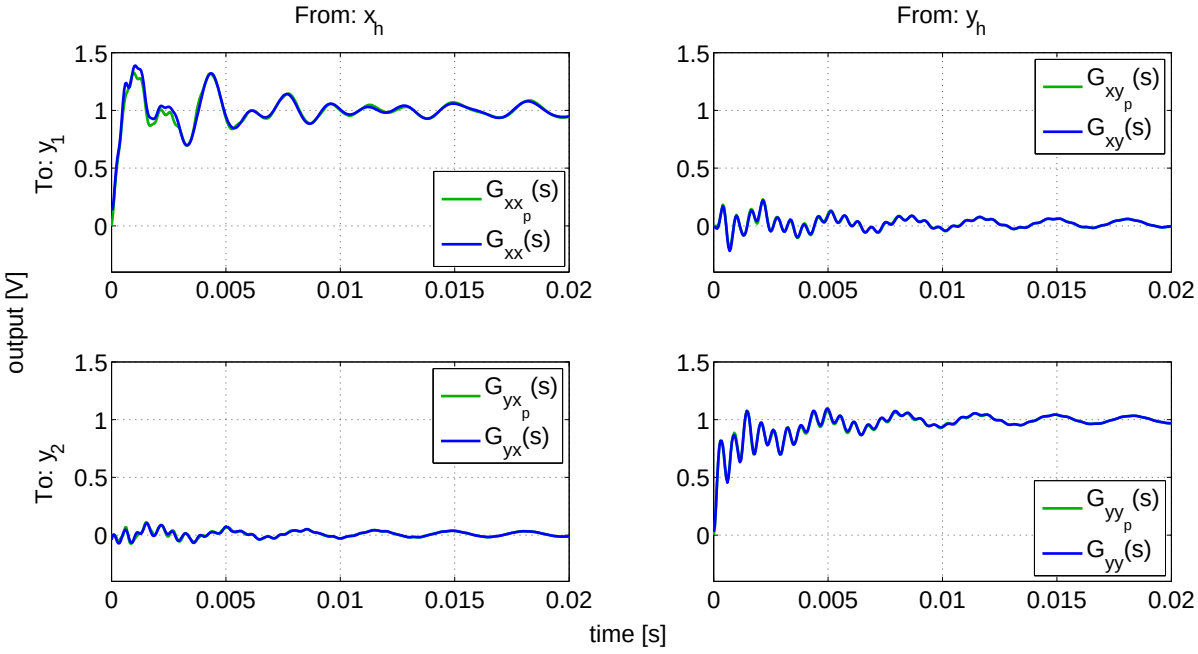


Figure 4.6: Step response of the full- and reduced-order TITO model.

The controlled system has to be robust w.r.t. the model uncertainty. In many practical situations the actual system can behave slightly differently from the model on the basis of

which the controler has been designed. The full-order ideal TITO model defined by (4.1) reflects the behavior of the real system with a high accuracy for all frequencies and thus it will be referred here as a perturbed model $G_p(s)$. However, for real-time implementation only the reduced-order model, referred here as nominal model $G(s)$, will be used. The uncertain system can be described in an additive or multiplicative way. The additive uncertainty is a simple way to represent the discrepancy between the perturbed and the nominal model by taking the difference between their respective transfer functions. In this work, however, the output multiplicative structure has been chosen to model the uncertain system as follows (see Fig. 4.7):

$$G_p(s) = (1 + W_\Delta(s)\Delta(s))G(s) \tag{4.3}$$

where $\Delta(s)$ is any stable transfer function, which represents the normalized complex perturbations such that $|\Delta(j\omega)| \leq 1$, $\forall\omega$ and $W_\Delta(s)$ is a rational transfer function representing the uncertainty weight chosen as follows:

$$|W_\Delta(j\omega)| \geq |W_\Delta(j\omega)\Delta(j\omega)| = l_\Delta(\omega) = \left|\frac{G_p(j\omega) - G(j\omega)}{G(j\omega)}\right|, \forall\omega \tag{4.4}$$

where $l_\Delta(\omega)$ represents relative magnitude of the neglected dynamics. In other words $W_\Delta(s)$ is chosen such that $|W_\Delta(j\omega)|$ is an upper bound on the relative errors $l_\Delta(\omega)$.

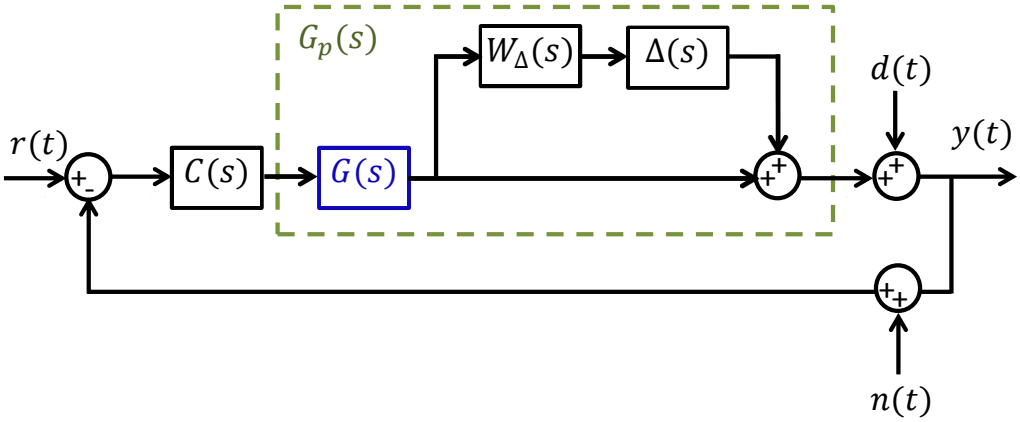


Figure 4.7: Feedback system with output multiplicative uncertainty.

## 4.3 LQG/LTR approach for vibration reduction

On the basis of the obtained model $G(s)$, a Linear Quadratic Gaussian with Loop Transfer Recovery (LQG/LTR) controller can be designed. Two SISO LTR controllers will be designed (each for one axis of the considered system). To that end, two components of $G(s)$ are taken into account, $G_{xx}(s)$ (for $C_x(s)$ controller design) and $G_{yy}(s)$ (for $C_y(s)$ controller design). These models in state-space are given by:

$$G_{xx} : \begin{cases} \dot{x}_{xx} = A_{xx}x_{xx} + B_{xx}x_h + w_{xx}; \quad x_{xx} \in \mathbb{R}^{10} \\ y_1 = C_{xx}x_{xx} + n_1 \end{cases} \tag{4.5}$$

$$G_{yy}: \begin{cases} \dot{x}_{yy} = A_{yy}x_{yy} + B_{yy}y_h + w_{yy}; \quad x_{yy} \in \mathbb{R}^{11} \\ y_2 = C_{yy}x_{yy} + n_2 \end{cases} \tag{4.6}$$

with the control inputs $x_h$ and $y_h$ (the subscript $h$ means that the system is already compensated for hysteresis). $w_{xx}$, $w_{yy}$ and $n_1$, $n_2$ are its process and measurement noises, respectively. To assure zero steady-state tracking error, the forward path of the controlled system must contain an integrator, thus both systems (4.5) and (4.6) are augmented with an integral action before controller design procedure (see Fig. 4.8). The augmented system for the X axis is expressed as:

$$G_{xx_a}: \begin{cases} \begin{pmatrix} \dot{x}_{xx} \\ \dot{x}_h \end{pmatrix} = \underbrace{\begin{pmatrix} A_{xx} & B_{xx} \\ 0 & 0 \end{pmatrix}}_{A_{xx_a}} \underbrace{\begin{pmatrix} x_{xx} \\ x_h \end{pmatrix}}_{x_{xx_a}} + \underbrace{\begin{pmatrix} 0 \\ 1 \end{pmatrix}}_{B_{xx_a}} \dot{x}_h + \underbrace{\begin{pmatrix} 0 \\ w_{xx} \end{pmatrix}}_{w_{xx_a}}; \quad x_{xx_a} \in \mathbb{R}^{11} \\ y_1 = \underbrace{\begin{pmatrix} C_{xx} & 0 \end{pmatrix}}_{C_{xx_a}} \begin{pmatrix} x_{xx} \\ x_h \end{pmatrix} + n_1 \end{cases} \tag{4.7}$$

Similarly, the augmented system for the Y axis is expressed as:

$$G_{yy_a}: \begin{cases} \begin{pmatrix} \dot{x}_{yy} \\ \dot{y}_h \end{pmatrix} = \underbrace{\begin{pmatrix} A_{yy} & B_{yy} \\ 0 & 0 \end{pmatrix}}_{A_{yy_a}} \underbrace{\begin{pmatrix} x_{yy} \\ y_h \end{pmatrix}}_{x_{yy_a}} + \underbrace{\begin{pmatrix} 0 \\ 1 \end{pmatrix}}_{B_{yy_a}} \dot{y}_h + \underbrace{\begin{pmatrix} 0 \\ w_{yy} \end{pmatrix}}_{w_{yy_a}}; \quad x_{yy_a} \in \mathbb{R}^{12} \\ y_2 = \underbrace{\begin{pmatrix} C_{yy} & 0 \end{pmatrix}}_{C_{yy_a}} \begin{pmatrix} x_{yy} \\ y_h \end{pmatrix} + n_2 \end{cases} \tag{4.8}$$

The optimal LQR solutions $\dot{x}_h^* = -K_{c_{xx_a}} x_{xx_a}$ and $\dot{y}_h^* = -K_{c_{yy_a}} x_{yy_a}$ minimize the following cost functions on trajectories of (4.7) and (4.8), respectively:

$$J_x(\dot{x}_h) = \int_0^\infty (x_{xx_a}^T Q_{xx_a} x_{xx_a} + \dot{x}_h^T R_{xx_a} \dot{x}_h) dt \tag{4.9}$$

$$J_y(\dot{y}_h) = \int_0^\infty (x_{yy_a}^T Q_{yy_a} x_{yy_a} + \dot{y}_h^T R_{yy_a} \dot{y}_h) dt \tag{4.10}$$

Here, we consider an LTR design on the plant output (the loop can be recovered also on the plant input, since the problems are dual). From Fig.4.8 one can see that the loop transfer function for X direction (resp. Y direction) obtained by breaking the LQG loop at point $P_{1_x}$ (resp. $P_{1_y}$) (*i.e.* Kalman Filter (KF) loop transfer function) is:

$$LTF_{P_{1_x}}(s) = C_{xx_a} \Phi_{xx_a}(s) K_{f_{xx_a}}; \quad \Phi_{xx_a}(s) = (sI_{11\times 11} - A_{xx_a})^{-1} \tag{4.11}$$

$$LTF_{P_{1_y}}(s) = C_{yy_a} \Phi_{yy_a}(s) K_{f_{yy_a}}; \quad \Phi_{yy_a}(s) = (sI_{12\times 12} - A_{yy_a})^{-1} \tag{4.12}$$

and the loop transfer function obtained by breaking the LQG loop at point $P_{2_x}$ (resp. $P_{2_y}$) is simply an open loop transfer function $L_x(s)$ (resp. $L_y(s)$):

$$LTF_{P_{2_x}}(s) = L_x(s) = G_{xx_a}(s) K_{x_{LQG/LTR}}(s) = G_{xx}(s) \frac{1}{s} K_{x_{LQG/LTR}}(s) \tag{4.13}$$

$$LTF_{P_{2_y}}(s) = L_y(s) = G_{yy_a}(s)K_{y_{LQG/LTR}}(s) = G_{yy}(s)\frac{1}{s}K_{y_{LQG/LTR}}(s) \tag{4.14}$$

Now, the aim of LTR procedure is to make $LTF_{P_{2_x}}(s)$ (resp. $LTF_{P_{2_y}}(s)$) to approach to $LTF_{P_{1_x}}(s)$ (resp. $LTF_{P_{1_y}}(s)$) by properly designed respective LQR controller. In other words, the LQG/LTR design consists of two steps:
1) **Loop transfer design** - design LQG loop transfer function on the basis of LQR (full-state feedback) at point $P_{1_x}$ (resp. $P_{1_y}$).
2) **Loop transfer recovery (LTR)** - approximate the desired loop transfer function obtained from step 1 with a recovery procedure at point $P_{2_x}$ (resp. $P_{2_y}$) (which is the plant output).

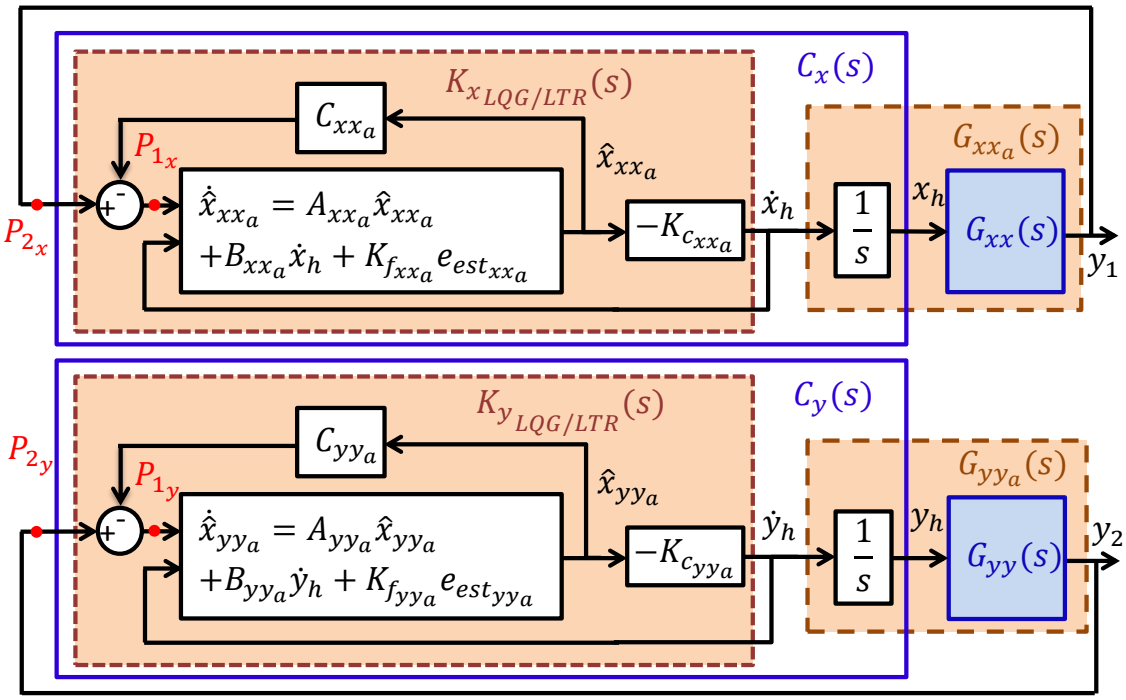


Figure 4.8: Feedback loop with two SISO LQG/LTR controllers (based only on the diagonal part of $G(s)$).

*Step 1):* (the full state design) is done via Kalman Filter Algebraic Riccati Equation (KF ARE) for X and Y axes as follows:

$$A_{xx_a}P_{xx_a} + P_{xx_a}A_{xx_a}^T - K_{f_{xx_a}}N_1K_{f_{xx_a}}^T + W_{xx_a} = 0 \tag{4.15}$$

$$A_{yy_a}P_{yy_a} + P_{yy_a}A_{yy_a}^T - K_{f_{yy_a}}N_2K_{f_{yy_a}}^T + W_{yy_a} = 0 \tag{4.16}$$

with properly chosen process and measurement covariance matrices:

$$W_{xx_a} = E[w_{xx_a}w_{xx_a}^T] = B_{xx_a}B_{xx_a}^T, \quad N_1 = E[n_1n_1^T] = \rho_xI_{1\times1}, \rho_x = 1 \tag{4.17}$$
$$W_{yy_a} = E[w_{yy_a}w_{yy_a}^T] = B_{yy_a}B_{yy_a}^T, \quad N_2 = E[n_2n_2^T] = \rho_yI_{1\times1}, \rho_y = 1 \tag{4.18}$$

*Step 2):* (LQR loop recovery at plant output) is done via LQR ARE:

$$A_{xx_a}^T S_{xx_a} + S_{xx_a} A_{xx_a} - K_{c_{xx_a}}^T R_{xx_a} K_{c_{xx_a}} + Q_{xx_a} = 0 \tag{4.19}$$

$$A_{yy_a}^T S_{yy_a} + S_{yy_a} A_{yy_a} - K_{c_{yy_a}}^T R_{yy_a} K_{c_{yy_a}} + Q_{yy_a} = 0 \tag{4.20}$$

with the weighting matrices for the state and the control effort:

$$Q_{xx_a} = q_x C_{xx_a}^T C_{xx_a}, \quad R_{xx_a} = I_{1\times 1} \tag{4.21}$$

$$Q_{yy_a} = q_y C_{yy_a}^T C_{yy_a}, \quad R_{yy_a} = I_{1\times 1} \tag{4.22}$$

Once the controllers $K_{x_{LQG/LTR}}(s)$ and $K_{y_{LQG/LTR}}(s)$ are designed for the augmented systems (4.7) and (4.8), the integrators are finally inferred into the controllers to control the original systems (see Fig. 4.8) as follows:

$$C_x(s) = \frac{1}{s} K_{x_{LQG/LTR}}(s) \tag{4.23}$$

$$C_y(s) = \frac{1}{s} K_{y_{LQG/LTR}}(s) \tag{4.24}$$

The Nyquist plots of the loop transfer functions $LTF_{P_{2_x}}(s)$ (resp. $LTF_{P_{2_y}}(s)$) for X (resp. Y) axis are shown in Fig.4.9a (resp. Fig.4.9b) in dashed lines (from green to black) and the respective bode plots for X (resp. Y) axis are shown in Fig.4.9c (resp. Fig.4.9d). One can observe their convergence to the desired optimal LQR loop transfer function $LTF_{P_{1_x}}(s)$ (resp. $LTF_{P_{1_y}}(s)$), shown in solid blue line, when the recovery gain $q_x$ (resp. $q_y$) is increased. One can say that the nice properties of LQR have been recovered. Having the open-loop transfer functions $L_{x_p}(s)$ and $L_{y_p}(s)$ for the perturbed systems $G_{xx_p}(s)$ and $G_{yy_p}(s)$ defined as follows:

$$L_{x_p}(s) = G_{xx_p}(s) C_x(s) \tag{4.25}$$

$$L_{y_p}(s) = G_{yy_p}(s) C_y(s) \tag{4.26}$$

and the open-loop transfer functions $L_x(s)$ and $L_y(s)$ for the nominal systems $G_{xx}(s)$ and $G_{yy}(s)$ defined by (4.13) and (4.14), the robust stability of the closed-loop systems w.r.t. model uncertainties is assured by the following conditions (see also Landau):

$$|L_{x_p}(j\omega) - L_x(j\omega)| < |1 + L_x(j\omega)|, \quad \forall\omega \tag{4.27}$$

$$|L_{y_p}(j\omega) - L_y(j\omega)| < |1 + L_y(j\omega)|, \quad \forall\omega \tag{4.28}$$

The recovered open-loop transfer functions $LTF_{P2_x}$, $LTF_{P2_y}$ are shown in Fig. 4.10a and Fig. 4.10b, respectively and the graphical verification of robust stability conditions (4.27), (4.28) is shown in Fig. 4.10c and Fig. 4.10d, respectively. The obtained LQG/LTR SISO controllers ($C_x(s)$ and $C_y(s)$), are applied to the nominal ($G_{xx}(s)$ and $G_{yy}(s)$) and perturbed ($G_{xx_p}(s)$ and $G_{yy_p}(s)$) SISO models, which are the diagonal parts of TITO nominal and perturbed models ($G(s)$ and $G_p(s)$). Figs. 4.11a-4.11b show magnitude plot of the perturbed SISO models in open-loop and of both perturbed and nominal SISO models in closed-loop. One can see that the resonant peaks were successfully damped for both axes and as a result

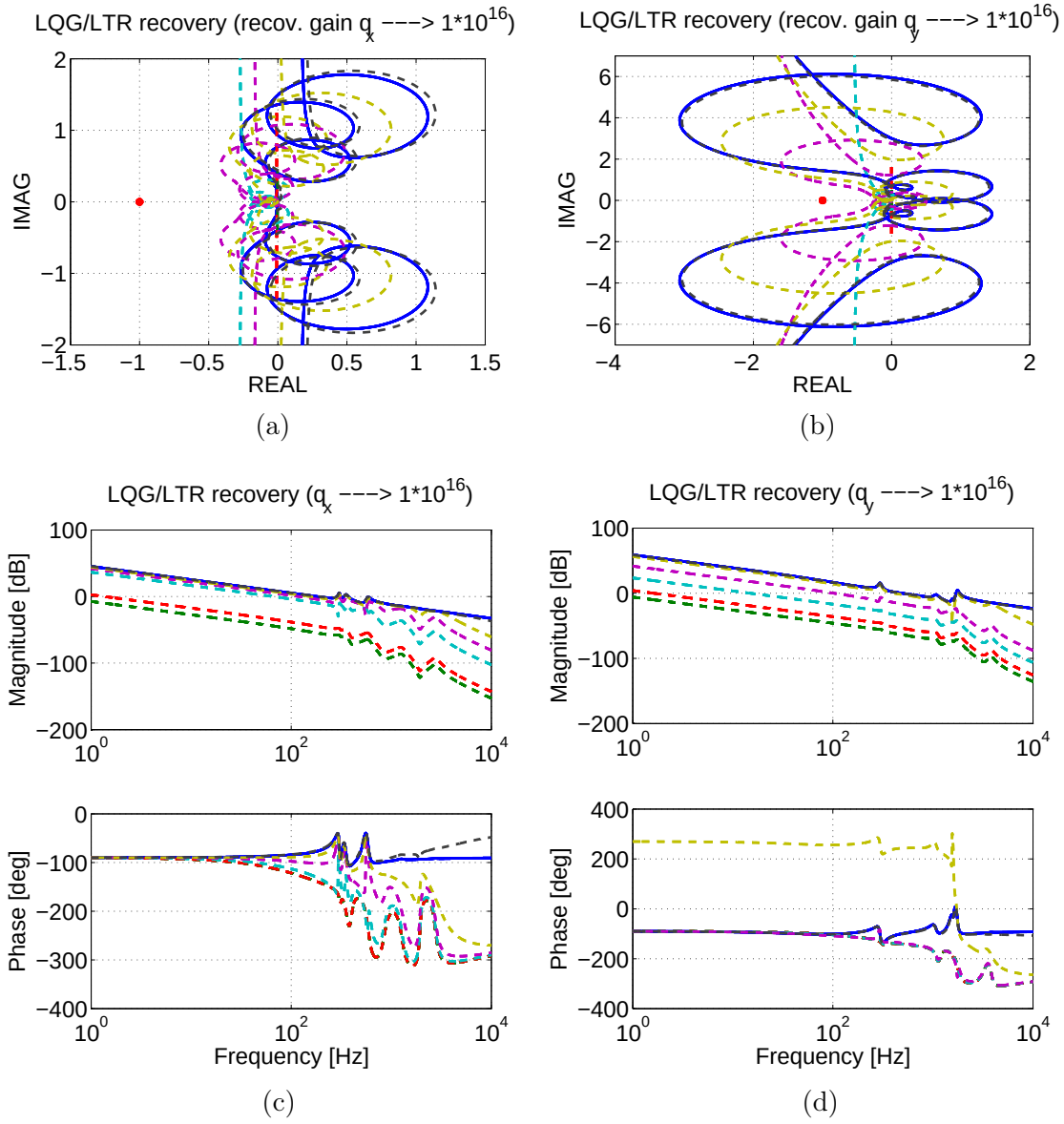


Figure 4.9: LTR with increasing recovery gain $q_i = [1, 10, 10^2, 10^6, 10^8, 10^{10}, 10^{16}]$ ($LTF_{P_{2_i}}(s)$ is in dashed line from green to black, the desired $LTF_{P_{1_i}}(s)$ is in solid blue line): a) Nyquist plot for $i = x$. b) Nyquist plot for $i = y$. c) Bode plot for $i = x$. d) Bode plot for $i = y$.

the structural vibration has been significantly reduced as shown in step tracking in Figs. 4.11c-4.11d. However, it is the TITO model and TITO plant that should be controlled and which contain the model of couplings, omitted in the controller design procedure. The behavior of the TITO plant in closed-loop, controlled by the two designed LQG/LTR SISO controllers is given in section 4.4.3 at the end of this chapter together with other control approaches for the comparison reason.

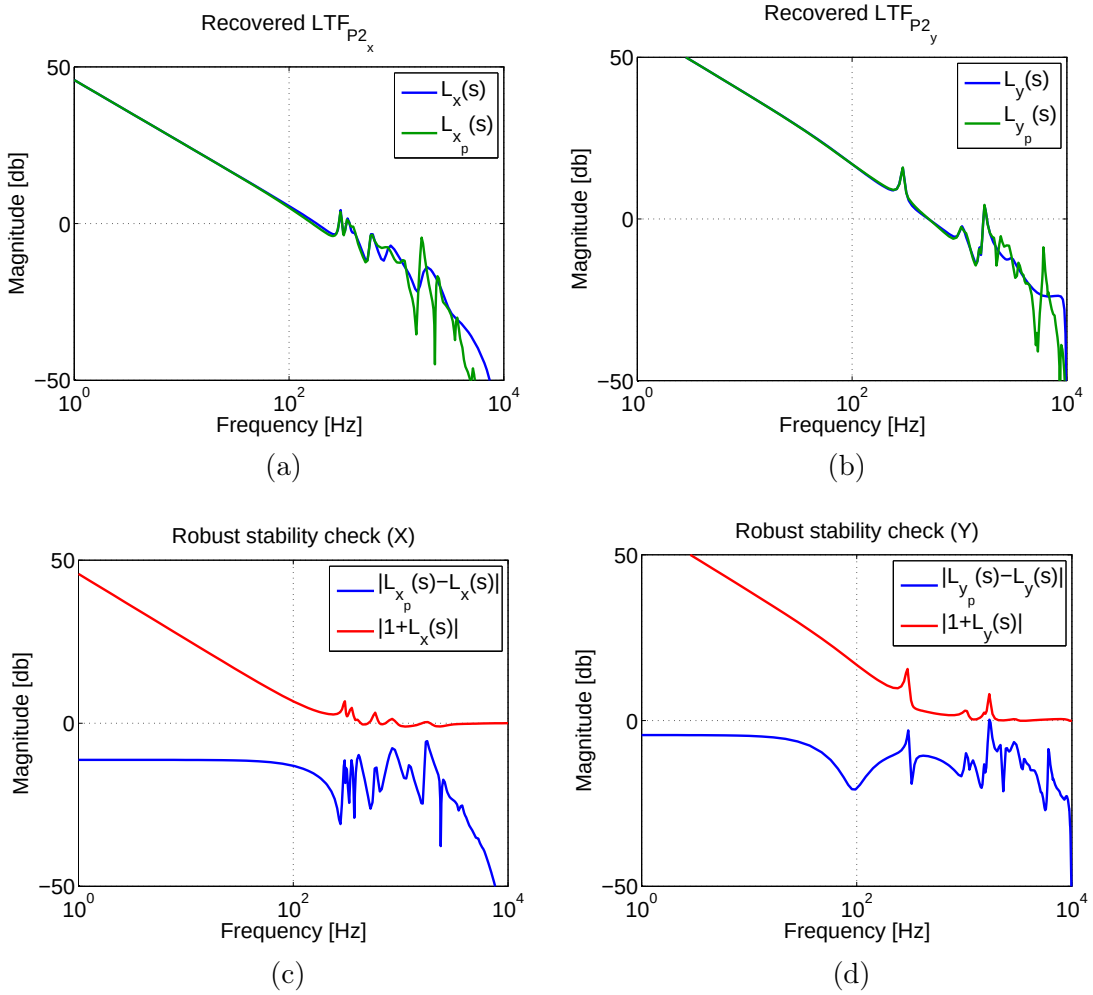


Figure 4.10: Robustness w.r.t. model uncertainty: a), b) Recovered $LTF_{P2}$ for X and Y axis, respectively. c), d) Robust stability check for X and Y axis, respectively.

## 4.4 $\mathcal{H}_\infty$ approach for vibration reduction

### 4.4.1 General $\mathcal{H}_\infty$ problem

The $\mathcal{H}_\infty$ optimal control problem can be formulated as follows: Among all stabilizing controllers $C(s)$ find an optimal one $C^*(s)$ that minimizes the the $\mathcal{H}_\infty$ norm of the lower linear fractional transformation $F_l(P(s), C(s))$, *i.e.*:

$$\gamma^* = \min_{C(s)} ||F_l(P(s), C(s))||_\infty = ||F_l(P(s), C^*(s))||_\infty \tag{4.29}$$

where $\gamma^*$ is an optimal cost and $P(s)$ is an augmented plant (plant $G(s)$ with weighting functions). There is no guarantee that there exists controller which achieves that minimum.

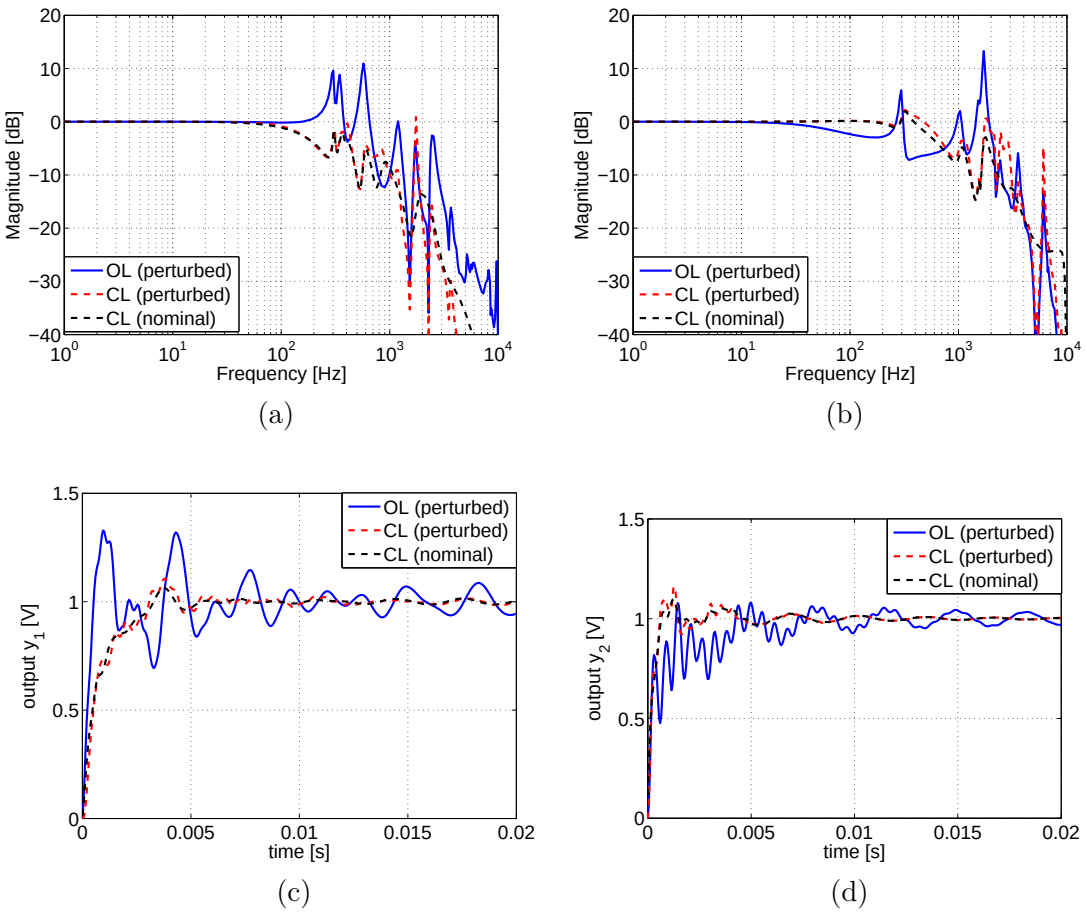


Figure 4.11: Performance of SISO LQG/LTR controllers: a), b) Magnitude response of the system in open-loop and closed-loop (with real and nominal system) for X and Y axis, respectively. c), d) Step response of the system in open-loop and closed-loop (with real and nominal system) for X and Y axis, respectively.

Therefore the optimal problem (4.29) is often formulated as a sub-optimal one as follows:

$$\gamma^* = \inf_{C(s)} ||F_l(P(s), C(s))||_\infty \leq ||F_l(P(s), C^*(s))||_\infty \leq \gamma \tag{4.30}$$

where inf stands for infimum and $\gamma$ is an upper bound of $||F_l(P(s), C^*(s))||_\infty$, which we would like to make as close as possible to the optimal value $\gamma^*$.

In this work, the Mixed-sensitivity $\mathcal{H}_\infty$ control problem is considered. It consists of the design of the $\mathcal{H}_\infty$ optimal controller while shaping the sensitivity function $S(s)$, the control sensitivity function $R(s)$ and the complementary sensitivity function $T(s)$, defined as follows:

$$\begin{aligned} S(s) &= (I + G(s)C(s))^{-1} \\ R(s) &= (I + G(s)C(s))^{-1}C(s) \\ T(s) &= (I + G(s)C(s))^{-1}G(s)C(s) \end{aligned} \tag{4.31}$$

The objective is to minimize the $\mathcal{H}_\infty$ norm of the system, for a given performance vector. In the mixed sensitivity problem, this vector is composed of the sensitivity functions (4.31), multiplied by the respective weights $W_S(s)$, $W_R(s)$ and $W_T(s)$ and the problem is expressed as follows:

$$\begin{aligned} \gamma^* &= \inf_{C(s)} ||N(C(j\omega))||_\infty \leq \gamma \\ N(C(s)) &= \begin{bmatrix} W_S(s)S(s) \\ W_R(s)R(s) \\ W_T(s)T(s) \end{bmatrix} = \begin{bmatrix} W_S(s)S(s) \\ W_R(s)C(s)S(s) \\ W_T(s)T(s) \end{bmatrix}, \end{aligned} \tag{4.32}$$

where $\gamma^*$, $\gamma$ are the optimal and the obtained cost values, respectively. The weights are used to shape their respective sensitivity functions according to the desired requirements. The tracking error from Fig. 4.7 can be expressed as follows:

$$e(t) = r(t) - y(t) = S(s)(r(t) - d(t)) + T(s)n(t) \tag{4.33}$$

We want to keep this error small in both the tracking and the disturbance band. However, from the constraint $S(s) + T(s) = 1$ we can see that keeping the output sensitivity function $S(s)$ small will imply complementary sensitivity function $T(s)$ to be close to one, which will cause propagation of the noise $n(t)$ into the tracking error. Therefore, since usually the disturbance rejection $d(t)$ and tracking the reference $r(t)$ is in lower frequencies, one tries to keep $S(s)$ small only in this band of interest. The desired requirements in our case are defined as follows:

1) **Robust stability in face of model uncertainty**. The controlled system has to be robustly stable w.r.t. the model uncertainty. From small gain theorem (see Zames 1966), it is known that the autonomous system described as a feedback interconnection of a stable systems $S_1(s)$ and $S_2(s)$ is asymptotically stable if the following condition is fulfilled:

$$||S_1(j\omega)S_2(j\omega)||_\infty < 1 \tag{4.34}$$

In our case (for the output multiplicative uncertainty like in Fig.4.7) if we set $S_1(s) = T(s)$ and $S_2(s) = W_\Delta(s)\Delta(s)$ and taking into account that $|\Delta(j\omega)| \leq 1, \forall\omega$ we will assure (4.34) when the following condition is true (see also for instance [Skogestad and Postlethwaite, 2005]):

$$||T(j\omega)W_\Delta(j\omega)||_\infty < 1 \tag{4.35}$$

We define the following high-pass $n_\Delta^{\text{th}}$-order weighting function with lower and upper bounds determined by $A_\Delta$ and $M_\Delta$, respectively:

$$W_\Delta(s) = \left( \frac{s + \omega_\Delta A_\Delta^{1/n_\Delta}}{1/M_\Delta^{1/n_\Delta} s + \omega_\Delta} \right)^{n_\Delta} \tag{4.36}$$

in order to impose an upper bound on the relative magnitude of the neglected dynamics by properly choosing the bandwidth $\omega_\Delta$.

2) **Good robustness margins**. Good robustness margins can be assured if $\Delta G \geq 2$ and $\Delta\phi \geq 29°$, where $\Delta G$ and $\Delta\phi$ stand for the gain and phase margins, respectively. Both conditions can be assured if $\Delta M \geq 0.5$, where $\Delta M$ is the modulus margin. These conditions in terms of constraints on the sensitivity functions can be expressed as follows:

$$||S(j\omega)||_\infty \leq 6dB, \quad \forall\omega \tag{4.37}$$

$$||T(j\omega)||_\infty \leq 3.5dB, \quad \forall\omega \tag{4.38}$$

3) **Reference tracking and disturbance rejection**. We define the following low-pass $n_e^{\text{th}}$-order weighting function with lower and upper bounds determined by $A_e$ and $M_e$, respectively:

$$W_e(s) = \left(\frac{1/M_e^{1/n_e} + \omega_e}{s + \omega_e A_e^{1/n_e}}\right)^{n_e} \tag{4.39}$$

in order to impose the desired performance for tracking accuracy (by choosing $A_e$ possibly small to mitigate an integral action for low frequencies and as a result to eliminate the steady-state error and other disturbances up to the desired bandwidth $\omega_e$).

4) **Control moderation and noise rejection**. We define the following high-pass $n_u^{\text{th}}$-order weighting function with lower and upper bounds determined by $A_u$ and $M_u$, respectively:

$$W_u(s) = \left(\frac{s + \omega_u A_u^{1/n_u}}{1/M_u^{1/n_u} s + \omega_u}\right)^{n_u} \tag{4.40}$$

in order to impose the limit on the actuator force and thus eliminate possible saturations in the controlled system (by choosing properly the value of $A_u$ as an inverse of the maximal control effort within the bandwidth detetmined by $\omega_u$, which is used to attenuate the effect of noise at high frequencies).
By choosing $M_e = 2$ in (4.39) we will immediately assure (4.37). Thus the weight for shaping the output sensitivity function will take the form:

$$W_S(s) = W_e(s), \quad M_e = 2 \tag{4.41}$$

By choosing $A_\Delta = 1/1.5$ in (4.36) we will immediately assure (4.38). Thus the weight for shaping the complementary sensitivity function will take the form:

$$W_T(s) = W_\Delta(s), \quad A_\Delta = 1/1.5 \tag{4.42}$$

By choosing properly $\omega_u$ in (4.40) we will assure the attenuation of the noise influence on the control input (in our case we want to reject the noise influence for the frequencies beyond 2 kHz). Thus the weight for shaping the control sensitivity function will take the form:

$$W_R(s) = W_u(s), \quad \omega_u = 2\pi \cdot 2000 \; rad/s \; (2 \; kHz) \tag{4.43}$$

More details about the numerical values of the rest of parameters of the weighing functions are given in the next section.

### 4.4.2 SISO design

In this subsection two SISO decentralized controllers $C_x(s)$ and $C_y(s)$ are designed for lateral X and Y axes of the considered system, respectively. The controllers are based on the model of the respective axis only (*i.e.* in the design procedure only the diagonal parts of $G(s)$ (*i.e.* $G_{xx}(s)$ and $G_{yy}(s)$) are used., the cross-coupling models $G_{xy}(s)$ and $G_{yx}(s)$ are neglected and seen as a disturbance acting on the output of the respective axis).

For SISO transfer function $H(s)$ the $\mathcal{H}_\infty$ norm is defined as follows:

$$||H||_\infty \stackrel{\text{def}}{=} \max_\omega |H(j\omega)| \geq |H(j\omega)| \tag{4.44}$$

The Mixed sensitivity problem (4.32) for the case of two SISO decentralized controllers is given by:

$$\left|\left| \begin{matrix} W_{S_x}(j\omega)S_x(j\omega) \\ W_{R_x}(j\omega)R_x(j\omega) \\ W_{T_x}(j\omega)T_x(j\omega) \end{matrix} \right|\right|_\infty \leq \gamma_x, \quad \left|\left| \begin{matrix} W_{S_y}(j\omega)S_y(j\omega) \\ W_{R_y}(j\omega)R_y(j\omega) \\ W_{T_y}(j\omega)T_y(j\omega) \end{matrix} \right|\right|_\infty \leq \gamma_y \tag{4.45}$$

where $\gamma_x$ and $\gamma_y$ are the cost values of optimization procedure. This is equivalent to:

$$\begin{matrix} ||W_{S_x}(j\omega)S_x(j\omega)||_\infty \leq \gamma_x & ||W_{S_y}(j\omega)S_y(j\omega)||_\infty \leq \gamma_y \\ ||W_{R_x}(j\omega)R_x(j\omega)||_\infty \leq \gamma_x, & ||W_{R_y}(j\omega)R_y(j\omega)||_\infty \leq \gamma_y \\ ||W_{T_x}(j\omega)T_x(j\omega)||_\infty \leq \gamma_x & ||W_{T_y}(j\omega)T_y(j\omega)||_\infty \leq \gamma_y \end{matrix} \tag{4.46}$$

Using the Cauchy-Schwartz inequality, if we have the following conditions, conditions (4.46) will be satisfied as well:

$$\begin{matrix} ||W_{S_x}(j\omega)||_\infty||S_x(j\omega)||_\infty \leq \gamma_x & ||W_{S_y}(j\omega)||_\infty||S_y(j\omega)||_\infty \leq \gamma_y \\ ||W_{R_x}(j\omega)||_\infty||R_x(j\omega)||_\infty \leq \gamma_x, & ||W_{R_y}(j\omega)||_\infty||R_y(j\omega)||_\infty \leq \gamma_y \\ ||W_{T_x}(j\omega)||_\infty||T_x(j\omega)||_\infty \leq \gamma_x & ||W_{T_y}(j\omega)||_\infty||T_y(j\omega)||_\infty \leq \gamma_y \end{matrix} \tag{4.47}$$

or equivalently:

$$\begin{matrix} ||S_x(j\omega)||_\infty \leq \dfrac{\gamma_x}{||W_{S_x}(j\omega)||_\infty} & ||S_y(j\omega)||_\infty \leq \dfrac{\gamma_y}{||W_{S_y}(j\omega)||_\infty} \\ ||R_x(j\omega)||_\infty \leq \dfrac{\gamma_x}{||W_{R_x}(j\omega)||_\infty}, & ||R_y(j\omega)||_\infty \leq \dfrac{\gamma_y}{||W_{R_y}(j\omega)||_\infty} \\ ||T_x(j\omega)||_\infty \leq \dfrac{\gamma_x}{||W_{T_x}(j\omega)||_\infty} & ||T_y(j\omega)||_\infty \leq \dfrac{\gamma_y}{||W_{T_y}(j\omega)||_\infty} \end{matrix} \tag{4.48}$$

Using (4.44), conditions (4.48) can be finally expressed as follows:

$$\begin{matrix} |S_x(j\omega)| \leq \dfrac{\gamma_x}{|W_{S_x}(j\omega)|} & |S_y(j\omega)| \leq \dfrac{\gamma_y}{|W_{S_y}(j\omega)|} \\ |R_x(j\omega)| \leq \dfrac{\gamma_x}{|W_{R_x}(j\omega)|}, & |R_y(j\omega)| \leq \dfrac{\gamma_y}{|W_{R_y}(j\omega)|} \\ |T_x(j\omega)| \leq \dfrac{\gamma_x}{|W_{T_x}(j\omega)|} & |T_y(j\omega)| \leq \dfrac{\gamma_y}{|W_{T_y}(j\omega)|} \end{matrix} \tag{4.49}$$

The two perturbed systems can be expressed in the output multiplicative structure as follows:

$$\begin{aligned} G_{xx_p}(s) &= (1 + W_{x_\Delta}(j\omega)\Delta_{xx}(s))G_{xx}(s) \\ G_{yy_p}(s) &= (1 + W_{y_\Delta}(j\omega)\Delta_{yy}(s))G_{yy}(s) \end{aligned} \tag{4.50}$$

where $\Delta_{xx}(s)$ and $\Delta_{yy}(s)$ represent the normalized complex perturbations such that $|\Delta_{xx}(j\omega)| \leq 1,\ |\Delta_{yy}(j\omega)| \leq 1,\ \forall\omega$ and $W_{x_\Delta}(j\omega)$, $W_{y_\Delta}(j\omega)$ are the uncertainty weights for X and Y axes, respectively. They are chosen as follows:

$$|W_{x_\Delta}(j\omega)| \geq |W_{x_\Delta}(j\omega)\Delta_{xx}(j\omega)| = l_{\Delta_{xx}}(\omega) = \left|\frac{G_{xx_p}(j\omega) - G_{xx}(s)(j\omega)}{G_{xx}(s)(j\omega)}\right|, \forall\omega \tag{4.51}$$

$$|W_{y_\Delta}(j\omega)| \geq |W_{y_\Delta}(j\omega)\Delta_{yy}(j\omega)| = l_{\Delta_{yy}}(\omega) = \left|\frac{G_{yy_p}(j\omega) - G_{yy}(s)(j\omega)}{G_{yy}(s)(j\omega)}\right|, \forall\omega \tag{4.52}$$

Since they are the upper bounds on the relative errors (relative neglected dynamics) $l_{\Delta_{xx}}(\omega)$ and $l_{\Delta_{yy}}(\omega)$ as shown in Fig. 4.12, they can infer them directly to the controller design procedure, so that it can be robust against them. They were chosen like in (4.36) with the following numerical values for X and Y axes, respectively:

$$n_{\Delta_x} = 3,\ A_{\Delta_x} = 1/10,\ M_{\Delta_x} = 10,\ w_{\Delta_x} = 2\pi \cdot 600\ rad/s \tag{4.53}$$

$$n_{\Delta_y} = 2,\ A_{\Delta_y} = 1/40,\ M_{\Delta_y} = 8,\ w_{\Delta_y} = 2\pi \cdot 800\ rad/s \tag{4.54}$$

The robust stability condition (4.35) takes the following form:

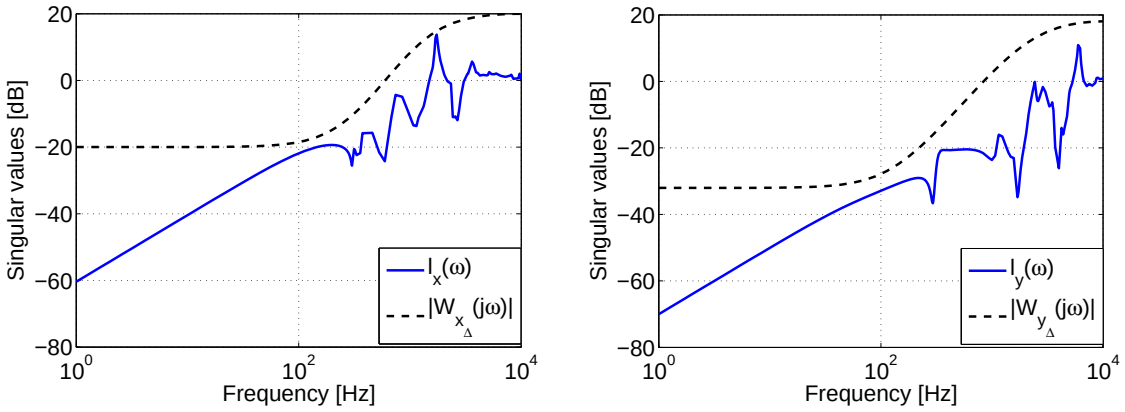


(a) (b)

Figure 4.12: Magnitude plot of the weighting function and relative errors for X (left) and b) for Y (right) axis: a) $|W_{x_\Delta}(j\omega)| \geq l_{\Delta_{xx}}(\omega)$ b) $|W_{y_\Delta}(j\omega)| \geq l_{\Delta_{yy}}(\omega)$.

$$||T_x(j\omega)W_{x_\Delta}(j\omega)||_\infty < 1, \quad ||T_y(j\omega)W_{y_\Delta}(j\omega)||_\infty < 1 \tag{4.55}$$

The weighting functions for the tracking error were chosen like in (4.39) with the following numerical values for X and Y axes, respectively:

$$n_{e_x} = 1,\ A_{e_x} = 1/1000,\ M_{e_x} = 2,\ w_{e_x} = 2\pi \cdot 400\ rad/s \tag{4.56}$$

$$n_{e_y} = 1,\ A_{e_y} = 1/1000,\ M_{e_y} = 2,\ w_{e_y} = 2\pi \cdot 600\ rad/s \tag{4.57}$$

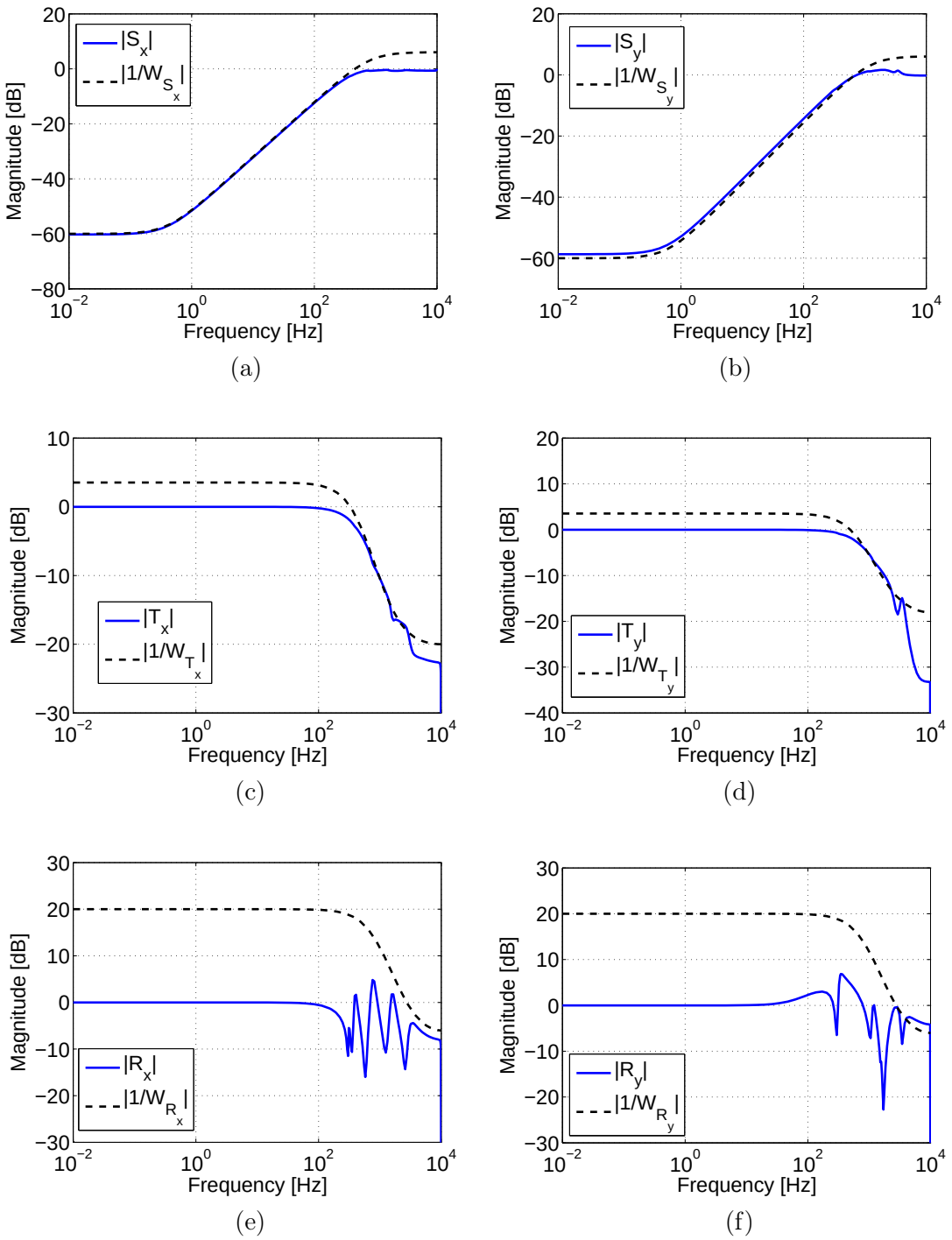


Figure 4.13: Sensitivity functions for the nominal plant and the obtained controller for X (left) and for Y (right) axis: a), b) Output sensitivity function. c), d) Complementary sensitivity function. e), f) Control sensitivity function.

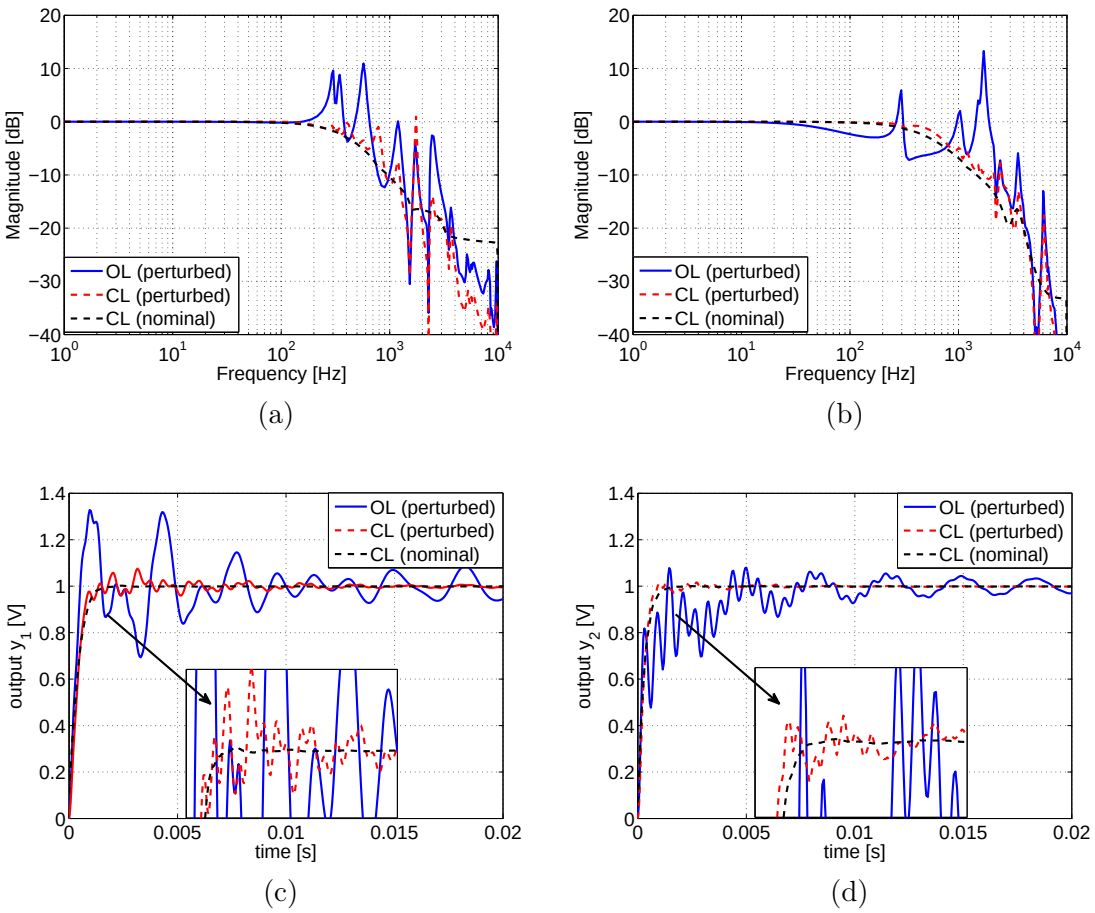


Figure 4.14: Performance of SISO $H_\infty$ controllers: a), b) Magnitude response of the system in open-loop and closed-loop (with real and nominal system) for X and Y axis, respectively. c), d) Step response of the system in open-loop and closed-loop (with real and nominal system) for X and Y axis, respectively.

Finally the weighting functions for control moderation were chosen like in (4.40) with the following numerical values for X and Y axes, respectively:

$$n_{u_x} = 1,\ A_{u_x} = 1/10,\ M_{u_x} = 2,\ w_{u_x} = 2\pi \cdot 2000\ rad/s \tag{4.58}$$

$$n_{u_y} = 1,\ A_{u_y} = 1/10,\ M_{u_y} = 2,\ w_{u_y} = 2\pi \cdot 2000\ rad/s \tag{4.59}$$

Final weightings for the sensitivity functions were chosen like in (4.41), (4.42) and (4.43), which means that the numerical values for $A_{\Delta_x}$ and $A_{\Delta_y}$ in (4.53)-(4.54) were reset to the higher value 1/1.5 in order to assure good robustness margins. Now, using mixed sensitivity procedure of Matlab two optimal SISO controllers $C_x(s)$ and $C_y(s)$ were found with their corresponding cost values as follows:

$$\begin{aligned} \gamma_x &= 1.18, \quad \text{for} \quad C_x(s) \\ \gamma_y &= 1.34, \quad \text{for} \quad C_y(s) \end{aligned} \tag{4.60}$$

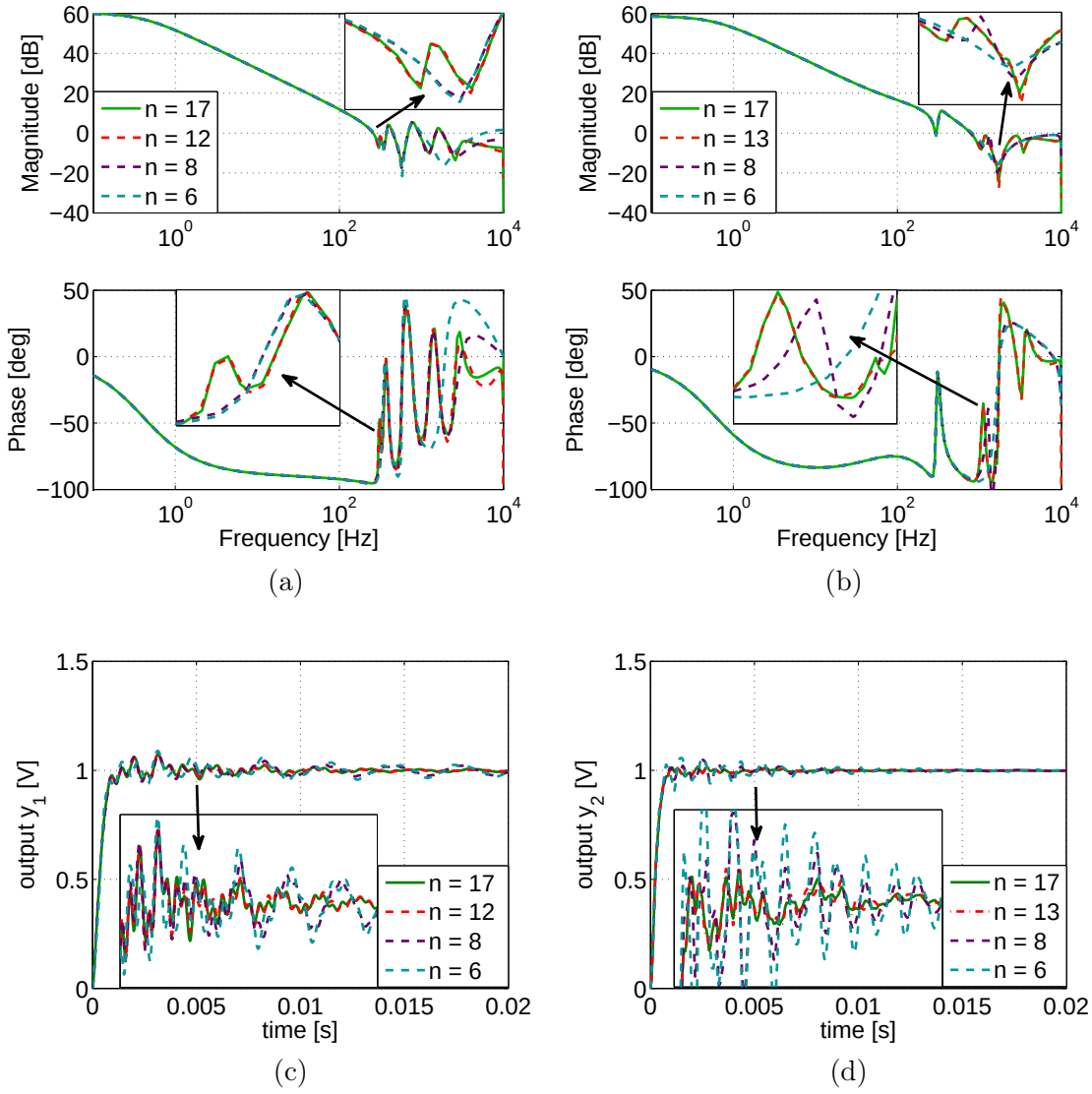


Figure 4.15: Reduction of SISO $H_\infty$ controllers with 17 states: a), b) Frequency response of $n^{th}$ order controller for X and Y axis, respectively. c), d) Step response of the closed-loop system with $n^{th}$ order controller and real system for X and Y axis, respectively.

The obtained values are only slightly greater than one, meaning that our requirements are almost met (more precisely they are met w.r.t. the values (4.60), see also equations (4.49)). Fig. 4.13 shows the sensitivity functions for the obtained controllers $C_x(s)$ and $C_y(s)$ and their corresponding nominal systems $G_{xx}(s)$, $G_{yy}(s)$. One can see that our requirements are more severe for the Y axis. They can be relaxed for both axes in order to obtain the cost functions (4.60) less than one by for example decreasing the required bandwidth. Nevertheless, we are satisfied with the obtained performance (see Fig. 4.14). Figs. 4.14a-4.14b show magnitude plot

of the real plant in open-loop and of both real and nominal plant in closed-loop. One can see that the resonant peaks were successfully damped for both axes and as a result the structural vibration has been significantly reduced as shown in step tracking in Figs. 4.14c-4.14d.

The $H_\infty$ method produces controllers with high order (which is the sum of the order of the plant, on the basis of which the controller has been computed, and the orders of the weighting functions). In our case this order is $17^{\text{th}}$ for each axis and it can be reduced using for example balanced truncation method (like previously for the plant model reduction). The frequency response of the full- and reduced-order SISO controllers are shown in Fig.4.15a (for the X axis) and Fig.4.15b (for the Y axis) and their corresponding step reference tracking performance is shown in Fig. 4.15c and Fig. 4.15d. One can see that significant controller reduction can be achieved (with almost no performance deterioration for $12^{\text{th}}$- and $13^{\text{th}}$-order and with some performance deterioration for $8^{\text{th}}$- and $6^{\text{th}}$-order). We will keep $12^{\text{th}}$-order for the X axis and $13^{\text{th}}$-order for the Y axis (the same order as for the obtained LQG/LTR controllers in the previous sections in order to compare them at the end of this chapter). If lower performance is required the low-order controllers can be chosen.

### 4.4.3 MIMO design

The Mixed sensitivity problem is similar as for the SISO case, with this difference that the measure of the gain of the system at each frequency are the singular values of this system. They are satisfactory definition of gain (range of gain) for a matrix transfer function (see [Skogestad and Postlethwaite, 2005]). For MIMO transfer matrix $\boldsymbol{H}(s)$ the $\mathcal{H}_\infty$ norm is defined as follows:

$$||\boldsymbol{H}||_\infty \stackrel{\text{def}}{=} \max_\omega \bar{\sigma}(\boldsymbol{H}(j\omega)) \geq \bar{\sigma}(\boldsymbol{H}(j\omega)), \tag{4.61}$$

where $\bar{\sigma}(\boldsymbol{H}(j\omega))$ denote maximum singular value of $\boldsymbol{H}(s)$.
By multivariable transfer function shaping we understand the shaping of singular values of appropriately specified transfer functions. For the mixed sensitivity problem (4.32) the MIMO counterpart is given as follows:

$$\begin{aligned} ||\boldsymbol{W}_S(j\omega)\boldsymbol{S}(j\omega)||_\infty &< \gamma \\ ||\boldsymbol{W}_T(j\omega)\boldsymbol{T}(j\omega)||_\infty &< \gamma \\ ||\boldsymbol{W}_R(j\omega)\boldsymbol{R}(j\omega)||_\infty &< \gamma \end{aligned} \tag{4.62}$$

where $\boldsymbol{S}(s)$, $\boldsymbol{T}(s)$, $\boldsymbol{R}(s)$ are sensitivity functions matrices and $\gamma$ is a cost value of the optimization procedure. Using (4.61), the conditions (4.62) can be expressed as follows:

$$\begin{aligned} \bar{\sigma}(\boldsymbol{S}(j\omega)) &< \gamma\bar{\sigma}(\boldsymbol{W}_S^{-1}(j\omega)) \\ \bar{\sigma}(\boldsymbol{R}(j\omega)) &< \gamma\bar{\sigma}(\boldsymbol{W}_R^{-1}(j\omega)) \\ \bar{\sigma}(\boldsymbol{T}(j\omega)) &< \gamma\bar{\sigma}(\boldsymbol{W}_T^{-1}(j\omega)) \end{aligned} \tag{4.63}$$

For comparison reason, the same requirements and thus the same weighting functions were considered as in SISO $H_\infty$ approach. The mixed sensitivity procedure gave the cost value

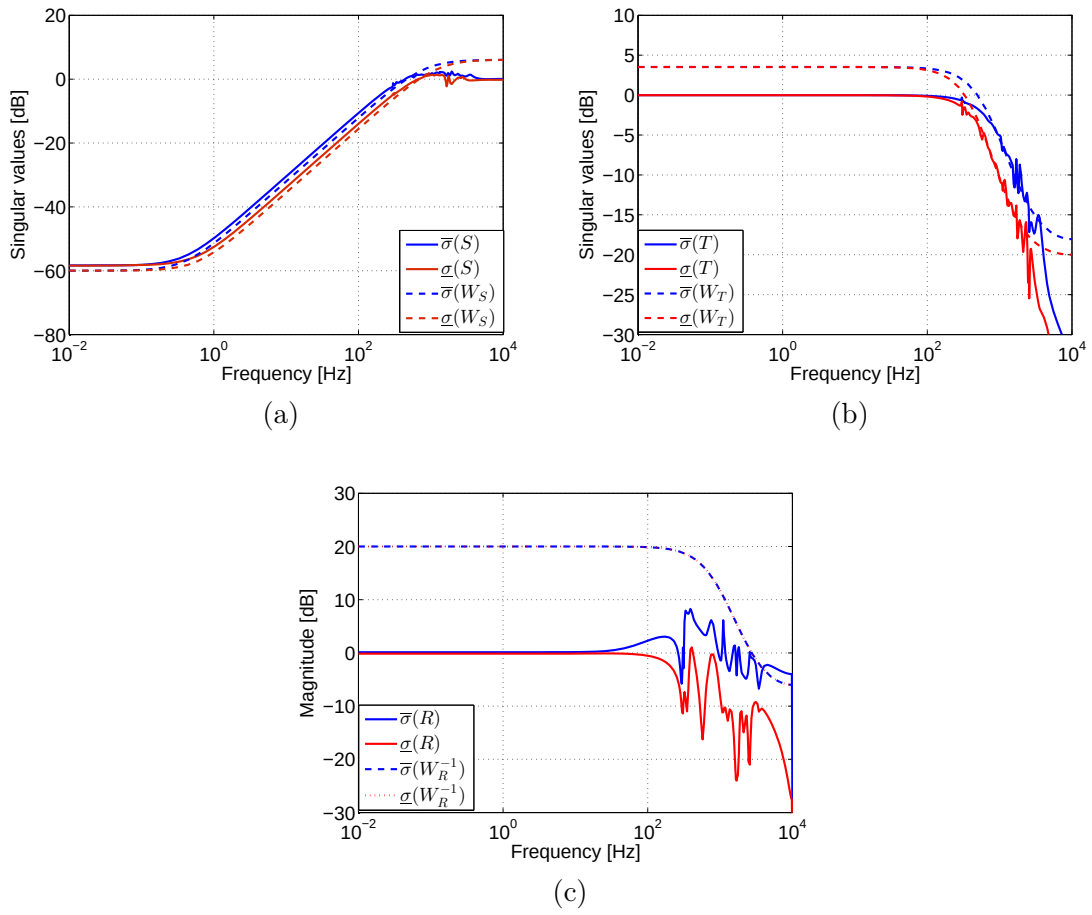


Figure 4.16: Frequency response of an open-loop and closed-loop perturbed system for different control approaches for structural vibration reduction.

$\gamma = 1.38$. This means that the requirements were almost met as seen in Fig.4.16, showing the singular values of the sensitivity functions and the singular values of their corresponding weightings. The order of the obtained sub-optimal centralized TITO controller is 54 (which is the sum of the orders of four subsystems $G_{xx}$, $G_{yy}$, $G_{xy}$, $G_{yx}$) and the used weighting functions. This order can be finally reduced using balanced truncation method resulting in $30^{\text{th}}$-order controller.

To compare all of the considered control approaches for structural vibration reduction, the SISO decentralized controllers obtained via LQG/LTR and $H_\infty$ procedures are compared together with MIMO $H_\infty$ centralized controller for control of the TITO plant $G_p(s)$ as shown in Fig.4.17. Fig. 4.18 and Fig. 4.19 show the frequency response of the system in open-loop and closed-loop when different controllers are used with the nominal and perturbed plant, respectively. For the diagonal parts of the TITO model, $H_\infty$ SISO approach give slightly better results than SISO LQG/LTR approach, but both of them do not reduce cross-couplings (the off-diagonal parts of the model), being however still better than in open-loop.

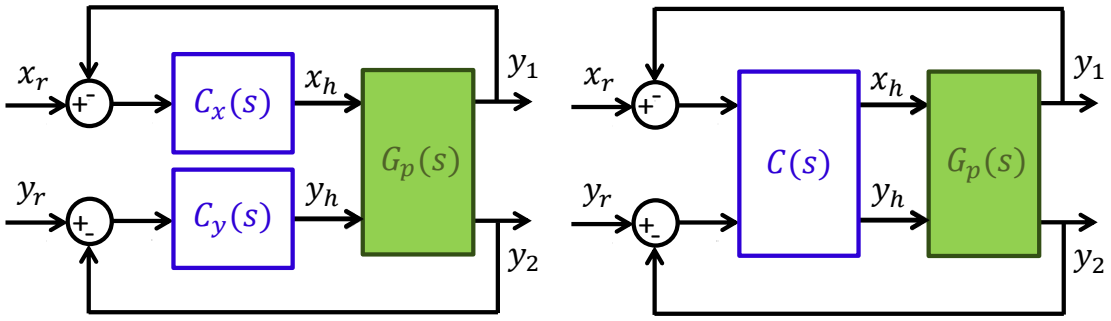


(a) (b)

Figure 4.17: Closed-loop controlled TITO system: a) SISO control. b) MIMO control.

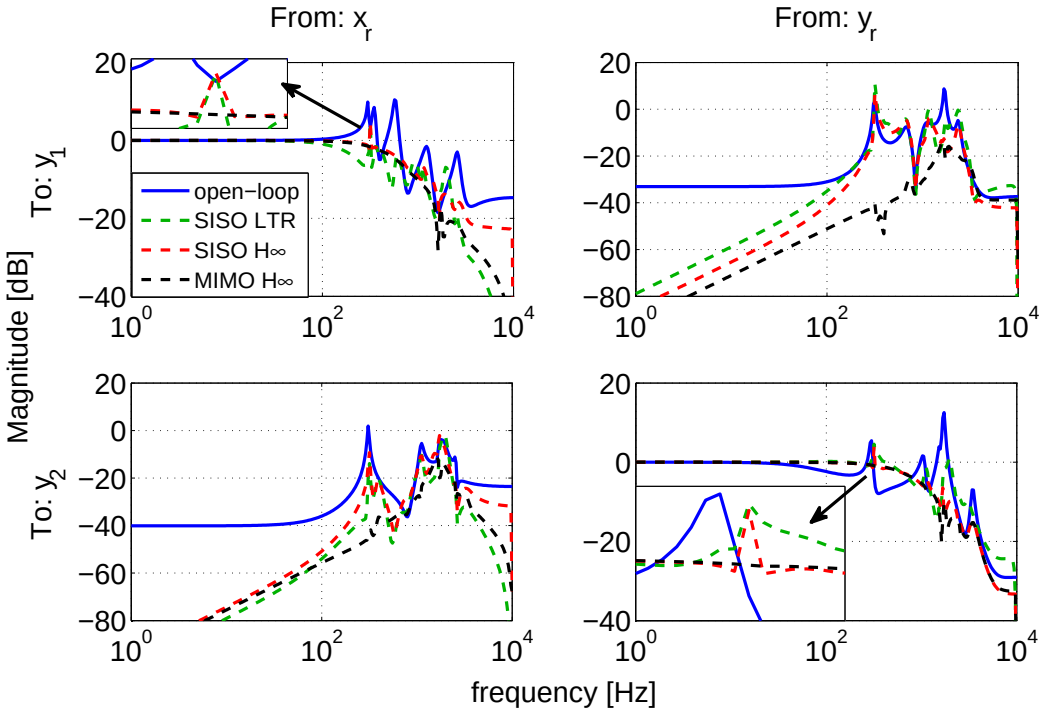


Figure 4.18: Frequency response of an open-loop and closed-loop nominal system for different control approaches for structural vibration reduction.

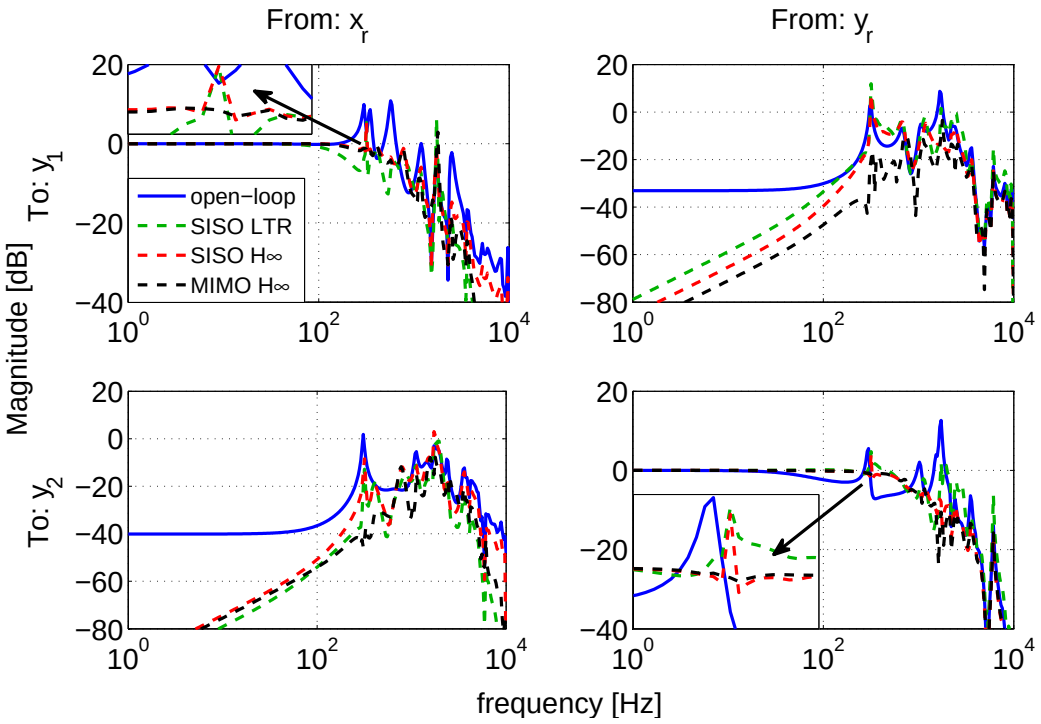


Figure 4.19: Frequency response of an open-loop and closed-loop perturbed system for different control approaches for structural vibration reduction.

Moreover, because of coupling phenomena one can see the undesirable peaks even in the diagonal parts (see the insets in Fig. 4.18 and Fig. 4.19). One can clearly see that $H_\infty$ MIMO approach outperforms other approaches and successfully reduce the resonant peaks for both direct models and couplings.

Tracking the step reference of 1 V for the real system and the considered approaches is shown in Fig. 4.20 when one axis (either X or Y) is excited in the same moment. One can see that all of the approaches successfully reduce the structural vibrations w.r.t. the open-loop case. The performance of $H_\infty$ SISO and $H_\infty$ MIMO controllers is comparable for the diagonal parts and better than in case of SISO LQG/LTR controllers, however only MIMO approach deals with cross-coupling phenomena. Fig. 4.21 shows the step responses when both X and Y axes are excited in the same moment (each response is the sum of the responses of the diagonal part and the corresponding coupling) showing the effect of coupling directly on the diagonal responses and the superiority of MIMO approach over the other ones.

## 4.5 Conclusion

The MIMO approach outperforms the SISO approach while controlling the MIMO plant, since it takes into account the whole model including cross-coupling between the axes. The $H_\infty$ control appears to give better results than classical LQG/LTR approach, since by properly

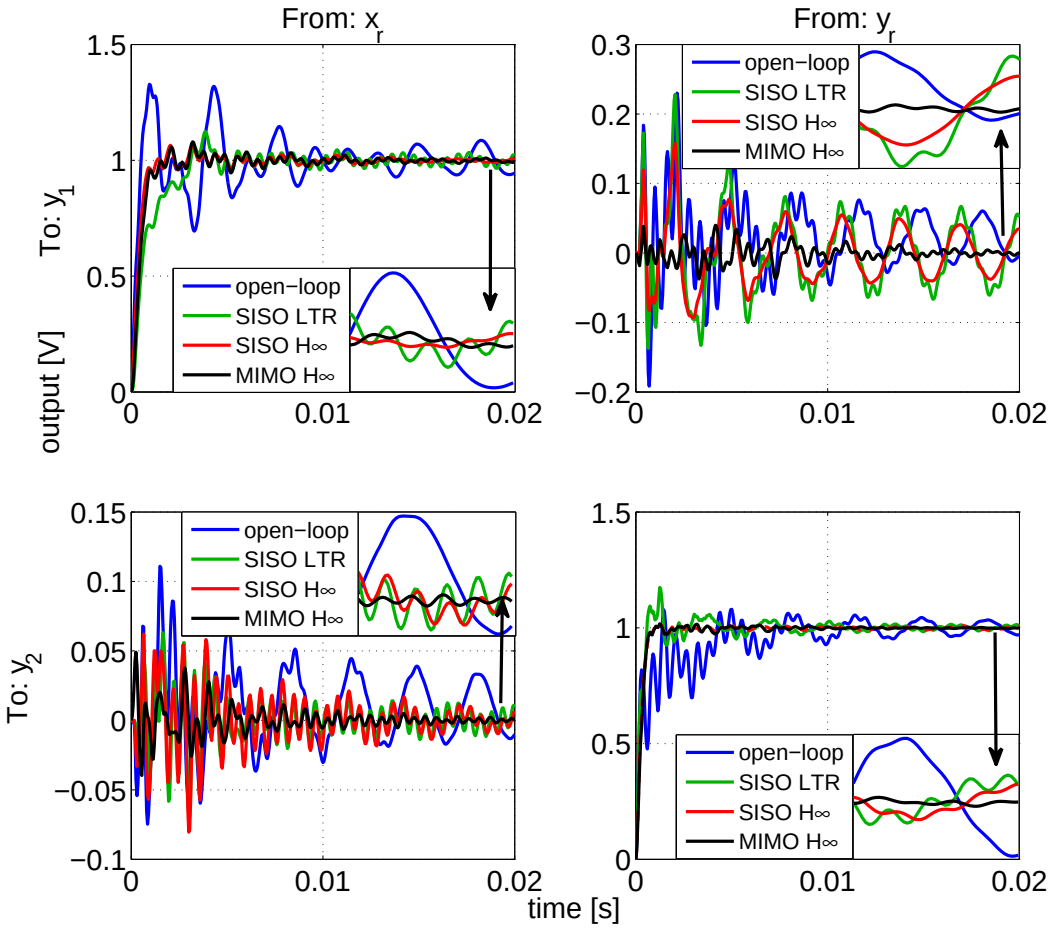


Figure 4.20: Step response of an open-loop and closed-loop real system for different control approaches for structural vibration reduction when only one axis is excited at the same time.

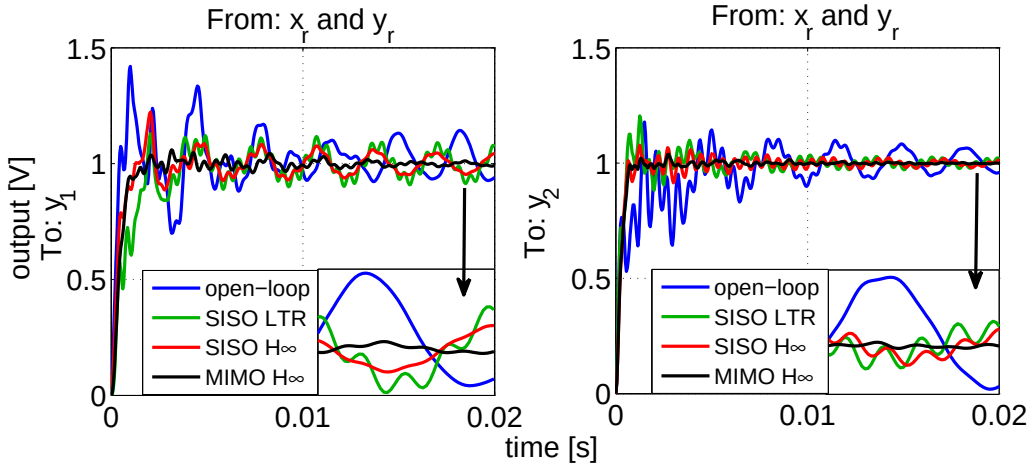


Figure 4.21: Step response of an open-loop and closed-loop real system for different control approaches for structural vibration reduction when only one axis is excited at the same time.

designed weighting functions, it can assure more gain at low frequencies, while rolling-offs the higher-frequency part. The classical LQG/LTR has less degrees of freedom in loop-shaping design - *i.e.* the loop is shaped by properly chosen either Kalman Filter covariance matrices (in case of recovery at the plant output) or LQR weightings (in case of recovery at the plant input) and the recovery part is done automatically. However these design parameters are the same for all frequencies and if the model is uncertain, choosing a "high-gain" controller will excite higher frequency part, and thus we have to limit the desired bandwidth. There exist of course non-classical methods, like frequency-based LQG, where the weighting matrices are frequency-dependent, but the classical LQG/LTR approach assumes one shot parameters while $H_\infty$ loop-shaping does not. On the other hand the latter method produces controllers of high order (which is the sum of the order of the plant and order of the weighting functions) and subsequent model reduction is needed. The existence of weighting functions makes the tuning procedure more difficult, however more degrees of freedom allow to shape the loop closer to the desired one. The last issue is whether MIMO control is really worth of consideration. If the MIMO plant is strongly non-diagonal (*i.e.* with significant cross-couplings) the approach may be interesting, provided that a precision plays more important role than the required hardware resources and if the designed controller will fit to the hardware limitations. If this is not the case or the cross-couplings are not significant the SISO approach can be more satisfactory.

Chapter 5

# Tunneling current

Contents



## 5.1 Introduction

In chapter 2 the tunneling phenomenon has been described in details. It has been shown that this quantum phenomenon takes place when a conductive tip approaches a conductive surface at a distance lower than 1 nm and when these metals are biased w.r.t. each other with constant voltage $V_b$. This chapter is focused on the issues connected with this phenomenon which is a heart of the experimental platform of GIPSA-lab. The general block scheme of the nonlinear plant in Z direction is shown in Fig. 5.1. The focus is given to the tunneling current phenomenon, hence the cantilever model is not taken into account in this section (its displacement is replaced by the surface variations $z_s(t)$). The cross-couplings from the horizontal axes are not considered here either. The tunneling tip is approaching the fixed part

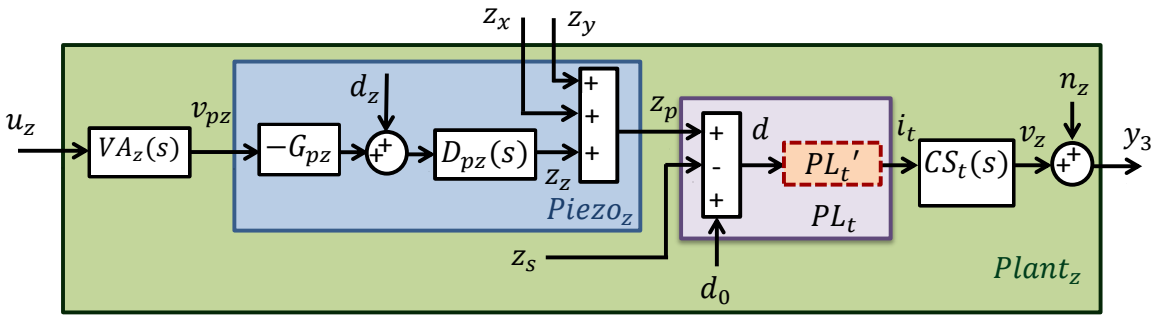


Figure 5.1: Block scheme of nonlinear plant in vertical Z direction.

of the cantilever (surface). The nonlinear model is first identified and linearized around an equilibrium point, then a robust pole-placement controller with sensitivity functions shaping with RS structure is designed using the framework described in details in [Landau and G., 2006] and applied to our experimental platform (as in [Ryba et al., 2014a]).

## 5.2 Nonlinear and linearized model

In chapter 2 the full nonlinear model in 3 dimensions has been developed. Taking into account differential equations for the vertical direction from the input $u_z(t)$ to the output $y_3(t)$ from (2.51), without taking into account the couplings from the horizontal axes ($z_x(t)$ and $z_y(t)$), one obtains the following nonlinear state-space model:

$$\begin{cases} \dot{x}_{1,vz}(t) = -\omega_{vz} x_{1,vz}(t) + u_z(t) \\ \dot{x}_{1,pz}(t) = x_{2,pz}(t) \\ \dot{x}_{2,pz}(t) = -\omega_{pz}^2 x_{1,pz}(t) - 2\xi_{pz}\omega_{pz} x_{2,pz}(t) + \omega_{pz}^2(-G_{pz}G_{vz}\omega_{vz} x_{1,vz}(t) + d_z(t)) \\ \dot{x}_{1,t}(t) = x_{2,t}(t) \\ \dot{x}_{2,t}(t) = -\omega_t^2 x_{1,t}(t) - 2\xi_t\omega_t x_{2,t}(t) + \omega_t^2 G_t g V_b e^{-k(d_0 + x_{1,pz}(t) - z_s(t))} \\ y_3(t) = x_{1,t} + n_3(t) \end{cases} \tag{5.1}$$

We can recall that the first equation of (5.1) represents first order model of the voltage amplifier described by the following transfer function:

$$VA_z(s) = \frac{v_{pz}(s)}{u_z(s)} = \frac{G_{vz}\omega_{vz}}{s + \omega_{vz}} \tag{5.2}$$

The effect of hysteresis in the vertical direction is negligible and the creep phenomenon is considered as a disturbance $d_z(t)$, which can be eliminated in the feedback loop. Hence, the piezoelectric actuator (second and third equations of (5.1)) is expressed as the following linear system:

$$Piezo_z(s) : \frac{z_p(s)}{v_{pz}(s)} = -G_{pz}D_{pz}(s) = \frac{-G_{pz}\omega_{pz}^2}{s^2 + 2\xi_{pz}\omega_{pz}s + \omega_{pz}^2} \tag{5.3}$$

The last three equations of (5.1) describe the physical law subsystem $PL_t'$ (see Fig. 5.1) together with the current sensor $CS_t(s)$. The source of nonlinearity of (5.1) is the exponential dependency of the tunneling current on the distance $d(t) = d_0 + z_p(t) - z_s(t)$, when this distance is less than 1 nm and the constant bias voltage $V_b$ is applied between the tip and the surface:

$$i_t(t) = \begin{cases} gV_b e^{-kd(t)} & \text{if } 0 < d(t) \leq 1\,\text{nm} \\ 0 & \text{if } d(t) > 1\,\text{nm} \end{cases} \tag{5.4}$$

The small value of tunneling current is finally amplified by the high-gain current sensor:

$$CS_t(s) = \frac{v_z(s)}{i_t(s)} = \frac{G_t\omega_t^2}{s^2 + 2\xi_t\omega_t + \omega_t^2} \tag{5.5}$$

The numerical parameters used for the model described in this chapter are summarized in Table 5.1. The constant parameter values of $k = 1.65$ Å$^{-1}$ and $g = 0.0011$ were experimentally

Table 5.1: System parameters for the vertical system.

| | | |
|---|---|---|
| $\omega_{vz}$ | Voltage amplifier bandwidth | 4 kHz |
| $G_{vz}$ | Voltage amplifier gain | 15 V/V |
| $\omega_{pz}$ | Piezoactuator bandwidth | 120 kHz |
| $G_{pz}$ | Piezoactuator gain | 1.2 nm/V |
| $\xi_{pz}$ | Piezoactuator damping | 0.9 |
| $\omega_t$ | Current sensor bandwidth | 13 kHz |
| $G_t$ | Current sensor gain | $10^9$ V/A |
| $d_0$ | Initial distance tip/surface | 1 nm |
| $V_b$ | Bias voltage | 1.025 V |
| $g$ | Tunneling current constant 1 | 0.0011 |
| $k$ | Tunneling current constant 2 | 1.65 $Å^{-1}$ |
| $i_{eq}$ | Equilibrium tunneling current | 1 nA |
| $d_{eq}$ | Equilibrium distance tip/surface | 8.4 Å (angstroms) |
| $m_e$ | Electron mass | $9.109 \cdot 10^{-31}$ kg |
| $e$ | Electron charge | $1.602 \cdot 10^{-19}$ C |
| eV | Electronvolt | $1.602 \cdot 10^{-19}$ J |

found by fitting the nonlinear function $i_t(t) = gV_b e^{-kd(t)}$ to the experimental data as shown in Fig. 5.2. For identification purpose it was assumed that the tunneling current appears

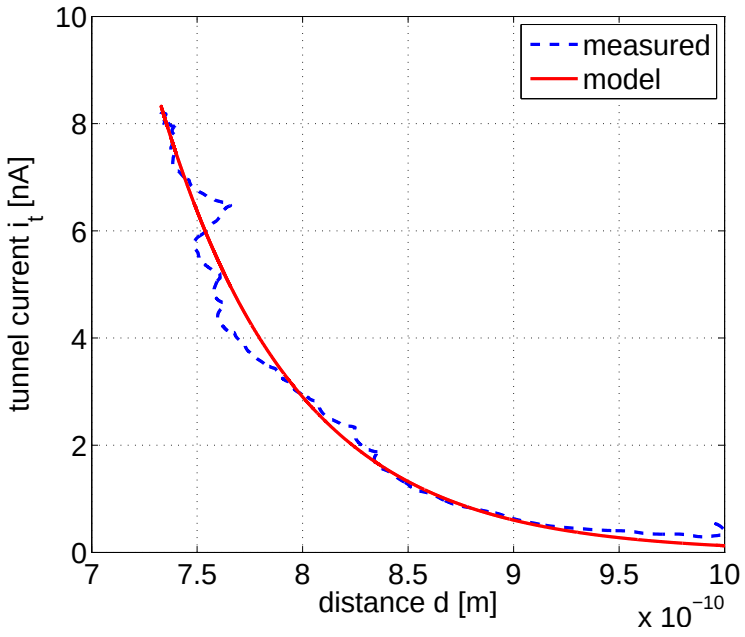


Figure 5.2: Fitting the model (solid-red) $i_t = gV_b e^{-kd}$ to the experimental data (dashed-blue).

when the distance is less than 1 nm. The data used for identification are the output from the current sensor $y_3(t)$ and the piezo control voltage $u_z(t)$. Since the hysteresis phenomenon is negligible for such small piezo displacement $z_p(t)$, the latter can be deduced from the control

signal (knowing the piezo gain $G_{pz}$). The tip moves slowly towards the surface and when the tunneling current appears, the control voltage is set to zero, which corresponds to the initial distance $d_0 = 1$ nm. Since the obtained data are quite noisy, they are smoothed using the moving average method before the curve fitting. Fig. 5.2 shows that this fitting is quite well, which proves the exponential behavior of the tunneling nonlinearity. From chapter 2, $k = c_e\sqrt{\phi}$, where $c_e = 2\sqrt{2m_e}/\hbar = 1.02^{-1}/(\text{eV})^{\frac{1}{2}} \approx 2.548 \cdot 10^{19}$. The identified value of $k$ corresponds to the effective work function tip/surface $\phi \approx 4.2$ eV, which is in accordance with the work functions for metals.

The physical law (5.4) is nonlinear and it is linearized around an equilibrium point $(d_{eq}, i_{eq})$ before linear control design. The first order Taylor expansion of (5.4) gives:

$$i_t(t) = i_{eq} + \frac{di_t}{dd}_{|d(t)=d_{eq}}(d(t) - d_{eq}) = i_{eq} - ki_{eq}(d(t) - d_{eq}) \tag{5.6}$$

and subsequently:

$$\Delta i_t = i_t(t) - i_{eq} = -ki_{eq}(d(t) - d_{eq}) = -ki_{eq}\Delta d \tag{5.7}$$

or in terms of transfer function:

$$PL'_t(s) = \frac{i_t(s)}{d(s)} = -ki_{eq} = \frac{i_t(s)}{z_p(s)} = PL_t(s) \tag{5.8}$$

Combining (5.2), (5.3), (5.8), and (5.5) altogether gives:

$$\begin{aligned} G_z(s) = \frac{y_3(s)}{u_z(s)} &= CS_t(s)PL_t(s)Piezo_z(s)VA_z(s) \\ &= \frac{G_t\omega_t^2}{s^2 + 2\xi_t\omega_t + \omega_t^2} ki_{eq} \frac{G_{pz}\omega_{pz}^2}{s^2 + 2\xi_{pz}\omega_{pz}s + \omega_{pz}^2} \frac{G_{vz}\omega_{vz}}{s + \omega_{vz}} \end{aligned} \tag{5.9}$$

The bandwidths of the voltage amplifier, the piezoelectric actuator and the current sensor in the Z axis are equal to 4 kHz, 120 kHz and 13 kHz, respectively. Since, the bandwidth of the open-loop system is determined by the smallest bandwidth among all of its components (in this case voltage amplifier) and the desired closed-loop bandwidth is similar to the one in open-loop (4 kHz), hence in practice both piezoelectric actuator and current sensor can be taken as static gains. Therefore only the dynamics of the voltage amplifier is taken into account for the controller design procedure. For that reason (5.9) reduces to:

$$G_z(s) = \frac{y_3(s)}{u_z(s)} = G_t ki_{eq} G_{pz} \frac{G_{vz}\omega_{vz}}{s + \omega_{vz}} \tag{5.10}$$

## 5.3 Digital control using Pole-placement with sensitivity functions shaping

In this subsection a pole placement with sensitivity functions shaping controller for vertical motion of the tip is designed. In [Ahmad et al., 2012b] it was experimentally shown that this method gives better results than simple PI control. The digital controller has an RS structure

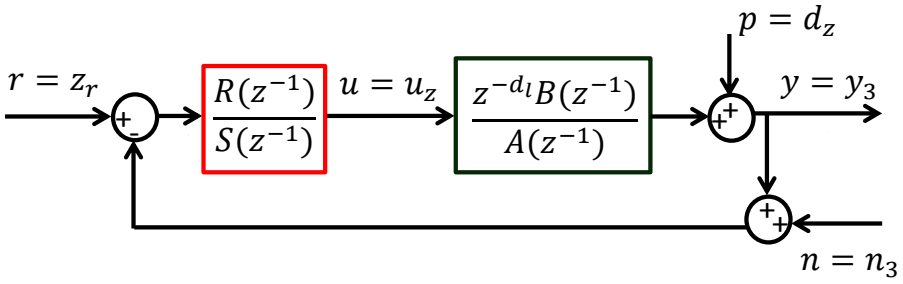


Figure 5.3: Closed-loop digital control system with RS controller.

as described in [Landau and G., 2006] and is shown in Fig. 5.3. The linear continuous-time model (5.10) is first discretized with ZOH giving a discrete-time model used for digital controller design, which can be expressed in the frequency domain as follows:

$$H(z^{-1}) = \frac{z^{-d_l}B(z^{-1})}{A(z^{-1})} \tag{5.11}$$

with $z^{-1}$ variable defined as:

$$z^{-1} = e^{-j\omega} = \cos\,\omega - j\sin\,\omega, \quad \omega = 2\pi\ f/f_s \tag{5.12}$$

where $f/f_s$ is a normalized frequency (w.r.t. the sampling frequency), $d_l$ stands for system pure delay expressed in number of sampling periods, $B(z^{-1}) = b_1 z^{-1} + ... + b_{n_B} z^{-n_B}$, $A(z^{-1}) = 1 + a_1 z^{-1} + ... + a_{n_A} z^{-n_A}$ are polynomials of the numerator and denominator of the plant model, respectively. The closed-loop transfer function (complementary sensitivity function) from the reference $r(t) = z_r(t)$ to the output $y(t) = y_3(t)$ is given by:

$$S_{yr}(z^{-1}) = H_{CL}(z^{-1}) = \frac{z^{-d_l}B(z^{-1})R(z^{-1})}{A(z^{-1})S(z^{-1}) + z^{-d_l}B(z^{-1})R(z^{-1})} \tag{5.13}$$

The aim is to find unknown coefficients of the following controller polynomials:

$$R(z^{-1}) = r_0 + r_1 z^{-1} + ... + r_{n_R} z^{-n_R} \tag{5.14}$$

$$S(z^{-1}) = 1 + s_1 z^{-1} + ... + s_{n_S} z^{-n_S} \tag{5.15}$$

assuming that the plant polynomials $A(z^{-1})$ and $B(z^{-1})$ are known. Desired performances are defined in terms of requirements on the shape of the output sensitivity function (from $p(t) = d_z(t)$ to $y(t) = y_3(t)$) and of the input (control) sensitivity function (from $n(t) = n_3(t)$ or $p(t) = d_z(t)$ to $u(t) = u_z(t)$) defined respectively as follows:

$$S_{yp}(z^{-1}) = \frac{A(z^{-1})S(z^{-1})}{A(z^{-1})S(z^{-1}) + z^{-d_l}B(z^{-1})R(z^{-1})} \tag{5.16}$$

$$S_{un}(z^{-1}) = S_{up}(z^{-1}) = -\frac{A(z^{-1})R(z^{-1})}{A(z^{-1})S(z^{-1}) + z^{-d_l}B(z^{-1})R(z^{-1})} = -\frac{R(z^{-1})}{S(z^{-1})}S_{yp}(z^{-1}) \tag{5.17}$$

Note that:

$$S_{yr}(z^{-1}) + S_{yp}(z^{-1}) = 1 \tag{5.18}$$

The desired closed-loop poles are defined by the polynomial $P(z^{-1})$ given by:

$$P(z^{-1}) = P_D(z^{-1})P_F(z^{-1}) \tag{5.19}$$

where $P_D(z^{-1})$ contains the dominant closed-loop poles (the poles that determine the 'main' dynamics of the closed-loop system) and they are the roots of the denominator of the following discretized normalized continuous-time second-order system:

$$\frac{\omega_0^2}{s^2 + 2\xi\omega_0 s + \omega_0^2} \tag{5.20}$$

with the desired closed-loop bandwidth $\omega_0$ and damping $\xi$. Polynomial $P_F(z^{-1})$ defines auxiliary closed-loop poles that are faster than the dominant poles (*i.e.* they are placed at the frequency higher than $\omega_0/2\pi$).
Now, the controller polynomials (5.14) and (5.15) can be found by solving the following equation (so called "Bezout identity"):

$$P(z^{-1}) = A(z^{-1})S(z^{-1}) + z^{-d_l}B(z^{-1})R(z^{-1}) \tag{5.21}$$

The right part of (5.21) is the denominator of the closed-loop transfer function (5.13) and the left part contains the desired-closed loop poles defined by (5.19).
The controller polynomials (5.14) and (5.15) may contain prespecified fixed parts $H_R(z^{-1})$ and $H_S(z^{-1})$, respectively. Then polynomials $R(z^{-1})$ and $S(z^{-1})$ can be expressed as:

$$R(z^{-1}) = H_R(z^{-1})R'(z^{-1}) \tag{5.22}$$

$$S(z^{-1}) = H_S(z^{-1})S'(z^{-1}) \tag{5.23}$$

From (5.12), $z^{-1} = 1$ for $f = 0$, hence by introducing a fixed part $H_S(z^{-1}) = 1 - z^{-1}$ (which is equal to zero at the zero frequency), one assures zero gain for the output sensitivity function (5.16) at this frequency (since from (5.23) $S(1) = 0$). This implies zero tracking error at the steady-state. Similarly, $z^{-1} = -1$ for the Shannon frequency $f = 0.5f_s$, hence by introducing a fixed part $H_R(z^{-1}) = 1 + z^{-1}$, one assures zero gain for the input sensitivity function (5.17) at this frequency (since from (5.22) $R(-1) = 0$). This implies that the controller does not react to signals close to the Shannon frequency, and the operation is like in open-loop. This is to avoid an actuator stress for high frequencies, where the cascade interconnection actuator-plant has generally low gain (see [Landau and G., 2006]).
Inserting (5.22) and (5.23) into (5.21) gives a new expression of Bezout equation (5.21) (including fixed parts):

$$P(z^{-1}) = A'(z^{-1})S'(z^{-1}) + z^{-d_l}B'(z^{-1})R'(z^{-1}) \tag{5.24}$$

where

$$A'(z^{-1}) = A(z^{-1})H_S(z^{-1}) \tag{5.25}$$

$$B'(z^{-1}) = B(z^{-1})H_R(z^{-1}) \tag{5.26}$$

and the problem boils down to resolution of (5.24) w.r.t. the polynomials $R'(z^{-1})$ and $S'(z^{-1})$. If $A(z^{-1})$ and $B(z^{-1})$ do not have common factors, equation (5.24) has an unique solution

with minimal degree provided that the following constraints on the degree of polynomials are fulfilled:

$$\begin{aligned} n_P &= deg(P(z^{-1})) \leq n_A + n_{H_S} + n_B + n_{H_R} + d_l - 1 \\ n_S &= deg(S(z^{-1})) \leq n_B + n_{H_R} + d_l - 1 \\ n_R &= deg(R(z^{-1})) \leq n_A + n_{H_S} - 1 \end{aligned} \tag{5.27}$$

The details on how to solve (5.24) can be found in [Landau and G., 2006]. Once the polynomials $R'(z^{-1})$ and $S'(z^{-1})$ are found, they are inserted into (5.22) and (5.23), respectively, giving the final RS controller ready for implementation.

In the considered case, using the parameters from Table 5.1, the model after discretization with ZOH defined by (5.11), has the following numerical parameters: $a_1 = -0.2846$, $b_1 = 212.5$, $d_l = 1$. The following characteristics on the designed controller were imposed:
- *Closed-loop dominant poles* $P_D$: Poles placed at frequency $\omega_0 = 2\pi \times 4000\ rad/s$ and with damping $\xi = 0.9$, which corresponds to the highly damped desired system without overshoot and with the closed-loop bandwidth similar to the open-loop one.
- *Closed-loop auxiliary poles* $P_F$: Double high frequency real poles placed at -0.2 to improve the closed-loop robustness without affecting significantly the desired closed-loop performances.
- *Controller fixed part* $H_S$ : $H_S(z^{-1}) = 1 - z^{-1}$, an integrator to assure zero steady-state tracking error and low frequency disturbance rejection.
- *Controller fixed part* $H_R$: $H_R(z^{-1}) = 1 + z^{-1}$, a real zero added at Shannon frequency 0.5 $f_s$ in order to shape the input sensitivity function and to impose an open-loop behavior close to this frequency.
With the above characteristics, the obtained RS controller for the Z axis has the following numerical form:

$$\begin{aligned} R(z^{-1}) &= 10^{-3} \times (1.1634 - 0.8331z^{-1} + 0.3301z^{-2}) \\ S(z^{-1}) &= 1 - 0.6664z^{-1} - 0.0723z^{-2} - 0.2613z^{-3} \end{aligned} \tag{5.28}$$

The closed-loop sensitivity functions of the the model with the designed RS controller are given in Fig. 5.4. From the output sensitivity function, shown in Fig. 5.4a, one can see that at low frequencies the gain is almost zero, which is due to the integral action introduced by the fixed part $H_S(z^{-1})$. The closed-loop system has also a good stability margin ($||S_{yp}(z^{-1})||_\infty < 6dB$). At the Shannon frequency $|S_{yp}(z^{-1})| = 1$ and from (5.18) it follows that $|S_{yr}(z^{-1})| = |H_{CL}(z^{-1})| = 0$, which in turn implies $|S_{up}(z^{-1})| = 0$ at this frequency (see Fig. 5.4b and Fig. 5.4c). This is due to signal blocking at $0.5f_s$, introduced by the fixed part $H_R(z^{-1})$. Finally, Fig. 5.4d shows the step response of the digital control system. The response is without oscillations, due to the high desired damping factor $\xi = 0.9$. The settling time $t_s \approx 0.17$ ms and the obtained closed-loop bandwidth $\omega_{b_{CL}} = 2\pi/t_s \approx 3.7$ kHz, which is close to the open-loop bandwidth $\omega_{b_{OL}} = 4$ kHz (the difference is due to the auxiliary poles added to improve system robustness).

## 5.4 Obtaining tunneling current - experimental validation

In this subsection, the previously designed RS controller is connected with the Z axis of the experimental platform as shown in Fig. 5.5. The procedure for obtaining tunneling current

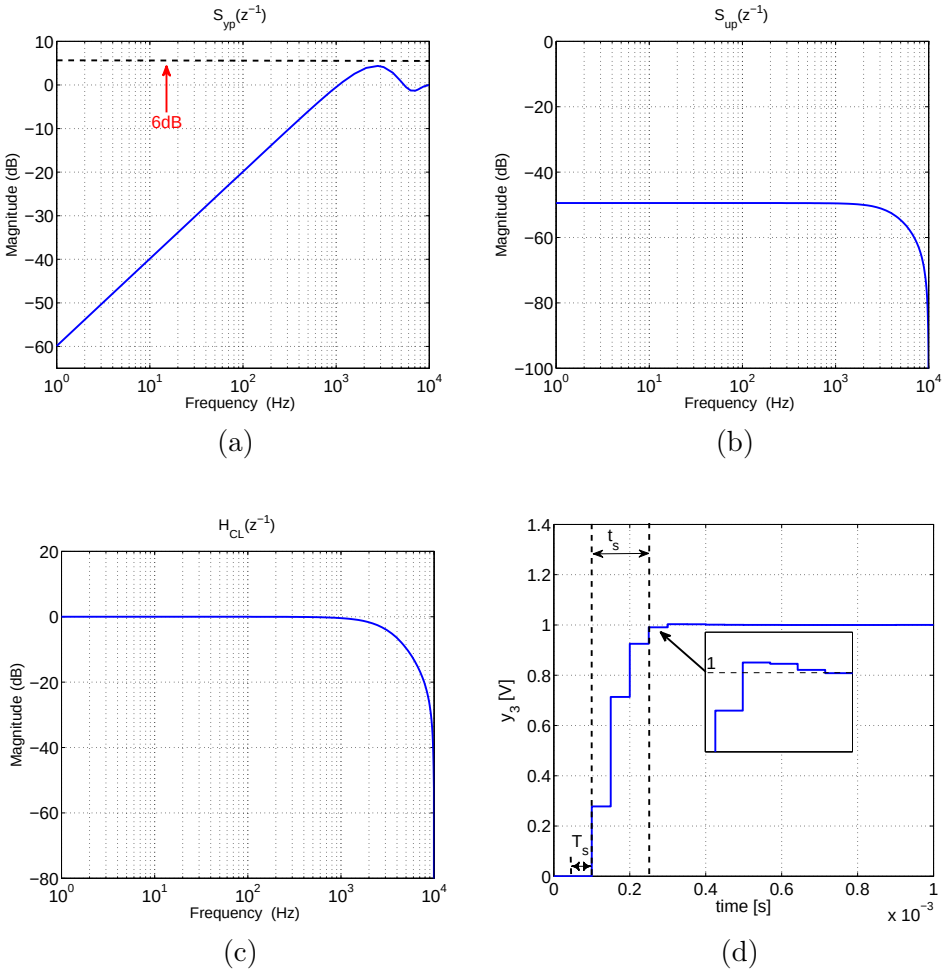


Figure 5.4: Performance of the closed-loop system model with RS controller: a) Output sensitivity function $S_{yp}(z^{-1})$, b) Input (control) sensitivity function $S_{up}(z^{-1})$. c) Closed-loop pulse transfer function $H_{CL}(z^{-1})$ (complementary sensitivity function). d) Step response of the closed-loop system.

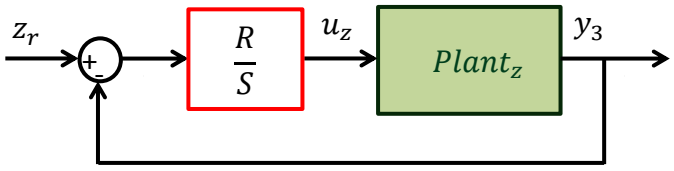


(a)

Figure 5.5: Closed-loop control system with real plant.

consists of two consecutive steps:
- *Manual approach* - During this step (called also a "coarse approach") the tip is approached

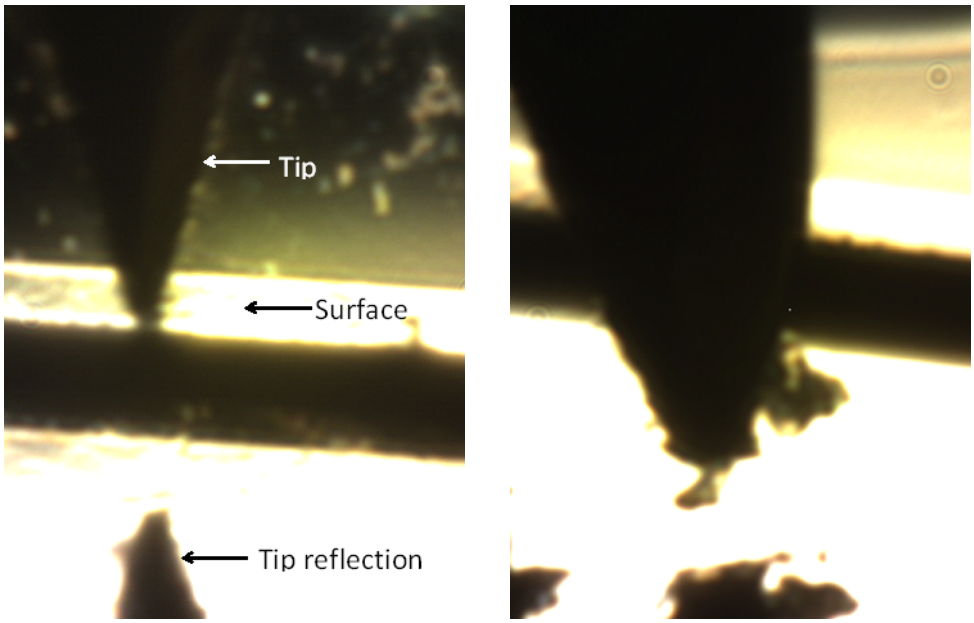


(a) (b)

Figure 5.6: Manual approach (view via high-precision camera): (a) The tip and the surface. (b) Tip deformation after contact with the surface.

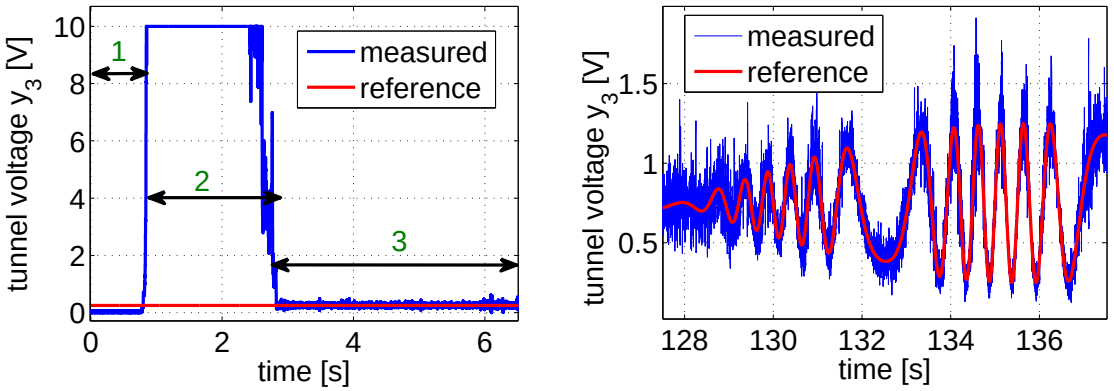


(a) (b)

Figure 5.7: Fine approach and tunneling current control: (a) Fine approach of the tip with tunneling current stabilization, (b) Tracking the sinusoidal reference of tunneling current.

to the surface manually using the micrometer screws until both the tip and the surface are visible through the camera as shown in Fig. 5.6a. Attention must be paid to avoid physical contact between the tip and the surface so as not to crash/deform the tip apex, as shown in Fig. 5.6b, since it can have an adverse influence on the quality of the obtained tunneling current (therefore a sharp tip and a clean surface is usually required).

- *Fine approach* - This step is done in three stages via proper control as shown in Fig. 5.7a.

In the first step, the vertical piezo moves the tip closer to the surface until the tunneling current appears and saturates (1 in the figure). The saturation indicates that the value of the tunneling current is too high to be measured by the card with the range 0-10V. Therefore, in the second stage, the piezo "withdraws" the tip away from the surface and compares the actual value of tunneling voltage with the reference one (imposed by the user) until they are equal (2 in the figure), and if this occurs, the previously designed RS controller is switched on and the loop is closed (3 in the figure). Fig. 5.7a shows the case of tunneling current stabilization around the reference value $z_r$=0.5 V and Fig. 5.7b shows tracking the sinusoidal reference. Despite quite significant noise at such small scale arising mainly from the high-gain current sensor the results are satisfactory. To minimize noise effect, a Faraday cage is used and the presence of the anti-vibration table helps to attenuate external disturbances.

## 5.5 Conclusion

In this chapter, a vertical dynamical model has been examined and used to design a digital controller with a polynomial structure in order to control the tunneling current. To that end, the pole placement with sensitivity functions shaping method has been used. The procedure to obtain the tunneling current has been described and the results for its stabilization and tracking have been presented. The behavior of this current, when positioned in three dimensions is described in the next chapter.

Chapter 6

# 3D results for nanopositioning and STM applications

Contents



## 6.1 Introduction

In this chapter, two kinds of applications are under consideration. In section 6.2 a nanopositioning application in three dimensions is validated experimentally, while in section 6.3 STM-like results (surface reconstruction) are given in simulation. In the first case, the tip is positioned along X, Y, and Z axes using three piezoelectric actuators. At each time instant the tip is moved to the $(x(t), y(t))$ point of the X-Y plane using a prespecified scanning trajectory. In the vertical direction the piezo tracks the prespecified reference signal, which plays the role of "virtual surface". In the second case, the STM application is presented in simulation and two control strategies are settled with a purpose of surface reconstruction. SISO PID decentralized control is first tested, where unlike in the previous case, the tunneling current is kept on a constant level and the surface topography is reconstructed from the control signal of the vertical piezo. Then a multivariable centralized Linear Quadratic Integral (LQI) control is proposed, where the tunneling current is again kept constant and the surface topography is reconstructed via Kalman observer. Various adverse phenomena like tunneling nonlinearity, actuator hysteresis, creep, vibrations and cross-couplings are compensated. Both strategies are compared at the end and the results are presented in the form of 3D and more common 2D images, similar to the ones obtained from STM/AFM. Each value of the tunneling voltage $y_3(t)$ from the current sensor has corresponding points in X-Y plane ($y_1(t)$, $y_2(t)$), expressed

in volts (or $\mu$m) as well (for the horizontal X,Y axes 1V corresponds to the displacement of 5$\mu$m, and for the vertical Z axis 1V corresponds to the tunneling current of 1nA).

To move the tip in X-Y plane, two kinds of scanning trajectories are used: raster and more recent spiral pattern [Mahmood and Moheimani, 2009a], shown in Fig. 6.1. In the raster pattern, a triangle input voltage is used in one (fast) direction (here X, see Fig. 6.1a) and a linear ramp in the other (slow) direction (here Y, see Fig. 6.1c) as follows:

$$x_r(t) = x_{r_0} + A_r \left| 2f_r \left( t - \frac{1}{f_r} \left\lfloor tf_r + \frac{1}{2} \right\rfloor \right) (-1)^{\left\lfloor tf_r + \frac{1}{2} \right\rfloor} \right| \tag{6.1}$$

$$y_r(t) = y_{r_0} + \alpha_r t \tag{6.2}$$

where $x_{r_0}$ and $y_{r_0}$ are the starting points for the signals $x_r(t)$ and $y_r(t)$, respectively, $A_r$, $f_r$ are the amplitude and frequency of the triangle signal, respectively, $\alpha_r$ defines the slope of the ramp signal and the symbol $\lfloor x \rfloor$ represents the floor function of $x$.

The spiral pattern centered at point $(x_{r_0}, y_{r_0})$ is generated by the pair $(r_s(t), \theta_s(t))$ in polar coordinates, where $r_s(t)$ and $\theta_s(t)$ are the instantaneous spiral radius and spiral angle at time $t$, respectively. The following differential equation defines the spiral radius time evolution (see [Mahmood and Moheimani, 2009a]):

$$\frac{dr_s(t)}{dt} = \frac{P_s \omega_s(t)}{2\pi} \tag{6.3}$$

with the angular velocity $\omega_s$ and the spiral pitch $P_s$ given by:

$$P_s = \frac{2R_s}{N_s - 1} \tag{6.4}$$

where $R_s$ is the non-instantaneous spiral radius and $N_s$ is defined as the number of times the spiral curve crosses the line $y(t) = y_{r_0}$ (in Fig. 6.1f $N_s = 8$ and the crossing places are numbered from 1 to 8). Separating variables and integrating both sides of equation (6.3) with $r_s(0) = 0$ gives:

$$r_s(t) = \frac{P_s}{2\pi} \omega_s t \tag{6.5}$$

and the spiral angle at time $t$ is expressed by:

$$\theta_s(t) = \omega_s t \tag{6.6}$$

Since the piezoelectric actuators are moved in X and Y directions, one needs to translate the polar coordinates $(r_s(t), \theta_s(t))$ to the Cartesian ones as follows:

$$x_r(t) = x_{r_0} + r_s(t)\cos\,\theta_s(t) \tag{6.7}$$

$$y_r(t) = y_{r_0} + r_s(t)\sin\,\theta_s(t) \tag{6.8}$$

where $x_{r_0} = x_r(0)$ and $y_{r_0} = y_r(0)$ define a center in the Cartesian space of the spiral reference. This center is chosen such that the whole spiral curve lies in positive quadrant of the Cartesian space, since only the positive input voltages are used.

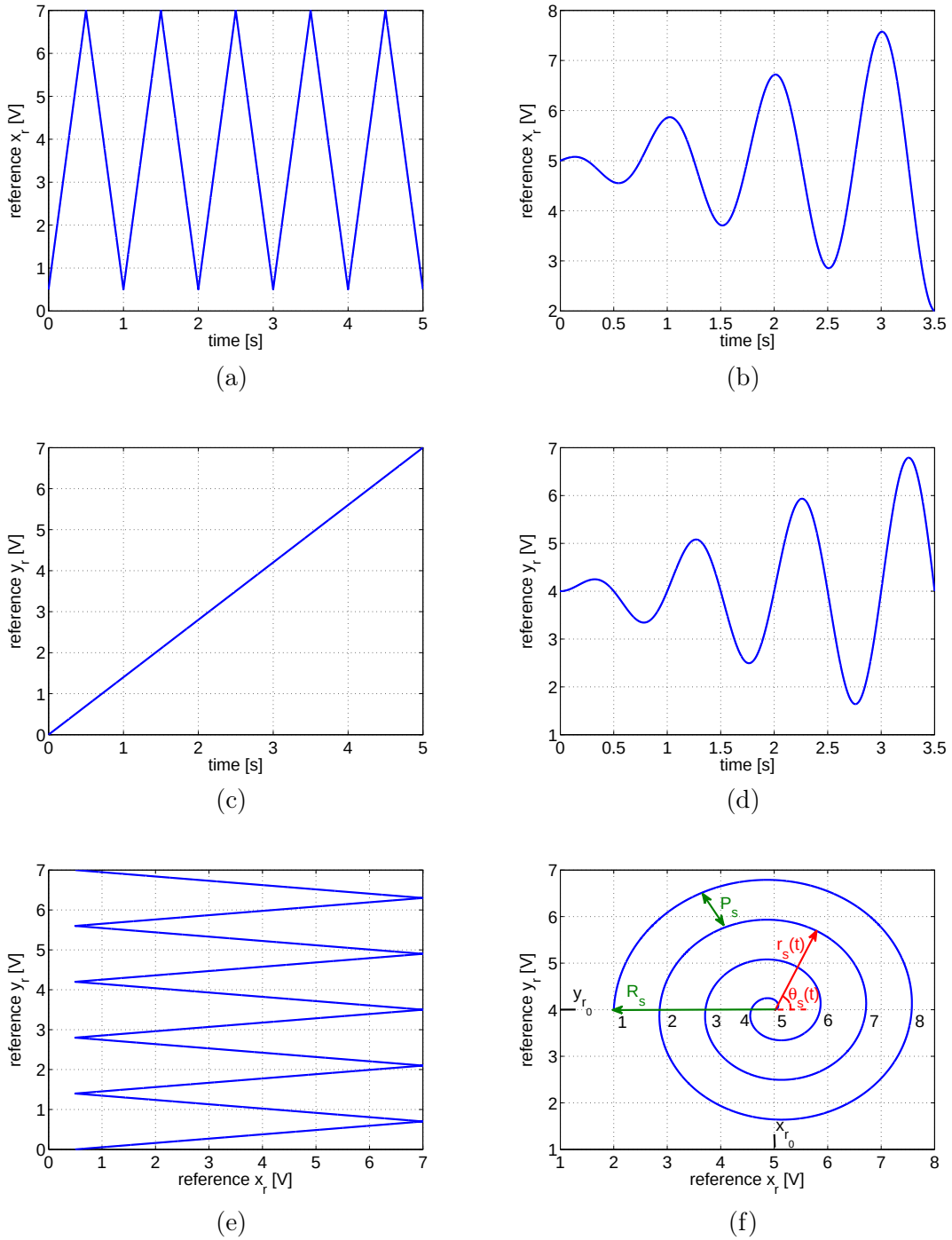


Figure 6.1: Signals used for the raster (left column) and the spiral (right column) pattern generation: (a), (b) Reference $x_r(t)$. (c), (d) Reference $y_r(t)$. (e), (f) Reference pattern in X-Y plane.

## 6.2 Nanopositioning in 3D - experimental validation

In this section the positioning of the tip in three dimensions is validated experimentally. To that end, the 3D STM-like micro/nanopositioning platform developed in GIPSA-lab is used. In the horizontal scanning directions the hysteresis and creep are eliminated using the techniques developed in chapter 3. Due to much smaller displacements, the hysteresis effect in the Z direction is negligible. The performance of open-loop MPI alone, closed-loop DOB alone (based on the affine hysteresis approximation) and a hybrid approach (DOB, based on MPI hysteresis approximation) is compared, while simultaneously controlling the tunneling current in the Z direction, using pole placement controller with sensitivity functions shaping [Landau and G., 2006], [Ahmad et al., 2012b], designed in chapter 5. The scanning frequency in the horizontal X-Y axes is not too high in order not to cause coupling-based positioning errors in the vertical Z axis and not to lose the tunneling current. Future work can be devoted to identify and compensate these couplings. In real STM, the aim is to scan the surface in the X-Y plane and to keep the tunneling current constant (as discussed in simulation in the next section). In this way the surface topography is retrieved via the control signal. Here instead, the "virtual surface" is imposed by the proper reference tunneling voltage $z_r(t)$ tracked while moving in X-Y plane (nanopositioning application).

First test is done using DOB in both horizontal axes in order to eliminate the hysteresis and creep phenomenon and the amplitude of the reference is small, which implies low signal to noise ratio (the noise in the Z direction is reasonably high w.r.t. the amplitude of the reference tunneling voltage). This reference $z_r(t)$ being sinusoidal variations between 0.25 V and 1.25 V (which corresponds to tunneling current $i_t(t)$ between 0.25 nA and 1.25 nA or the distance $d(t)$ between 9.3 Å and 8.3 Å, respectively) is shown in Fig. 6.2a and Fig. 6.2b in 3D and 2D view, respectively. The raster scan is used in X-Y plane - a triangle signal (6.1) of $A_r$ =2 $\mu$m amplitude and slow frequency $f_r$ =0.5 Hz is applied to the piezoactuator in the X direction and a linear ramp signal (6.2) in the Y direction as shown in Fig. 6.1e. In our case both forward and backward movements along the X direction produce a line of the scanned samples, while moving slowly in the Y direction. For the clarity of results the hysteresis and creep are already compensated for the Y axis. 2D and 3D images of the "virtual surface" without creep and hysteresis compensation for X axis for 1 $\mu m$ $\times$1 $\mu$m (0.2 V $\times$ 0.2 V) range are shown in Fig. 6.2c and Fig. 6.2d, respectively and with compensation in Fig. 6.2e and Fig. 6.2f, respectively. The scanning trajectory without and with compensation is shown in Fig. 6.2g and Fig. 6.2h, respectively. The difference between the reference image and the image without compensation can be more pronounced when none of the two axes is compensated. In X-Y plane, the obtained image with observer-based hysteresis and creep compensation resembles the reference one better than wihout compensation (compare Fig. 6.2d and Fig. 6.2f with Fig. 6.2b), however, the vertical resolution can be deteriorated due to the fact that the observers work in a feedback loop, thus the measurement noise can be propagated to the system input. This can be however improved as shown later using a low-pass filter on the observers' output as well as by properly tuned their corresponding covariance matrices. The RS controller tracks the reference tunneling voltage well. However, our lab-made system at ambient conditions has signal-to-noise ratio not as high as commercial STM, especially at this

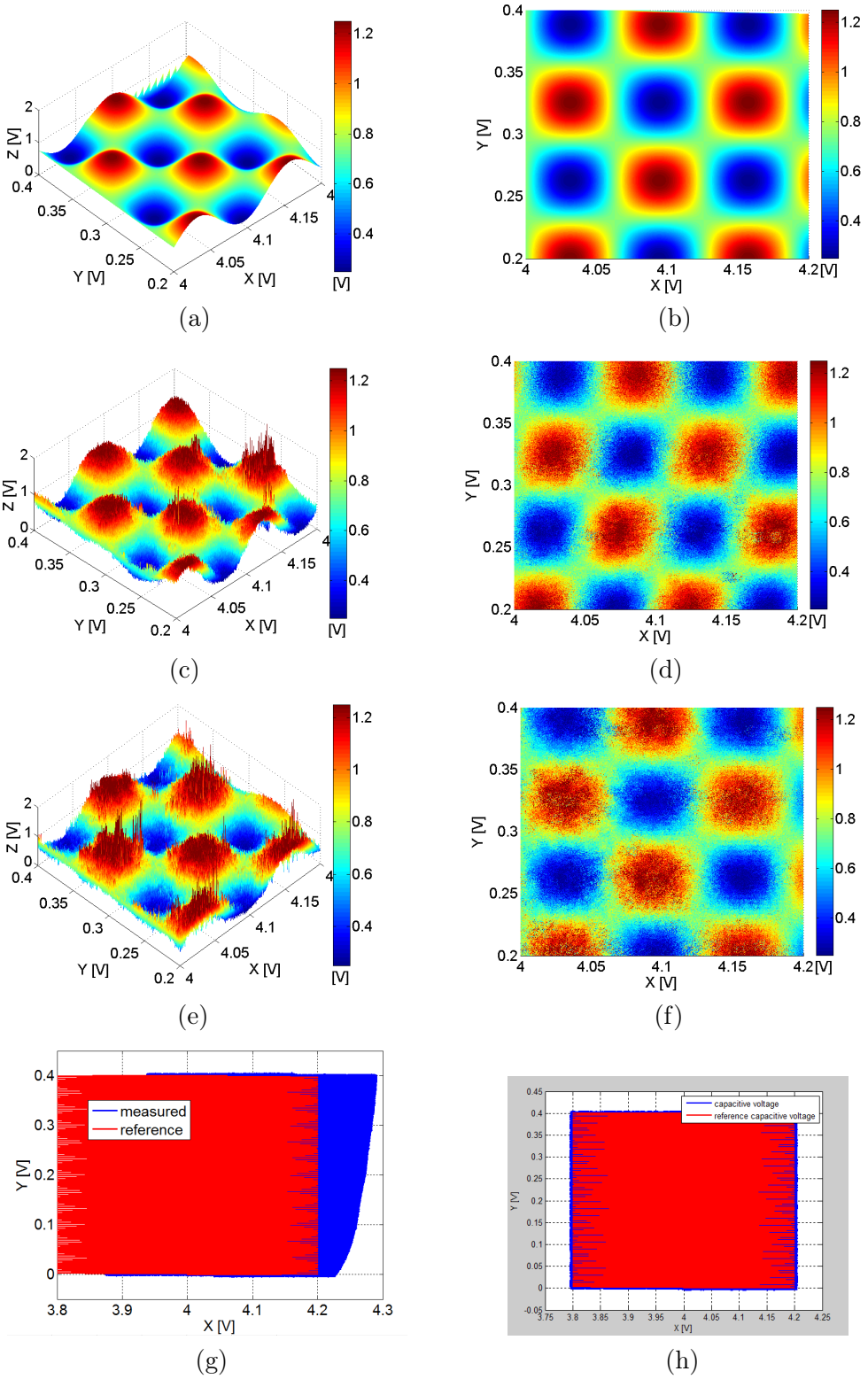


Figure 6.2: Experimental results for 3D operation of the platform and low signal to noise ratio: (a) Reference tunneling current (3D view). (b) Reference tunneling current (2D view). (c) Tunneling current without hysteresis and creep compensation (3D view). (d) Tunneling current without hysteresis and creep compensation (2D view). (e) Tunneling current with hysteresis and creep compensation (3D view). (f) Tunneling current with hysteresis and creep compensation (2D view). (g) X-Y trajectory without hysteresis and creep compensation. (h) X-Y trajectory with hysteresis and creep compensation.

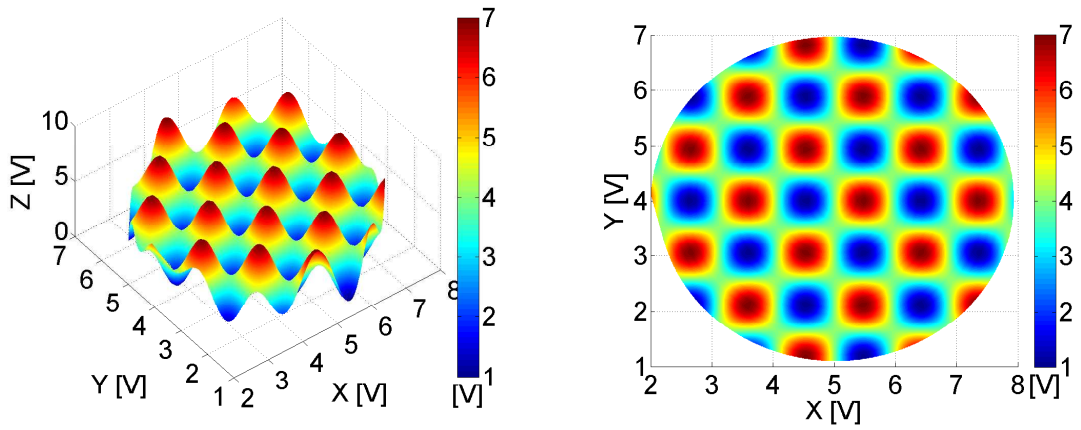


(a) (b)

Figure 6.3: Reference tunneling current: (a) 3D view. (b) 2D view.

Table 6.1: Tracking error-experimental result

| | MPI | | DOB | | MPI+DOB | |
|---|---|---|---|---|---|---|
| | rms ($\mu$m) | max ($\mu$m) | rms ($\mu$m) | max ($\mu$m) | rms ($\mu$m) | max ($\mu$m) |
| 1Hz | 0.0588 | 0.1557 | 0.0042 | 0.0137 | 0.0022 | 0.0074 |
| 10Hz | 0.0964 | 0.2045 | 0.0361 | 0.1334 | 0.0130 | 0.0590 |
| 20Hz | 0.1157 | 0.2390 | 0.0760 | 0.2808 | 0.0274 | 0.1070 |
| 50Hz | 0.1065 | 0.2839 | 0.1884 | 0.5086 | 0.0706 | 0.2490 |

sub-nanoscale. The system is sensitive to external disturbances, which can be sometimes seen as sudden high jumps of the tunneling voltage. Furthermore, an increase of scanning speed in the horizontal axes can cause coupling-based positioning errors in the vertical axis. This makes the control of the all system very challenging.

In the second test, to increase signal to noise ratio, the disturbance observers were "well-tuned" (their covariance matrices were set to give more trust in the model than to the measurement). Moreover, a low pass filter has been added on the observers' output and the amplitude of the reference signal was increased (*i.e.* one may expect to see better the hills and valleys of the signal when its amplitude is increased w.r.t. the noise). The sinusoidal reference $z_r(t)$ between 1 V and 7 V (which corresponds to tunneling current $i_t(t)$ between 1 nA and 7 nA or the distance $d(t)$ between 8.4 Å and 7.3 Å, respectively) is imposed as shown in Fig. 6.3a and Fig. 6.3b in 3D and 2D view, respectively. The aim of this test is to compare techniques for hysteresis and creep compensation developed in chapter 3, namely MPI, DOB and MPI/DOB approaches. The spiral scanning pattern described in section 6.1 is used (see (6.7) and (6.8)) to move the tip in horizontal directions. The tracking of the spiral pattern in X-Y plane for different scanning frequencies $2\pi\omega_s$ is shown in Fig. 6.4. The values of the center of the spiral reference $(x_{r_0}, y_{r_0}) = (5\text{V}, 4\text{V})$ and the non-instantaneous radius $R_s = 3\text{V}$. For the clarity of the presented results, the number of curves $N_s = 8$ (see equation (6.4)) was chosen. The

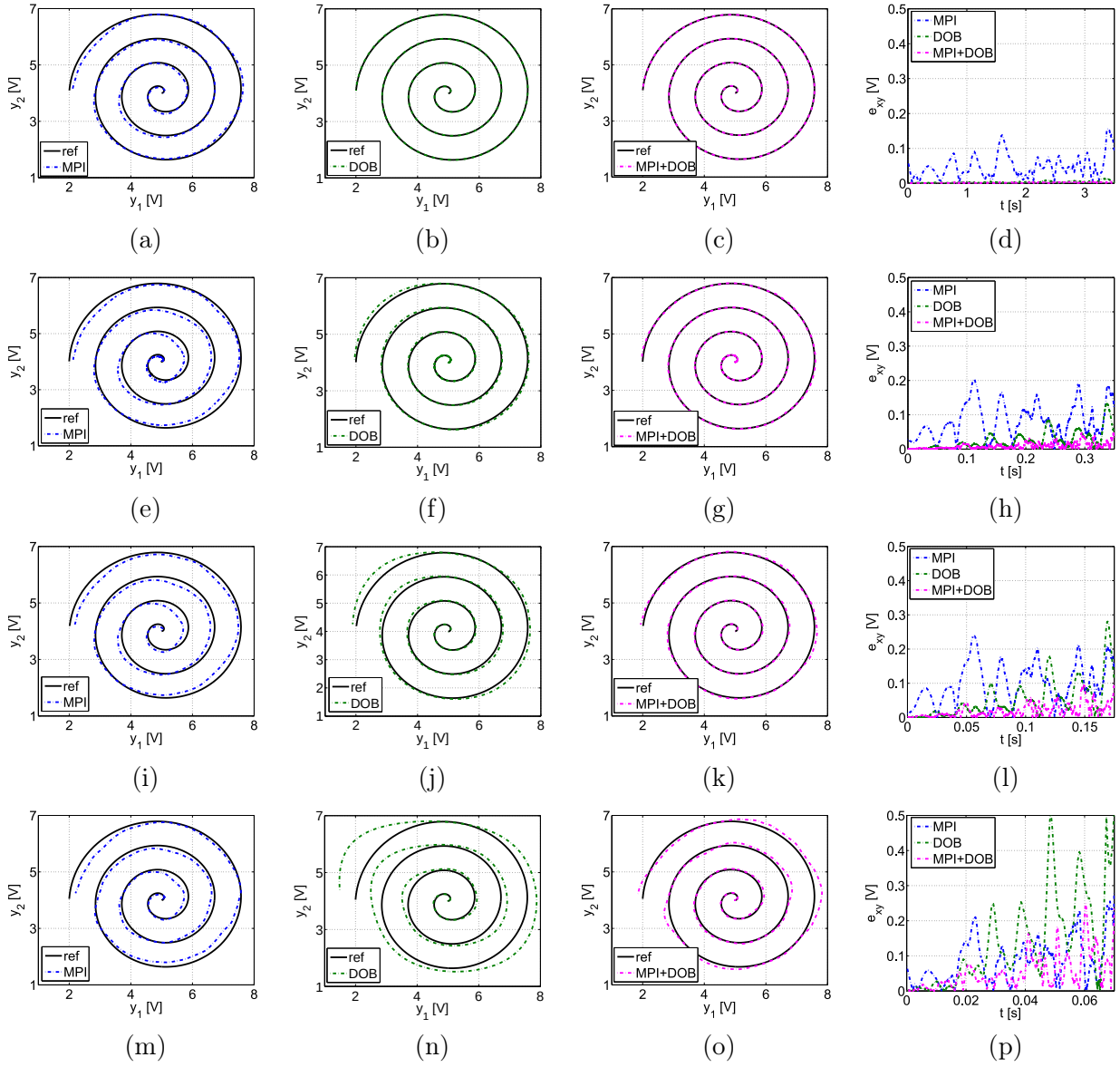


Figure 6.4: Tracking spiral trajectory of frequency $2\pi\omega_s$: (a)-(c) 1 Hz. (e)-(g) 10 Hz. (i)-(k) 20 Hz. (m)-(o) 50 Hz. (d), (h), (l), (p) Corresponding tracking errors.

corresponding RMS and maximal tracking errors are summarized in Table 6.1.

Comparing Fig. 6.4b with Fig. 6.4a and Fig. 6.4f with Fig. 6.4e, one can see the advantage of DOB w.r.t. MPI approach for low frequencies. This is due to the fact that DOB works in closed-loop, while MPI in open-loop. The performance of DOB worsens w.r.t. MPI model when the input frequency is increased (compare Fig. 6.4j with Fig. 6.4i and Fig. 6.4n with Fig. 6.4m). This can be explained by the fact that DOBs are based on low (second) order model and their accuracy for higher frequencies can be improved by increasing this order, which increases the model complexity. The accuracy can be also improved by combining DOB

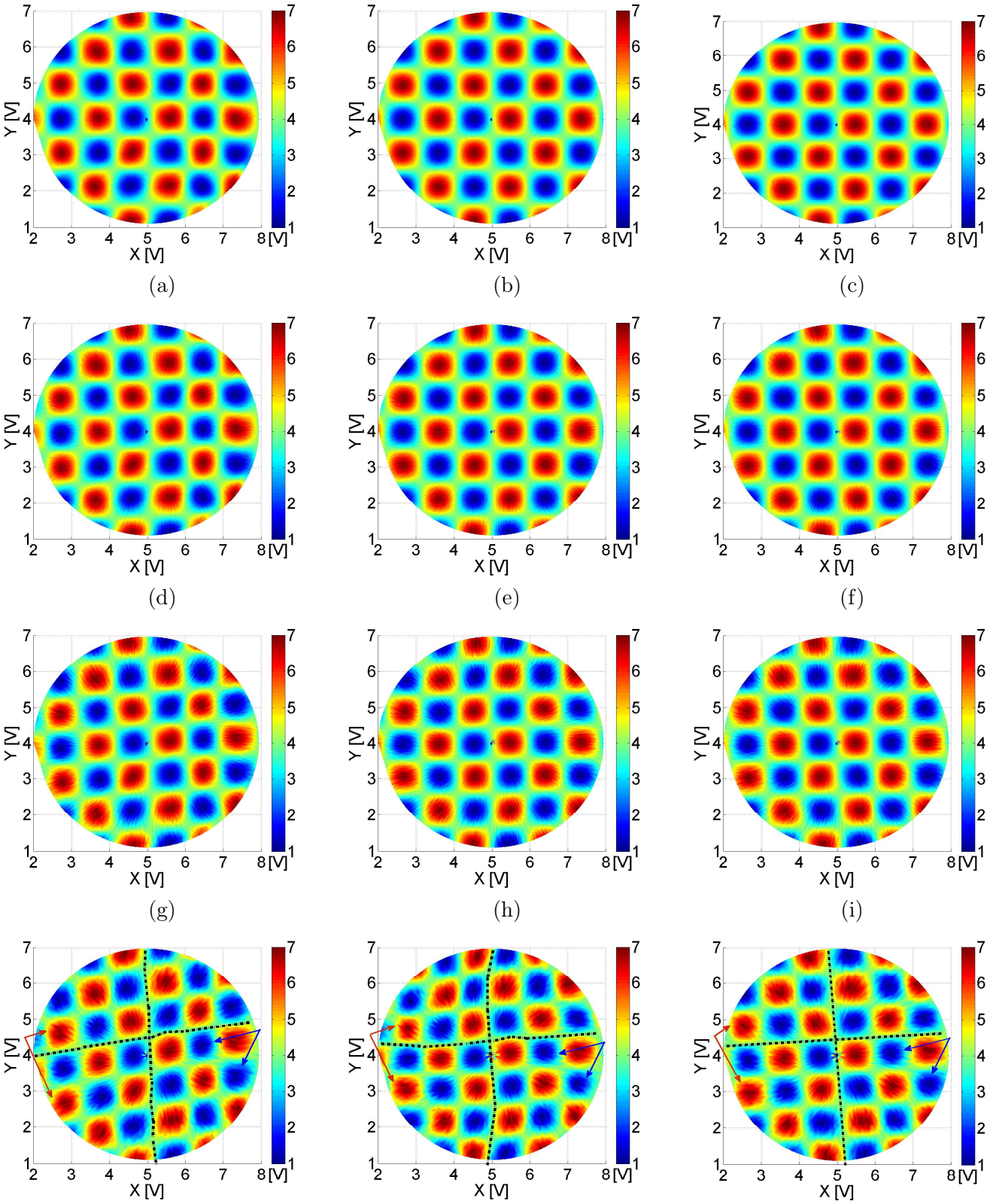


Figure 6.5: Tunneling current obtained using only MPI (left), only DOB (middle) and combined MPI+DOB (right) approach for the scanning frequencies $2\pi\omega_s$: (a)-(c) 1 Hz. (d)-(f) 10 Hz. (g)-(i) 20 Hz. (j)-(l) 50 Hz.

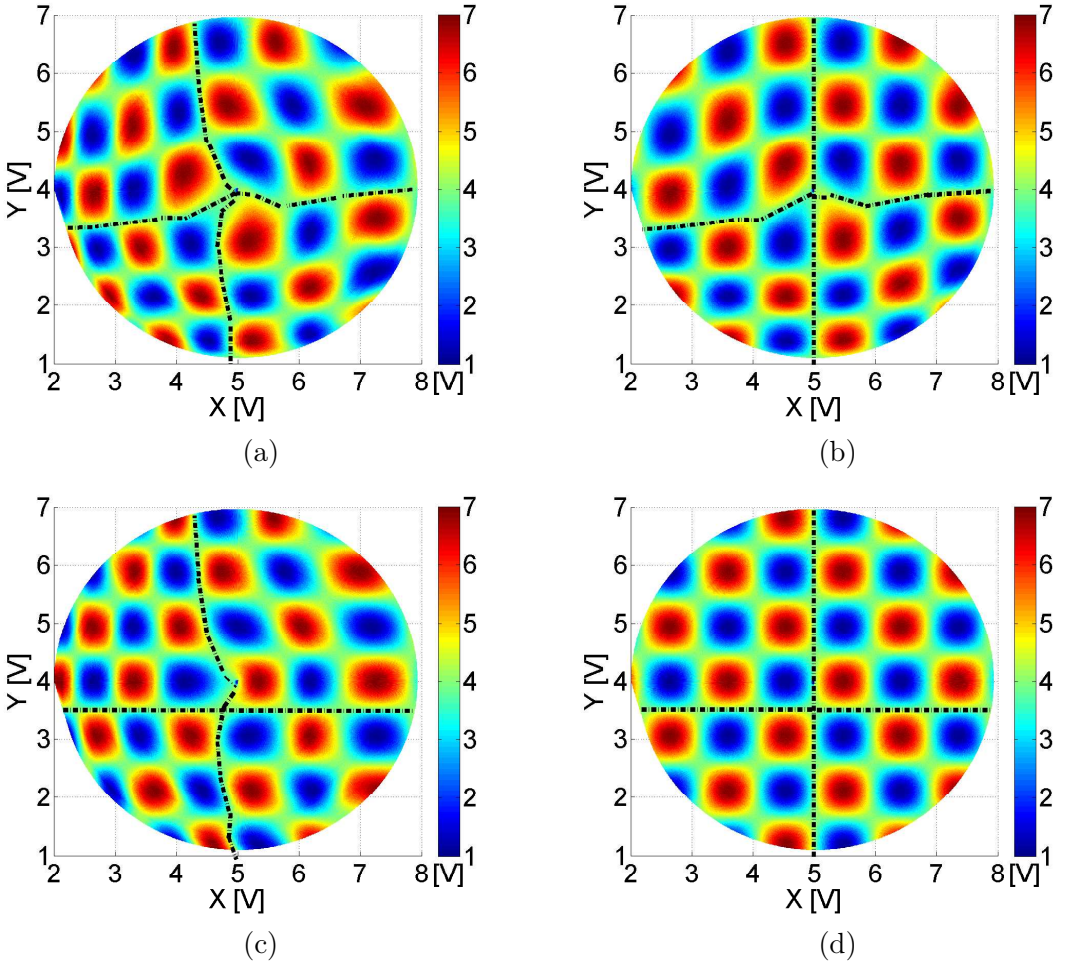


Figure 6.6: Tunneling current obtained for scanning frequency 1 Hz and MPI+DOB. (a) Without any compensation for X and Y axes. (b) With compensation only for X axis. (c) With compensation only for Y axis. (d) With compensation for both X and Y axes.

with MPI, which gives the best performance among all considered configurations as shown in the third column of Fig. 6.4. The last column of Fig. 6.4 shows the corresponding tracking errors. For correct image presentation, the number of curves has to be dense enough and has been increased to $N_s = 50$. The corresponding images of the "virtual surface" in the Z direction for different scanning frequencies are shown in Fig. 6.5. The advantage of hybrid MPI+DOB approach over MPI or DOB alone is visible especially for higher frequencies (see Fig. 6.5j-Fig. 6.5l). The level of deformation/improvement is indicated by dash-dotted lines. The red and blue arrows point at two hills and two valleys, respectively. The MPI model linearizes piezoelectric actuator and improves the performance of low-order observer, while the presence of DOB assures robustness w.r.t. the hysteresis modeling uncertainties and external disturbances. Next, MPI+DOB approach is used for 1 Hz scanning frequency and the result for hysteresis and creep compensation is shown in Fig. 6.6. The adverse phenomena of hysteresis and creep strongly deform the obtained image, when none of the axis is compensated as shown in Fig.6.6a. Fig. 6.6b -Fig. 6.6d show the compensation results only for X axis, only for Y

axis and for both X and Y axes, respectively. One can see that after compensation the details (hills and valleys) of the surface, generated by the tunneling voltage are equalized in terms of shape and size and the obtained image from Fig. 6.6d can be compared with the reference one from Fig. 6.3b.

## 6.3 Surface reconstruction in STM application in simulation

In the previous section, experimental results for nanopositioning in three dimensions were given, where the tunneling current tracked the prespecified reference, called "virtual surface". In this section the STM application is presented in simulation. The tunneling current is kept on a constant level (constant current mode), while simultaneously scanning in X-Y plane. The surface topography is retrieved via control signal in the Z direction. Cross-couplings from the horizontal X and Y axes to the vertical Z axis are modeled and the results for two approaches are presented: SISO approach (3 PID decentralized controllers together with decoupling compensators) and MIMO approach (a centralized Linear Quadratic Integral Controller (LQI), which takes into account the whole system model with cross-couplings).

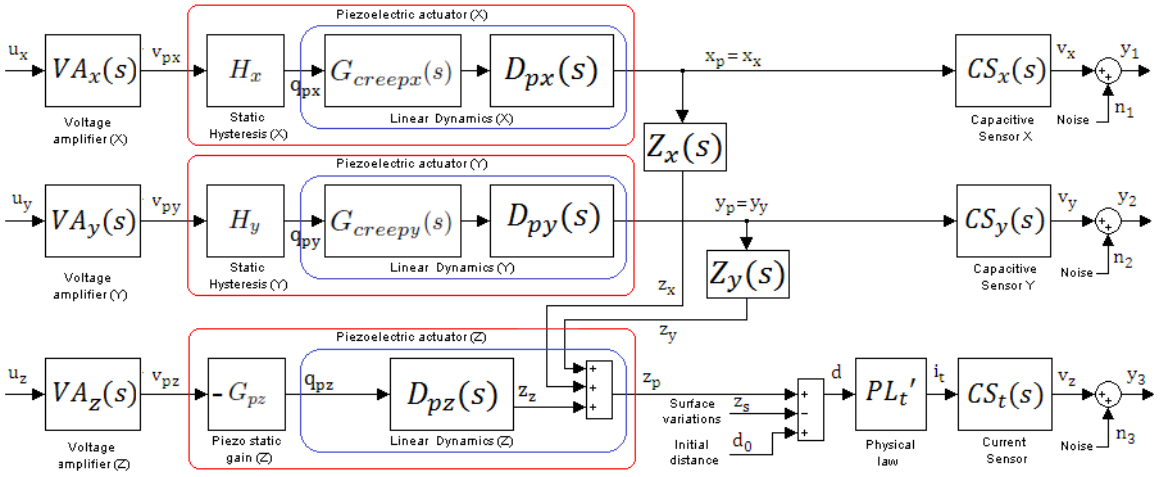


Figure 6.7: Simulation plant model used for surface variation $z_s(t)$ reconstruction.

### 6.3.1 Plant simulation model

The plant model simulated in this subsection, shown in Fig. 6.7, was developed in the early stage of the work and differs a little from the model considered in chapter 2. For example it does not take into account the cross-couplings between the horizontal axes (*i.e.* $x_y(t) = y_x(t) = 0$). As a result $x_p(t) = x_x(t) + x_y(t) = x_x(t)$ and $y_p(t) = y_y(t) + y_x(t) = y_y(t)$ in the full nonlinear model block schema from Fig. 2.3. The hysteresis in X (resp. Y) direction is modeled as a symmetrical nonlinearity $H_x[v_{px}](t)$ (resp. $H_y[v_{py}](t)$) using classical Prandtl-Ishlinskii model described in chapter 3 and is compensated via its inverse model cascaded in a feedforward

path of the corresponding axis. The creep phenomenon for X (resp. Y) directions has been modeled as a linear system $G_{creepx}(s)$ (resp. $G_{creepy}(s)$), used only in the simulated plant model. However, from the control point of view nothing changes and the creep is still assumed to be a disturbance $d_x(t)$ and $d_y(t)$, compensated via feedback control (PID or LQI). This phenomenon in the Z direction has been neglected since the surface variations are changing rapidly.

Most of the subsystems are modeled as in chapter 2. Here, this model is recalled with some modifications. Each horizontal motion is driven by the piezoelectric actuator fed by the voltage amplifier and read by the capacitive sensor. Like before, the voltage amplifier is described by the following low-pass system:

$$\begin{array}{ll} \dot{x}_{1,vx}(t) & = -\omega_{vx} x_{1,vx}(t) + u_x(t) \\ v_{px}(t) & = G_{vx}\omega_{vx} x_{1,vx}(t) \end{array} \tag{6.9}$$

or in Laplace domain:

$$VA_x(s) = \frac{v_{px}(s)}{u_x(s)} = \frac{G_{vx}\omega_{vx}}{s+\omega_{vx}} \tag{6.10}$$

The piezoelectric actuator exhibits the adverse phenomenon of hysteresis $H_x[v_{px}](t)$ and also tends to drift in response to a slowly varying input. This drift (creep phenomenon) in the considered simulated plant is described by a 3$^{\text{rd}}$ order transfer function as in [Croft et al., 2001] as follows:

$$G_{creepx}(s) = \frac{s^3 + 0.630s^2 + 0.0216 + 6.25 \cdot 10^{-5}}{s^3 + 0.516s^2 + 0.0171 + 4.69 \cdot 10^{-5}}. \tag{6.11}$$

The proper vibration part $D_{px}(s)$ of piezo is given by:

$$D_{px}(s) = \frac{\omega_{px}^2}{s^2 + 2\xi_{px}\omega_{px}s + \omega_{px}^2} \tag{6.12}$$

This yields a nonlinear model made of a static nonlinearity $H_x[v_{px}]$, followed by the linear dynamics $G_{creepx}(s)D_{px}(s)$, known as a Hammerstein structure [Giri and Bai, 2010] and the simulated piezo in the plant model from Fig. 6.7 is given by:

$$Piezo_x : \begin{cases} q_{px}(t) = H_x\left[v_{px}(t)\right] \\ \frac{x_x(s)}{q_{px}(s)} = G_{creepx}(s)D_{px}(s) \\ x_p(t) = x_x(t) \end{cases} \tag{6.13}$$

However, for the controller design, the creep phenomenon is considered as a disturbance $d_x(t)$ and the control model of piezo takes the following form:

$$Piezo_x : \begin{cases} q_{px}(t) = H_x\left[v_{px}(t)\right] + d_x(t) \\ \frac{x_x(s)}{q_{px}(s)} = D_{px}(s) = \frac{\omega_{px}^2}{s^2+2\xi_{px}\omega_{px}s+\omega_{px}^2} \\ x_p(t) = x_x(t) \end{cases} \tag{6.14}$$

or in state space with state variables $x_{px,1}(t) = x_p(t)$ and $x_{px,2}(t) = \dot{x}_p(t)$:

$$\begin{array}{ll} \dot{x}_{1,px}(t) & = x_{2,px}(t) \\ \dot{x}_{2,px}(t) & = -\omega_{px}^2 x_{1,px}(t) - 2\xi_{px}\omega_{px}x_{2,px}(t) + \omega_{px}^2 q_{px}(t) \\ x_p(t) & = x_{1,px}(t) \end{array} \tag{6.15}$$

In [Croft et al., 2001] an inverse-based feedfoward control approach is used to compensate for hysteresis, creep and vibration parts of piezo. Here instead, only hysteresis is compensated using feedforward inverse-based classical Prandtl-Ishlinskii model, and then the feedback control is used to compensate for the creep and vibration.
Finally, the capacitive sensor is described as in chapter 2 as follows:

$$\begin{array}{ll} \dot{x}_{1,capx}(t) & = -\omega_{capx} x_{1,capx}(t) + x_p(t) \\ v_x(t) & = G_{capx}\omega_{capx} x_{1,capx}(t) \end{array} \tag{6.16}$$

or in Laplace domain:

$$CS_x(s) = \frac{v_x(s)}{x_p(s)} = \frac{G_{capx}\omega_{capx}}{s + \omega_{capx}} \tag{6.17}$$

The final sensor output is disturbed by measurement noise as follows:

$$y_1(t) = v_x(t) + n_1(t) \tag{6.18}$$

Identical modeling is done for the Y axis, and is not given here for brevity.

The modeling in the Z direction is the same as in chapter 2 with the difference that the creep phenomenon $d_z(t)$ of piezo is neglected in this case, since it is assumed that the surface variations are changing fast enough. The voltage amplifier is described as follows:

$$\begin{array}{ll} \dot{x}_{1,vz}(t) & = -\omega_{vz} x_{1,vz}(t) + u_z(t) \\ v_{pz}(t) & = G_{vz}\omega_{vz} x_{1,vz}(t) \end{array} \tag{6.19}$$

or in Laplace domain:

$$VA_z(s) = \frac{v_{pz}(s)}{u_z(s)} = \frac{G_{vz}\omega_{vz}}{s + \omega_{vz}} \tag{6.20}$$

The piezoelectric actuator of the gain $G_{pz}$ and the bandwidth $\omega_{pz}$ in the Z axis together with cross-couplings from the horizontal axes to the vertical axis ($Z_x(s)$ and $Z_y(s)$) is described by the following linear model (the displacements along this axis are very small and the effect of hysteresis is negligible):

$$Piezo_z : \begin{cases} q_{pz}(t) = -G_{pz} v_{pz}(t) \\ D_{pz}(s) : \begin{cases} \dot{x}_{1,pz}(t) = x_{2,pz}(t) \\ \dot{x}_{2,pz}(t) = -\omega_{pz}^2 x_{1,pz}(t) - 2\xi_{pz}\omega_{pz} x_{2,pz}(t) + \omega_{pz}^2 q_{pz}(t) \\ z_z(t) = x_{1,pz}(t) \end{cases} \\ Z_x(s) : \begin{cases} \dot{x}_{1,zx}(t) & = -\omega_{zx} x_{1,zx}(t) + x_p(t) \\ z_x(t) & = -G_{zx}\omega_{zx} x_{zx,1}(t) + G_{zx} x_p(t) \end{cases} \\ Z_y(s) : \begin{cases} \dot{x}_{1,zy}(t) & = -\omega_{zy} x_{1,zy}(t) + y_p(t) \\ z_y(t) & = -G_{zy}\omega_{zy} x_{1,zy}(t) + G_{zy} y_p(t) \end{cases} \\ z_p(t) = z_z(t) + z_x(t) + z_y(t) \end{cases} \tag{6.21}$$

where the cross-coupling subsystems $Z_x(s)$ and $Z_y(s)$ are the first order high-pass systems expressed in Laplace domain as follows:

$$Z_x(s) = \frac{z_x(s)}{x_p(s)} = \frac{G_{zy} s}{s + \omega_{zy}} \tag{6.22}$$

$$Z_y(s) = \frac{z_y(s)}{y_p(s)} = \frac{G_{zy}s}{s + \omega_{zy}} \tag{6.23}$$

where $G_{zx}$, $\omega_{zx}$ (resp. $G_{zy}$, $\omega_{zy}$) are the gain and the bandwidth of $Z_x(s)$ (resp. $Z_y(s)$).

The physical tunneling law is the heart of the considered STM-like system and is modeled like before as the exponential dependency of the tunneling current on the distance tip/surface $d(t)$, when the latter is less than 1nm and the bias voltage $V_b$ is applied between the two materials as follows:

$$PL'_t: \quad i_t(t) = \begin{cases} gV_b e^{-kd(t)}, & 0 < d(t) \leq 1\,\text{nm} \\ 0, & d(t) > 1\,\text{nm} \end{cases} \tag{6.24}$$

where the distance $d(t)$ is given by:

$$d(t) = d_0 + z_p(t) - z_s(t) \tag{6.25}$$

with initial distance $d_0$ between the tip and the surface, piezo displacement $z_p(t)$ (disturbed by the cross-coupling phenomena) and surface variations $z_s(t)$.
The tunneling current is captured and amplified by the high-gain sensor of the gain $G_t$ and the bandwidth $\omega_t$ modeled like before as follows:

$$\begin{aligned} \dot{x}_{1,t}(t) &= x_{2,t}(t) \\ \dot{x}_{2,t}(t) &= -\omega_t^2 x_{1,t}(t) - 2\xi_t\omega_t x_{2,t}(t) + \omega_t^2 G_t i_t(t) \\ v_z(t) &= x_{1,t}(t) \end{aligned} \tag{6.26}$$

or in Laplace domain:

$$CS_t(s) = \frac{v_z(s)}{i_t(s)} = \frac{G_t\omega_t^2}{s^2 + 2\xi_t\omega_t + \omega_t^2} \tag{6.27}$$

providing a noisy output:

$$y_3(t) = v_z(t) + n_3(t) \tag{6.28}$$

### 6.3.2 SISO approach - 3 PID controllers with decoupling compensators

Fig. 6.8 shows the block schema of the considered SISO controlled system. As mentioned before, the inverse Prandtl-Ishlinskii model ($H_x^{-1}$ and $H_y^{-1}$) is used to linearize piezoelectric actuators in both horizontal directions and such a linearized system is controlled by two PID controllers, which compensate the creep phenomena as well. The third PID controller in the Z direction keeps the tip/surface distance on a desired constant level. The cross-couplings $Z_x(s)$ and $Z_y(s)$ from the horizontal axes to the vertical one can be quite strong, thus a proper compensation is looked for in order to obtain correct image of the surface topography.

As in [Shi et al., 2009], for X to Z coupling identification, the Y axis remains unexcited (*i.e.* the reference $y_r$ is set to 0), which means that there is no influence on the Z axis coming from the Y axis (*i.e.* $z_y(t) \approx 0$). It is assumed also that the scanned surface is chosen to be "more or less" flat (*i.e.* $z_s(t) \approx 0$). The reason behind this is that the surface variations $z_s(t)$, as well as coupling positioning errors $z_x(t)$, $z_y(t)$ are viewed as external disturbances on the tip position $z_p(t)$ as shown in Fig. 6.7. The coupling from Y to Z axis is identified in the

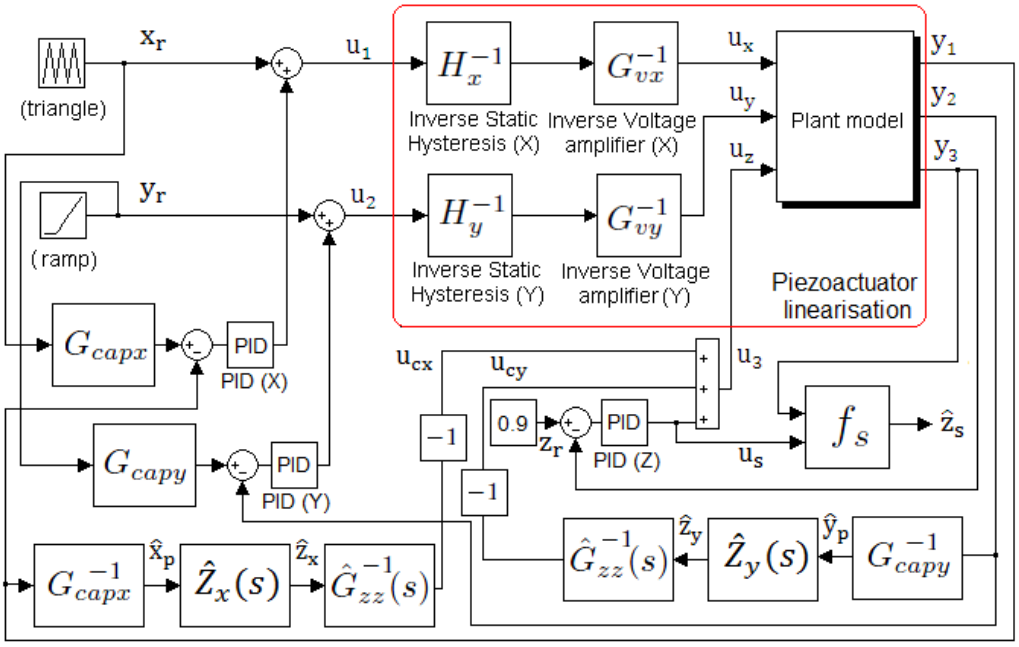


Figure 6.8: STM-like controlled system with decentralized PID SISO controllers and decoupling compensators.

similar way.
Assuming both capacitive sensors $CS_x(s)$ and $CS_y(s)$ as static gains one obtains:

$$x_p(t) \approx \hat{x}_p(t) = \frac{y_1(t)}{G_{capx}}, \quad y_p(t) \approx \hat{y}_p(t) = \frac{y_2(t)}{G_{capy}} \tag{6.29}$$

The transfer functions describing the identified coupling models are given by:

$$\hat{Z}_x(s) = \frac{\hat{z}_x(s)}{\hat{x}_p(s)} = \frac{\hat{G}_{zx}s}{s+\hat{\omega}_{zx}}, \quad \hat{Z}_y(s) = \frac{\hat{z}_y(s)}{\hat{y}_p(s)} = \frac{\hat{G}_{zy}s}{s+\hat{\omega}_{zy}} \tag{6.30}$$

where $\hat{G}_{zx}$, $\hat{\omega}_{zx}$, $\hat{G}_{zy}$, $\hat{\omega}_{zy}$ are identified parameters of the coupling subsystems. Neglecting the dynamics of the piezoactuator $D_{pz}(s)$ and the dynamics of the voltage amplifier $VA_z(s)$ in the Z direction one obtains:

$$\hat{G}_{zz}(s) = \frac{\hat{z}_z(s)}{u_z(s)} = -G_{pz}G_{vz} \tag{6.31}$$

The control signal in the Z direction $u_z(t)$ consists of two parts: the part that is used for cross-couplings compensation $u_c(t)$ and the proper (non-compensating) part $u_s(t)$ that is used to adjust the tip/surface distance when the cross-couplings are compensated as follows:

$$u_z(t) = u_c(t) + u_s(t) = u_{cx}(t) + u_{cy}(t) + u_s(t) \tag{6.32}$$

where the compensating components for $Z_x(s)$ and $Z_y(s)$ couplings are given by:

$$u_{cx}(t) = -\frac{\hat{Z}_x(s)}{\hat{G}_{zz}(s)}\hat{x}_p(t), \quad u_{cy}(t) = -\frac{\hat{Z}_y(s)}{\hat{G}_{zz}(s)}\hat{y}_p(t) \tag{6.33}$$

After cross-couplings compensation one can assume that $z_p(t) \approx z_z(t) \approx -G_{pz}G_{vz}u_s(t)$. Neglecting the dynamics of the current sensor $CS_t(s)$, the estimated distance can be expressed as follows:

$$\hat{d}(t) = -\frac{1}{k}\ln\left(\frac{1}{gV_b}\frac{y_3(t)}{G_t}\right) \tag{6.34}$$

Finally, the surface is reconstructed from the current sensor output $y_3(t)$ and the proper part of the control signal $u_s(t)$ as follows:

$$\hat{z}_s(t) = d_0 + z_p(t) - \hat{d}(t) = f_s(u_s(t), y_3(t)) = d_0 - G_{pz}G_{vz}u_s(t) + \frac{1}{k}\ln\left(\frac{1}{gV_b}\frac{y_3(t)}{G_t}\right) \tag{6.35}$$

The results for the surface reconstruction are given in subsection 6.3.4 together with the results obtained for MIMO design, for comparison.

### 6.3.3 MIMO approach - Linear Quadratic Integral Controller (LQI)

In this subsection, a Linear Quadratic Integral (LQI) controller is designed. It is Linear Quadratic Gaussian controller with an integral action (*i.e.* LQG for tracking). The technique is a model-based approach, and is based on the model developed in subsection 6.3.1, with a state vector $x(t) \in \mathbb{R}^{(15\times1)}$ [composed of the following state variables: $x_{1,vx}(t)$, $x_{1,px}(t)$, $x_{2,px}(t)$, $x_{1,capx}(t)$, $x_{1,vy}(t)$, $x_{1,py}(t)$, $x_{2,py}(t)$, $x_{1,capy}(t)$, $x_{1,vz}(t)$, $x_{1,pz}(t)$, $x_{2,pz}(t)$, $x_{1,zx}(t)$, $x_{1,zy}(t)$, $x_{1,t}(t)$ and $x_{2,t}(t)$], an output vector $y(t) \in \mathbb{R}^{(3\times1)}$ made of $y_1(t), y_2(t)$ and $y_3(t)$, and an input vector $u(t) \in \mathbb{R}^{(3\times1)}$ made of $u_1(t), u_2(t)$ [assuming hysteresis compensation on X and Y axes as before - see Fig. 6.9] and $u_3(t) = u_z(t)$ is considered. The model, still nonlinear with exponential tunneling nonlinearity (6.24), is then linearized around an equilibrium point $(d_{eq}, i_{eq})$ as in chapter 5 as follows:

$$i_t(t) - i_{eq} = -ki_{eq}(d(t) - d_{eq}) \tag{6.36}$$

resulting in a final linear model used for the LQI controller design:

$$\begin{aligned} \Delta\dot{x}(t) &= A\Delta x(t) + B\Delta u(t) + B_d z_s(t) + w(t) \\ \Delta y(t) &= C\Delta x(t) + n(t) \end{aligned} \tag{6.37}$$

where $\Delta x(t) = x(t) - x_{eq}$, $\Delta u(t) = u(t) - u_{eq}$, $\Delta y(t) = y(t) - y_{eq}$ are deviations of respective variables around their equilibrium. It is assumed that process noise $w(t)$ and measurement noise $n(t)$ are zero-mean Gaussian noises with covariances $W = E[w(t)w(t)^T]$ and $N = E[n(t)n(t)^T]$, respectively ($E[x]$ stands for the expected value of $x$). A classical LQG controller is an interconnection of a Kalman estimator and a Linear Quadratic Regulator (LQR), which is used for a stabilization around zero. The purpose is to scan the surface in in X-Y plane and to keep the tunneling current on a constant non-zero level in the Z direction, hence the LQG with an integral action (referred here as LQI) is adopted as shown in Fig. 6.9. The reference vector $r(t)$ is composed of the references for each direction: $x_r(t)$, $y_r(t)$, $z_r(t)$.

**Observer Design.** The surface variations $z_s(t)$ are considered as an unknown disturbance on the tip position $z_p(t)$. The aim of the designed observer is to reconstruct not only the state

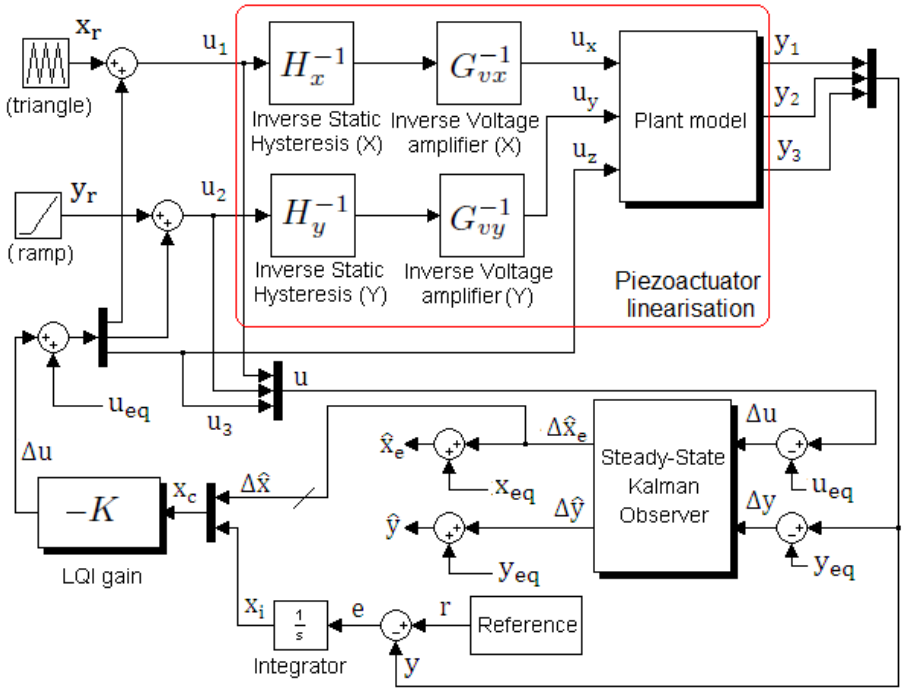


Figure 6.9: STM-like controlled system with centralized LQI MIMO controller.

$x(t)$ of the system, but also the surface variations. If the observer parameters are chosen in such a way that its dynamics is sufficiently fast, the surface variations can be assumed constant (i.e. $\dot{z}_s(t) \approx 0$) from the controller point of view (*i.e.* the observer reconstruction speed is much faster than the surface variations). The covariance matrices $W$ and $N$ are chosen to guarantee both stability and proper dynamics of this observer.

The state vector for reconstruction is extended into $\Delta x_e(t) = [\Delta x(t)\ z_s(t)]^T$ and is a part of the following state space representation:

$$\begin{aligned} \Delta\dot{x}_e(t) &= A_e \Delta x_e(t) + B_e \Delta u(t) + w(t) \\ \Delta y(t) &= C_e \Delta x_e(t) + n(t) \end{aligned} \tag{6.38}$$

with the state space matrices defined as follows:

$$A_e = \begin{pmatrix} A & B_d \\ 0 & 0 \end{pmatrix}, \quad B_e = \begin{pmatrix} B \\ 0 \end{pmatrix}, \quad C_e = \begin{pmatrix} C & 0 \end{pmatrix} \tag{6.39}$$

The steady-state Kalman observer for such observable system is given by:

$$\Delta\dot{\hat{x}}_e(t) = A_e \Delta\hat{x}_e(t) + B_e \Delta u(t) + L(\Delta y(t) - C_e \Delta\hat{x}_e(t)) \tag{6.40}$$

where $\Delta\hat{x}_e(t)$ is an optimal state estimate of (6.38) in terms of minimizing the mean square error $E[\Delta\hat{x}_e(t) - \Delta x_e(t)]$ if the observer gain matrix $L = PC_e^T N^{-1}$ is properly chosen. The matrix $P$ is a solution of the following Algebraic Riccati Equation (ARE):

$$A_e P + P A_e^T - LNL^T + W = 0 \tag{6.41}$$

**Controller Design.** As mentioned before, the LQG has to be adapted to the tracking problem in order to ensure that the output $y(t)$ tracks the reference signal $r(t)$, which can be easily done via extending the classical LQG feedback from the system state estimate $\Delta\hat{x}(t)$ (the state estimate $\Delta\hat{x}(t)$ is used and not the extended state estimate $\Delta\hat{x}_e$, since $z_s(t)$ is not controllable) with the feedback from integrated error $x_i(t)$ such that $\Delta u(t) = -Kx_c(t)$, where $x_c(t) = [\Delta\hat{x}(t)\ x_i(t)]^T$. The integrated error $x_i(t)$ is given by:

$$x_i(t) = \int e(t)dt = \int [r(t) - y(t)]dt \tag{6.42}$$

The following cost function is minimized:

$$J(u(t)) = \int_0^\infty [x_c(t)^T Q x_c(t) + \Delta u(t)^T R \Delta u(t)]dt \tag{6.43}$$

with the feedback matrix $K = R^{-1}B_c^T S$, where $S$ is a solution of the following ARE:

$$A_c^T S + S A_c - K^T R K + Q = 0 \tag{6.44}$$

$$A_c = \begin{pmatrix} A & 0 \\ -C & 0 \end{pmatrix}, \quad B_c = \begin{pmatrix} B \\ 0 \end{pmatrix} \tag{6.45}$$

where $Q$ is a positive semi-definite weighting matrix for the state with integral action $x_c(t)$ and $R$ is a positive definite weighting matrix for the control $\Delta u(t)$.

### 6.3.4 Simulation results for surface reconstruction

The final simulation results for surface reconstruction in the STM-like system for both SISO and MIMO design are presented in this subsection. The numerical values used for simulation are summarized in Table 6.2. Most of them are with a good accordance with the parameters' values of the experimental platform under development in GIPSA-lab (see e.g. [Ahmad et al., 2012b], [Ryba et al., 2013]). The raster scan is used to scan the surface in X-Y plane, while simultaneously keeping the tunneling current on the constant level (here 0.9 nA). The X axis is assumed as the fast scanning axis, where a triangle signal of amplitude 1 $\mu$m and frequency 100 Hz is applied and the Y axis is the slow axis, where a linear ramp is applied, which moves the tip to the next line in a raster pattern. It is assumed that the data are collected only during the forward movement of the tip (rising part of the triangle).

The influence of different adverse phenomena (cross-couplings, hysteresis, creep and vibration) on the surface reconstruction are investigated here for both SISO and MIMO designs from the previous subsections. It is assumed that all these phenomena are already compensated for the Y axis and subsequently eliminated for the X axis. Fig. 6.10a shows the reference surface topography being the sinusoidal variations of amplitude 5 Å. Due to large cross-coupling from the horizontal axes to the vertical one, the image of the surface without any compensation can be completely deteriorated as shown in Fig. 6.10b. Two decoupling compensators designed in SISO design in subsection 6.3.2 were switched on and the obtained image shown in Fig. 6.10c

Table 6.2: System parameters used for simulation.

| | | |
|---|---|---|
| $\omega_{vx}$, $\omega_{vy}$, $\omega_{vz}$ | Bandwidth of voltage amplifier | 4 kHz |
| $G_{vx}$, $G_{vy}$, $G_{vz}$ | Gain of voltage amplifier | 15 V/V |
| $\omega_{px}$, $\omega_{py}$, ($\omega_{pz}$) | Bandwidth of piezoactuator | 630, (120000) Hz |
| $G_{px}$, $G_{py}$, ($G_{pz}$) | Gain of piezoactuator | 25, (1.2) nm/V |
| $\xi_{px}$, $\xi_{py}$, $\xi_{pz}$ | Damping of piezoactuator | 0.9 |
| $\omega_{capx}$, $\omega_{capy}$ | Bandwidth of capacitive sensor | 8.5 kHz |
| $G_{capx}$, $G_{capy}$ | Gain of capacitive sensor | 200 V/mm |
| $\omega_t$ | Bandwidth of current sensor | 13 kHz |
| $G_t$ | Gain of current sensor | $10^9$ V/A |
| $d_0$ | Initial distance tip-surface | 1 nm |
| $V_b$ | Biased voltage | 1.025 V |
| $g$ | Tunneling current constant | 0.0011 |
| $k$ | Tunneling current constant | 1.65 $Å^{-1}$ |
| $i_{eq}$ | Equilibrium tunneling current | 0.9 nA |
| $d_{eq}$ | Equilibrium distance tip-surface | 8.5 Å |
| $\omega_{zx}$, $\omega_{zy}$ | Bandwidth of cross-coupling | 100 Hz |
| $G_{zx}$, $G_{zy}$ | Cross-coupling gains (maximum positioning error w.r.t. scanning displacement) | 3% |

resembles the reference sinusoidal surface variations. The difference is due to other remaining phenomena of hysteresis, creep and vibrations. Fig. 6.10d shows the image after hysteresis compensation and Fig. 6.10e after the creep and vibration compensation. These results have been obtained for the SISO design with three PID controllers and in this classical approach the surface is reconstructed from the control signal of vertical piezo [Abramovitch et al., 2007]. However, in case of large model uncertainties and measurement noise, the performance of this approach deteriorates. In case of MIMO design described in subsection 6.3.3, the surface is reconstructed via the state observer together with the system state. Since the whole model is taken into account, including the cross-coupling phenomena and the level of noise is decreased by properly chosen covariance matrices $W$ and $V$, the reconstructed surface is better than in SISO case as shown in Fig. 6.10f. The difference can be seen also in tunneling voltage stabilization at $z_r$ =0.9V (corresponding to 9 nA of tunneling current) as shown in Fig. 6.11.

## 6.4 Conclusion

In this chapter two applications have been investigated: nanopositioning validated experimentally on the 3D lab-made micro-/nanopositioning device, and STM-like surface reconstruction tested in simulation. In the first application, the piezoactuated tip followed a prespecified trajectory in X, Y and Z directions. In the horizontal X and Y axes raster and spiral trajectories were used, and in the vertical Z direction the prespecified sinusoidal trajectory has been imposed playing the role of "virtual surface". First, the amplitude of this surface was chosen to be small enough w.r.t. the measurement noise (low signal to noise ratio). The obtained images were influenced by noise, however the surface details can be well-distinguished.

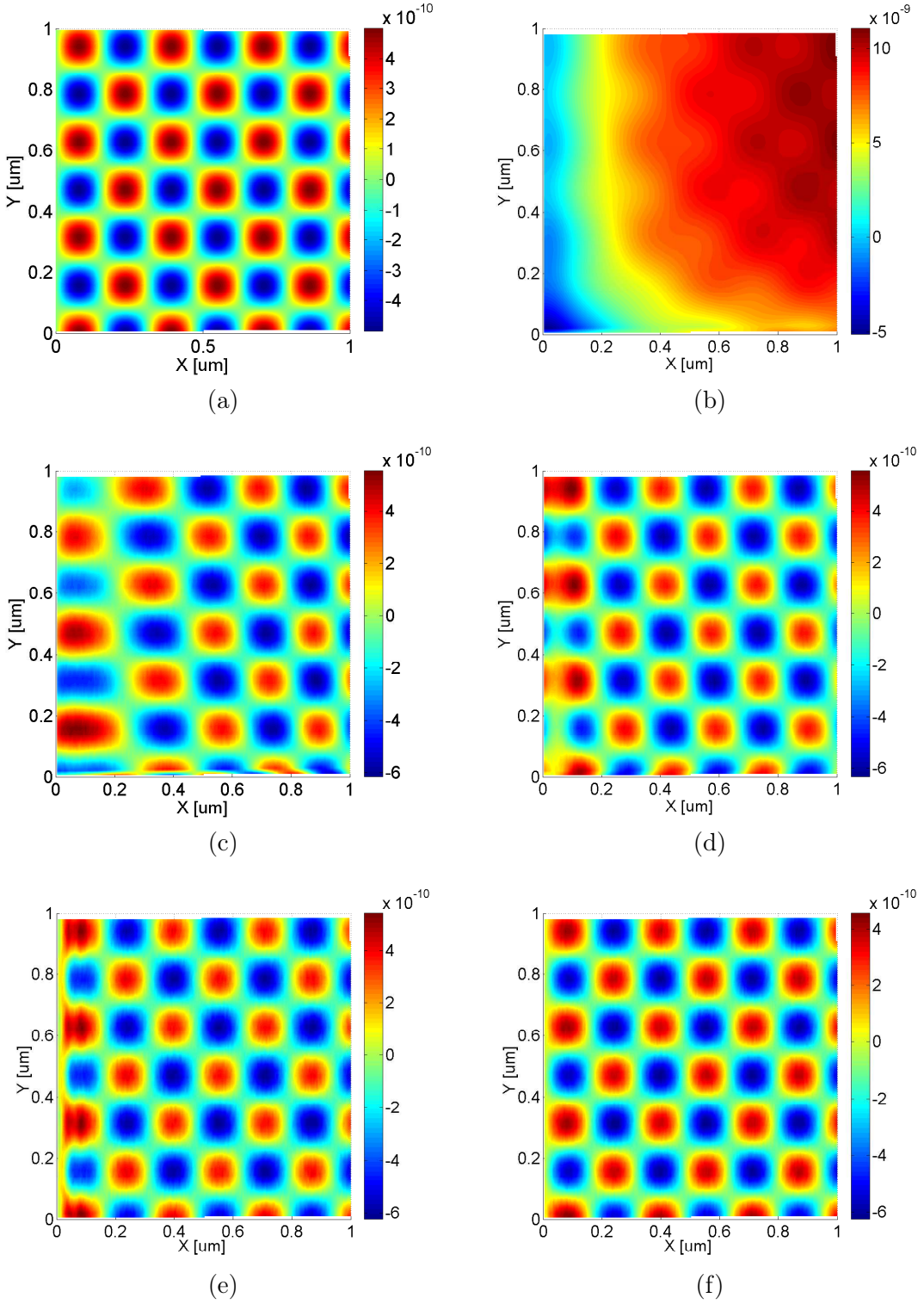


Figure 6.10: Surface reconstruction: (a) Reference surface variations $z_r(t)$. (b) Without any compensation. SISO approach with subsequent compensation of: (c) cross-couplings, (d) hysteresis, (e) creep and vibrations. (f) MIMO approach.

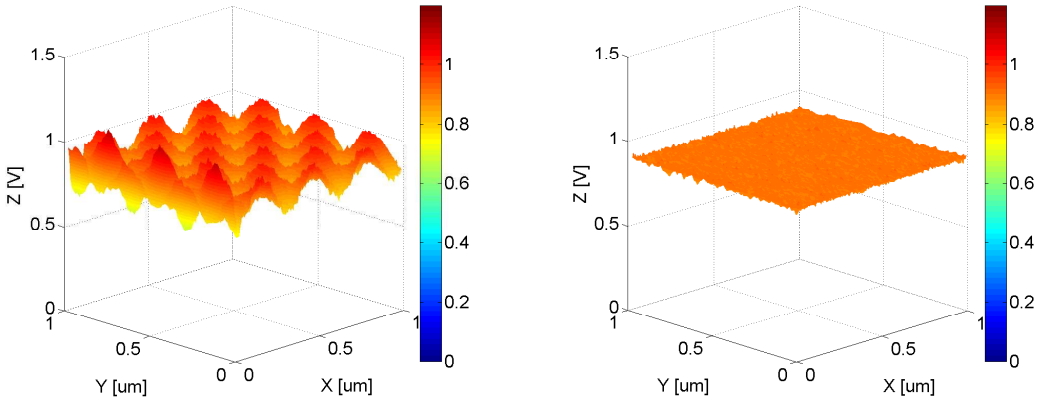


(a) (b)

Figure 6.11: Tunneling current: (a) SISO approach, (b) MIMO approach.

The low-pass filters added on the observers' output as well as increased signal to noise ratio improved significantly the presented results and the performance of the following compensation methods for hysteresis and creep was compared: Modified Prandtl-Ishlinskii (MPI), disturbance observer (DOB) and hybrid MPI + DOB. Illustrative results show, that all of the approaches give significantly better results than without any compensation among which the hybrid MPI+DOB approach gives the best results.

The second application - STM-like surface reconstruction was tested in simulation. Two control strategies were analyzed: decentralized SISO control, where three PID controllers were used (each for one axis of the considered system) and MIMO centralized control using Linear Quadratic Integral (LQI) controller. In the first approach the surface was reconstructed via control signal of the vertical piezo, while in the second approach estimated via state observer. In both approaches the hysteresis was first compensated using classical Prandtl-Ishlinskii model. Illustrative surface images have been presented for subsequent cross-couplings, hysteresis, creep and vibration compensation for SISO approach. The MIMO approach outperforms its SISO counterpart in terms of both surface reconstruction and tunneling current stabilization, since it is based on the whole system model (including cross-coupling phenomena) and appears more robust to model uncertainties and measurement noises.

Chapter 7

# Cantilever nanopositioning with electrostatic actuation

**Contents**



## 7.1 Introduction

This chapter is devoted to modeling and control of the electrostatically actuated cantilever based on the tunneling current measurement. The idea is to consider here the (multi-mode) dynamics of the cantilever. The electrostatic actuator is used to keep the tunneling gap constant, while the piezoelectric actuator adjusts the tip (and as a result positions the cantilever, since the gap cantilever/tip is already maintained constant). This extends the former study of [Blanvillain et al., 2014], which considered a one-mode cantilever model without proximity force compensation. The numerical data (such as cantilever dimensions) used for simulation have been taken from the cantilever provider from Nano World company and are summarized in Table 7.1 ($t_c$ stands for the cantilever thickness in order to avoid confusion with the time $t$). The multi-mode model of the cantilever from [Salapaka et al., 1997] is borrowed for further studies and analysis for $n = 3$ first modes. Some "singular points" of the modal shape functions along horizontal $x$ position of the cantilever are emphasized and used for actuator/sensor location. Near these singular points the model is degenerating (*i.e.* the corresponding shaped modes are vanishing) and as a result the model order can be reduced. The success in damping the resonances for the piezoelectric actuators in the horizontal axes, shown in chapter 4, motivated the use of $\mathcal{H}_\infty$ approach to control the tunneling gap via resonant cantilever. The proximity force is approximated from the tunneling current measurement and then compensated via PID controller which actuates the tip via piezoelectric actuator.

Table 7.1: Numerical data concerning the cantilever.

| | | |
|---|---|---|
| $w$ | Cantilever width | 100 $\mu$m |
| $L$ | Cantilever length | 500 $\mu$m |
| $t_c$ | Cantilever thickness | 1 $\mu$m |
| $E$ | Cantilever Young's modulus of elasticity | 180 GPa |
| $Q$ | the Q factor | 33 |
| $n$ | Number of first modes used for simulation | 3 |

## 7.2 Multi-mode cantilever model analysis

In chapter 2 the equations describing the multi-mode model of the cantilever have been presented. In this section this model is used and simulated for the first 3 modes. Recalling equation (2.30), the cantilever motion subject to proximity force $-F_p(t)$ and damping force $p_d(x,t)$ (constant per unit length) can be described as follows (see Fig. 7.1a):

$$EI\frac{\partial^4 z_c(x,t)}{\partial x^4} + p_d(x,t) + \rho A\frac{\partial^2 z_c(x,t)}{\partial t^2} = -F_p(t) \tag{7.1}$$

where $I = wt_c^3/12$ is the moment of inertia of the cantilever and $A = wt_c$ is its cross sectional area. The force $F_p(t)$ is the interaction force between the tip and the cantilever and is acting

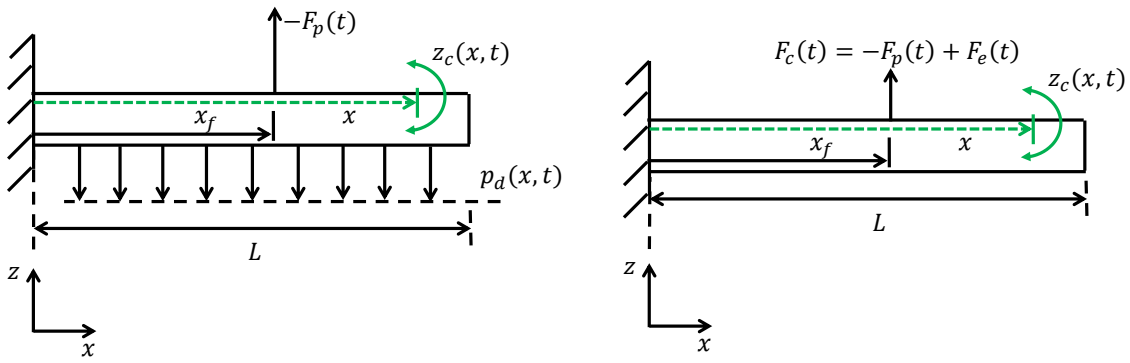


(a) (b)

Figure 7.1: Schematic showing the cantilever: (a) Subjected to the external force of value $-F_p(t)$ acting at a distance $x_f$ from the base of the cantilever with the the damping force $p_d(x,t)$, assumed constant per unit length. (b) The equivalent schematic with the total net force $F_c(t) = -F_p(t) + F_e(t)$.

at the distance $x_f$ from the base of the cantilever. The damping force $p_d(x,t)$ is the sum of the natural structural damping force of the cantilever and the external damping force (here the electrostatic force $F_e(t)$) as follows:

$$p_d(x,t) = \xi\frac{\partial z_c(x,t)}{\partial t} - F_e(t) \tag{7.2}$$

with the damping factor $\xi = 3.515/Q\sqrt{EI\rho A/L^4}$ (assumed constant for all modes). Inserting (7.2) into (7.1) gives (see Fig. 7.1b):

$$EI\frac{\partial^4 z_c(x,t)}{\partial x^4} + \xi\frac{\partial z_c(x,t)}{\partial t} + \rho A\frac{\partial^2 z_c(x,t)}{\partial t^2} = \underbrace{F_c(t)}_{-F_p(t)+F_e(t)} \tag{7.3}$$

where $F_c(t) = -F_p(t) + F_e(t)$ is the total net force acting at a distance $x_f$ from the base of the cantilever, which can be distributed over the cantilever length $L$.

The cantilever displacement is expressed as the sum of the fundamental deformations $q_j(t)$ shaped by the modal shape functions $\phi_j(x)$ $(j = 1..3)$ as follows:

$$z_c(x,t) = \sum_{j=1}^{3} \phi_j(x) q_j(t) \tag{7.4}$$

where $\phi_j(x)$ is given by (2.34) and $q_j(t)$ is the solution of (2.38). The displacement depends not only on the time $t$ but also on the horizontal position $x$ along the cantilever. However, as mentioned in chapter 2, the modal shape function $\phi_j(x)$ allows to distribute in space the modal contributions $q_j(t)$ and it only depends on position, while the modal part depends only on time. Recalling equation (2.50), the cantilever displacement in Laplace domain can be expressed as follows (assuming zero initial conditions $q_j(0) = \dot{q}_j(0) = 0$):

$$z_c(x,s) = \sum_{j=1}^{3} \phi_j(x) \frac{\phi_j(x_f)}{s^2 + \frac{c_j}{m_j}s + \frac{k_j}{m_j}} \frac{1}{m_j} F_c(s) \tag{7.5}$$

with the modal parameters defined by (2.39)-(2.42). The computed parameters for the considered 3-mode model are summarized in Table 7.2. Note that one can rewrite equation (7.5) as follows:

$$z_c(x,s) = \sum_{j=1}^{3} \frac{1}{\frac{m_j}{\phi_j(x)\phi_j(x_f)}s^2 + \frac{c_j}{\phi_j(x)\phi_j(x_f)}s + \frac{k_j}{\phi_j(x)\phi_j(x_f)}} F_c(s) \tag{7.6}$$

Now taking only the first mode of (7.6) one obtains the equivalent single-mode model, at

Table 7.2: Parameters computed for the first three modes.

| $j$ | $\lambda_j$ | $\phi_j(L)$ | $m_j$ | $k_j$ | $c_j$ |
|---|---|---|---|---|---|
| 1 | $0.3798 \times 10^4$ | -8.5673 | $2.1446 \times 10^{-9}$ | 2.7311 | $2.3184 \times 10^{-6}$ |
| 2 | $0.9392 \times 10^4$ | 107.6972 | $3.3694 \times 10^{-7}$ | $1.6850 \times 10^4$ | $3.6424 \times 10^{-4}$ |
| 3 | $1.5710 \times 10^4$ | $-2.5803 \times 10^3$ | $1.9389 \times 10^{-4}$ | $7.6025 \times 10^7$ | $2.0961 \times 10^{-1}$ |

the force location $x_f$ and sensor location $x$, with the following parameters:

$$m_{single} = \frac{m_1}{\phi_1(x)\phi_1(x_f)}, \quad c_{single} = \frac{c_1}{\phi_1(x)\phi_1(x_f)}, \quad k_{single} = \frac{k_1}{\phi_1(x)\phi_1(x_f)} \tag{7.7}$$

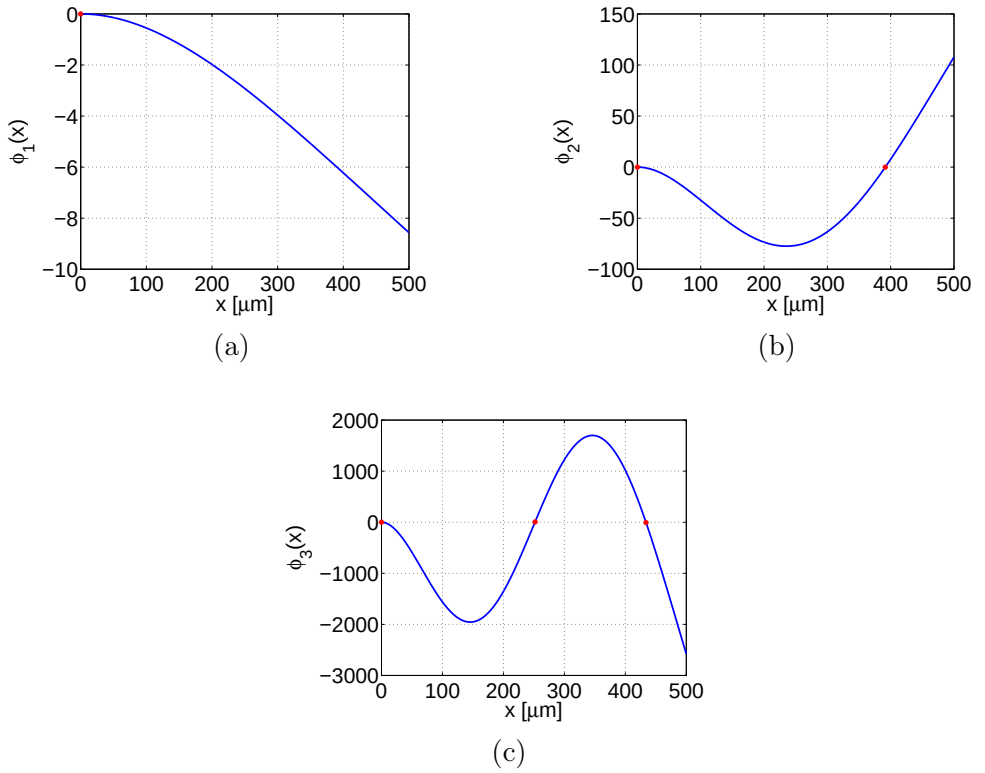


Figure 7.2: Modal shape functions for 3 modes with singular points (pointed in red): (a) 1st mode. (b) 2nd mode. (c) 3rd mode.

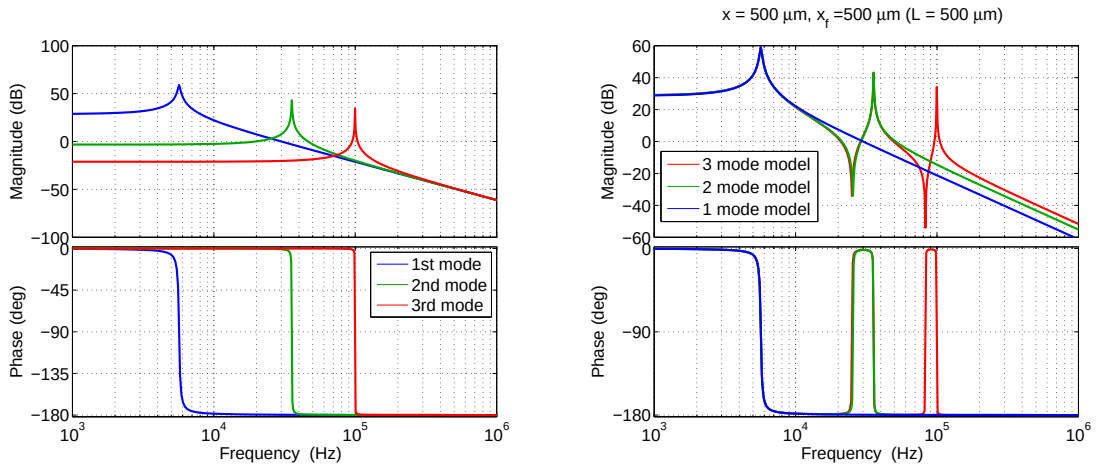


Figure 7.3: Frequency response of (a) shaped modal and (b) total displacement (sum of shaped modes) when the applied input force and measured output displacement are at the distance $x = L = 500\ \mu m$ (*i.e.* cantilever end).

Three resonant frequencies were found using parameters from Table 7.2 according to the formula $f_j = \omega_j/(2\pi) = \sqrt{k_j/m_j}/(2\pi) = \lambda_j^2\sqrt{EI/(\rho A)}/(2\pi)$ and they are equal to 5.68 kHz, 35.59 kHz and 99.65 kHz. The force constant at the end of cantilever is given by the formula $k_f(L) = Ewt_c^3/(4L^3) = 0.036$ N/m.

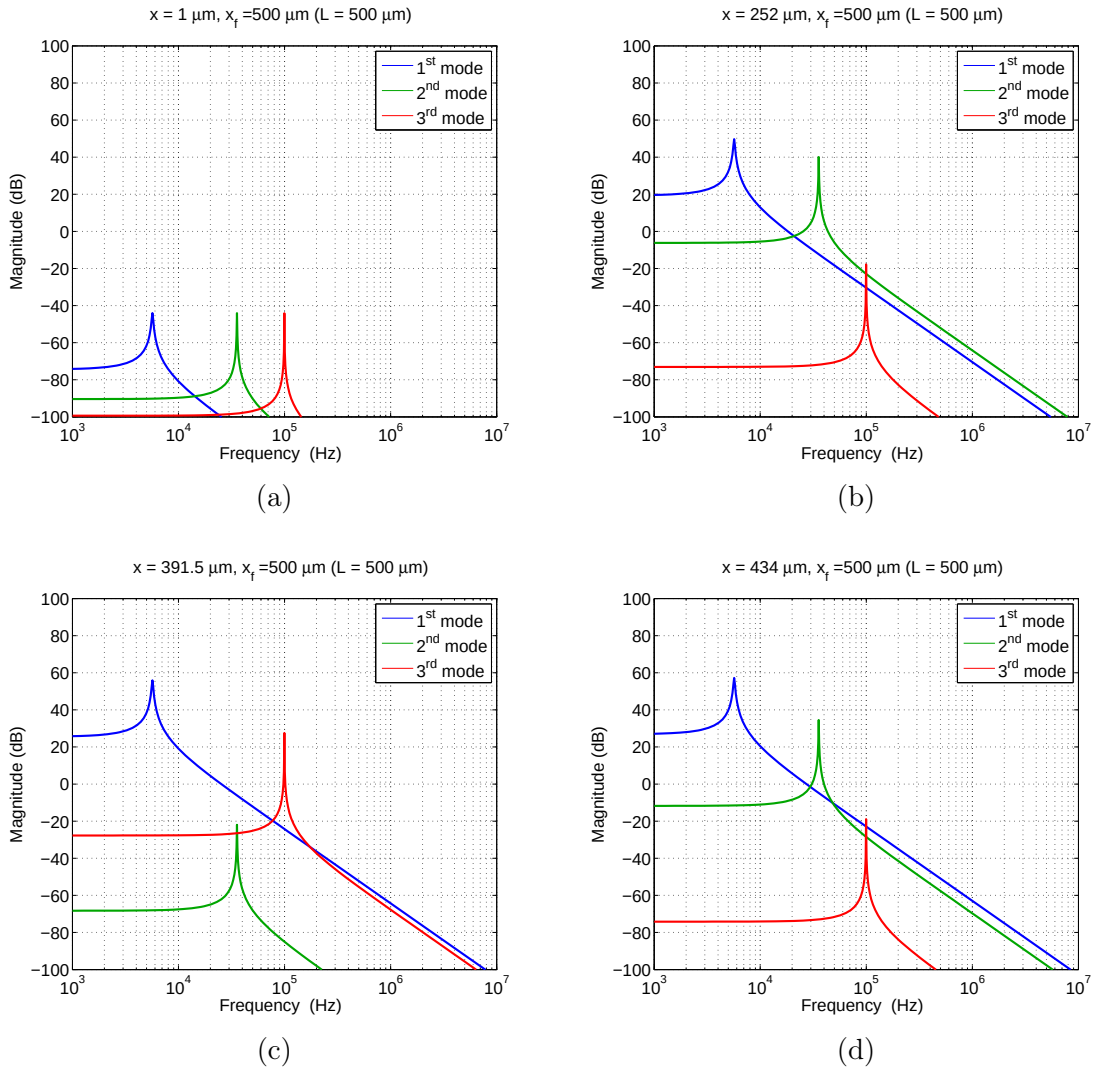


Figure 7.4: Magnitude plot of different shaped modes at singular points, when the applied force is at $x_f = 500$ $\mu$m (cantilever end): (a) $x = 1$ $\mu$m $\approx 0$ $\mu$m. (b) $x = 252$ $\mu$m. (c) $x = 391.5$ $\mu$m. (d) $x = 434$ $\mu$m.

Analyzing the model (7.5), it can be noticed that depending on the position $x$, the contribution of the $j^{th}$ mode to the total displacement is different and can vanish completely when its corresponding modal shape function $\phi_j(x)$ is equal to zero. Here, the positions where this happens are called the singular points. Fig. 7.2 shows the modal shape functions $\phi_j(x)$ for the considered model. The singular points are pointed by the red points and it appears that $j^{th}$ mode has $j$ singular points. It can be also noticed that all modes have singular point at

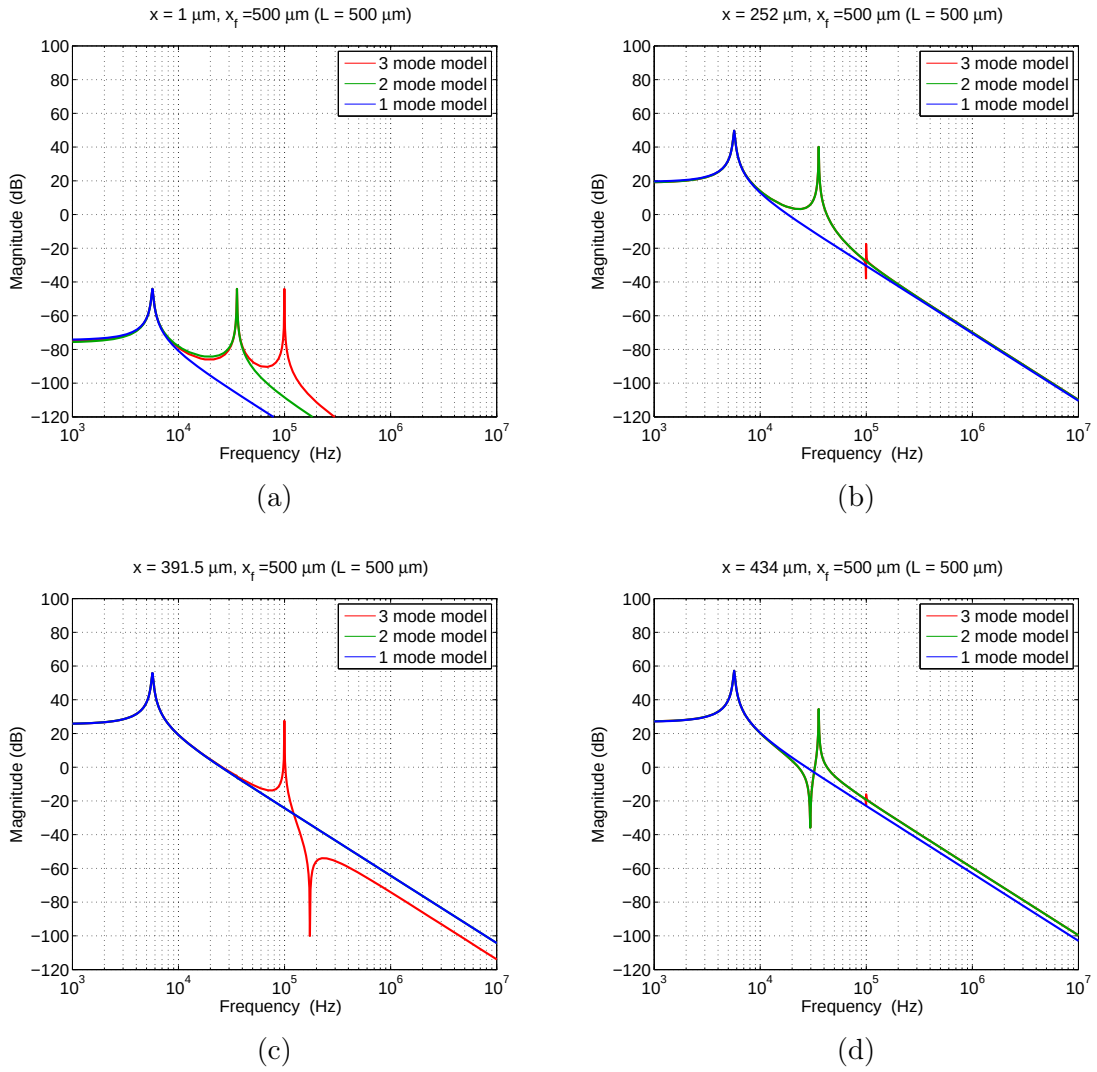


Figure 7.5: Magnitude plot of the cantilever total displacement at singular points, when the applied force is at $x_f = 500$ $\mu$m (cantilever end): (a) $x = 1$ $\mu$m $\approx 0$ $\mu$m. (b) $x = 252$ $\mu$m. (c) $x = 391.5$ $\mu$m. (d) $x = 434$ $\mu$m.

$x = 0$ $\mu m$ (cantilever fixed part). Fig. 7.3a shows the bode diagram of the shaped modes individually and Fig. 7.3b the bode diagram of the whole model (sum of the one, two and three shaped modes) from the input force $F_c(t)$ to the output cantilever displacement $z_c(x,t)$, where both the applied input force and captured output displacement are taken at the end of cantilever ($x = x_f = L = 500$ $\mu m$). Fig. 7.4 shows the frequency response (magnitude plot) of the individual shaped modes at singular points, when the input force is applied at the cantilever end ($x_f = L$). It can be clearly seen that all the modes are vanishing at $x = 0$ $\mu m$ (see Fig. 7.4a), the second mode vanishes at $x = 391.5$ $\mu m$ (see Fig. 7.4c) and the third one at $x = 252$ $\mu m$ and $x = 434$ $\mu m$ (see Fig. 7.4b and Fig. 7.4d, respectively). The corresponding frequency response for the total displacement is shown in Fig. 7.5. One can see that placing

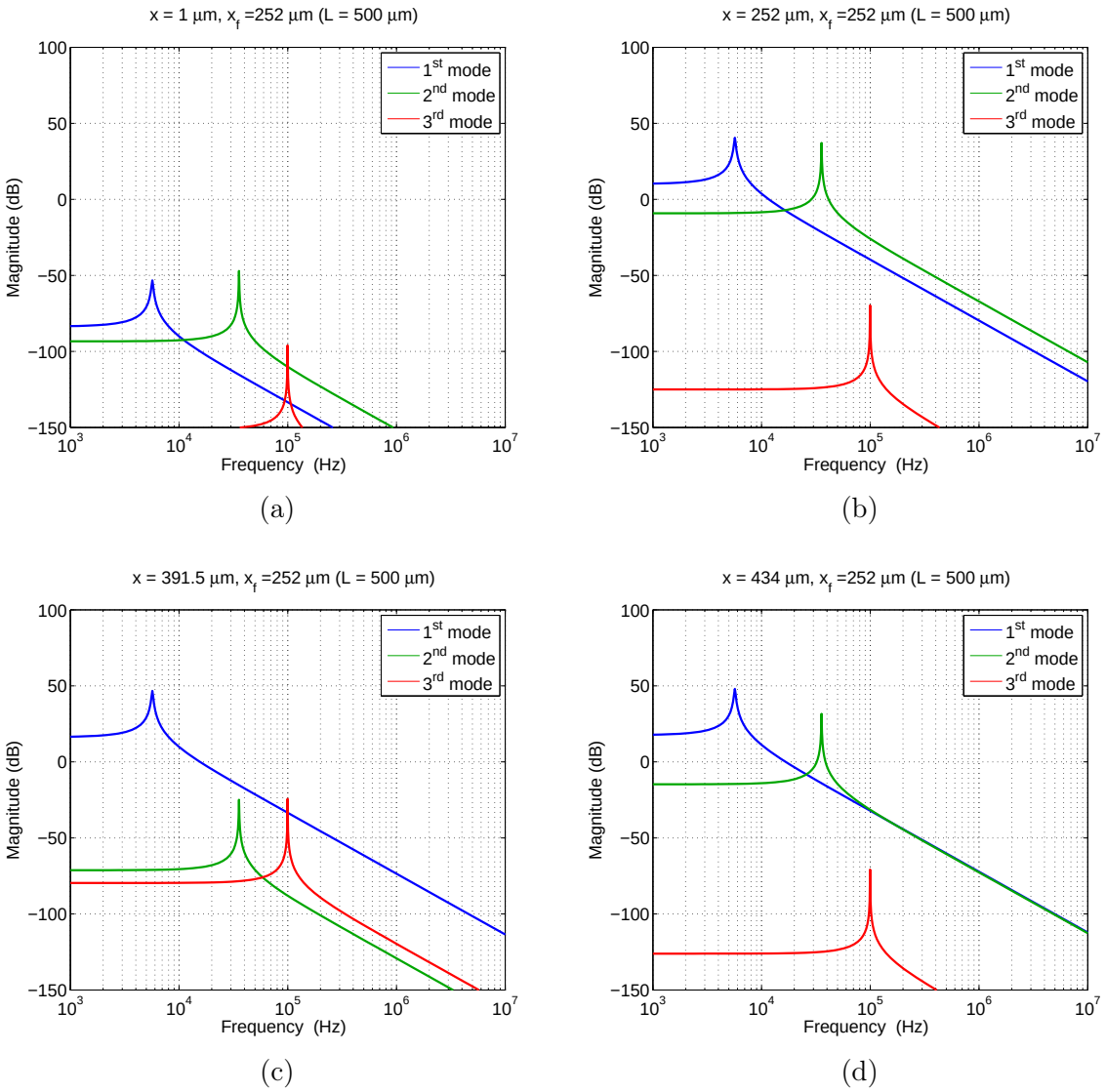


Figure 7.6: Magnitude plot of different shaped modes at singular points, when the applied force is at $x_f = 252$ $\mu$m: (a) $x = 1$ $\mu$m $\approx 0$ $\mu$m. (b) $x = 252$ $\mu$m. (c) $x = 391.5$ $\mu$m. (d) $x = 434$ $\mu$m.

the displacement sensor (if such exists) at the position near the singular point can damp the associated mode and in a consequence reduce the model order. These results have been obtained for the fixed position for the applied force ($x_f = L$). What happens when this position is also placed in one of the singular points (*i.e.* when $\phi_j(x_f) = 0$)? From model (7.5) it appears immediately that the $j^{th}$ mode contribution will vanish as well in this case. Fig. 7.6 shows the frequency response (magnitude plot) of the shaped modes at singular points in such a case, where the input force is applied at the position $x_f = 252$ $\mu m$ (one of the singular points for the third mode). One can notice, that at each plot the third mode is vanishing, thus its contribution to the total displacement (see Fig. 7.7) is almost zero. Moreover, at the

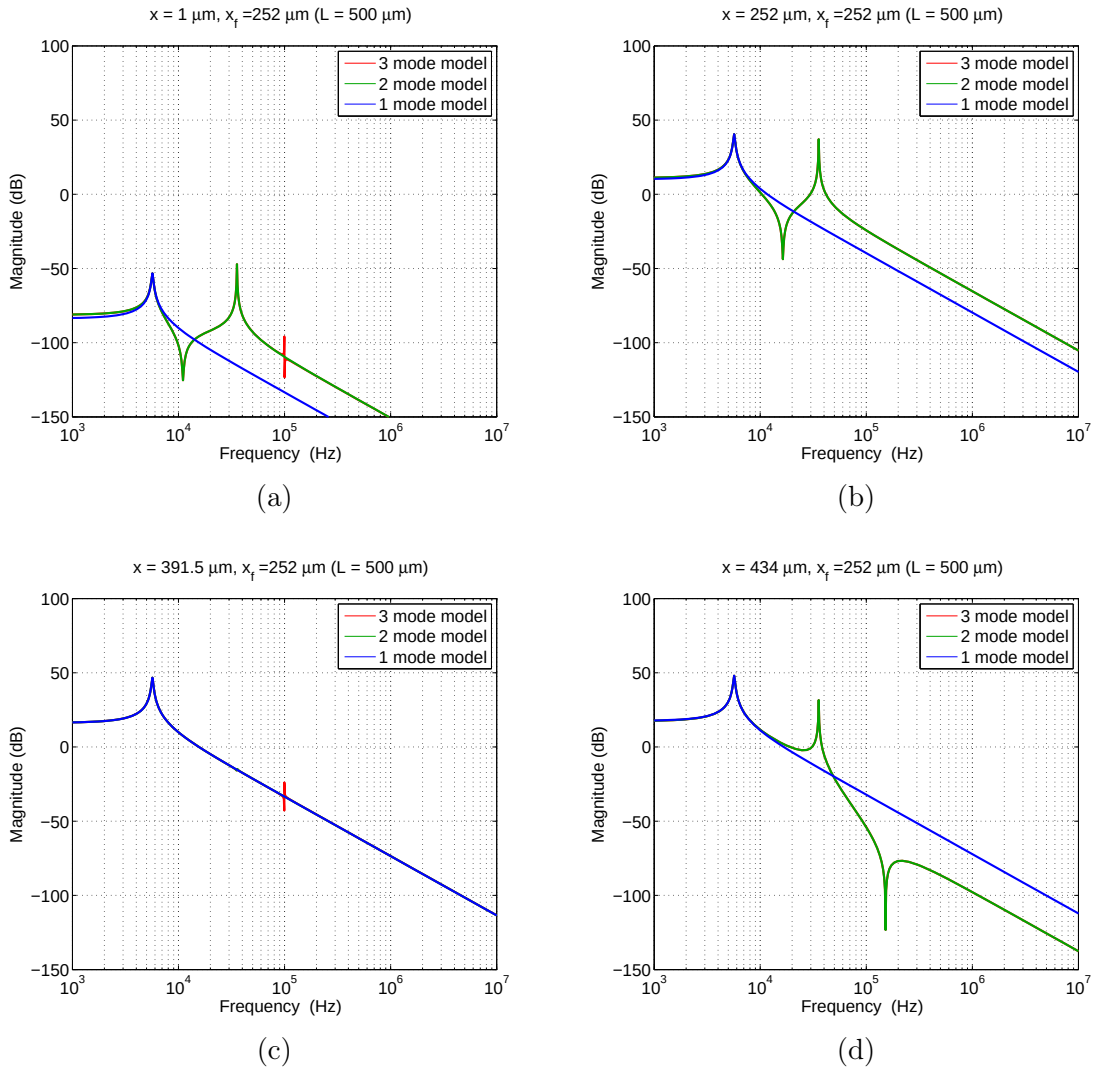


Figure 7.7: Magnitude plot of the cantilever total displacement at singular points, when the applied force is at $x_f = 252$ $\mu$m: (a) $x = 1$ $\mu$m $\approx 0$ $\mu$m. (b) $x = 252$ $\mu$m. (c) $x = 391.5$ $\mu$m. (d) $x = 434$ $\mu$m.

location $x = 391.5$ $\mu m$, the second mode is vanishing as well (see Fig. 7.6c) and as a result the corresponding model for the total displacement can be reduced in this case to the first mode only as shown in Fig. 7.7c. From this observation one can conclude that the model order can be reduced by both sensor and actuator locations.

Fig. 7.8a and Fig. 7.8c show the input force being the step function with random Gaussian noise with signal to noise ratio SNR=30 dB and SNR=15 dB, respectively while Fig. 7.8b and Fig. 7.8d show the corresponding cantilever total displacement with modal contributions (forced at $x_f = L = 500$ $\mu m$ and measured at $x = 150$ $\mu m$). Fig. 7.9 shows the case corresponding to Fig. 7.7 where the force (of SNR = 15 dB) from Fig. 7.8c is kept at $x_f =$

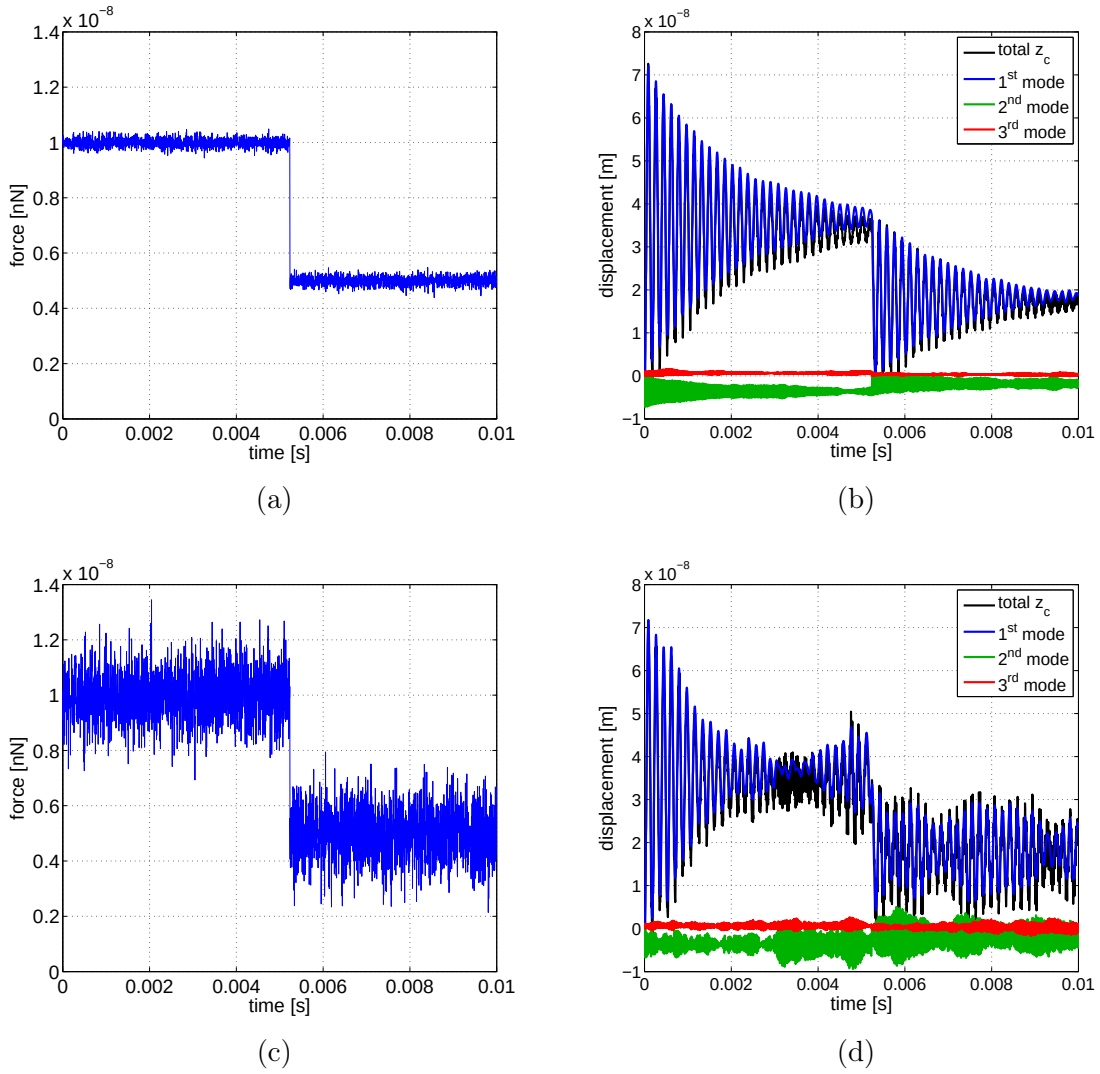


Figure 7.8: Input/output data: (a), (c) Input force $F_c(t)$ for SNR = 30 dB and 15 dB, respectively. (b), (d) Corresponding output displacements $z_c(x,t)$ (total and coming from individual shaped modes), captured at the position $x = 150\ \mu m$, when the input force $F_c(t)$ is applied at $x_f = L = 500\ \mu m$.

$L = 252\ \mu m$ (singular point for the third mode) and is captured at four singular points. In all cases, the contribution coming from the third mode is zero, since the force is applied at the singular point of the modal shape function $\phi_3(x_f)$. The total displacement in Fig. 7.9a at $x = 1\ \mu m$ is almost zero and is increasing with the position $x$. As expected, for $x = 391.5\ \mu m$ (singular point of the modal shape function $\phi_2(x_f)$), the second mode is additionally vanishing and the total displacement of the full 3-mode model is exacly equal to the displacement of the 1-mode model.

In the case of the considered tunneling current-based platform, the displacement sensor

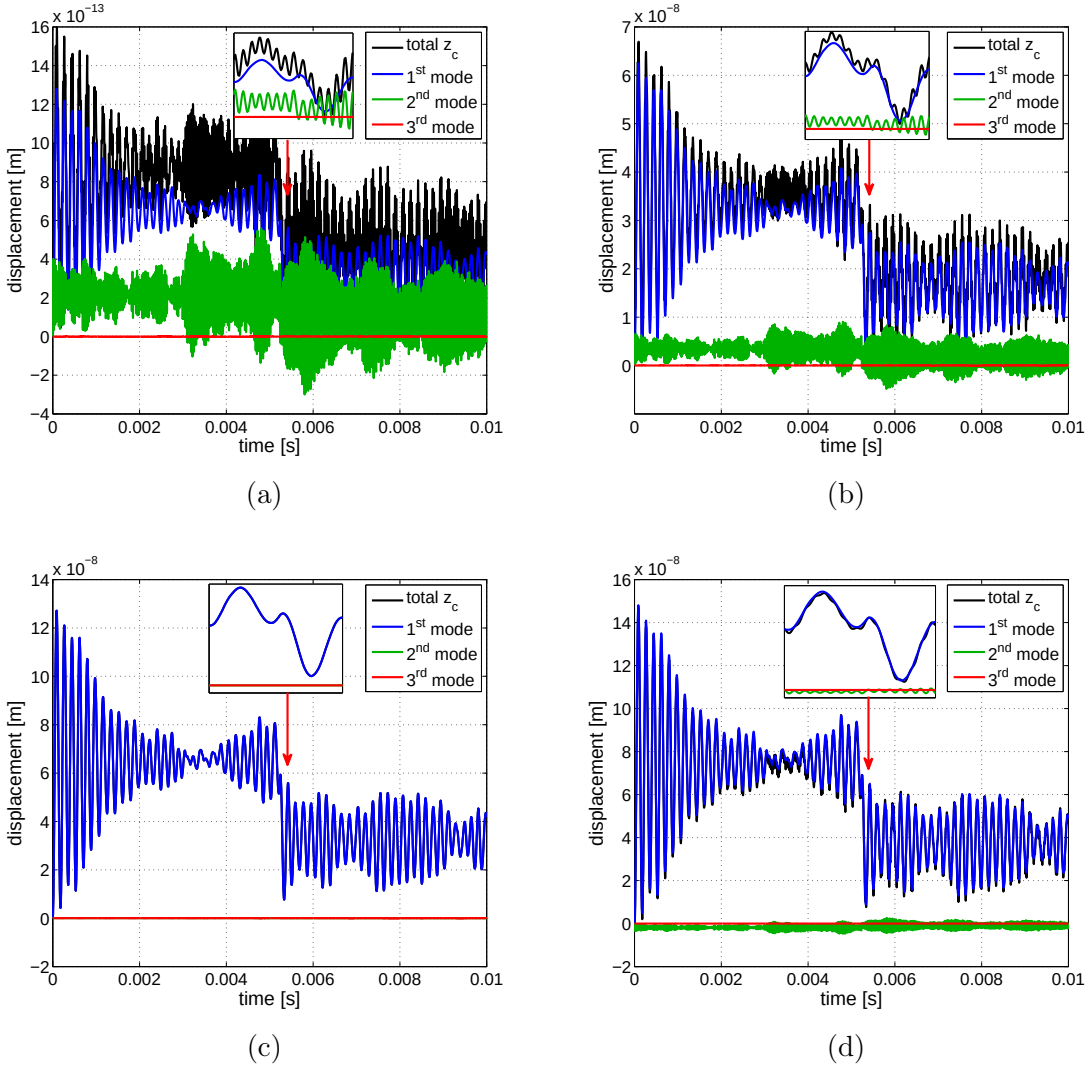


Figure 7.9: Output displacements of the cantilever (shaped modal and total) at singular points, when the applied force is at $x_f = 252$ $\mu$m: (a) $x = 1$ $\mu$m $\approx 0$ $\mu$m. (b) $x = 252$ $\mu$m. (c) $x = 391.5$ $\mu$m. (d) $x = 434$ $\mu$m.

is not present and the only sensor in the vertical direction measures the tunneling current (or the gap between the tip and the cantilever). The cantilever displacement $z_c(x_f, t)$ causes the change in this gap according to (2.16) which in turn affects the value of the current. In this case, the measurement and the force location is constrained to the same position $x = x_f$ (tip position). According to the previous observations, in order to damp the mode, $x = x_f$ should be located near one of the singular points, corresponding to this mode. Here, $x = x_f$ is set to $0.81L = 405$ $\mu m$, which is between the singular points for the second and the third mode, in order to obtain a satisfactory damping of the two. This can be seen in Fig. 7.10 showing frequency response of shaped modal and total displacement. Comparing this figure with Fig. 7.3, where the $x = x_f = L$, a significant damping can be noticed. Fig. 7.11a and

Fig. 7.11b show the displacement at $x = x_f = 0.81L = 405\ \mu m$ in response to the excitation force from Fig. 7.8a and Fig. 7.8c, respectively. The contributions from the second and third mode to the total displacement are negligible.

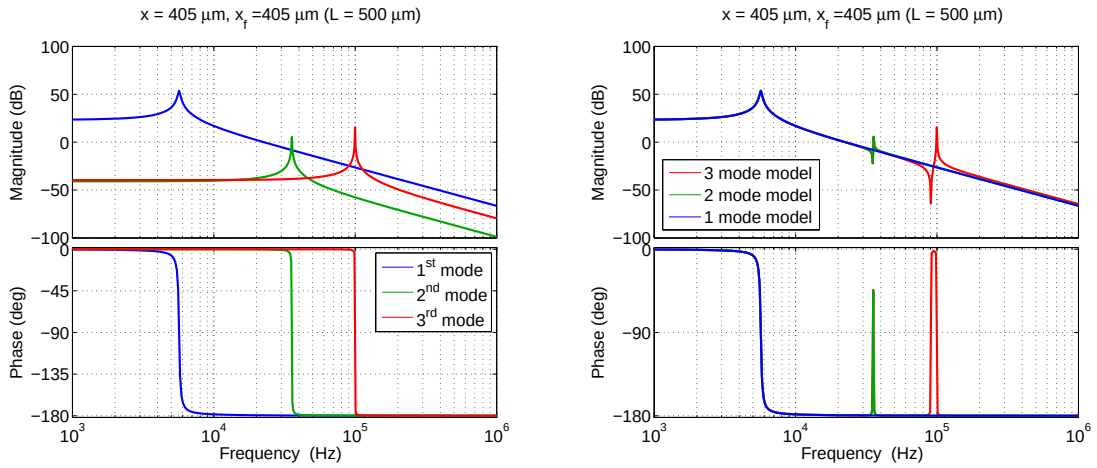


(a) (b)

Figure 7.10: Frequency response of (a) shaped modal and (b) total displacement (sum of shaped modes) when the applied input force and measured output displacement are at the distance $x = x_f = 0.81L = 405\ \mu m$.

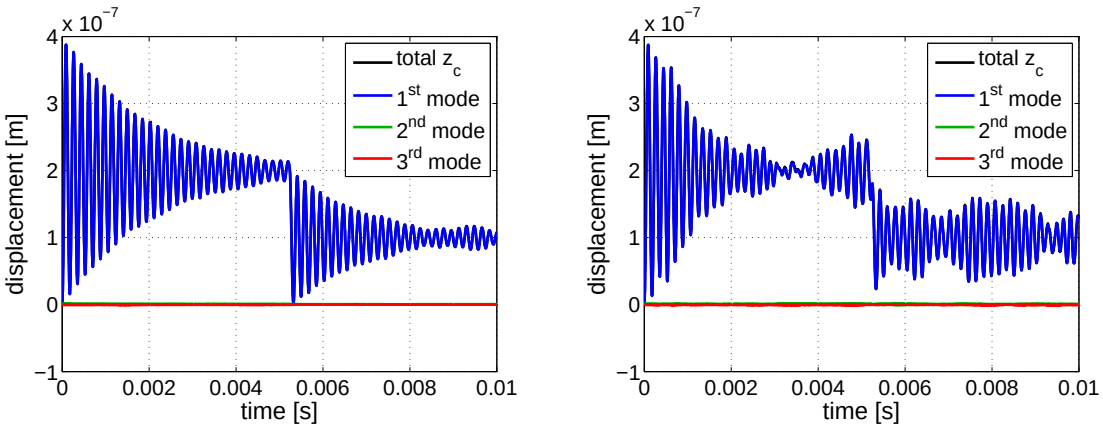


(a) (b)

Figure 7.11: Output displacement of the cantilever (shaped modal and total) for $x = x_f = 0.81L = 405\ \mu m$ for the input force with: (a) SNR = 30 dB (Fig. 7.8a). (b) SNR = 15 dB (Fig. 7.8c).

## 7.3 Tunneling current-based cantilever nanopositioning with electrostatic actuation and piezoelectric tip actuation

Fig. 7.12 shows the considered controlled vertical system (more details about its control is given in the following subsections). It consists of two closed-loops, one inside the other one

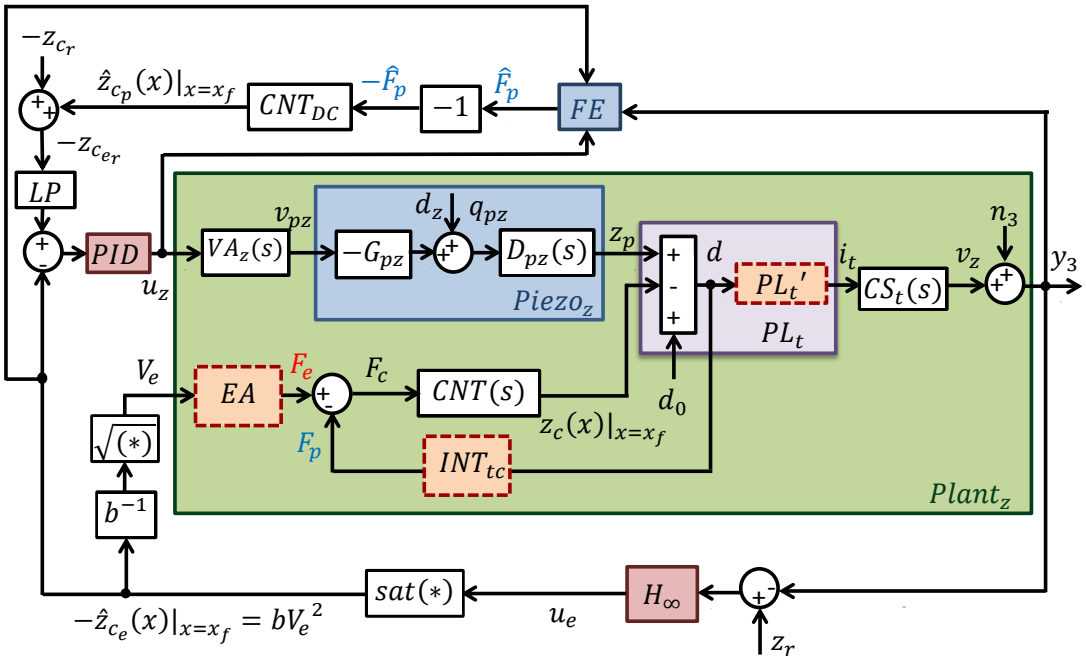


Figure 7.12: Closed-loop control of the vertical subsystem. The tunneling gap $d = z_t - z_c(x_f) = d_0 + z_p - z_c(x_f)$ is regulated by the $\mathcal{H}_\infty$ controller via cantilever position $z_c(x_f) = z_{c_p}(x_f) + z_{c_e}(x_f)$ by keeping the tunneling voltage $y_3$ (and as a result the tunneling gap) on the constant level of $z_r$. The interaction (proximity) force $F_p$ between the tip and the cantilever is estimated via $FE$ subsystem from the tunneling voltage $y_3$ and the control signals $u_z$ and $u_e$ and eliminated by adjusting the position of the tunneling tip $z_p$ via outer closed-loop with PID controller, tuned automatically using Matlab & Simulink software.

and proximity force estimator $FE$. The inner closed-loop consists of the nonlinear physical law $PL_t'$ with the current sensor $CS_t(s)$ and linear cantilever $CNT(s)$ actuated by the nonlinear electrostatic actuator $EA$, controlled by $H_\infty$ controller which is designed to control the tunneling gap on the constant level (*i.e.* tunneling voltage $y_3$ on the desired level $z_r$). Recalling equation (2.27), the nonlinear electrostatic actuator can be described by:

$$F_e(t) = -\frac{1}{2}\frac{\varepsilon_0 A_e}{l(t)^2} V_e(t)^2 \tag{7.8}$$

where $l(t) = l_0 + z_c(x_f, t)$, $l_0$ is the distance between the unbended cantilever and the electrostatic plate (see Fig. 2.4) and $z_c(x_f, t)$ is the total cantilever displacement at the tip position $x_f$, defined as the superposition of the displacements caused by the proximity and the elec-

trostatic forces as follows:

$$z_c(x_f,t) = z_{c_p}(x_f,t) + z_{c_e}(x_f,t) \tag{7.9}$$

Since in static conditions this force can be approximated as $F_e(t) \approx k_f z_{c_e}(x_f,t)$ (where $k_f$ is cantilever effective stiffness (force constant)), one gets the expression which links directly $z_{c_e}(x_f,t)$ with the input voltage $V_e(t)$ as follows:

$$z_{c_e}(x_f,t) \approx -\frac{1}{k_f}\frac{\varepsilon_0 A_e}{2l(t)^2}V_e(t)^2 = -\frac{1}{k_f}\frac{\varepsilon_0 A_e}{2(l_0+z_c(x_f,t))^2}V_e(t)^2 \tag{7.10}$$

Finally, since $l_0 >> z_c(x_f,t)$ further approximation of (7.10) gives (see also [Blanvillain et al., 2014]):

$$z_{c_e}(x_f,t) \approx -\frac{1}{k_f}\frac{\varepsilon_0 A_e}{2l_0^2}V_e(t)^2 = -bV_e(t)^2 \tag{7.11}$$

The nonlinear electrostatic actuator can be expressed finally as follows:

$$F_e(t) \approx k_f z_{c_e}(x_f,t) \approx -k_f b V_e(t)^2 \tag{7.12}$$

where the cantilever effective force constant $k_f$ is equal to the inverse of the cantilever DC gain $k_f = CNT_{DC}^{-1}$. In order to linearize the actuator an exact linearization is used as follows:

$$V_e(t) = \sqrt{\frac{u_e}{b}} \tag{7.13}$$

where $u_e = bV_e^2 = -\hat{z}_{c_e}(x_f)$. Therefore, the control signal $u_e$ (with minus sign) serves as an estimation of the cantilever position coming from the electrostatic force $F_e$. Since this force is negative it bends the cantilever downwards ($z_{c_e}(x_f) < 0$). The presence of the square root in (7.13) restricts $u_e$ to be positive. One can design the controller with anti-windup design, however here the positiveness of $u_e$ will be assured by restricting the cantilever displacement coming from the electrostatic force $z_{c_e}$ to be negative, therefore $u_e = \mathrm{sat}(u_e) = -\hat{z}_{c_e}$ almost ever and the saturation block is added only for the security reason. Recalling (5.8), the linearization of the nonlinear physical tunneling law $PL_t'$ around equilibrium point gives:

$$PL_t'(s) = \frac{i_t(s)}{d(s)} = -ki_{eq} = -\frac{i_t(s)}{z_c(s)} = PL_t(s) \tag{7.14}$$

Taking into account the two linearizations (7.13) and (7.14), the $H_\infty$ linear controller is based on the following linearized model from $u_e$ to $y_3$:

$$G_{u_e->y_3}(s) = -CS_t(s)ki_{eq}CNT(s)CNT_{DC}^{-1} \tag{7.15}$$

Once the inner loop is closed, a well tuned PID controls the tip position (and the cantilever position as well, since the gap is kept constant by the inner closed-loop). This two-loop scheme enables positioning the cantilever and tip above 1 nm, which is not possible with only one loop, since the gap must be kept below this distance. The force estimator $FE$ estimates the proximity force on the basis of the measured tunneling voltage $y_3$ and the control signals of the piezoelectric and electrostatic actuators ($u_z$ and $u_e$, respectively) and will be described in the last subsection. Since the total cantilever displacement is the sum of the

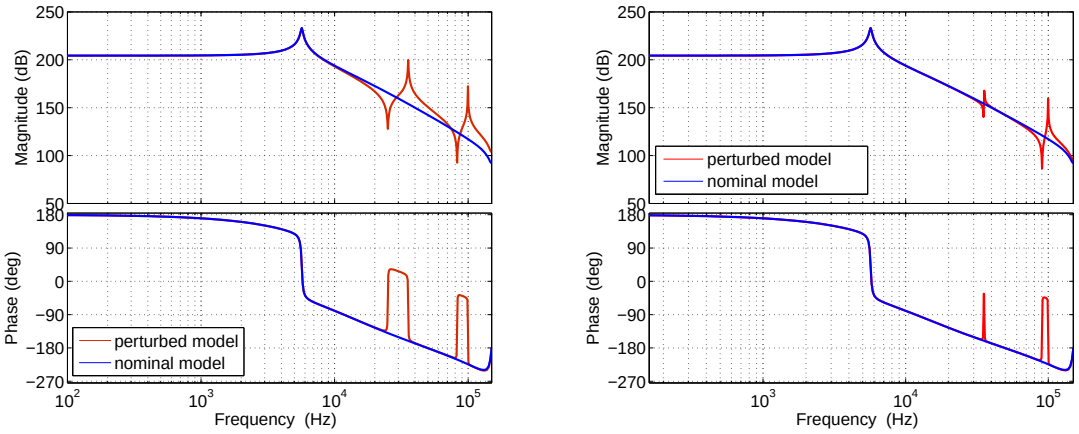


Figure 7.13: The perturbed 3-mode model (in red) and the nominal 1-mode model (in blue) in case of: (a) $x = x_f = L = 500\ \mu m$. (b) $x = x_f = 0.81L = 405\ \mu m$.

displacement components coming from the electrostatic and proximity forces (*i.e.* $z_c(x_f) = z_{c_e}(x_f) + z_{c_p}(x_f) \approx \frac{1}{k_f}(-F_p + F_e) = \frac{1}{k_f}F_c$ in the static case), knowing the estimated cantilever displacement $\hat{z}_{c_p}$ taken from the estimated proximity force $\hat{F}_p$ allows to adjust the reference for the cantilever displacement coming from the electrostatic force (with minus sign) $-z_{c_{e_r}}$ in such a way that the total cantilever displacement $z_c$ is kept on the reference level $z_{c_r}$. The low-pas filter $LP$ with cut-off frequency of 70 Hz is added on the reference $-z_{c_{e_r}}$ in order to eliminate the influence of its high frequency components on the tunneling current.

### 7.3.1 $\mathcal{H}_\infty$ design for tunneling gap control via electrostatically actuated cantilever

In this section $\mathcal{H}_\infty$ controller is designed for the two models corresponding to the two positions highlighted in the previous section (*i.e.* $x = x_f = L = 500\ \mu m$ and $x = x_f = 0.81L = 405\ \mu m$). In both cases the controller for the 3-mode model (called the perturbed model) is designed on the basis of the 1-mode model (called the nominal model) as shown in Fig. 7.13a and Fig. 7.13b. The linearized perturbed model from the input $u_e$ to the output $y_3$ (see Fig. 7.12) including the 3-mode model of the cantilever is given by:

$$G_{u_e->y_{3_p}}(s) = -CS_t(s)ki_{eq}CNT_{3m}(s)CNT^{-1}_{3m_{DC}} \tag{7.16}$$

where $CNT_{3m_{DC}}$ is the DC gain of the cantilever model $CNT_{3m}(s)$. The considered nominal model corresponds to model (7.16) but with 1-mode model of the cantilever and is given by:

$$G_{u_e->y_3}(s) = -CS_t(s)ki_{eq}CNT_{1m}(s)CNT^{-1}_{1m_{DC}} \tag{7.17}$$

The output multiplicative structure has been chosen to model the uncertain system (7.16) as

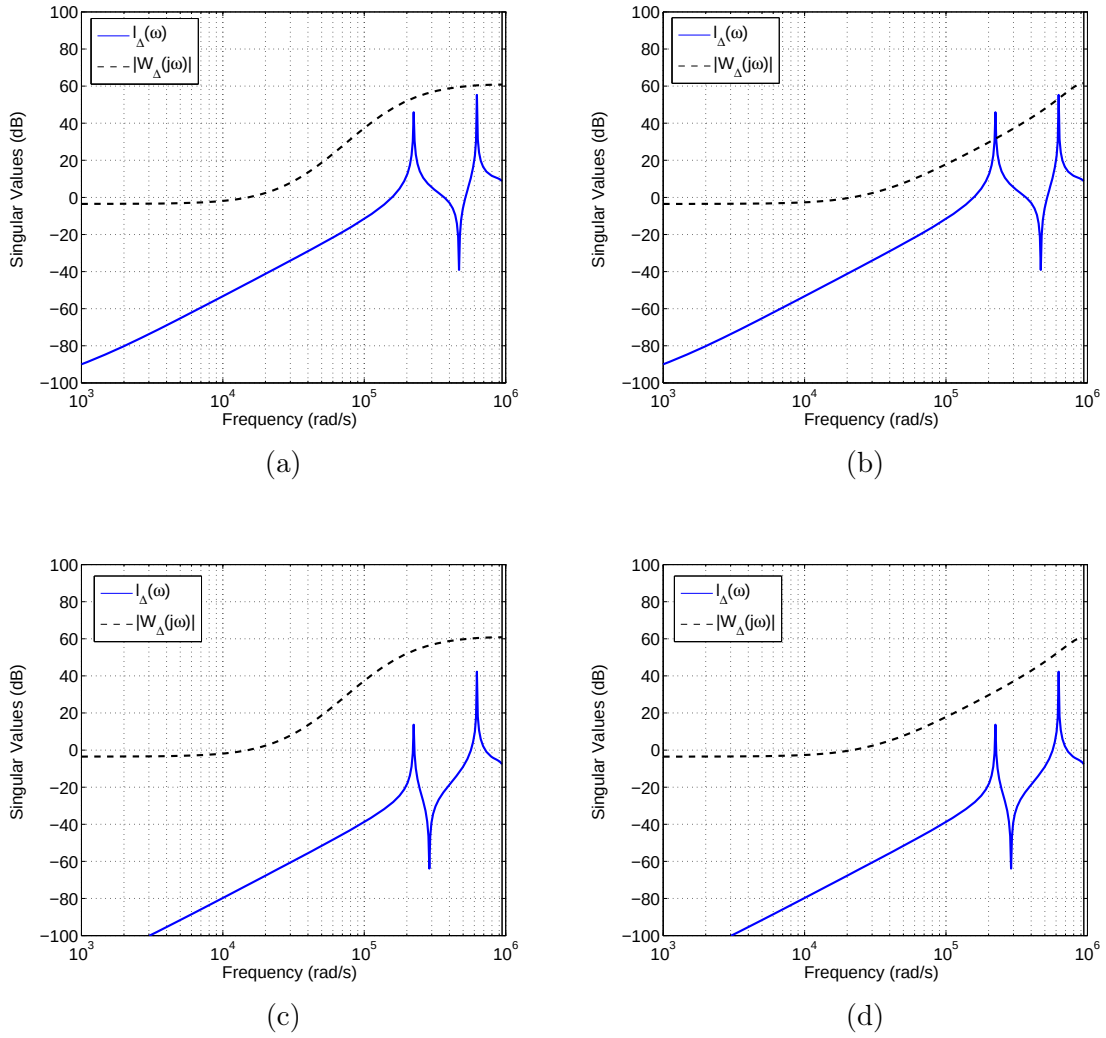


Figure 7.14: The relative errors $l_\Delta(\omega)$ together with their upper bounds $|W_\Delta(j\omega)|$ used for $H_\infty$ design: (a) $x = x_f = L = 500\ \mu m$ and $5^{\text{th}}$ order weight $W_\Delta(s)$. (b) $x = x_f = L = 500\ \mu m$ and $2^{\text{nd}}$ order weight $W_\Delta(s)$. (c) $x = x_f = 0.81L = 405\ \mu m$ and $5^{\text{th}}$ order weight $W_\Delta(s)$. (d) $x = x_f = 0.81L = 405\ \mu m$ and $2^{\text{nd}}$ order weight $W_\Delta(s)$.

follows:

$$G_{u_e->y_{3_p}}(s) = (1 + W_\Delta(s)\Delta(s))G_{u_e->y_3}(s) \tag{7.18}$$

where $\Delta(s)$ is any stable transfer function, which represents the normalized complex perturbations such that $|\Delta(j\omega)| \leq 1$, $\forall\omega$ and $W_\Delta(s)$ is a rational transfer function representing the uncertainty weight chosen as follows:

$$|W_\Delta(j\omega)| \geq |W_\Delta(j\omega)\Delta(j\omega)| = l_\Delta(\omega) = \left| \frac{G_{u_e->y_{3_p}}(j\omega) - G_{u_e->y_3}(j\omega)}{G_{u_e->y_3}(j\omega)} \right|, \forall\omega \tag{7.19}$$

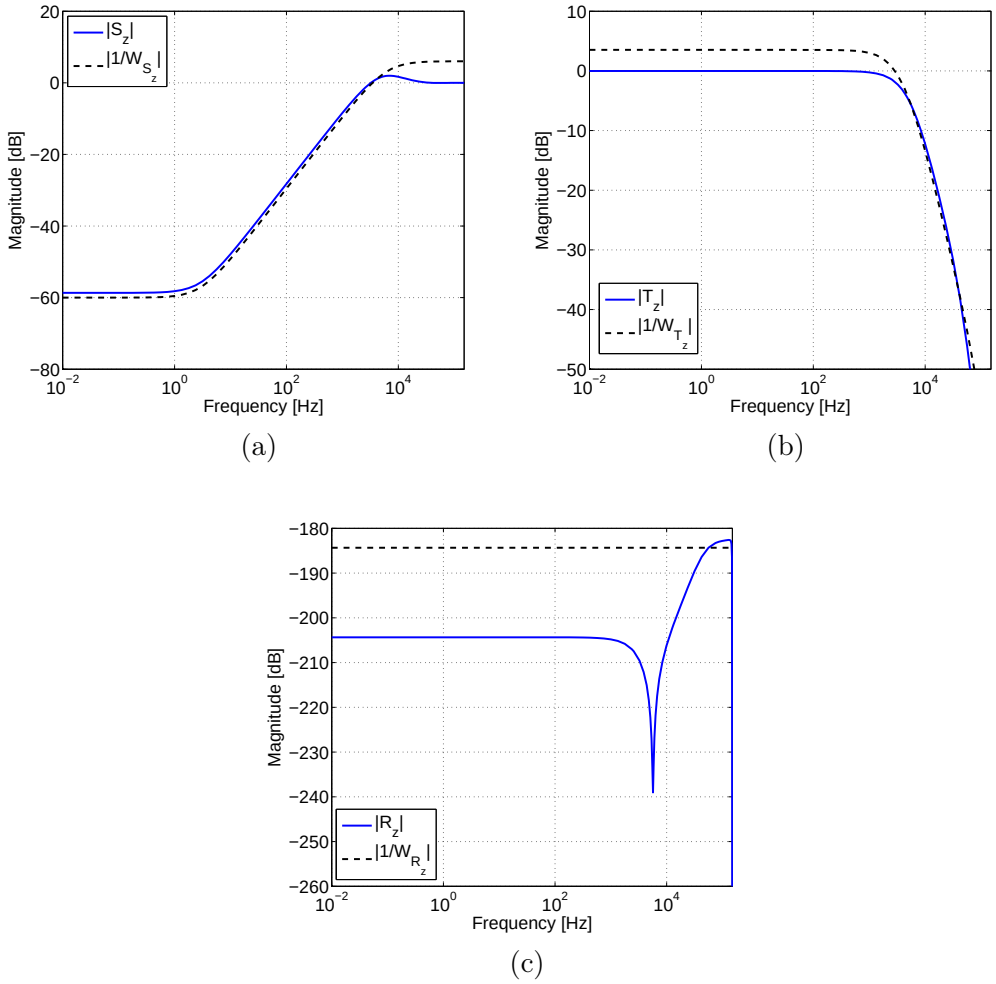


Figure 7.15: Sensitivity functions for the nominal plant and the obtained $H_\infty$ controller for the desired bandwidth 5 kHz and $2^{\text{nd}}$ order uncertainty weight $W_\Delta(s)$: a) Output sensitivity function. b) Complementary sensitivity function. c) Control sensitivity function.

where $l_\Delta(\omega)$ represents relative magnitude of the neglected dynamics (*i.e.* one chooses $W_\Delta(s)$ such that $|W_\Delta(j\omega)|$ is an upper bound on the relative errors $l_\Delta(\omega)$). Fig. 7.14 shows the relative errors $l_\Delta(\omega)$ together with $|W_\Delta(j\omega)|$ for the $5^{\text{th}}$ and $2^{\text{nd}}$ order weight $W_\Delta(s)$ with cross-over frequency of 5 kHz and for two cases, where $x = x_f = L = 500\ \mu m$ and $x = x_f = 0.81L = 405\ \mu m$ (for both cases $W_\Delta(s)$ are exactly the same). Since $W_\Delta(s)$ will shape the complementary sensitivity function, to assure good robustness margin, it is already constrained at low frequencies by the 3.5 dB from below. It can be seen that for the considered bandwidth 5 kHz, the $5^{\text{th}}$ order weight $W_\Delta(s)$ successfully bounds the relative errors from above for the two cases. For the $2^{\text{nd}}$ order weight, the robust stability of the model corresponding to $x = x_f = L = 500\ \mu m$ is not achieved, while for the case where $x = x_f = 0.81L = 405\ \mu m$ it is. Moreover, in the second case the bandwidth can be furtherly increased, since there is still a little space for robust stability. The following weights have been chosen to shape the

sensitivity functions:

$$W_{S_z}(s) = \frac{s + 6.283 \times 10^4}{2s + 62.83} \tag{7.20}$$

$$W_{T_z}(s) = W_\Delta(s) \tag{7.21}$$

$$W_{R_z}(s) = -G_t k i_{eq}/10 = -1.65 \times 10^9 \tag{7.22}$$

Fig. 7.15 shows the sensitivity functions shaped by the associated weights ($2^{\text{nd}}$ order uncertainty weight $W_\Delta(s)$ in this case). The optimal cost function $\gamma = 1.35$ has been obtained. Fig. 7.16 shows the reference tracking corresponding to the two cases and weights. The open-loop response of the model has been scaled by its gain in order to be with the same scale with the closed-loop one. The performance achieved is the same apart from the case where robust stability is not achieved ($x = x_f = L = 500\ \mu m$ and $2^{\text{nd}}$ order weight $W_\Delta(s)$). One can conclude that proper location of the actuator and sensor allows to reduce the order of

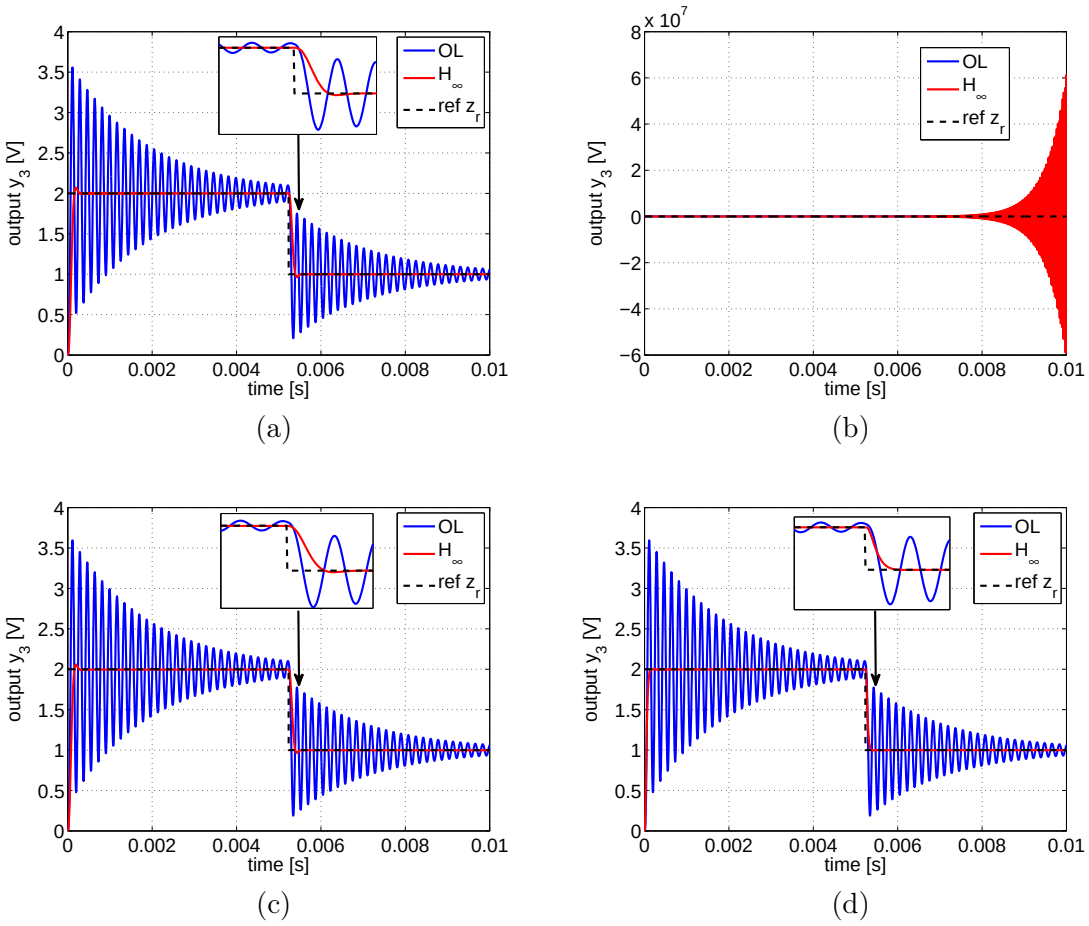


Figure 7.16: $H_\infty$ control of the linearized model from the input $u_e$ to the output $y_3$ (without the noise) (the open- loop response of the plant has been scaled by its gain in order to be with the same scale with the closed-loop one): (a) $x = x_f = L = 500\ \mu m$ and $5^{\text{th}}$ order weight $W_\Delta(s)$. (b) $x = x_f = L = 500\ \mu m$ and $2^{\text{nd}}$ order weight $W_\Delta(s)$. (c) $x = x_f = 0.81L = 405\ \mu m$ and $5^{\text{th}}$ order weight $W_\Delta(s)$. (d) $x = x_f = 0.81L = 405\ \mu m$ and $2^{\text{nd}}$ order weight $W_\Delta(s)$.

the controller and/or increase the desired bandwidth. Fig. 7.17a and Fig. 7.17b show the frequency response (magnitude) of the scaled open-loop and closed-loop system for the two considered cases. The comparison with the simple PID controller has been shown in Fig. 7.18.

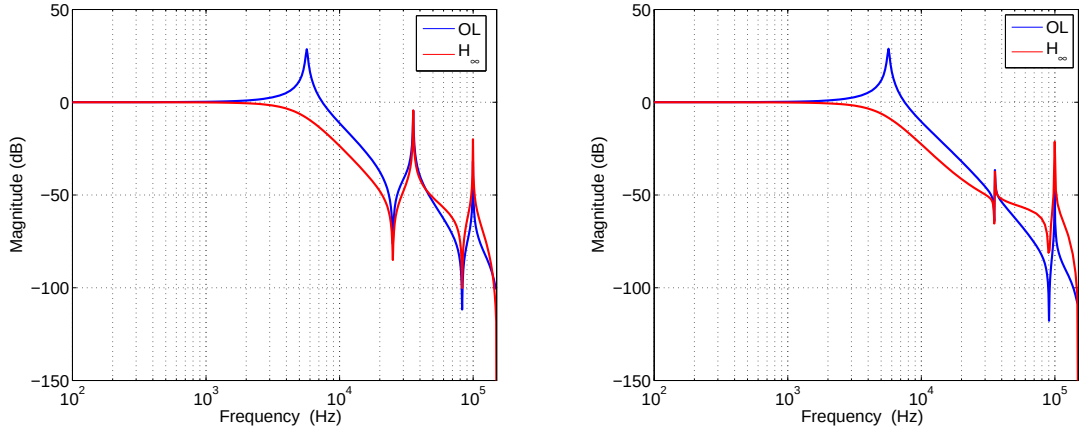


(a) (b)

Figure 7.17: Bode diagrams of the scaled open-loop (OL) and closed-loop system with $H_\infty$ controller (with $5^{\text{th}}$ order weight $W_\Delta(s)$) and the perturbed plant model: (a) $x = x_f = L = 500\ \mu m$. (b) $x = x_f = 0.81L = 405\ \mu m$.

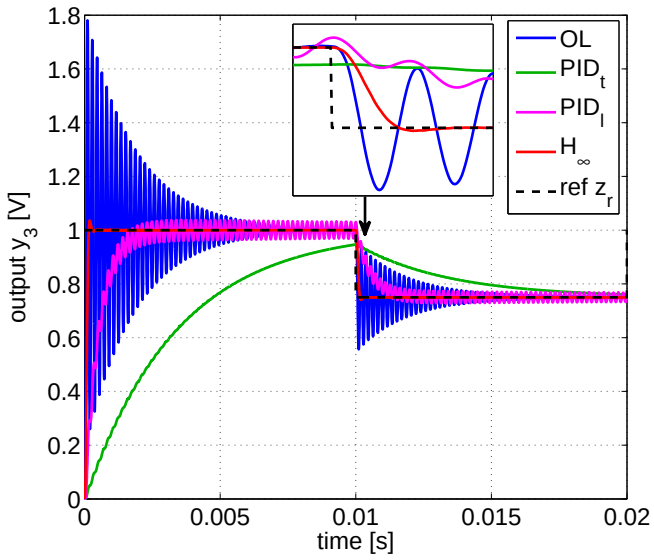


Figure 7.18: Comparison of $H_\infty$ control with the PID controller ($\text{PID}_\text{t}$ is the closed-loop response with the first shot parameters of PID proposed by Matlab & Simulink and $\text{PID}_\text{l}$ refers to the fastest possible PID controller before the stability loss).

The PID gains have been tuned using Matlab & Simulink software. The proposed solution ($\text{PID}_\text{t}$) has quite low bandwidth and can be increased, however this introduces at some point significant oscillations until the system is on the stability limit ($\text{PID}_\text{l}$). The model-based $H_\infty$ controller clearly outperforms PID.

### 7.3.2 Cantilever positioning via piezoelectrically actuated tip with proximity force compensation

Recalling equation (2.24), the proximity interaction force between the tunneling tip and the cantilever is expressed as follows:

$$F_p(t) = INT_{tc}(d(t)) = \begin{cases} -HR/6d(t)^2, & d(t) \geq a_p \\ -HR/6a_p^2 + \frac{4}{3}E^*_{eff}\sqrt{R}(a_p - d(t))^{3/2}, & d(t) < a_p \end{cases} \tag{7.23}$$

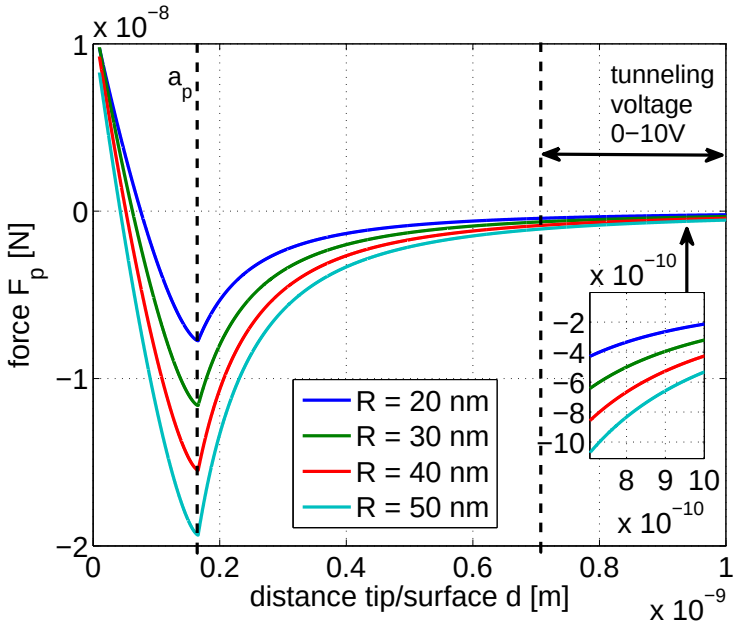


Figure 7.19: Simulated proximity force for different tip curvature radius $R$. Here, the interatomic distance $a_p = 0.166$ nm. The inset plot shows the zoom of the proximity forces in the tunneling voltage measuring range (*i.e.* 0-10 V, which corresponds to the tip/surface distance 0.7-1 nm).

Fig. 7.19 shows the behavior of proximity force (7.23) for the following numerical values: different tip curvature radius $R = [20, 30, 40, 50]$ nm, the Hamaker constant $H = 6.4 \times 10^{-20}$ J, interatomic value $a_p = 0.166$ nm, the effective contact stiffness $E^*_{eff} = [(1 - v_t^2)/E_t + (1 - v^2)/E]^{-1}$ with the Poisson ratios $v_t = 0.28$ and $v = 0.17$ and the elastic moduli $E_t = 129$ GPa and $E = 180$ GPa of the tip and the cantilever, respectively. As mentioned before, the interatomic value $a_p$ separates the region where only attractive van der Waals force is present

from the region where the repulsive adhesive force is added to the van der Waals force. When the two forces become equal (proximity force $F_p = 0$) the materials are in mechanical contact and the total net proximity force starts to be repulsive. In the considered case the measuring range of the tunneling voltage is constrained to the standard value of the data acquisition cards between 0 and 10 V, which corresponds to the tip/surface distance below 1 nm and down to 0.7 nm and therefore during normal operation (where the tunneling current can be measured) only the attractive proximity force should appear (non-contact mode). The proximity force could be estimated from the measurement of $z_c(x_f)$ if the cantilever displacement sensor (like in AFM) was available as follows (in static case):

$$\hat{F}_p = \hat{F}_e - F_c \approx k_f \hat{z}_{c_e}(x_f) - k_f z_c(x_f) = k_f u_e - k_f z_c(x_f) \tag{7.24}$$

In the considered case the only available measurement is the tunneling voltage $y_3$. The proximity force can be then approximated from the measurement $y_3$ and the control signals $u_e$ and $u_z$ as proposed below:

$$\hat{F}_p = \hat{F}_e - \hat{F}_c \approx k_f u_e - k_f \hat{z}_c(x_f) \tag{7.25}$$

where $\hat{z}_c(x_f)$ is given by:

$$\hat{z}_c(x_f) = \hat{z}_t - \hat{d} = \underbrace{(-G_{pz}G_{vz}u_z + d_0)}_{\hat{z}_t} - \underbrace{\left\{-\frac{1}{k}\ln\left(\frac{y_3}{G_t g V_b}\right)\right\}}_{\hat{d}} \tag{7.26}$$

Fig. 7.20 shows the performance of the two closed-loop scheme from Fig. 7.12, when the proximity force is absent. The tunneling current is kept on the constant level of 1 nA (which corresponds to the tunneling voltage of 1 V) via electrostatic actuator, by the $H_\infty$ controller as shown in Fig. 7.20a. This corresponds to the distance $d = 0.84$ nm. The corresponding control signal $u_e$ is shown in Fig. 7.20b. Note that $u_e = -\hat{z}_{c_e}$ (*i.e.* it is the estimation of the $z_{c_e}$ taken with minus sign). The displacements $z_t$ and $z_c$ of the tip and the cantilever, respectively are shown in Fig. 7.20c. One can see that the PID controller of the outer loop controls the cantilever position $z_c$ around the reference $z_{c_r}$ by adjusting the tip position $z_t$ via piezoelectric actuator (it is possible since the gap between the tip and the cantilever is already kept on the constant level of 0.84 nm by the $H_\infty$ controller of the inner loop). The low-pass filter $LP$ added on the cantilever reference allows to reduce the peaks appearing in the tunneling current measurement due to the square signal of this reference. The creep phenomenon which acts as a disturbance $d_z$ over the tip position has been successfully canceled (which can be also seen on the control signal $u_z$ of the tip, which drifts as shown in Fig.7.20d).

Fig. 7.21 shows the performance of the two closed-loop scheme in the presence of the proximity force. First, the case when the creep $d_z$ of the tip is not present is considered. Fig.7.21a shows the tip and the cantilever displacements without ($z_{tu}$ and $z_{cu}$) and with ($z_{tc}$ and $z_{cc}$) proximity force compensation. Without compensation the cantilever cannot be positioned at the reference signal $z_{c_r}$, since the force $-F_p$ attracts it upwards. As a result the tip moves upwards as well in order to keep the tunneling gap constant. When the interaction force is compensated, the proper cantilever and tip positioning is possible. The estimated proximity force is shown in Fig. 7.21b. Notice that Fig. 7.21c and Fig. 7.21d

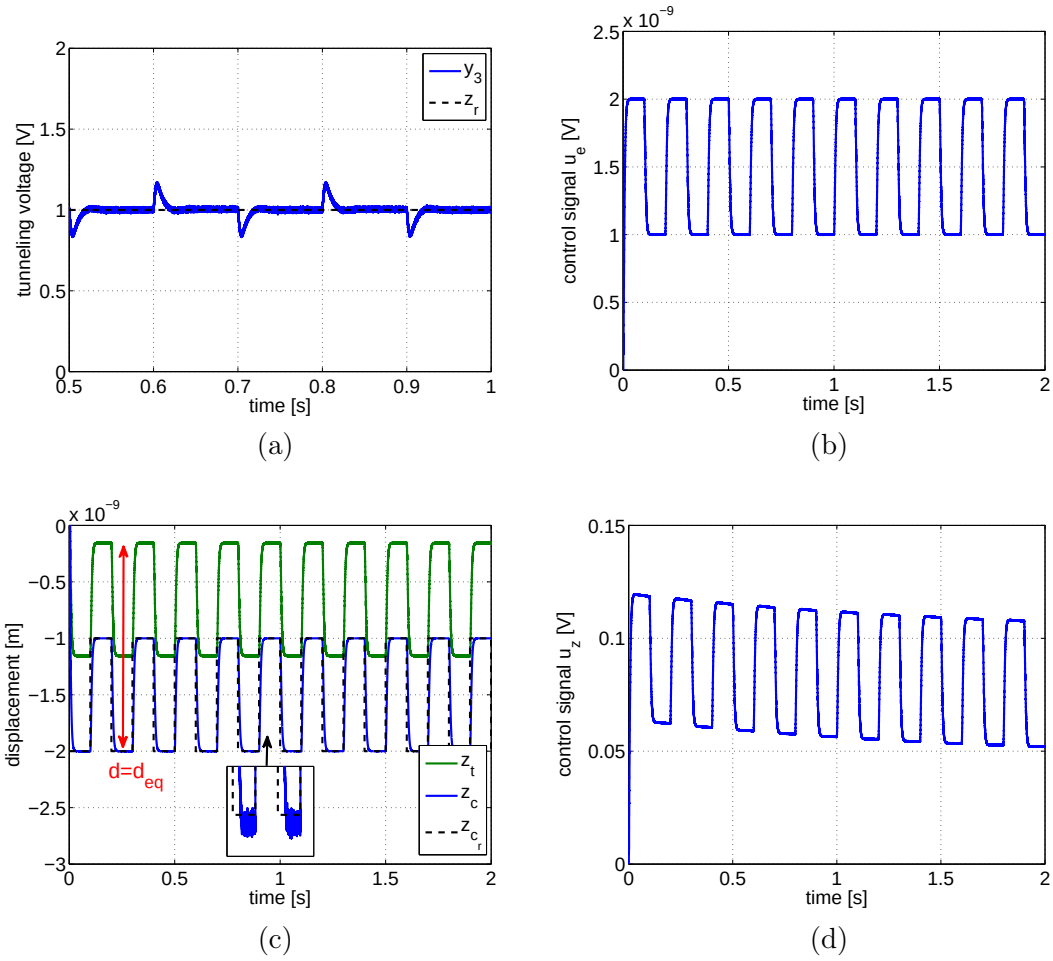


Figure 7.20: The performance of the two closed-loop scheme from Fig. 7.12 when the proximity force $F_p$ is absent: (a) Tunneling voltage $y_3$. (b) Control signal $u_e$ of the inner loop with $H_\infty$ controller. (c) Cantilever and tip displacements. (b) Control signal $u_z$ of the outer loop with PID controller.

correspond to the case when the creep phenomenon of piezoactuated tip is present. In this case the proximity force cannot be well estimated, however the results are still much better than without compensation. The performance could be improved when the creep model of the piezo was taken into account in the proximity force estimator. It should be stressed that this compensation depends on the accuracy of the parameters used in the estimator and other phenomena like creep.

## 7.4 Conclusion

In this chapter simulation results for the 3-mode cantilever model have been presented. Knowing the singular points of the modal shape functions allows to place the actuator/sensor near

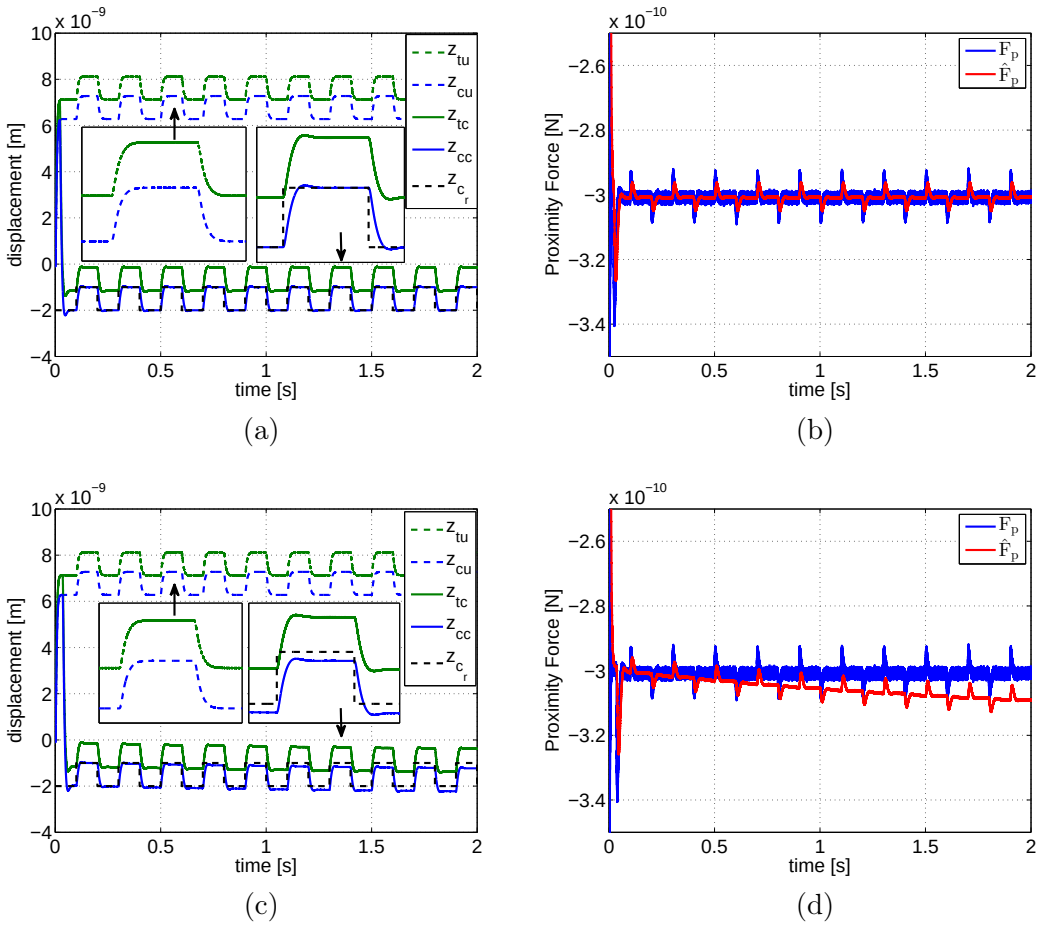


Figure 7.21: The performance of the two closed-loop scheme from Fig. 7.12 when the proximity force $F_p$ is present: (a) Tip and cantilever displacements without ($z_{tu}$ and $z_{cu}$) and with ($z_{tc}$ and $z_{cc}$) proximity force compensation (without the creep phenomenon). (b) Estimated proximity force $F_p$ (without the creep phenomenon). (c) Tip and cantilever displacements without ($z_{tu}$ and $z_{cu}$) and with ($z_{tc}$ and $z_{cc}$) proximity force compensation (with the creep phenomenon). (d) Estimated proximity force $F_p$ (with the creep phenomenon).

them in order to damp the associated modes and as a result to reduce the order and increase the bandwidth of the system. The application of such a 3-mode cantilever nanopositioning has been considered on the basis of the tunneling current. The tunneling gap is kept constant via electrostatically actuated cantilever by $H_\infty$ control. The positioning over the distance of 1 nm was possible using a second closed-loop, which controls the cantilever position through the tip position via piezoelectrically actuated tunneling tip. To that end, a proximity force estimator has been designed in order to compensate it, on the basis of the measured tunneling current and two control signals.

Chapter 8

# Conclusions and perspectives

## Conclusions:

Summing up, the main goal of this thesis was to develop 3D model for the nanopositioning system corresponding to the experimental set-up developed in GIPSA-lab, its proper control with high accuracy over possibly high bandwidth and experimental validation of the proposed techniques. To that end, the platform has been equipped for 3D operation with capacitive sensors for both X and Y horizontal displacements in addition to the vertical actuation.

The developed 3D model finally consists of piezoelectrically actuated scanning horizonal X and Y axes and vertical probing Z axis. The latter is equipped with piezoelectrically actuated tunneling tip (like in STM) and with electrostatically actuated micro-cantilever (like in AFM). Such a model is quite complex and due to several nonlinearities (exponential nonlinearity of tunneling current, hysteresis of piezoelectric actuators, quadratic nonlinearity of electrostatic actuator) and other adverse phenomena (creep, vibration, cross-couplings between piezo axes, high measurement noise of tunneling current sensor), it is a real challenge to control it with nanoscale accuracy. First, hysteresis and creep phenomena exhibited by piezoelectric actuators in horizontal axes have been compensated in real-time using different techniques (classical Prandtl-Ishlinskii (PI) model, its modified version (MPI), disturbance observer (DOB) and a combination of MPI with DOB, as well as an adaptive approach). An identification with subsequent order reduction of such linearized horizontal 2D model allowed to design several linear controllers (LQG/LTR, SISO $\mathcal{H}_\infty$, MIMO $\mathcal{H}_\infty$) for piezo vibration and cross-coupling reduction between X and Y axes. Their comparative experimental validation has been presented. The real challenge is a control of the vertical motion (Z axis), based on the tunneling current phenomenon, due to several requirements (nanoscale operating range, high sensitivity to measurement noise and external disturbances, sharp tip, clean surface etc.). A two-stage procedure for approaching the tip to the surface and obtaining tunneling current has been used (coarse approach done manually and fine approach done automatically). Tunneling current proper control using pole placement with sensitivity functions shaping methodology has been experimentally validated. Finally, illustrative results for three applications have been presented:

- 3D nanopositioning application (without cantilever motion), validated experimentally. The tunneling tip tracks prespecified reference signals in X, Y and Z directions (in the Z direction the reference is called "virtual surface", since it imitates surface variations). The adverse phenomena of hysteresis, creep, vibrations and cross-couplings in the horizontal axes were eliminated using above mentioned techniques with tunneling current

control in vertical axis using pole placement with sensitivity functions shaping methodology.

- STM-like application, validated in simulations. The tip is moved along the X and Y axes, while the reference for the Z axis is kept constant. To that end, two control strategies have been compared: SISO PID decentralized control (3 PIDs, each for one axis, with decoupling compensators) and one MIMO LQI centralized controller. In the first approach, the surface topography is retrieved from the control signal of the vertical piezo (classical approach) and in the second approach it is reconstructed via Kalman observer (proposed approach). The second approach gave more satisfactory results.

- Multi-mode cantilever positioning application, tested in simulations. A scheme consisting of two closed-loops (an inner closed-loop with electrostatically actuated cantilever using $\mathcal{H}_\infty$ controller and an outer closed-loop with piezoelectrically actuated tunneling tip using PID controller) allowed to position the cantilever on a distance larger than 1 nm. The interaction force appearing between the tip and the cantilever has been compensated via proximity force estimator.

## Perspectives:

Several perspectives/extensions can be deduced in view of the obtained results:

- The multi-mode cantilever model tested in simulations needs to be validated in experiments. To that end, the sampling frequency should be increased in order to catch at least two modes. However, the acquisition cards in the present configuration limit the sampling frequency to 30 kHz. High speed data acquisition, based for example on FPGA technology can be used for that purpose.

- Cross-couplings from the horizontal to the vertical axes should be compensated. However, it is hard to identify them from the tunneling-current measurement, since it is affected also by the surface variations (for that purpose the surface should be ideally flat). For high frequencies, the tip can move outside the operating range as well, resulting in loss of tunneling current.

- For the second application (STM-like application), in order to be experimentally validated, a proper reference grating (surface) should be used. Here instead, a "virtual surface" was imposed as the reference in the vertical direction, which only imitated the real surface (the first application - 3D nanopositioning). For that reason, the first application has been tested in experiments, while the second one in simulations only.

- Accurate model parameters are needed for the proximity force compensation using the proposed estimator. Adding for example another sensor which measures the cantilever displacement could help with exact force estimation.

# Bibliography


Abramovitch, D.Y., Andersson, S.B., Pao, L. Y., and Schitter, G. (2007). "A Tutorial on the Mechanisms, Dynamics, and Control of Atomic Force Microscopes". In: *2007 American Control Conference (ACC 2007)*, pp. 3488–3502 (cit. on pp. 6, 11, 14, 118).

Ahmad, I. (2011). "Analyse et commande d'un système de mesure à courant tunnel". PhD thesis. GIPSA-Lab, l'Université de Grenoble (cit. on p. 1).

Ahmad, I., Voda, A., and Besançon, G. (2010). "Robust $\mathcal{H}_\infty$ control of a scanning tunneling microscope under parametric uncertainties". In: *2010 American Control Conference (ACC 2010)*, pp. 6555–6560 (cit. on p. 19).

Ahmad, I., Voda, A., and Besancon, G. (2012a). "Experimental Validation of $\mathcal{H}_\infty$ SISO control for high performance tunneling current measurement system and MIMO extension". In: *2012 IEEE International Conference on Control Applications (CCA 2012)*, pp. 581–586 (cit. on pp. 19, 20).

Ahmad, I., Voda, A., Besancon, G., and Buche, G. (2012b). "Robust digital control approach for high performance tunneling current measurement system". In: *Control Engineering Practice* 20(7), pp. 643–653 (cit. on pp. 19, 94, 104, 117).

Alexander, S., Hellemans, L., Marti, O., Schneir, J., Elings, V., Hansma, P. K., Longmire, M., and Gurley, J. (1989). "An atomic-resolution atomic-force microscope implemented using an optical lever". In: *Journal of Applied Physics* 65(1), pp. 164–167 (cit. on p. 19).

Amin-Shahidi, D. and Trumper, D.L. (2013). "Improved charge amplifier using hybrid hysteresis compensation". In: *Review of Scientific Instruments* 84(8), p. 085115 (cit. on p. 17).

Ang, W.T., Khosla, P.K., and Riviere, C.N. (2007). "Feedforward Controller With Inverse Rate-Dependent Model for Piezoelectric Actuators in Trajectory-Tracking Applications". In: *IEEE Transactions on Mechatronics* 12(2), pp. 134–142 (cit. on pp. 13, 16, 37, 42).

Aphale, S.S., Devasia, S., and Moheimani, S.O.R. (2008). "High-bandwidth control of a piezoelectric nanopositioning stage in the presence of plant uncertainties". In: *Nanotechnology* 19(12), pp. 125503–125512 (cit. on p. 17).

Bashash, S. and Jalili, N. (2008). "A Polynomial-Based Linear Mapping Strategy for Feedforward Compensation of Hysteresis in Piezoelectric Actuators". In: *Journal of Dynamic Systems, Measurement, and Control* 130(3), p. 031008 (cit. on p. 13).

Bertotti, G. and Mayergoyz, I.D. (2006). *The Science of Hysteresis: Mathematical Modeling and Applications*. New York, NY, USA: Academic Press (cit. on p. 12).

Bhikkaji, B. and Moheimani, S.O.R. (2008). "Integral Resonant Control of a Piezoelectric Tube Actuator for Fast Nanoscale Positioning". In: *IEEE/ASME Transactions on Mechatronics* 13(5), pp. 530–537 (cit. on p. 17).

Binnig, G. and Rohrer, H. (1986). "Scanning Tunneling Microscopy". In: *IBM Journal of Research and Development* 30, pp. 355–369 (cit. on pp. 5, 11).

Binnig, G., Quate, C. F., and Gerber, Ch. (1986). "Atomic force microscope". In: *Physical Review Letters* 56(9), pp. 930–933 (cit. on p. 6).

Blanvillain, S. (2010). "Contrôle nanoscopique du mouvement par courant tunnel: étude et réalisation". PhD thesis. GIPSA-Lab, l'Université de Grenoble (cit. on pp. 1, 19).

Blanvillain, S., Voda, A., and Besancon, G. (2008). "Pull-in control during nanometric positioning by near field position sensing". In: *47th IEEE Conference on Decision and Control (CDC 2008)*, pp. 5194–5199 (cit. on p. 19).

Blanvillain, S., Voda, A., Besancon, G., and Buche, G. (2009). "The tunnel current as a subnanometer motion sensor". In: *2009 European Control Conference (ECC 2009)*, pp. 5003–5008 (cit. on p. 19).

Blanvillain, S., Voda, A., Besancon, G., and Buche, G. (2014). "Subnanometer Positioning and Drift Compensation With Tunneling Current". In: *IEEE Transactions on Control Systems Technology* 22(1), pp. 180–189 (cit. on pp. 19, 121, 133).

Brinkerhoff, R. and Devasia, S. (2000). "Output Tracking for Actuator Deficient/Redundant Systems: Multiple Piezoactuator Example". In: *Journal of Guidance, Control and Dynamics* 23(2), pp. 370–373 (cit. on p. 19).

Butterworth, J.A., Pao, L.Y., and Abramovitch, D.Y. (2008). "Architectures for Tracking Control in Atomic Force Microscopes". In: *Proceedings of the 17th IFAC World Congress (IFAC 2008)*. Seoul, Korea, pp. 8236–8250 (cit. on p. 16).

Chuang, N., Petersen, I.R., and Pota, H.R. (2011). "Robust $H_\infty$ control in fast atomic force microscopy". In: *2011 American Control Conference (ACC 2011)*, pp. 2258–2265 (cit. on p. 17).

Chuntao, L. and Yonghong, T. (2004). "A neural networks model for hysteresis nonlinearity". In: *Sensors and Actuators A: Physical* 112(1), pp. 49 –54 (cit. on p. 13).

Clayton, G.M., Tien, S., Leang, K.K., Zou, Q., and Devasia, S. (2009). "A Review of Feedforward Control Approaches in Nanopositioning for High-Speed SPM". In: *Journal of Dynamic Systems, Measurement, and Control* 131(6), pp. 061101–19 (cit. on p. 17).

Croft, D. and Devasia, S. (1999). "Vibration compensation for high speed scanning tunneling microscopy". In: *Review of Scientific Instruments* 70(12), pp. 4600–4605 (cit. on p. 15).

Croft, D., Shed, G., and Devasia, S. (2001). "Creep, Hysteresis, and Vibration Compensation for Piezoactuators: Atomic Force Microscopy Application". In: *Journal of Dynamic Systems Measurement and Control* 123 (1) (cit. on pp. 14, 15, 17, 111, 112).

Cruz-Hernandez, J.M. and Hayward, V. (2001). "Phase control approach to hysteresis reduction". In: *IEEE Transactions on Control Systems Technology* 9(1), pp. 17–26 (cit. on p. 13).

Das, S.K., Pota, H.R., and Petersen, I.R. (2012). "Multi-variable resonant controller for fast atomic force microscopy". In: *2012 2nd Australian Control Conference (AUCC 2012)*, pp. 448–453 (cit. on pp. 18, 19).

Derjaguin, B.V, Muller, V.M, and Toporov, Y.P. (1975). "Effect of contact deformations on the adhesion of particles". In: *Journal of Colloid and Interface Science* 53(2), pp. 314 –326 (cit. on p. 29).

Devasia, S., Eleftheriou, E., and Moheimani, S.O.R. (2007). "A Survey of Control Issues in Nanopositioning". In: *IEEE Transactions on Control Systems Technology* 15(5), pp. 802–823 (cit. on pp. 11, 14, 19).

Dong, R. and Tan, Y. (2009). "A modified Prandtl–Ishlinskii modeling method for hysteresis". In: *Physica B: Condensed Matter* 404(8–11), pp. 1336 –1342 (cit. on p. 13).

Dong, R., Tan, Y., Chen, H., and Xie, Y. (2008). "A neural networks based model for rate-dependent hysteresis for piezoceramic actuators". In: *Sensors and Actuators A: Physical* 143(2), pp. 370 –376 (cit. on p. 13).

Doyle, J.C. and Stein, G. (1979). "Robustness with observers". In: *IEEE Transactions on Automatic Control*, pp. 607–611 (cit. on pp. 18, 66).

Doyle, J.C. and Stein, G. (1981). "Multivariable Feedback Design: Concepts for a Classical/Modern Synthesis". In: *IEEE Transactions on Automatic Control* 26(1), pp. 4–16 (cit. on pp. 18, 66).

El-Shaer, A.H., Janaideh, M.A., Krejci, P., and Tomizuka, M. (2013). "Robust performance enhancement using disturbance observers for hysteresis compensation based on generalized

Prandtl-Ishlinskii model". In: *Journal of Dynamic Systems, Measurement, and Control* 135(5), p. 051008 (cit. on p. 17).

García, R. and San Paulo, A. (2000). "Dynamics of a vibrating tip near or in intermittent contact with a surface". In: *Physical Review B* 61 (20), R13381–R13384 (cit. on p. 28).

Gentili, M., Giovannella, C., and Selci, S. (1993). *Nanolithography: A Borderland Between STM, EB, IB and X-Ray Lithographies*. Norwell, MA: Kluwer: NATO ASI Series E: Applied Science (cit. on p. 7).

Giri, F. and Bai, E.-W. (2010). *Block-oriented nonlinear system identification*. Springer-Verlag (cit. on p. 111).

Gu, G.-Y. and Zhu, L.-M. (2010). "High-speed tracking control of piezoelectric actuators using an ellipse-based hysteresis model". In: *Review of Scientific Instruments* 81(8), p. 085104 (cit. on p. 13).

Gu, G.-Y. and Zhu, L.-M. (2011). "Modeling of rate-dependent hysteresis in piezoelectric actuators using a family of ellipses". In: *Sensors and Actuators A: Physical* 165(2), pp. 303 –309 (cit. on p. 13).

Gu, G.-Y., Zhu, L.-M., and Su, C.-Y. (2014a). "Modeling and Compensation of Asymmetric Hysteresis Nonlinearity for Piezoceramic Actuators With a Modified Prandtl-Ishlinskii Model". In: *IEEE Transactions on Industrial Electronics* 61(3), pp. 1583–1595 (cit. on p. 16).

Gu, G.-Y., Zhu, L.-M., Su, C.-Y., Ding, H., and Fatikow, S. (2014b). "Modeling and Control of Piezo-Actuated Nanopositioning Stages: A Survey". In: *IEEE Transactions on Automation Science and Engineering* PP(99), pp. 1–20 (cit. on pp. 12, 14, 16).

Habib, H., Rehman, O.U., Pota, H.R., and Petersen, I.R. (2012). "Internal reference model based optimal LQG controller for atomic force microscope". In: *12th International Conference on Control Automation Robotics Vision (ICARCV 2012)*, pp. 294–299 (cit. on pp. 17, 19, 65).

Halim, D. and Moheimani, S.O.R. (2001). "Spatial resonant control of flexible structures-application to a piezoelectric laminate beam". In: *IEEE Transactions on Control Systems Technology* 9(1), pp. 37–53 (cit. on p. 18).

Horowitz, R., Chen, T.-L., Oldham, K., and Li, Y. (2004). *Microactuators for Dual-Stage Servo Systems in Magnetic Disk Files*. Berlin, Germany: Springer-Verlag, pp. 951–981 (cit. on p. 19).

Hu, X., Guo, W., Huang, T., and Chen, B.M. (1999). "Discrete-time LQG/LTR dual-stage controller design and implementation for high track density HDDs". In: *1999 American Control Conference (ACC 1999)*. Vol. 6, pp. 4111–4115 (cit. on pp. 7, 18, 66).

Hughes, D. and Wen, J.T. (1997). "Preisach modeling of piezoceramic and shape memory alloy hysteresis". In: *Smart Materials and Structures* 6(3), p. 287 (cit. on p. 16).

Janaideh, M.A., Su, C.-Y., and Rakheja, S. (2008). "Development of the rate-dependent Prandtl–Ishlinskii model for smart actuators". In: *Smart Materials and Structures* 17(3), p. 035026 (cit. on p. 13).

Janaideh, M.A., Rakheja, S., and Su, C.-Y. (2009a). "A generalized Prandtl–Ishlinskii model for characterizing the hysteresis and saturation nonlinearities of smart actuators". In: *Smart Materials and Structures* 18(4), p. 045001 (cit. on pp. 13, 16).

Janaideh, M.A., Rakheja, S., and Su, C.-Y. (2009b). "Experimental characterization and modeling of rate-dependent hysteresis of a piezoceramic actuator". In: *Mechatronics* 19(5), pp. 656 –670 (cit. on p. 12).

Jandt, K. D., Finke, M., and Cacciafesta, P. (2000). "Aspects of the physical chemistry of polymers, biomaterials and mineralised tissues investigated with atomic force microscopy (AFM)". In: *Colloids and Surfaces B: Biointerfaces* 19(4), pp. 301 –314 (cit. on p. 6).

Jiles, D.C. and Atherton, D.L. (1986). "Theory of ferromagnetic hysteresis". In: *Journal of Magnetism and Magnetic Materials* 61(1–2), pp. 48 –60 (cit. on p. 12).

Jung, H. and Gweon, D.-G. (2000). "Creep characteristics of piezoelectric actuators". In: *Review of Scientific Instruments* 71(4), pp. 1896–1900 (cit. on p. 14).

Jung, H., Shim, J.Y., and Gweon, D.-G. (2001). "Tracking control of piezoelectric actuators". In: *Nanotechnology* 12(1), 14–20 (cit. on p. 17).

Karny, M. (2006). *Optimized Bayesian Dynamic Advising: Theory and Algorithms*. Secaucus, NJ, USA: Springer-Verlag New York, Inc. (cit. on p. 56).

Krejci, P. and Kuhnen, K. (2001). "Inverse control of systems with hysteresis and creep". In: *IEE Proceedings - Control Theory and Applications* 148(3), pp. 185–192 (cit. on p. 17).

Kuhnen, K. (2003). "Modeling, identification and compensation of complex hysteretic nonlinearities: A modified Prandtl-Ishlinskii approach". In: *European Journal of Control* 9(4), 407–418 (cit. on p. 13).

Kuhnen, K. and Janocha, H. (1999). "Adaptive inverse control of piezoelectric actuators with hysteresis operators". In: *1999 European Control Conference (ECC 1999)*, pp. 791–796 (cit. on p. 16).

Kuhnen, K. and Janocha, H. (2001). "Inverse feedforward controller for complex hysteretic nonlinearities in smart-materials systems". In: *Control and and Intelligent Systems* 29(3), pp. 74–83 (cit. on p. 16).

Kuiper, S., Fleming, A., and Schitter, G. (2010). "Dual actuation for high speed atomic force microscopy". In: *5th IFAC Symposium on Mechatronic Systems*, pp. 220–226 (cit. on p. 18).

Kwakernaak, H. (1972). *Linear Optimal Control Systems*. John Wiley and Sons, Inc (cit. on pp. 18, 66).

Landau, I. D. and G., Zito (2006). *Digital Control Systems: Design, Identification and Implementation*. Springer-Verlag (cit. on pp. 92, 95–97, 104).

Leang, K.K. and Devasia, S. (2007). "Feedback-Linearized Inverse Feedforward for Creep, Hysteresis, and Vibration Compensation in AFM Piezoactuators". In: *IEEE Transactions on Control Systems Technology* 15(5), pp. 927–935 (cit. on p. 17).

Li, Ch.-X., Gu, G.-Y., Yang, M.-J., and Zhu, L.-M. (2013a). "Design, analysis and testing of a parallel-kinematic high-bandwidth XY nanopositioning stage". In: *Review of Scientific Instruments* 84(12), 125111(1–12) (cit. on p. 15).

Li, P., Yan, F., Ge, Ch., Wang, X., Xu, L., Guo, J., and Li, Pe. (2013b). "A simple fuzzy system for modelling of both rate-independent and rate-dependent hysteresis in piezoelectric actuators". In: *Mechanical Systems and Signal Processing* 36(1), pp. 182 –192 (cit. on p. 13).

Lin, Ch.-J. and Lin, P.-T. (2012). "Tracking control of a biaxial piezo-actuated positioning stage using generalized Duhem model". In: *Computers and Mathematics with Applications* 64(5), pp. 766 –787 (cit. on p. 12).

Mahmood, I.A. and Moheimani, S.O.R. (2009a). "Fast spiral-scan atomic force microscopy". In: *Nanotechnology* 20(36), 365503–365507 (cit. on pp. 18, 102).

Mahmood, I.A. and Moheimani, S.O.R. (2009b). "Improvement of accuracy and speed of a commercial AFM using positive position feedback control". In: *2009 American Control Conference (ACC 2009)*, pp. 973–978 (cit. on p. 17).

Mahmood, I.A. and Moheimani, S.O.R. (2009c). "Making a commercial atomic force microscope more accurate and faster using positive position feedback control". In: *Review of Scientific Instruments* 80(6), pp. 063705–13 (cit. on p. 18).

Mayergoyz, I.D. (1988). "Dynamic Preisach models of hysteresis". In: *IEEE Transactions on Magnetics* 24(6), pp. 2925–2927 (cit. on p. 13).

Merry, R., Uyanik, M., Koops, R., Molengraft, R. van de, Veghel, M. van, and Steinbuch, M. (2008). "Modeling, identification and control of a metrological Atomic Force Microscope with a 3DOF stage". In: *2008 American Control Conference (ACC 2008)*, pp. 2716–2721 (cit. on p. 19).

Moheimani, S.O.R. (2008). "Accurate and fast nanopositioning with piezoelectric tube scanners: emerging trends and future challenges". In: *Review of Scientific Instruments* 79(7), p. 071101 (cit. on p. 15).

Munteanu, E. and Ursu, I. (2008). "Piezo Smart Composite Wing with LQG/LTR Control". In: *IEEE International Symposium on Industrial Electronics, (ISIE 2008)*, pp. 1160–1165 (cit. on pp. 18, 66).

Necipoglu, S., Cebeci, S.A., Basdogan, C., Has, Y.E., and Guvenc, L. (2011). "Repetitive control of an XYZ piezo-stage for faster nano-scanning: Numerical simulations and experiments". In: *Mechatronics* 21(6), pp. 1098 –1107 (cit. on p. 17).

Pedrak, R., Ivanov, T., Ivanova, K., Gotszalk, T., Abedinov, N., Rangelow, I. W., Edinger, K., Tomerov, E., Schenkel, T., and Hudek, P. (2003). "Micromachined atomic force microscopy sensor with integrated piezoresistive sensor and thermal bimorph actuator for high-speed tapping-mode atomic force microscopy phase-imaging in higher eigenmodes". In: *Journal of Vacuum Science and Technology B* 21(6), pp. 3102–3107 (cit. on p. 19).

Rakotondrabe, M. (2011). "Bouc-Wen Modeling and Inverse Multiplicative Structure to Compensate Hysteresis Nonlinearity in Piezoelectric Actuators". In: *IEEE Transactions on Automation Science and Engineering* 8(2), pp. 428–431 (cit. on pp. 12, 16).

Rakotondrabe, M., Clevy, C., and Lutz, P. (2010). "Complete Open Loop Control of Hysteretic, Creeped, and Oscillating Piezoelectric Cantilevers". In: *IEEE Transactions on Automation Science and Engineering* 7(3), pp. 440–450 (cit. on pp. 16, 37).

Ryba, L., Voda, A., and Besancon, G. (2013). "Modelling and control of 3D STM-like scanning device with application to surface reconstruction". In: *Methods and Models in Automation and Robotics (MMAR), 2013 18th International Conference on*, pp. 479–484 (cit. on pp. 20, 117).

Ryba, L., Voda, A., and Besancon, G. (2014a). "3DOF nanopositioning control of an experimental tunneling current-based platform". In: *2014 IEEE Conference on Control Applications (CCA 2014, part of MSC 2014)*, pp. 1976–1981 (cit. on pp. 36, 92).

Ryba, L., Voda, A., and Besancon, G. (2014b). "An LQG/LTR approach towards piezoactuator vibration reduction with observer-based hysteresis compensation". In: *Proceedings of the 19th IFAC World Congress (IFAC 2014)*, pp. 5623–5628 (cit. on pp. 17–19, 36).

Ryba, L., Dokoupil, J., Voda, A., and Besancon, G. (2015a). "A real-time inverse-based hysteresis compensation with adaptation". In: *54th IEEE Conference on Decision and Control (CDC 2015) (accepted)* (cit. on pp. 36, 53).

Ryba, L., Voda, A., and Besancon, G. (2015b). "Experimental comparison of disturbance observer and inverse-based hysteresis compensation in 3D nanopositioning piezoactuation". In: *Sensors and Actuators A: Physical* 236, pp. 190–205 (cit. on pp. 36, 46).

Safonov, M.G. and Athans, M. (1977). "Gain and phase margin for multiloop LQG regulators". In: *IEEE Transactions on Automatic Control* 22(2), pp. 173–179 (cit. on pp. 18, 65).

Salapaka, M.V., Bergh, H.S., Lai, J., Majumdar, A., and McFarland, E. (1997). "Multi-mode noise analysis of cantilevers for scanning probe microscopy". In: *Journal of Applied Physics* 81(6), pp. 2480 –2487 (cit. on pp. 30, 121).

Schitter, G., Stark, R.W., and Stemmer, A. (2002). "Sensors for closed-loop piezo control: strain gauges versus optical sensors". In: *Measurement Science and Technology* 13(4), N47–N48 (cit. on p. 19).

Schitter, G., Thurner, P.J., and Hansma, P.K. (2008a). "Design and input-shaping control of a novel scanner for high-speed atomic force microscopy". In: *Mechatronics* 18(5–6), pp. 282 –288 (cit. on pp. 17, 18).

Schitter, G., Rijkee, W.F., and Phan, N. (2008b). "Dual actuation for high-bandwidth nanopositioning". In: *47th IEEE Conference on Decision and Control (CDC 2008)*, pp. 5176–5181 (cit. on p. 18).

Schneir, J., McWaid, T.H., Alexander, J., and Wilfley, B.P. (1994). "Design of an atomic force microscope with interferometric position control". In: *Journal of Vacuum Science and Technology B* 12(6), pp. 3561–3566 (cit. on p. 19).

Sebastian, A. and Salapaka, S.M. (2005). "Design methodologies for robust nano-positioning". In: *IEEE Transactions on Control Systems Technology* 13(6), pp. 868–876 (cit. on pp. 11, 18, 66).

Shan, Y. and Leang, K.K. (2012). "Accounting for hysteresis in repetitive control design: Nanopositioning example". In: *Automatica* 48(8), pp. 1751 –1758 (cit. on p. 12).

Shi, J., Wu, Y., Su, Ch., and Zou, Q. (2009). "A control approach to cross coupling compensation of piezotube scanners in tapping-mode imaging". In: vol. 7378, 73781E–73781E–10 (cit. on pp. 15, 18, 113).

Silverman, L.M. (1969). "Inversion of multivariable linear systems". In: *IEEE Transactions on Automatic Control* 14(3), pp. 270–276 (cit. on p. 17).

Skogestad, S. and Postlethwaite, I. (2005). *Multivariable Feedback Control: Analysis and Design*. John Wiley & Sons (cit. on pp. 78, 85).

Smith, R. and Ounaie, Z. (2000). "A domain wall model for hysteresis in piezoelectric materials". In: *Journal of Intelligent Material Systems and Structures* 11(1), 62–79 (cit. on p. 12).

Stark, R.W., Schitter, G., Stark, M., Guckenberger, R., and Stemmer, A. (2004). "State-space model of freely vibrating and surface-coupled cantilever dynamics in atomic force microscopy". In: *Physical Review B* 69(8), pp. 085412–085421 (cit. on p. 28).

Sun, L., Ru, Ch., Rong, W., Chen, L., and Kong, M. (2004). "Tracking control of piezoelectric actuator based on a new mathematical model". In: *Journal of Micromechanics and Microengineering* 14(11), p. 1439 (cit. on p. 13).

Sun, Y. and Pang, J.H.L. (2006). "AFM image reconstruction for deformation measurements by digital image correlation". In: *Nanotechnology* 17(4), 933–939 (cit. on p. 17).

Tan, X. and Baras, J.S. (2005). "Adaptive identification and control of hysteresis in smart materials". In: *IEEE Transactions on Automatic Control* 50(6), pp. 827–839 (cit. on p. 16).

Tan, X. and Bennani, O. (2008). "Fast inverse compensation of Preisach-type hysteresis operators using field-programmable gate arrays". In: *2008 American Control Conference (ACC 2008)*, pp. 2365–2370 (cit. on p. 16).

Tien, S., Zou, Q., and Devasia, S. (2004). "Control of dynamics-coupling effects in piezoactuator for high-speed AFM operation". In: *2004 American Control Conference (ACC 2004)*. Vol. 4, pp. 3116–3121 (cit. on pp. 15, 18).

Tsukada, M., Kobayashi, N., Brandbyge, M., and Nakanishi, S. (2000). "Physics of artificial nano-structures on surfaces". In: *Progress in Surface Science* 64(3–8), pp. 139 –155 (cit. on p. 6).

Tuma, T., Lygeros, J., Kartik, V., Sebastian, A., and Pantazi, A. (2012). "High-speed multiresolution scanning probe microscopy based on Lissajous scan trajectories". In: *Nanotechnology* 23(18), 185501–185510 (cit. on p. 18).

Wu, Y. and Zou, Q. (2007). "Iterative Control Approach to Compensate for Both the Hysteresis and the Dynamics Effects of Piezo Actuators". In: *IEEE Transactions on Control Systems Technology* 15(5), pp. 936–944 (cit. on p. 17).

Xie, H., Onal, C., Régnier, S., and Sitti, M. (2012). *Atomic Force Microscopy Based Nanorobotics*. Springer-Verlag (cit. on p. 6).

Xu, Q. and Li, Y. (2010). "Dahl Model-Based Hysteresis Compensation and Precise Positioning Control of an XY Parallel Micromanipulator With Piezoelectric Actuation". In: *Journal of Dynamic Systems, Measurement, and Control* 132(4), p. 041011 (cit. on p. 12).

Yamanaka, K., Noguchi, A., Tsuji, T., Koike, T., and Goto, T. (1999). "Quantitative material characterization by ultrasonic AFM". In: *Surface and Interface Analysis* 27(5-6), pp. 600–606 (cit. on p. 6).

Yeh, T.-J., Wang, Ch.-D., and Wu, T.-Y. (2008). "Modeling and control of an atomic force microscope using a piezoelectric tuning fork for force sensing". In: *Simulation Modelling Practice and Theory* 16(7), pp. 768 –782 (cit. on pp. 18, 66).

Yi, J., Chang, S., and Shen, Y. (2009). "Disturbance-Observer-Based Hysteresis Compensation for Piezoelectric Actuators". In: *IEEE/ASME Transactions on Mechatronics* 14(4), pp. 456–464 (cit. on pp. 17, 35).

Yong, Y.K., Moheimani, S.O.R., and Petersen, I.R. (2010a). "High-speed cycloid-scan atomic force microscopy". In: *Nanotechnology* 21(36), 365503–365507 (cit. on p. 18).

Yong, Y.K., Liu, K., and Moheimani, S.O.R. (2010b). "Reducing Cross-Coupling in a Compliant XY Nanopositioner for Fast and Accurate Raster Scanning". In: *IEEE Transactions on Control Systems Technology* 18(5), pp. 1172–1179 (cit. on pp. 15, 18).

Zou, Q., Leang, K., Sadoun, E., Reed, M., and Devasia, S. (2004). "Control Issues in High-speed AFM for Biological Applications: Collagen Imaging Example". In: *Asian Journal of Control* 6(2), pp. 164–178 (cit. on p. 6).